Author:
Randall, Simon Robert

Title:
An investigation of processes which mediate the mobility of arsenic, cadmium, and chromium in soils and sediments.

An investigation of processes which mediate the mobility of arsenic, cadmium, and chromium in soils and sediments

Simon Robert Randall

A thesis submitted to the University of Bristol in accordance with the requirements of the degree of Ph.D. in the Faculty of Science.

Department of Earth Sciences

July 1999

Word count: 65,397

Abstract

Arsenic, cadmium and chromium are significant anthropogenic contaminants. This work provides an insight into the short- and longer term controls on their mobility.

Cadmium is known to be strongly adsorbed by iron and manganese oxyhydroxides. Extended X-ray absorption fine structure (EXAFS) spectroscopy and *ab initio* quantum mechanical calculations have shown that whilst cadmium prefers to adsorb to iron oxyhydroxides *via* 'edge-' rather than 'corner sharing' mechanisms, mineral morphology exerts a strong control on the relative importance of each mechanism. Cadmium has been shown to sorb on cryptomelane (KMn_8O_{16}) by exchanging with protons in the structural tunnels that this mineral possesses.

Ferrihydrite is a metastable iron oxyhydroxide that is known to be a very effective sorbent of As(V) and Cr(III). Over time it ages into more crystalline phases such as goethite (α-FeOOH) and/or hematite (α-Fe_2O_3). Arsenic is not released to solution during the ageing of As(V)-contaminated ferrihydrite, and all arsenic remains as surface complexes throughout the ageing process. Conversely, Cr(III) that is present during ferrihydrite nucleation forms a discrete $Cr(OH)_3{\cdot}nH_2O$ precipitate as this mineral ages, and ageing is accompanied by a persistent release of aqueous chromium. Increases in As(V) and Cr(III) loading retard the phase transformation process.

Green rust ($Fe_2^{(II)}Fe^{(III)}(OH)_5(SO_4)$) is of potentially great importance to trace metal mobility because of its mixed valence. However, As(V) is not reduced by this material, regardless of whether it is introduced before or after green rust nucleation. In contrast, Cr(VI) undergoes instantaneous reduction to Cr(III) following interaction with green rust.

Sulphidisation of As(V)-contaminated goethite results in the rapid reduction of As(V) and the formation of poorly crystalline mackinawite ($Fe_{1+x}S$). EXAFS analysis shows that the first coordination shell around As(III) is identical to that in poorly crystalline orpiment (As_2S_3).

Dedication and acknowledgements

This work is dedicated to my friends and family.

I am immensely grateful to my supervisors, Vala Ragnarsdottir and Dave Sherman, for all the assistance, guidance, opportunities and challenges that they have provided me with throughout my Ph.D. They have helped me to develop as a scientist and thereby undertake work that I am very proud of. However, it is the personal development that I have undergone whilst working with them that I will value the most in years to come.

All Bristol-based laboratory work was funded by British Nuclear Fuels plc., and the following BNFL staff are thanked for their assistance: Katherine Prastka, Anna Braithwaite and Rebecca Robins. The EXAFS data were collected exclusively at the Synchrotron Radiation Source (SRS) in Daresbury, Cheshire, UK. This was made possible by funding from EPSRC and the generous assistance of the following SRS staff: Bob Bilsborrow, Andy Dent, Fred Mosselmans, Lorrie Murphy and Gert van Dorrsen.

All sample preparation and non-EXAFS characterisation took place at the University of Bristol. Tony Kemp, Kim Goodman and John Dimery are thanked for their assistance with the ICP-MS, ICP-AES and surface area work, respectively. I am also indebted to Dudley Thompson and Roger Vincent for their time and effort in collecting the TEM images. Dr. Vincent also collected electron diffraction data from goethite and provided very helpful insights into its crystallography. Kim Goodman and Ian Mather provided invaluable help with UV-vis spectrophotometry, and Liz Loeffler (Department of Earth Sciences) provided samples of scorodite and orpiment for use as EXAFS reference standards.

I thank two anonymous reviewers for their constructive comments on the manuscript of chapter 3, and I am grateful of the direction provided by Igor Diakonov, Eric Oelkers and an anonymous reviewer whilst preparing the manuscript of chapter 4.

Author's declaration

I declare that the work in this dissertation was carried out in accordance with the Regulations of the University of Bristol. The work is original except where stated and referenced accordingly, and no part of the dissertation has been submitted for any other degree. The views expressed in this dissertation are those of the author and in no way represent those of the University of Bristol.

The dissertation has not been presented to any other University for examination either in the United Kingdom or overseas.

Signed ..... Date 1st June 1999.

Table of Contents

Abstracts of published papers

- An EXAFS Investigation of Cadmium Sorption on Cryptomelane (KMn_8O_{16}). Chemical Geology 151, 95-106 (1998)
- An EXAFS Investigation of the Mechanisms of Cadmium Attenuation on Fe and Mn (Oxyhydr)oxide Minerals. Mineralogical Magazine 62 A, pp. 1231-1232 (1998)
- The Mechanism of Cadmium Surface Complexation on Iron Oxyhydroxide Minerals. Geochimica et Cosmochimica Acta, *in press.*

Appendix

List of Figures

List of Tables

Chapter 1

The environmental geochemistry of arsenic, cadmium and chromium

1.0 INTRODUCTION

This chapter is an overview of the environmental geochemistry of arsenic, cadmium and chromium. It outlines the factors which have previously been identified in field and laboratory studies that exert the most significant control on the mobility of these three elements. The subsequent results chapters focus on a number of these factors in order to improve our understanding of the way that arsenic, cadmium and chromium behave on both short and long timescales in contaminated sediments and soils.

1.1 ARSENIC IN THE ENVIRONMENT

1.1.1 Introduction

Arsenic is widely distributed in nature. The natural background level of arsenic in soils ranges between 0.1 - 50 ppm (mean 5 - 6ppm) (Vinogradov, 1959; Backer and Chesnin, 1975; Bowen, 1979), but can reach far higher levels in contaminated soils. Arsenic has long been recognised as a toxin and carcinogen (Hering, 1994). Arsenic poisoning is known to result in melanosis, leucomelanosis, keratosis, hyperkeratosis, dorsum, non-petting oedema, gangrene and skin cancer (Mandal et al., 1996). It is also linked to the development of cancers on internal organs such as the bladder and lungs (Mandal et al., 1996). In recognition of the potential health risks associated with arsenic, the recommended maximum drinking water limit for arsenic is 10 ppb (WHO, 1993).

1.1.2 Sources of arsenic

1.1.2.1 Natural sources

As can be seen from Table 1.1, rocks contain by far the largest amount of arsenic, with relatively minor amounts in the oceans, soil, biota and atmosphere.

Under natural conditions, the main source of arsenic to the environment is weathering of parent geological materials. Arsenic is present in many clay minerals, phosphorites and manganese ores, but is especially concentrated in magmatic sulphide ores. The most important ores of arsenic are minerals such as arsenopyrite (FeAsS), realgar (AsS) and orpiment (As_2S_3). These minerals are often found in association with sulphide ores of other metals (e.g. in solid solution with pyrite, FeS_2), and hence terrains rich in sulphide-bearing strata can display elevated levels of arsenic in river and ground waters due to sulphide oxidation (Nriagu, 1994; Smedley et al., 1995) (Table 1.1). Mining activities can vastly increase the rate and extent of sulphide oxidation, and the resulting 'acid mine drainage' sediments can contain > 2000 ppm arsenic in some fractions (Bigham et al., 1990; Table 1.1).

Arsenic levels are increased by accumulation during weathering processes and translocation in colloidal fractions (Iimura, 1981). Hence, arsenic levels in shales (14.5 ppm on average; Bhumbla and Keefer, 1994), sediments (100-300 ppm; Branson and Patrick, 1987) and soils (7.2 ppm, Bhumbla and Keefer, 1994) are enriched relative to the 1.8 ppm crustal average (Iimura, 1981). Where not present in primary minerals, soil arsenic is often contained in secondary sedimentary minerals such as Al-, Ca-, Fe-, Mn- or Pb-arsenates (Yan-Chu, 1994).

Bangladesh and West Bengal are currently experiencing widespread poisoning from naturally occurring arsenic in drinking water abstracted from tube wells (Mandal et al., 1996). These provide 95% of Bangladesh's drinking water, and are sunk 20 to 100 metres into the fine alluvial sediments of the Ganges delta. The worst affected areas are located in the upper delta plain, mostly in the abandoned meander belt (Das et al., 1996). The major source of arsenic in the deltaic sediments is thought to be authigenic pyrite which can contain thousands of ppm arsenic. It seems that pumping from the tube wells has drawn down oxygenated water which has caused the oxidation of pyrite and the release of arsenic (Chakraborti, pers. comm.). Around 45% of the tube wells are producing water with an arsenic content greater than 50 ppb (the WHO's maximum permissible limit; WHO, 1993) (Mandal et al., 1996). This has profound consequences for human health; affected populations are now 80 million (out of 120 million) in Bangladesh and 9 million (out of 68 million) in West Bengal (Chakraborti, pers. comm). Additionally, the visible signs of disease are just the tip of the ice berg because external, skin-related problems present after internal organs have been affected (Chakraborti, pers. comm).

Table 1.1. The distribution of arsenic between different reservoirs and the abundance of arsenic in common rocks, sediments and soils.

Reservoir	**Approximate ratio with respect to soil**
Rocks	25,000
Oceans	4
Soil	1
Biota (plants, man, microbes)	0.0005
Atmosphere	0.000001
Rock type	**Average arsenic concentration (ppm)**
Crustal average	1.8[1]
Igneous	1.5
Limestone	2.6
Sandstone	4.1
Shale	14.5 (0.3 to 500 ppm range)
Average sediments	100-300[2]
$Fe(OH)_3(s)$ from rich acid mine drainage sediments	> 2000[3]
Average world soils	7.2 ppm
Soils close to/derived from sulphide ore deposits	8000[4]

All data from Bhumbla and Keefer (1994) except for [1] Iimura (1981); [2] Branson and Patrick (1987); [3] Bigham et al. (1990); [4] Levander (1977).

1.1.2.2 Anthropogenic sources

Arsenic may accumulate in soils through mining activities, the use of arsenical pesticides, application of fertilisers, irrigation, dust, the burning of fossil fuels and the disposal of industrial and animal wastes (Nriagu, 1994). The anthropogenic influence on the level of arsenic in soils depends on the intensity of human activity, the distance from the pollution sources, and the pollutant dispersion pattern (Yan-Chu, 1994).

1.1.3 The form of arsenic in the environment

Arsenic occurs naturally in the environment in oxidation states ranging between -3 and +5 (Smedley et al, 1995). However, in sediment-water and soil environments arsenic commonly exists in only the mono-, tri-, and pentavalent oxidation states:

As(V)	Arsenate
As(III)	Arsenite, and monomethyl arsonic acid (MMAA)
As(I)	Dimethyl arsinic acid (DMAA)

In natural waters, the organic forms of arsenic are relatively unimportant in comparison to inorganic As(III) and As(V) (Smedley et al., 1995). However, it has been suggested that methylated organic oxyacids (MMAA and DMAA) can be produced by a variety of organisms and their presence has been reported in a range of natural waters (Braman and Foreback, 1973; Andreae and Klumpp, 1979) and soils and sediments (Woolson, 1977).

It is clear from Fig. 1.1 that arsenic is stable in dissolved form over a wide range of Eh-pH space. Under conditions normally encountered in natural aqueous environments, the most common forms of inorganic arsenic are the arsenate oxyanions $H_2AsO_4^-$ and $HAsO_4^{2-}$ and the neutral arsenite species $H_3AsO_3^0$ (Masscheleyn, 1991b). Stability constants for these species are shown in Table 1.2.

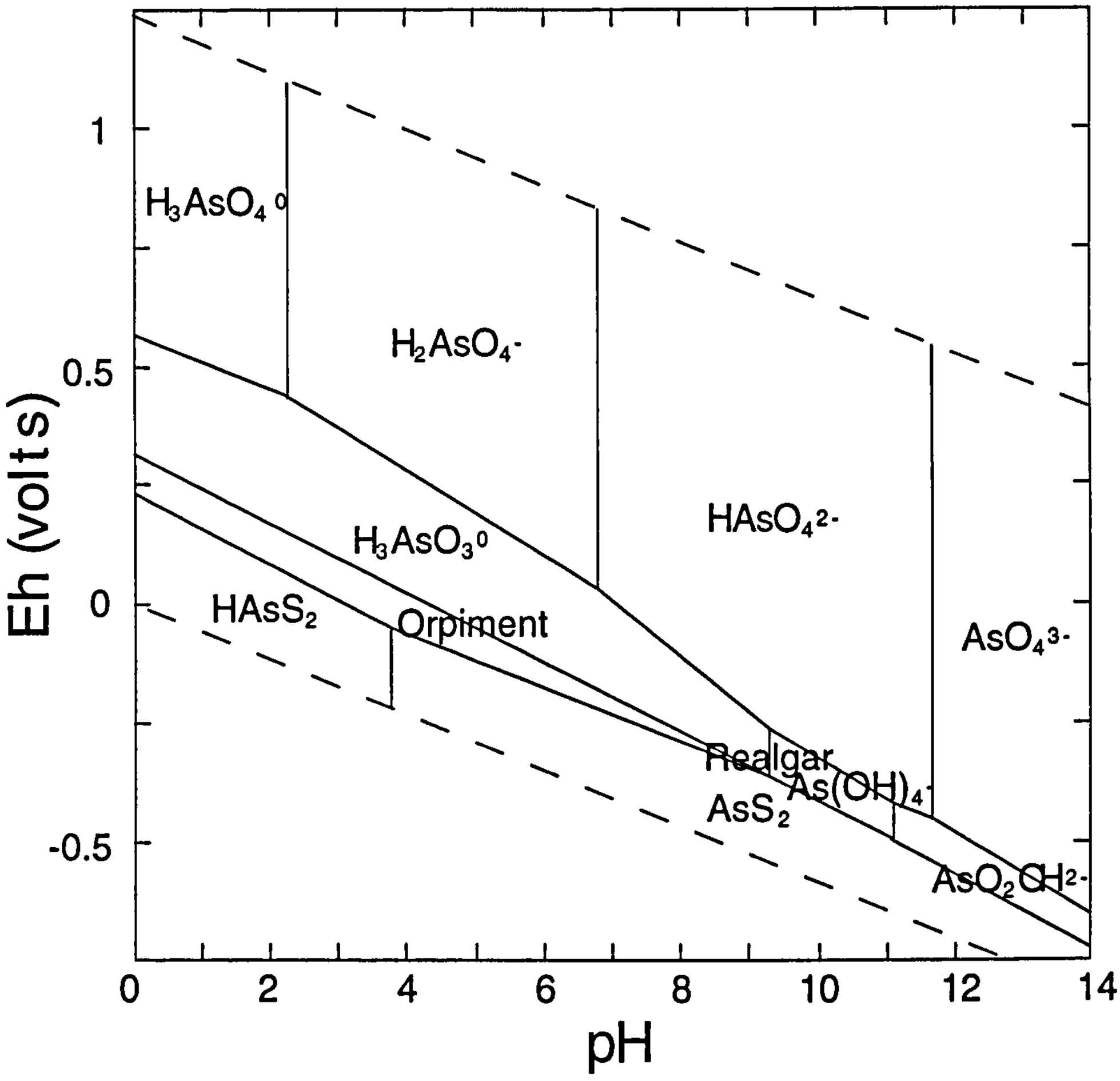

Fig. 1.1. Eh-pH diagram for part of the system As-C-S-O-H at 25°C and 1 atmosphere. The assumed activities are: As = 10^{-8}; C = 10^{-3}; S = 10^{-3}. It can be seen that arsenic is stable in dissolved form over a relatively wide range of Eh-pH space.

Table 1.2 Stability constants for arsenic species commonly found in the environment

Species	log K
As(V)	
$HAsO_4^{2-} + 2H^+ = H_3AsO_4^0$	9.1
$H_2AsO_4^- + H^+ = H_3AsO_4^0$	2.243
As(III)	
$H_2AsO_3^- + H^+ = H_3AsO_3^0$	9.228

Data from Appelo and Potsma (1993) Geochemistry, ground water and pollution, Appendix B. Balkema.

As(III) is much more toxic, soluble and mobile than As(V) (Yan-Chu, 1994). In general, the speciation, solubility, mobility, bioavailability and toxicity of arsenic depends on its oxidation state, and hence an understanding of the Eh - pH dependent transformations between various species is essential to our knowledge of arsenic behaviour in the environment (Masscheleyn et al., 1991b).

1.1.4 Factors controlling arsenic speciation and solubility

1.1.4.1 The effect of Eh conditions

Under oxidising conditions (200 - 500 mV), 65 - 95 % of dissolved arsenic exists as As(V) (Fig. 1.1). A strong correlation has been observed between levels of dissolved arsenic and iron in solution, suggesting that iron oxyhydroxides play an important role in controlling arsenic solubility under oxidising neutral to mildly acidic conditions (Masscheleyn et al., 1991a,b; Marin et al., 1993). The correlation between levels of soluble iron and arsenic suggests that As(V) species coprecipitate with iron oxyhydroxide. If this is the case, As(V) could only be released back to solution upon reductive dissolution of the host iron oxyhydroxide. However, an increase in soluble arsenic has been observed to precede dissolution (Masscheleyn et al., 1991b). This is probably due to desorption of any arsenic that was initially adsorbed rather than coprecipitated with the iron oxyhydroxide (Masscheleyn et al.,1991b). No correlation has been observed between soluble arsenic and aluminium or manganese concentrations, and oxidised suspensions are generally undersaturated with respect to Fe-, Al-, Mn-, Ca-, and Mg-arsenates. These observations indicate that neither aluminium- nor manganese oxides or the arsenates control arsenic concentrations in oxic soil and sediment environments (Masscheleyn et al., 1991a,b).

The more mobile As(III) species begins to dominate over the pentavalent form when Eh falls to between 0 and 200 mV. However, the greatest concentrations of soluble arsenic are generally found under the most reducing conditions (-200 mV), where levels of soluble arsenic can often be ten to twenty times greater than under oxidising conditions of equivalent pH (Masscheleyn, 1991a,b; Marin et al., 1993). Under highly reducing conditions, soluble arsenic concentrations often undergo a sudden decrease, and it has been suggested that this may be due to the formation of arsenic sulphides (Moore et al., 1988). Additionally, MnOOH becomes thermodynamically unstable under reducing conditions, and very small amounts of As(V) would be required to obtain saturation with respect to manganese arsenate minerals. Hence Masscheleyn et al. (1991b) suggest that the formation of

$Mn_3(AsO_4)_2$ could set an upper limit to dissolved arsenic concentrations under reducing conditions.

Arsenic is known to substitute for both iron and sulphur in pyrite, and it can account for up to 9 mole % (Kolker, pers. comm.). Thus, it is not surprising that the oxidation of authigenic pyrite in River Ganges deltaic sediments is resulting in serious arsenic contamination (Chakraborti pers. comm.). What is surprising is that the iron oxyhydroxides formed during pyrite oxidation do not appear to be acting as an effective sorbent of the released arsenic (Chakraborti pers. comm.). A possible explanation for this centres on the fact that arsenic will be present in pyrite as As(III). Once in solution, this is only weakly sorbed by iron oxyhydroxides in comparison to As(V). Since Chakraborti (pers. comm.) reports that the highest arsenic mobility is associated with oxygen-poor (but not anoxic) waters, it seems likely that in this case there is insufficient oxygen to generate As(V). Hence, arsenic remains highly mobile as As(III) and can be transported to drinking water supplies. Abiotic reactions do not appear to be involved in the release or transport of arsenic because it appears at the surface as inorganic arsenate or arsenite (Mandal et al., 1996) and not DMAA or MMAA (Chatterjee et al., 1995).

1.1.4.2 The effect of pH conditions

The redox equilibrium of arsenic is pH-dependent (Ferguson and Gavis, 1972; Fig. 1.1), and hence pH as well as Eh has a direct effect on arsenic speciation in solution (Pierce and Moore, 1982). The adsorption of arsenic species onto geological materials is also highly pH-dependent. The As(III) species (present as $H_3AsO_4^0$ up to pH 9) shows an adsorption maximum on most metal oxides and hydroxides at about pH 6 to 7 (Fig. 1.2) (Xu et al., 1988).

The extent of adsorption of the As(V) oxyanions ($HAsO_4^{-2}$ and $H_2AsO_4^-$) is generally greater than that of As(III) species (Xu et al., 1991). Adsorption of the negatively charged As(V) oxyanions is favoured under low pH conditions when the net positive mineral surface charge is high. Increasingly alkaline conditions cause a drastic decrease in As(V) adsorption as mineral surface charge becomes increasingly negative (Anderson et al., 1976; Pierce and Moore, 1982; Xu et al., 1988).

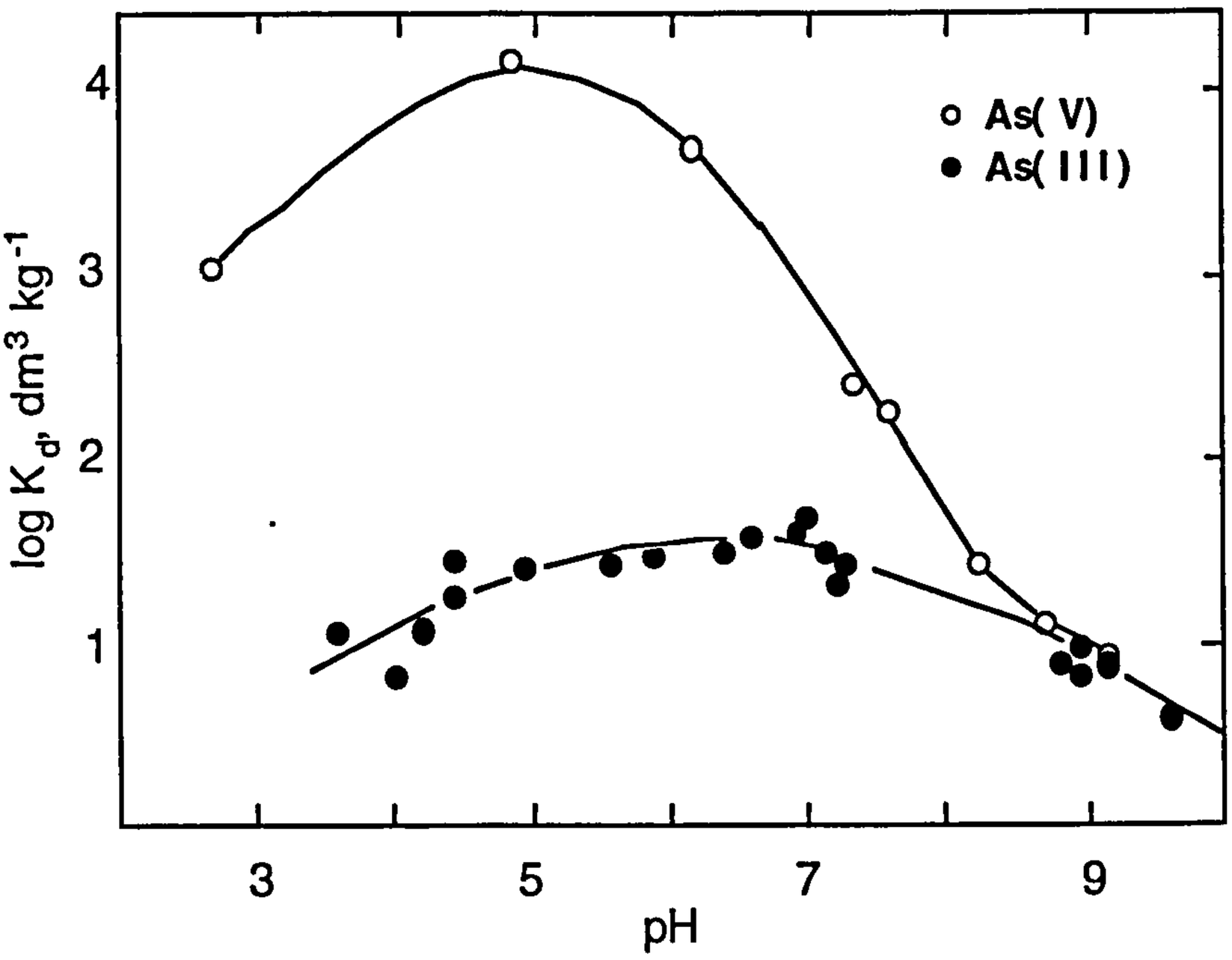

Fig. 1.2. Adsorption of As(V) and As(III) on alumina as a function of pH. [As(V)] and [As(III)] = 10^{-6} M. It is clear that the amount of As(V) oxyanion adsorption is significantly greater than that of the neutral As(III) species, and that adsorption of As(V) oxyanions is favoured at lower pH values where net mineral surface charge becomes increasingly positive. K_d is the distribution coefficient, and represents the ratio of adsorbed metal : metal in solution. From Xu et al. (1991).

Alumina (Al_2O_3) and hematite (Fe_2O_3) are significant adsorbents of arsenic since their net surface charge is positive below their pH_{ZPC} (pH of zero point of charge) values (~pH 6.5 - 7) (Xu et al., 1991; Fig. 1.3). Conversely, quartz has a net negative surface charge under most natural pH conditions because it has a pH_{ZPC} of ~ 2. Hence, it is not a favourable adsorbent for the predominantly negative and neutrally charged arsenic species (Xu et al., 1991) (Fig. 1.3).

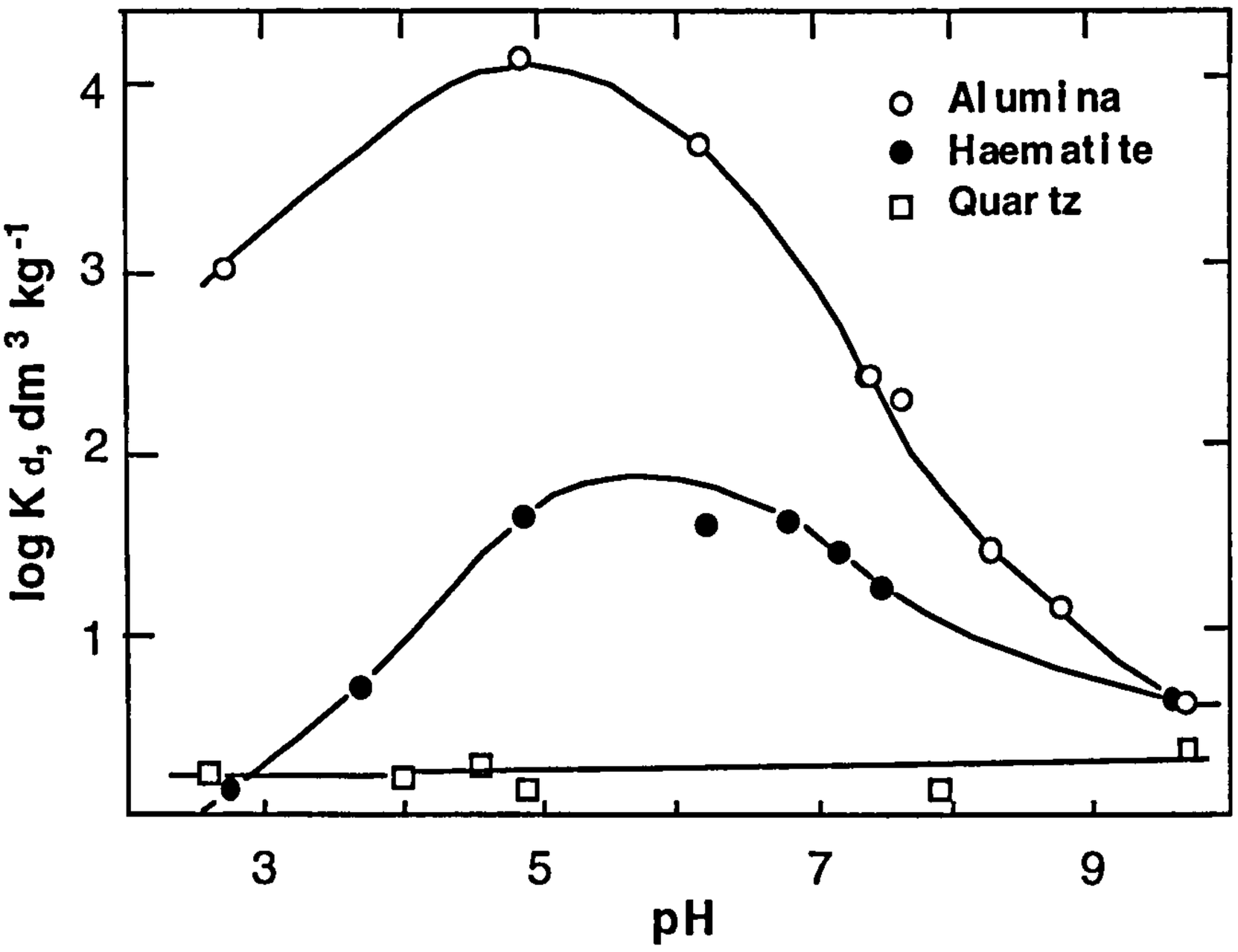

Fig. 1.3. Adsorption of As(V) on alumina, hematite and quartz. Alumina and hematite have pH_{ZPC} values in the range 6.5 - 7. The net positive surface charge developed under more acidic conditions makes them attractive adsorbents for As(V) oxyanions from solution. Quartz is not an important adsorbent of As(V) since it has a particularly low pH_{ZPC} value of 2 - 2.5. K_d is the distribution coefficient, and represents the ratio of adsorbed metal : metal in solution. From Xu et al. (1991).

The decrease in As(V) adsorption at very low values of pH (Fig. 1.3) is probably due to a shift in the $H_3AsO_4^0$: $H_2AsO_4^-$ ratio with decreasing pH (Fig. 1.1). Xu et al. (1991) suggest that the formation of positively charged $[Al\text{-}H_2AsO_4]^{2+}$ or $[Fe\text{-}H_2AsO_4]^{2+}$ complexes with solubilised Al^{3+} and Fe^{3+} may also contribute to this effect.

Although crystalline iron oxides such as hematite can clearly adsorb significant amounts of arsenic, amorphous iron oxyhydroxides have an even higher sorption capacity (Bowell, 1994). This is not surprising since the poorly crystalline, amorphous oxides and hydroxides of iron (and aluminium) possess a broad range of different sorption sites, and reactive surface areas are much greater than that of the equivalent crystalline phases.

1.1.4.3 The effect of organic acids

Xu et al. (1991) have found that the presence of fulvic acid (FA) generally decreases the adsorption of arsenic in the pH range of 4 to 8. As(V) adsorption is decreased most markedly at relatively high (≥ 25 ppm) FA concentrations because the FA anions can successfully compete for adsorption sites under such conditions. In contrast, As(III) adsorption is slightly decreased at lower (~ 10 ppm) but not

higher FA levels. The effects of FA under strongly acidic and basic conditions are minor (Xu et al., 1991).

1.1.5 Arsenic in the environment: Summary

The Eh-pH-dependent speciation of arsenic in solution largely determines its mobility since As(V) species are less soluble than As(III) species, and the different species display substantial differences in their adsorption behaviour (Fig. 1.2). Variations in the amount of arsenic in solution appear to be related to transformations between species, adsorption/desorption reactions, and the coprecipitation/dissolution of various mineral phases with changing Eh-pH conditions.

Iron oxyhydroxides generally limit the mobility of arsenic under oxic conditions by adsorbing or coprecipitating it as As(V). However, as witnessed in Bangladesh and West Bengal, the mobility of any As(III) which persists under oxic conditions will only be slightly limited by interaction with oxide mineral surfaces. Under reducing conditions iron and/or arsenic sulphides are likely to control arsenic concentrations (Moore et al., 1988), although $Mn_3(AsO_4)_2$ may also exert an influence (Masscheleyn et al., 1991a,b). Quartz is not important as an adsorbent of arsenic, but iron- and aluminium (oxyhydr)oxides are by virtue of their positive surface charge at pH levels of $\leq 6.5 - 7$.

Amorphous iron- and Al-hydroxide content (Pierce and Moore, 1982; Sakata, 1987), clay content (Elkhatib et al., 1984) and pH (Pierce and Moore, 1982; Elkhatib et al., 1984; Sakata, 1987) are the soil properties with the greatest reported effects on arsenic sorption in soils. Other factors such as the presence of organic compounds in solution (e.g. fulvic acid), and competitive adsorption (e.g. phosphate, fulvic acids) will also affect the mobility of arsenic in solution.

In summary, arsenic should be less mobile in oxidising environments because of the dominance of the less soluble and more readily sorbed As(V) species. Under reducing conditions, transformation of As(V) to the more soluble As(III) form and dissolution of As-containing solids (sorbents and coprecipitates) will lead to greater mobility of arsenic.

1.2 CADMIUM IN THE ENVIRONMENT

1.2.1 Introduction

Cadmium is a rare element in nature, having one thousandth the average abundance of zinc (which it is often found in association with) in the upper crust (Hem, 1972). Cadmium has no essential biological function and is highly toxic to plants and animals even at very low concentrations (Lehoczky et al., 1998). Cadmium has a biological half-time of 15-20 years in humans, and the major hazard it poses is its chronic accumulation in the kidneys. Food is the main route by which cadmium enters the body (Lehoczky et al., 1998), and exposure can cause a variety of adverse health effects. The most prominent are kidney dysfunction, lung diseases, disturbed calcium metabolism and bone defects (Jin et al., 1998).

1.2.2 Sources of cadmium

1.2.2.1 Natural sources

Cadmium contamination rarely has a natural source. This is because, even though the weathering of crustal minerals plays a major role in the natural cycle of cadmium, it rarely results in any marked enrichment of the metal in the environment (Krishna Murti et al., 1987). The ranges and mean concentrations of cadmium for some common igneous, sedimentary and metamorphic rocks and soils are given in Table 1.3.

Table 1.3 The abundance of cadmium in common rocks, sediments and soils.

Rock type	**Cadmium content (ppm)**	
	Mean	**Range**
Igneous		
Granite	0.09	0.001-0.60
Basalt	0.13	0.006-0.60
Ultramafic	0.026	0.001-0.03
Metamorphic		
Gneiss	0.04	0.007-0.26
Schist	0.02	0.005-0.87
Eclogite	0.11	0.04-0.26
Sedimentary		
Limestone	0.065	0.001-0.50
Sandstone	0.02	0.01-0.41
Shale, clay	0.03	0.02-11.0
Red clay	0.56	
Organic mud	0.39	
Deep ocean sediments	0.5	0.05-17
Oceanic manganese oxides	8.0	<3.0-21
Phosphorites	25	<10-500
Recent sediments		
Lake sediments	0.91	0.02-6.2
Stream sediments	0.16	0.03-0.40
Soils		
Cultivated, uncontaminated soil, N. France	1.1	0.75-1.5[1]
Cultivated uncontaminated soil, USA	0.27	0.005-2.4[2]
Unpolluted topsoil (subsoil), Japan	0.62 (0.28)[3]	
Polluted topsoil (subsoil), Japan	7.79 (4.61)[3]	
Natural, uncontaminated surface soils (15cm), Spain	0.09-0.33[4]	

[1] (Lamy et al., 1993); [2] (Page et al., 1987); [3] (Asami et al., 1995); [4] (Sanchez-Camazano et al., 1994)

The levels of cadmium in igneous rocks are relatively low and show little variation between rock-types. Cadmium is concentrated by sedimentation, and

hence is found at higher levels in sedimentary rocks than igneous rocks (Page et al., 1987). In particular, certain carboniferous shales are enriched with cadmium, and the soils derived from these deposits and the plants growing in them tend to contain elevated cadmium levels (Krishna Murti et al., 1987).

The major natural source of cadmium to the environment is the weathering of cadmium-bearing parent minerals such as sphalerite, ZnS, (which can contain cadmium in solid solution with zinc) in the primary host rock, or sediments formed by weathering of these rocks. Based upon the cadmium concentrations in common rock types (Table 1.3), soils derived from weathering of igneous rocks should contain the least cadmium, whilst those derived from weathering of sedimentary rocks should contain the most, with metamorphic rock-derived soils intermediate between the two.

1.2.2.2 Anthropogenic sources

Total anthropogenic input of cadmium to the environment is nearly ten times that of all natural sources (Nriagu, 1980). Since the major source of cadmium is industry, anthropogenic sources of cadmium tend to be far more localised and concentrated than any natural source. A considerable amount of the cadmium used each year probably escapes to the environment, either in the extraction and processing of ores, product manufacture or waste disposal (Moore and Ramamoorthy, 1984).

Mining of non-ferrous metal ores can be a significant source of cadmium contamination, especially in those mines which exploit zinc and lead ores. Zinc ores invariably contain the highest concentrations of cadmium, but the actual amount varies widely between different ore bodies (Krishna Murti et al., 1987). The mine tailings associated with mining activities can lead to cadmium contamination from wind-blown dust, whilst waterborne transport of cadmium-rich solid material and aqueous (leached) cadmium can cause contamination some distance downstream of mines. This form of dispersal is not confined to active mines, and many zinc-lead mines and mine tailings act as persistent sources of cadmium (Krishna Murti et al., 1987).

Cadmium, often in association with zinc, can be expected to escape to the atmosphere in processes in which it is melted (Hem, 1972), and an unknown amount of cadmium escapes to the environment as a zinc impurity during the processing of zinc ores. Cadmium also occurs as a natural by-product in crude oil, coal and gasoline, and hence another source of cadmium to the atmosphere is combustion of fossil fuels. As a consequence, increased cadmium and zinc levels have been observed to occur in soils and vegetation adjacent to heavily used roads (Lagerwerff and Specht, 1970).

About half of the cadmium used in the USA in the 1970's was consumed in electroplating processes, the remaining fifty percent being divided equally between production of pigments (used in paints, printing inks and plastics) and production of stabilisers for use in thermoplastics such as polyvinyl chloride (PVC). A smaller amount of cadmium was also used in the production of fluorescent and cathode-ray tubes, some types of batteries, bearing metals, and low-melting metal alloys (Krishna Murti et al., 1987).

In many countries, the liquid and solid wastes arising from the manufacture of the above items are discharged to sewage systems. In the absence of such networks, the wastes are presumably disposed to natural water courses or specified disposal areas (Krishna Murti et al., 1987).

Because cadmium is often present in products at low levels and as compounds, its recovery is both technically and economically restricted. Upon product disposal, there is only 5% recovery of cadmium from wastes compared to 40% for lead. Most cadmium-containing articles may enter the municipal waste disposal pathway, where their fate is either to be landfilled or incinerated (Krishna Murti et al., 1987).

In recent years there has been an increasing trend towards the disposal of heavy metal wastes, especially cadmium, into soils (Sanchez-Martin and Sanchez-Camanzano, 1993). This disposal has been in the form of organic-rich sewage and other sludges and power station fly-ash. It has occurred for practical and economic reasons since sludges are good fertilisers and this method of disposal is cheap (Lamy et al., 1993). Cadmium and lead have consequently become significant contaminants in soil and groundwater systems (Hutchinson and Meema, 1987; Tiller et al., 1987). The contamination-related problems are worst where the toxic heavy metals are co-disposed with large volumes of organic wastes (Pohland and Gould, 1986). This is because the mobility of cadmium is increased under certain pH conditions by the formation of soluble organic complexes (Lamy et al., 1993).

It is now recognised that soils with high cadmium levels are those which receive heavy applications of sewage sludge and phosphate fertilisers, those in areas of natural mineralisation, and those near to point sources of airborne cadmium, such as non-ferrous metal smelters (Krishna Murti et al., 1987).

1.2.3 Factors affecting cadmium mobility

Cadmium is generally recognised to be the most mobile trace metal in soils (Alloway et al., 1991; Schmitt and Sticher, 1991), although the importance and precise nature of cadmium associations in soils and soil solutions are not well known

(Lamy et al., 1993). The fate of cadmium which reaches the soil from anthropogenic sources depends essentially on its mobility in the host medium (Hem, 1972; Lamy et al., 1993). This, and the bioavailability of cadmium, in turn depend on metal speciation, solubility of solid phases and soil properties such as pH, mineralogy and organic matter content (Lamy et al., 1993; Sanchez-Martin and Sanchez-Camanzano, 1993).

Mineral and organic matter surface reactions such as adsorption are generally known to have predominant roles in the retention of cadmium in soils (Riffaldi and Levi-Minzi, 1975; Shuman, 1977). Additionally, surface precipitation on oxides, hydroxides, and carbonate surfaces may occur for metals such as cadmium and zinc (Dzombak and Morel, 1990). It is also possible for these heavy metal ions to penetrate the lattice of minerals and subsequently form coprecipitates and solid solutions (White and Yee, 1986; Brummer et al., 1988).

1.2.3.1 Inorganic speciation and solubility controls

Depending on the prevailing geochemical conditions, three important cadmium-containing solids have stability fields in the Cd-C-S-O-H system (Fig. 1.4); otavite, $CdCO_3(s)$, greenokite, $CdS(s)$, and $Cd(OH)_2(s)$.

Under oxidising conditions below pH 7.5-8.0 the dominant species is the free metal ion Cd^{2+} (Dryssen and Wedborg, 1980; Turner et al., 1981), the chemistry of which can be considered in terms of complexation of the Cd^{2+} cation with inorganic and organic ligands (e.g. the cadmium aquo ion, $[Cd(H_2O)_6]^{2+}$).

However, between pH 7.5 and pH 12.5 the major cadmium species in oxidised waters is cadmium carbonate (Fig. 1.4), the solubility of which is controlled by the following reactions (Rai et al., 1991b):

$$CdCO_3(s) = Cd^{2+} + CO_3^{2-} \qquad \log K = -12.2 \pm 0.1$$
$$Cd^{2+} + CO_3^{2-} = CdCO_3(aq) \qquad \log K = 4.7 \pm 0.1$$
$$Cd^{2+} + 2CO_3^{2-} = Cd(CO_3)_2^{2-} \qquad \log K = 6.4 \pm 0.1$$

These data suggest that the aqueous carbonate complex is dominant in the stability field of $CdCO_3(s)$. Due to the solubility of the carbonate complex, it is thought that the U.S. Public Health drinking water limit for cadmium (10 ppb) may be exceeded in river water and underground water under oxidising, highly alkaline conditions (Hem, 1972). Furthermore, the fact that the freshwater concentrations of cadmium are variable (Moore and Ramamoorthy, 1984) suggests that $CdCO_3(s)$ does not provide a reliable control of cadmium solubility.

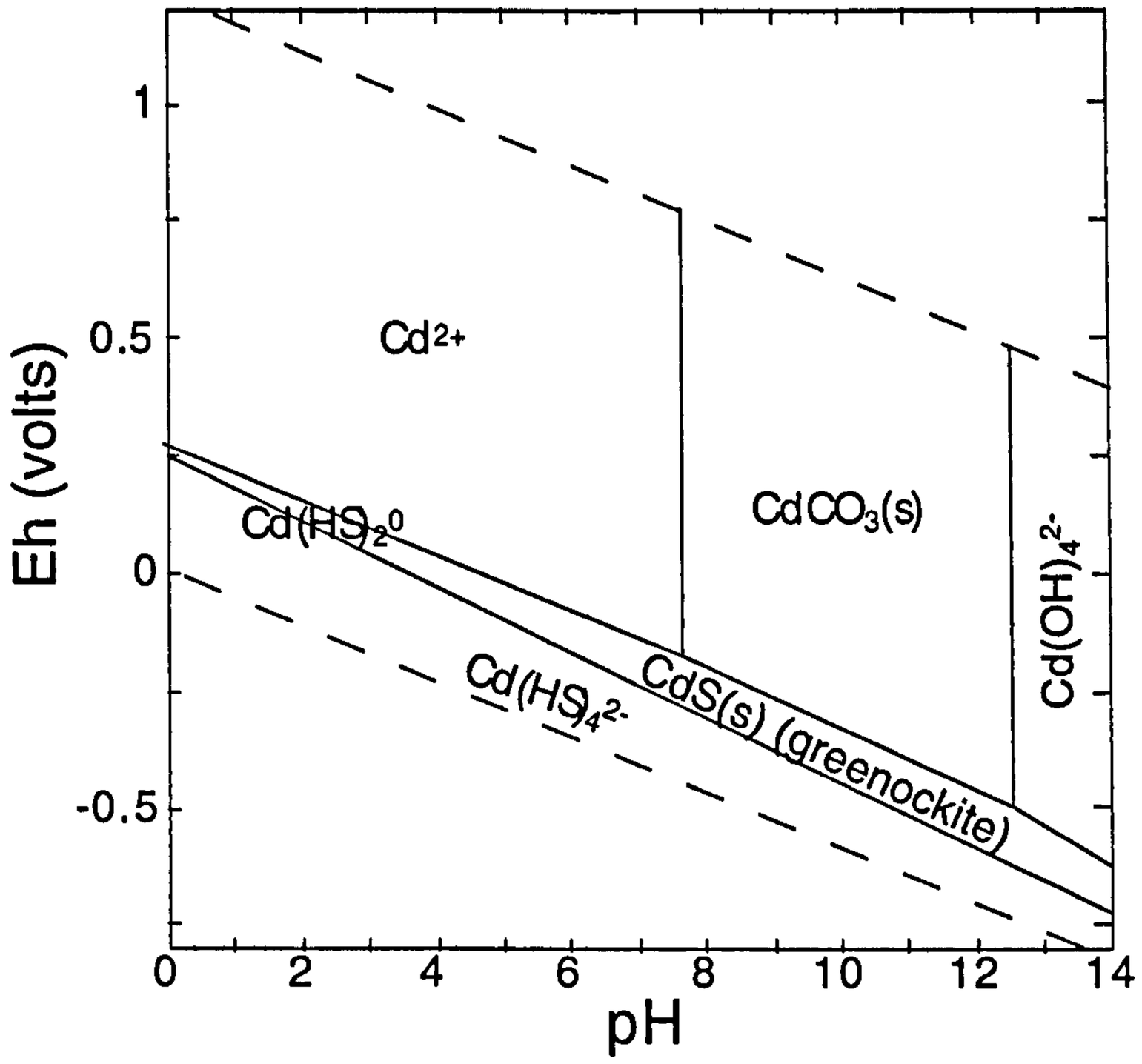

Fig. 1.4. Eh-pH diagram for part of the system Cd-C-S-O-H at 25°C and 1 atm. The assumed activities are: Cd = 10^{-8}; C = 10^{-3}; S = 10^{-3}. It can be seen that the free Cd^{2+} ion occupies a relatively large region of Eh-pH space.

Under the aquatic conditions commonly found in oxidising environments, the solubility of $Cd(OH)_2(s)$ is too great to provide any significant solubility control. However, $Cd(OH)_2(s)$ may start to occupy the $CdCO_3(s)$ stability field if $pCO_2(g)$ decreases, and it may start to exert some control on aqueous cadmium concentrations under such conditions. The solubility of $Cd(OH)_2(s)$ is controlled by the following reactions (Rai et al., 1991a):

$$Cd(OH)_2(s) = Cd^{2+} + 2OH^- \qquad \log K = -14.14 \pm 0.21$$
$$Cd(OH)_2(s) = Cd(OH)_2^0 \qquad \log K = -7.04 \pm 0.21$$
$$Cd(OH)_2(s) + 2OH^- = Cd(OH)_4^{2-} \qquad \log K = -5.62 \pm 0.32$$

Under certain conditions, other important dissolved cadmium species may exist in systems differing from that shown in Fig. 1.4. For instance, the chloride complex can become significant if chloride concentrations exceed 350 ppm (Hahne and Kroontje, 1973). Since cadmium is sulphophilic, the $CdSO_4^0$ ion pair may also have some influence if the sulphate concentration exceeds 1000 ppm (Hem, 1972).

The degree of hydrolysis and the strength of metal complexation follows the sequence Cd < Pb « Hg (Dryssen and Wedborg, 1980; Turner et al., 1981). Because Cd^{2+} forms relatively weak complexes, it is likely that the relatively simple Cd-C-S-

O-H system depicted in Fig. 1.4 correctly describes cadmium speciation in many natural river, lake and underground waters.

1.2.3.2 Typical fraction of cadmium in soils

Lead and copper are more strongly bound by soil organic matter than cadmium and zinc (Asami et al., 1995). These results are consistent with the fact that the solubility constants for heavy metal-soil humic acid interactions between pH 5 and pH 7 increase in the order Cd < Zn < Cu (Takenaga and Aso, 1975). Furthermore, it has been shown that heavy metal cations are adsorbed by various clay minerals (Abd-Elfattah and Wada, 1981) and iron- and Al- (oxyhydr)oxides (Kinniburgh et al., 1976; McKenzie, 1980; Benjamin and Leckie, 1981) with a very similar selectivity: Cd < Zn < Pb < Cu. As this sequence suggests, cadmium is more labile than the zinc, lead, or copper. This explains why cadmium is often observed to be the most bioavailable and leachable of the four metals, especially in contaminated soils (Robinson et al., 1998). Indeed, the high bioavailability of cadmium has caused it to become a great source of concern regarding terrestrial food-chain contamination (McLaughlin et al., 1999).

1.2.3.3 Adsorption and ion exchange

Cadmium adsorption increases with pH as mineral surface charge becomes increasingly negative. Percentage adsorption rises from <10% to 100% over a narrow pH range of 2-2.5 pH units known as the 'adsorption edge'. This is illustrated in Fig. 1.5 for goethite, alumina and silica. It is also clear from this plot that the order of sorption with increasing pH is Cu(II), Zn(II), Co(II) ~ Cd(II), consistent with Cd(II) being less strongly adsorbed than Cu(II) and Zn(II). Indeed, Kinniburgh et al. (1976) have shown that lead, copper, zinc and nickel all adsorb on ferrihydrite more strongly than cadmium. Thus, the co-existence of other dissolved heavy metals can decrease the extent of cadmium adsorption. The effect of this 'competitive adsorption' can be heightened still further in the presence of major groundwater/seawater ions; these have also been shown to inhibit the adsorption of cadmium and other heavy metals (e.g. Balistrieri and Murray, 1982; Cowan et al., 1991; Petersen et al., 1993; Naidu et al., 1994, Davis and Upadhyaya, 1996).

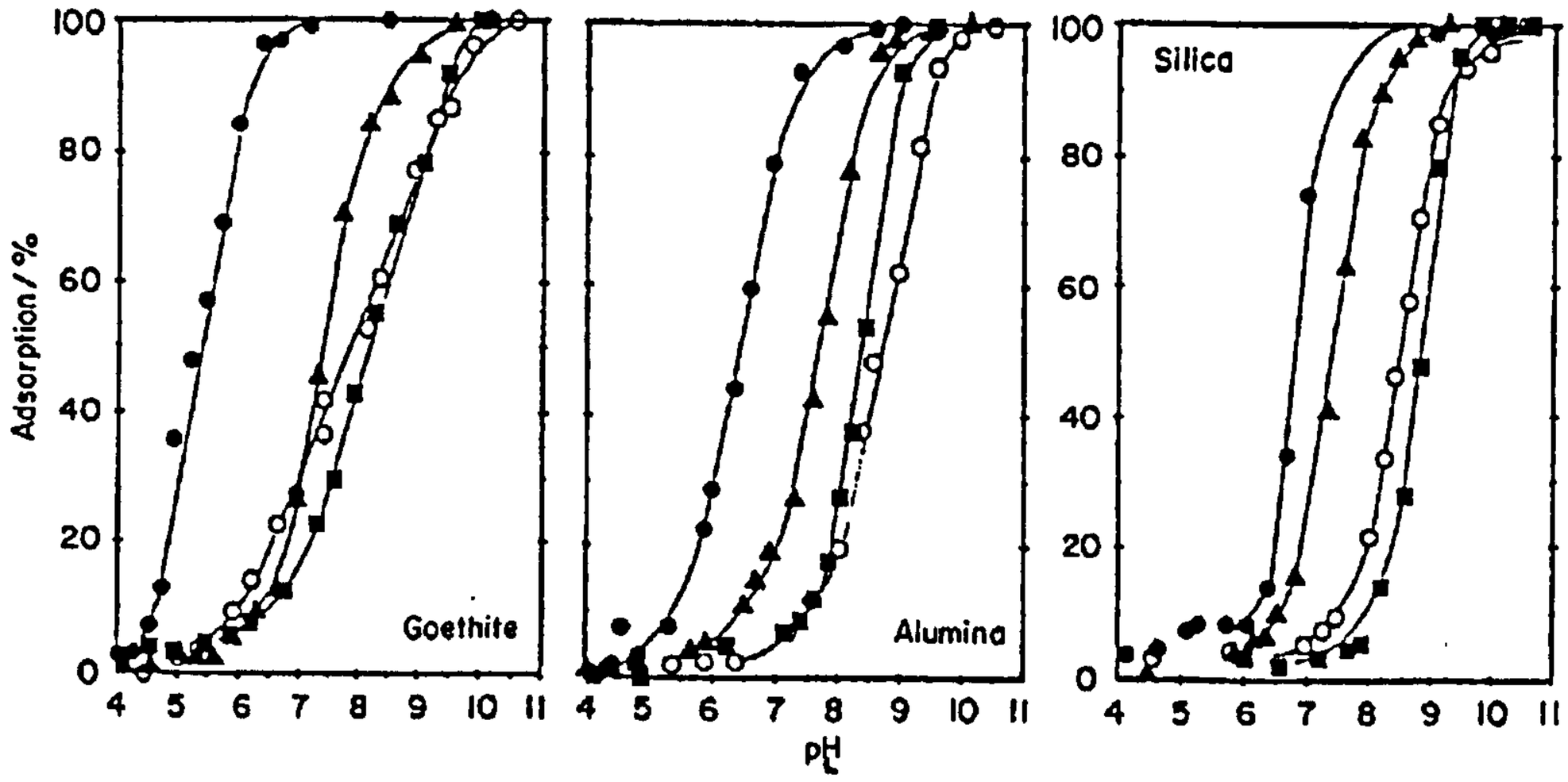

Fig. 1.5. Adsorption of Cu(II) (•), Zn(II) (▲), Co(II) (■) and Cd(II) (○) on goethite, alumina and silica at 25°C. BET surface area 45m^2dm^{-3}. Initial metal concentration 10^{-4} M, background electrolyte 10^{-3} M KNO_3. From Spark et al., 1995.

Cadmium adsorption also decreases with increasing adsorbate : adsorbent ratio (Fig. 1.6). This is because the availability of the most energetically favourable surface sites becomes limited as dissolved metal concentrations, and hence percentage surface loading, increase. This forces the occupation of less favourable sites which results in a drop in percentage adsorption at a given pH (e. g. Dzombak and Morel, 1990).

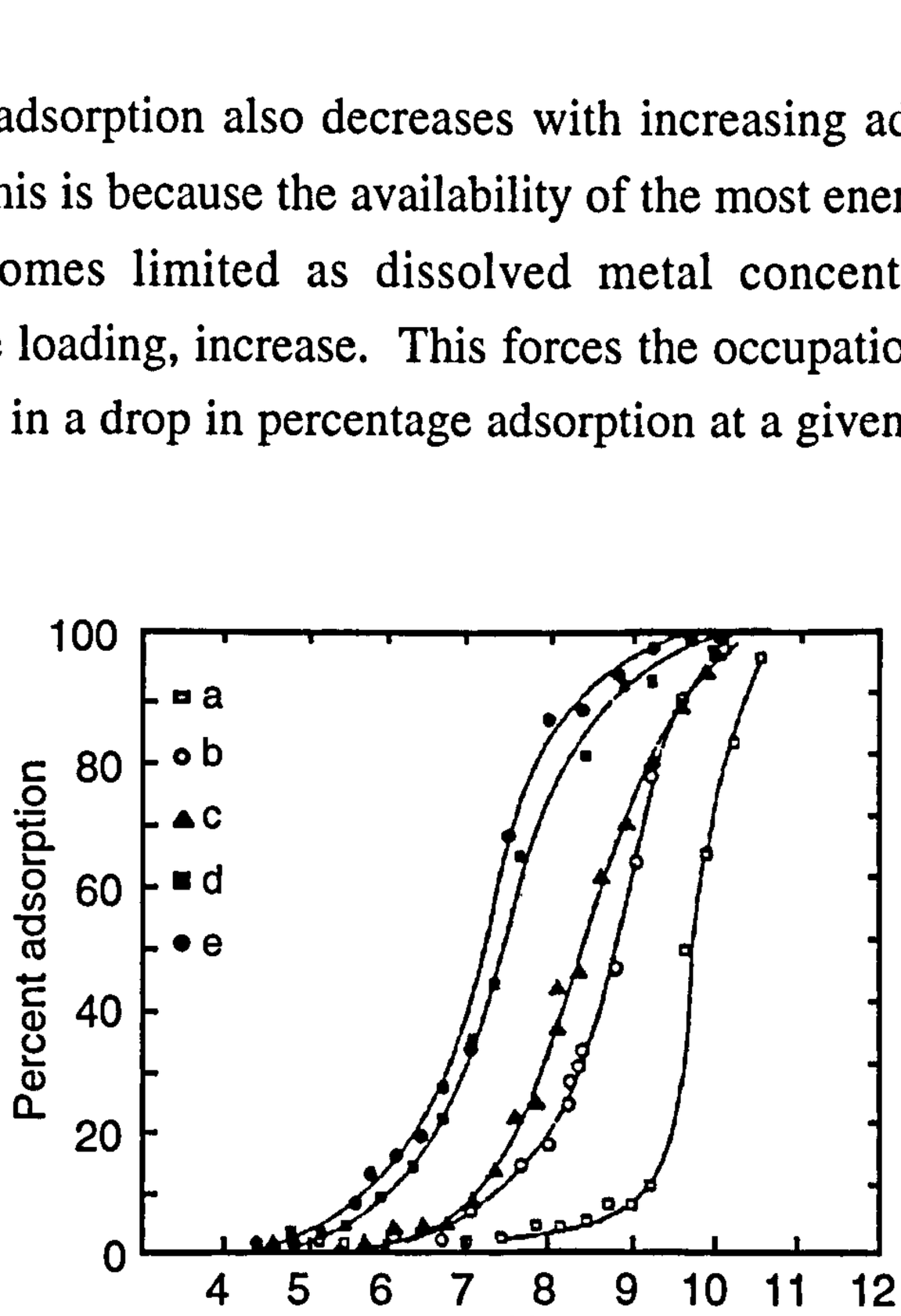

Fig. 1.6. (a) Precipitation curve for $1x10^{-4}$ M cadmium at 25°C, ionic strength = 0.01 M KNO_3. (b)-(e) Adsorption of cadmium at various concentrations on goethite: 55 m^2 L^{-1}, ionic strength = 0.01 M KNO_3 at 25°C; (b) $2x10^{-4}$ M; (c) $1x10^{-4}$ M; (d) $1x10^{-5}$ M; (e) $1x10^{-6}$ M. Increasing adsorbate/adsorbent ratio pushes the adsorption edge to increasingly high pH values. From Johnson, 1990.

Of the oxide minerals mentioned above, goethite is among the most effective sorbents of cadmium. Lamy et al. (1991) observe that cadmium desorption from this mineral is incomplete even at pH 4, suggesting that cadmium adsorption is of a specific and permanent nature. Moreover, the affinity of iron (oxyhydr)oxides in general for cadmium is illustrated by the fact that trace metal concentrations in soil oxide fractions are often orders of magnitude higher than in the bulk soils (Le Riche and Weir, 1963; Taylor and McKenzie, 1966; Hiller and Brummer, 1995).

Davis et al. (1987) observe the formation of a solid solution between calcium and cadmium following adsorption of cadmium onto calcite. This has important implications for the mobility of cadmium since its release back to solution from a coprecipitate with calcium (calcite) or iron (e.g. goethite) would require dissolution of the host mineral, but would be slow and sustained. The importance of calcite as an adsorbent phase is also indicated by the field findings of Fuller and Davis (1987). They found that clean grains of primary minerals such as quartz and aluminosilicates sorbed much less Cd^{2+} than grains which had surface patches of secondary minerals (e.g., carbonates, iron- and manganese oxides). Calcite grains were observed to sorb the greatest amount of Cd^{2+}, on a weight-normalised basis, despite the greater abundance of quartz.

1.2.3.4 The influence of organic matter

Iron (oxyhydr)oxides are generally thought to have dominant roles in the retention of cadmium by soils. This is largely because of their relatively high abundance in temperate acidic soils, and their high capacity for the retention of cadmium and other metals (Riffaldi and Levi-Minzi, 1975; Shuman, 1977). However, natural waters and soils also contain significant quantities of ill-defined organic matter such as humic acid (HA) and fulvic acid (FA) in addition to the inorganic surfaces and ligands considered above. These organic materials can alter the speciation patterns of heavy metals in solution (Turner, 1987), although the effects can be rather mild for cadmium because it forms relatively weak complexes with FA (Turner, 1987) and HA (Takenaga and Aso, 1975).

Since the sorption edge for cadmium on iron oxides is considerably higher (~pH 6.5 - 7.5; Benjamin and Bloom, 1981; Kuo and McNeal, 1984) than that of humic substances (~pH 2 - 3; Riffaldi and Levi-Minzi, 1975), the latter are expected to be more important sorbents than the oxides under low pH conditions (~ pH 4.5; Kuo and Jellum, 1991). Indeed, a number of studies have indicated that dissolved organic material and organic coatings (biofilms) on particulate matter can exert a strong control on the behaviour of trace metals in the environment, thereby masking the surface properties and reactivity of the underlying particles (e.g. Lion et al., 1988; Lamy et al., 1991; Tipping and Hurley, 1992; Sanchez-Martin and Sanchez-

Camanzano, 1993). However, it has also been shown that whilst organic material does have a notable effect on trace metal speciation and mobility under acidic conditions, this influence is decreased under conditions of near neutral to alkaline pH in lakes (Tessier et al., 1985, 1996) and soils (Anderson and Christensen, 1988). Furthermore, Tessier et al. (1985, 1996) have shown that trace metal adsorption under these conditions takes place by direct bonding to inorganic mineral surfaces, even in the presence of organics. An extended X-ray absorption fine structure (EXAFS) spectroscopy study has proven this conclusively for cadmium adsorption on iron oxyhydroxides (Collins et al., 1999).

Under acidic conditions, soil in the presence of soluble sludge organic matter (SSOM) sorbs more cadmium than soil alone (Lamy et al., 1993) (Fig. 1.7). This increased level of sorption may result from the participation of the SSOM in the fixation of cadmium by the soil; a cadmium-SSOM complex could form a cadmium-SSOM-mineral ternary complex by interacting with the solid phase. This would be in accordance with the work of Jardine et al. (1989), who showed that the fixation of dissolved organic C on soil mineral constituents depends on solution pH, with a maximum at pH 4 - 5.

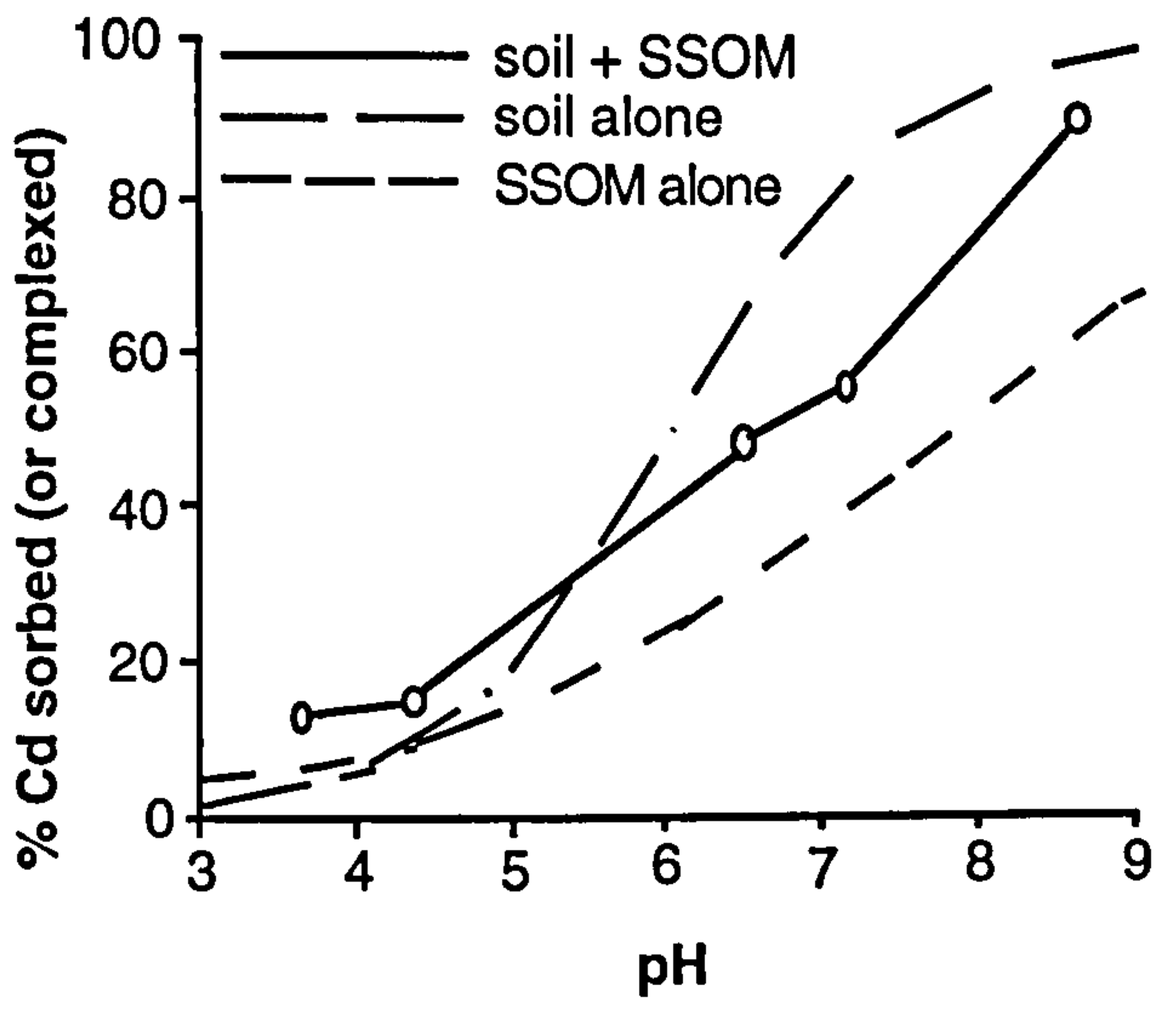

Fig. 1.7. Comparison of the behaviour of cadmium (200 µmol/L) in the mixed system (soil + SSOM) with the two simple systems: cadmium + soil alone and cadmium + SSOM alone (in the latter case, data correspond to complexed cadmium in solution). From Lamy et al. (1993).

Conversely, soil in the presence of SSOM above pH 5.5 sorbs less cadmium than soil alone (Lamy et al., 1993). Under such conditions, the SSOM can form soluble cadmium-organic matter complexes. These can limit the fixation of cadmium by soil by competing with its exchange capacity. However, when the

SSOM/soil ratio decreases, the sorption of cadmium by soil is found to be nearly identical in the presence or absence of SSOM (Lamy et al., 1993).

The calculated partitioning of cadmium between the solid and liquid phases during sewage sludge disposal is shown in Fig. 1.8. It can be seen that the formation of soluble cadmium-organic matter complexes is at a maximum between pH 5 and 7, and increased cadmium mobility is expected in this pH range (Lamy et al., 1993). This is in agreement with the work of Elliott et al. (1986), who concluded that increased soil organic matter should restrict mobility and bioavailability of cadmium (and copper) under acidic conditions, where soluble metal complex formation is limited. It is also consistent with the observation of Tessier et al. (1985, 1996) that the influence of organic matter on trace metal mobility decreases under near neutral pH conditions.

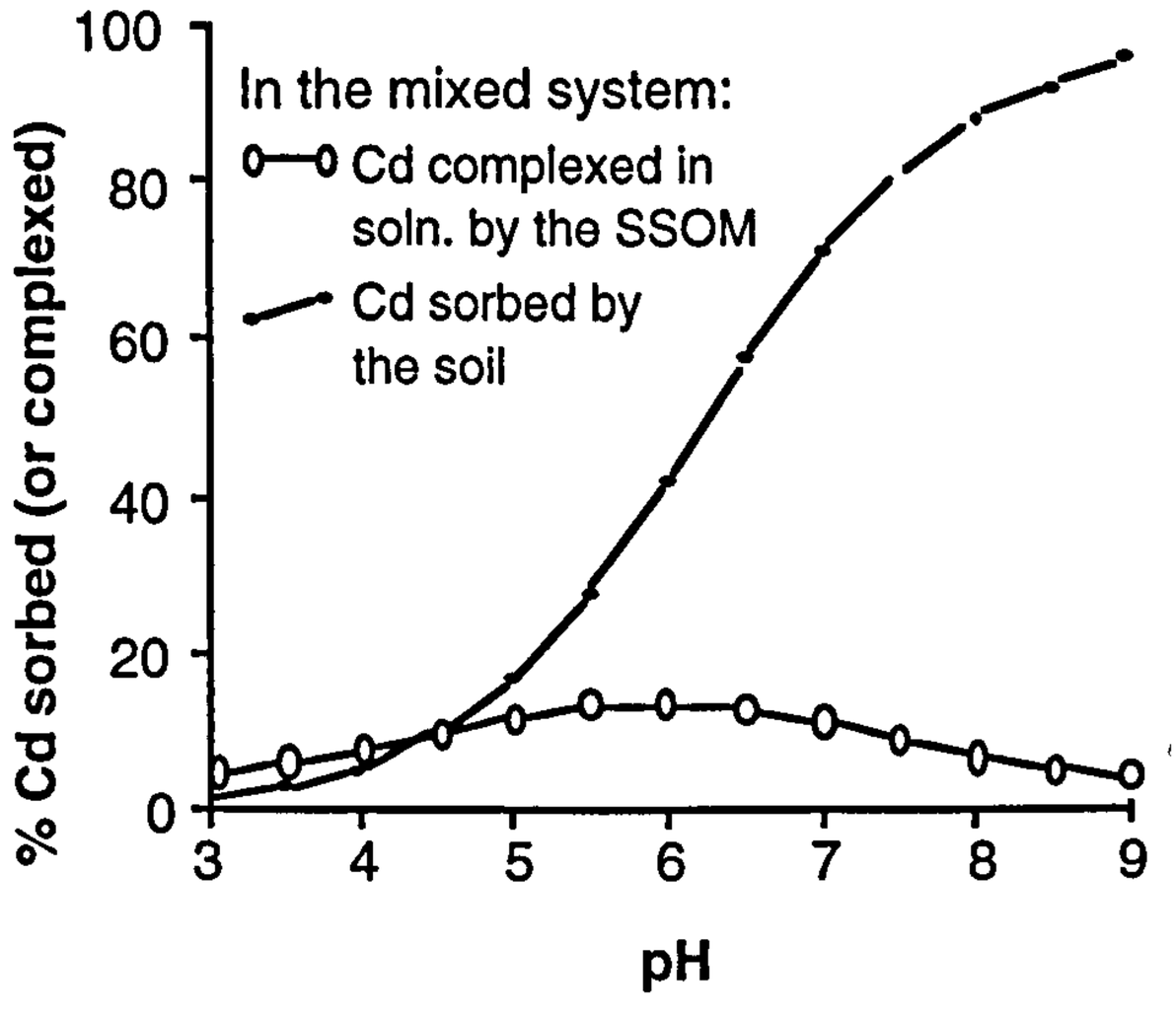

Fig. 1.8. Speciation of cadmium in the mixed system cadmium-soil-SSOM as predicted by Lamy et al., 1993.

1.2.3.5 Biochemical influences

Cadmium is known to be extracted from solution by the biota, and bioaccumulation in the food chain is a possibility (Moore and Ramamoorthy, 1984). The strength of this accumulation is very high in some terrestrial plants. For instance, Indian mustard (*Brassica juncea* (L.) Czern) seedlings have been shown to concentrate Pb(II), Sr(II), Cd(II), and Ni(II) 500-2000 times relative to the contaminated material they were grown in (Salt et al., 1997). Accumulation can occur by several routes, but usually involves ingestion or uptake across biological membranes followed by the formation of organo-metallic complexes. For instance, higher plants, algae and some yeasts detoxify heavy metals by sequestration with heavy metal-binding peptides called phytochelatins or their precursor, glutathione (Zhu et al., 1999b). The strong accumulation of various contaminants forms the

basis of 'phytoremediation' which uses 'hyperaccumulating' plant species to remove toxic substances from contaminated soils, sediments and waters (e. g. Robinson et al., 1998; Zhu et al., 1999a).

1.2.4 Cadmium in the environment: Summary

Cadmium is one of the most mobile trace elements in soils, and the parent mineral phases exert little control on the levels of dissolved cadmium in solution; in most natural surface waters, free Cd^{2+} as the aquo ion ($[Cd(H_2O)_6]^{2+}$) is the dominant cadmium species. Relative to other trace metals such as copper, zinc, lead and mercury, the degree of hydrolysis and strength of cadmium complexation is rather low, and cadmium is generally only bound weakly by a single ligand in its complexes.

Adsorption, cation exchange capacity and pH appear to exert the most significant controls on cadmium mobility in natural, uncultivated soils. It seems likely that adsorption on iron (oxyhydr)oxides (e.g. goethite) is of a specific and permanent nature. Sorption on calcite may also be important. Adsorption of cadmium generally increases with increasing pH and adsorbate/adsorbent ratio. Under low cadmium concentrations where there is an excess of sorption sites, adsorption capacity is independent of the soil properties, and levels of cadmium sorption are close to 100% (Christensen, 1984). Under high cadmium concentrations, however, soil properties start to exert an influence on the extent and mechanism(s) of cadmium sorption (Anderson and Christensen, 1988).

The importance of inorganic complexes in cadmium speciation is questionable, since the chloride and sulphate complexes only become significant when the concentration of the respective ligands reach 350 ppm and 1000 ppm.

However, natural soils and waters often also contain significant quantities of ill-defined organic matter (such as humic and fulvic acids). Cadmium forms quite weak organometallic complexes relative to other cations such as lead and copper. Notwithstanding this, organic matter may play an important role in cadmium speciation, especially under acidic conditions. The ultimate effect of organics on the mobility of cadmium is dependent on the metal/ligand ratio, the nature of the ligands, and the nature of the metal-ligand complexes. The effect of organics generally only becomes significant when the ligands are in present in excess (e.g., [cadmium]/[EDTA] <1) (Bermond and Bourgeois, 1992).

1.3 CHROMIUM IN THE ENVIRONMENT

1.3.1 Introduction

Chromium has an average concentration in the earth's crust of 100 ppm, and it is most commonly found in ultrabasic rocks (Matzat and Shiraki, 1974). Chromium is one of the most widely used metals in industry, and is essential in trace amounts for plant and animal metabolism (Richard and Bourg, 1991). However, when accumulated in excess it can result in nausea, skin ulcerations, lung cancer, and gastro-intestinal and liver diseases. It can be lethal if concentrations reach 0.1 mg g^{-1} body weight (100 ppm) (Mertz, 1974; Ajmal et al. 1984; Nieboer and Jusys, 1988). The range of chromium concentrations in natural waters is quite large, but is generally below the 50 ppb (approximately 1 µmole L^{-1}) total chromium drinking water limit recommended by the Commission of European Communities, The World Health Organisation, and the U. S. Environmental Protection Agency (Richard and Bourg, 1991). This level takes account of the toxic effects of the soluble Cr(VI) species (solubility of the parent solid, $CrO_3(s)$ is 625.3 g L^{-1} at 20°C (Nieboer and Jusys, 1988)) and the possibility of oxidation of the less toxic and less soluble Cr(III) species to Cr(VI) (Calder, 1988).

1.3.2 Sources of chromium

1.3.2.1 Natural sources

The chromium content of natural solids varies widely with the type and nature of rocks or sediments (Table 1.4). Granites, carbonates and sandy sediments generally have the lowest chromium content, whilst shales, river suspended matter and soils tend to exhibit the highest levels (Richard and Bourg, 1991).

Table 1.4. Chromium concentration in common rocks, sediments and soils.

Material	Concentration (ppm)	Reference
Ultramafic rocks	2400	1
Basalts	40-600	2
Granites	2-100	2
Metamorphic rocks	90	1
Pelagic sediments	80	1
Shales	30-600	2
Sandstones	35-90	2
Phosphorite	300-3000	2
Sedimentary iron ore	150-800	2
Limestones	10-60	2
Dolomites	300-1000	2
Soil	80-200	2
Western U.S. Soil	3-2000 (geometric mean: 41)	3

1. Matzat and Shiraki, 1974.; 2. Nriagu, 1988; Fleischer, 1972.; 3. Shacklette and Boerngen, 1984.

Although there are about forty chromium-containing minerals, only chromite ($(Mg^{2+}, Fe^{2+})O \cdot (Cr^{3+}, Fe^{3+}, Al)_2(O)_3$), is of economic importance (Nriagu, 1988). This mineral generally occurs in one of three geological settings (Nriagu, 1988):

a) Stratiform-type deposits associated with layered mafic intrusions (such as the Bushveldt Complex of South Africa), which constitute about 90% of the known world chromium ore resources;
b) Podiform-type or Alpine-type deposits, which are usually associated with island arcs and major tectonic fold belts. Peridotites are the usual host rocks in this setting, and such deposits account for about 10% of world chromium ore resources;
c) Lateritic (placer) deposits, which are generally derived from the weathering of chromium-bearing peridotites; these deposits have a relatively low ore concentration, and are of little economic importance.

The primary natural source of chromium to the environment is the weathering of parental geological materials. Chromium is commonly contained at the highest levels in the finest grain size fraction of soils derived from weathering of basalt and serpentine, where concentrations range from 5 to 3000 ppm (Bowen, 1966). It primarily occurs in soils as the Cr(III) species in chromite. The insolubility of this mineral ($FeCr_2O_4$, K_{sp} = -28.4; Schmidt, 1984) together with the fact that aqueous (leached) Cr(III) adsorbs strongly to solid material in soils and sediments (and is therefore highly immobile) means that natural occurrences of chromium at potentially harmful concentrations are thought to be rare. Most high concentrations of chromium observed in natural waters are associated with the very soluble and highly mobile chromate [Cr(VI)] species (Robertson, 1975).

Wherever Cr(III) is found in nature, it is often in close association with Al(III) and Fe(III) because substitution of one for another can occur in a variety of mineral and organic structures (Bartlett and James, 1988). For instance, Cr(III) can substitute for small amounts of octahedral aluminium in clay minerals (Bartlett and James, 1988), and amorphous [Fe(III), Cr(III)] hydroxide is probably the main chromium solubility-controlling phase in natural environments (Richard and Bourg, 1991) (see section 1.3.3.1).

1.3.2.2 Anthropogenic sources

Almost all reported incidents of chromium ground water contamination have an industrial origin. Major sources of chromium to the environment are the metal plating industries, wood treatment and tannery facilities, chromium mining and milling operations (Calder, 1988), and chemical manufacturing (Richard and Bourg, 1991). Typically, chromium-containing wastes have been disposed of by discharging them to surface holding ponds or lagoons, and leakage from these has been quite common (Calder, 1988). Large plumes of chromium-contaminated groundwater can result (Perlmutter and Lieber, 1970; Deutsch, 1972; Stollenwork and Grove, 1984), especially in sand and gravel aquifers where groundwater flow rates are often high (0.5 to 1 m per day) and chromium retention is low (Calder, 1988).

1.3.3 Factors affecting the mobility of chromium

1.3.3.1 Speciation and the solubility of chromium-bearing minerals

Chromium exists in a range of oxidation states from Cr(0) to Cr(VI). However, only the trivalent and hexavalent forms are stable in the natural environment (Calder, 1988). Chromium speciation in ground water is determined by oxidising potential (Eh) and pH conditions (Fig. 1.9).

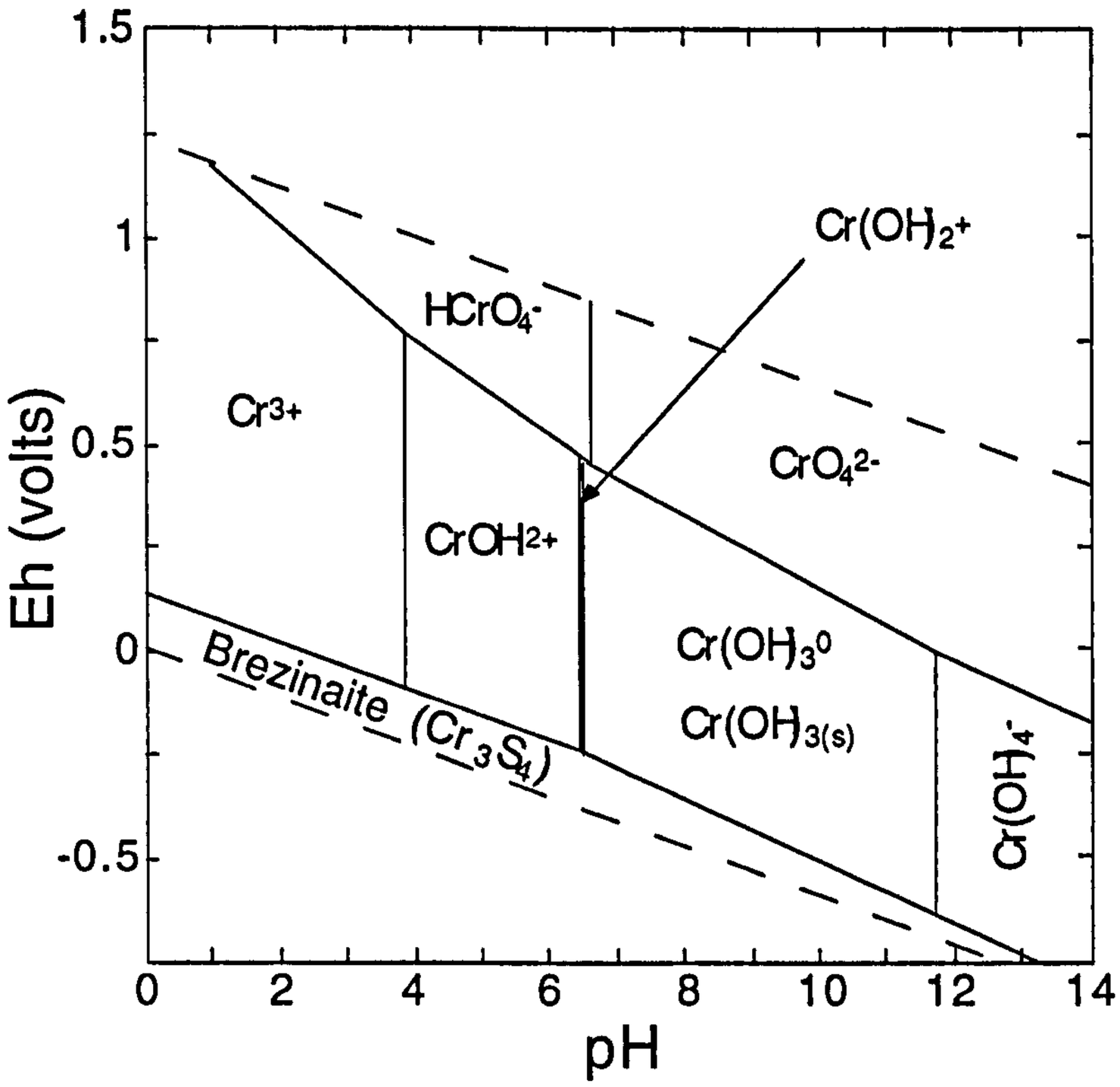

Fig. 1.9 Eh-pH diagram of part of the Cr-C-S-O-H system at 25°C and 1 atmosphere pressure. It is clear that chromium is present as dissolved species throughout much of Eh-pH space. $Cr(OH)_3(s)$ solubility data from Rai et al., 1987.

As Fig. 1.9 shows, Cr(VI) species predominate under oxidising conditions whereas Cr(III) species predominate under more reducing conditions. Oxidising conditions are generally encountered in shallow aquifers within a few metres of the water table, where there is a continual replenishment of oxygen from the atmosphere via the unsaturated zone. Oxygen in ground water tends to be consumed by hydrochemical and biochemical oxidation reactions, usually involving organic matter. In shallow ground waters, this oxygen is replaced from the atmosphere. In deeper ground waters that are isolated from the atmosphere, oxygen replenishment cannot occur and reducing conditions develop (Calder, 1988).

Cr(VI) is extensively hydrolysed in water, and at total chromium concentrations below 500 ppm (0.01 M), the dominant Cr(VI) species are the oxyanions $HCrO_4^-$ and CrO_4^{2-} (Calder, 1988). The equilibrium between these two species is pH dependent (Calder, 1988):

$$HCrO_4^- \Leftrightarrow CrO_4^{2-} + H^+$$

Under oxidising conditions in most natural ground waters (pH 6 to 8) CrO_4^{2-} is the dominant species, but under more acidic conditions $HCrO_4^-$ becomes

predominant (Calder, 1988). At Cr(VI) concentrations above 520 ppm, $HCrO_4^-$ dimerises to form dichromate ($Cr_2O_7^{2-}$) in acidic environments (Baes and Mesmer, 1977; Armienta and Quéré, 1995). However, since Cr(VI) levels rarely exceed 50 ppm in contaminated ground water (Calder, 1988), $Cr_2O_7^{2-}$ is an unimportant species in nature.

Chromate minerals are very scarce in nature because of their solubility and instability under reducing conditions. As a consequence, minerals such as $CrO_3(s)$ do not control the solubility of Cr(VI). However, in environments rich in barium or lead, Cr(VI) solubility is controlled primarily by $PbCrO_4$ (pK_{sp} = 13.7; Schmidt, 1984), whilst $BaCrO_4$ (pK_{sp} = 8.9) has been shown to form rapidly under the environmental conditions in which Cr(VI) is stable (Rai et al., 1988). Soluble chromium salts, such as $CaCrO_4$ (pK_{sp} = 3.15) have been suggested to precipitate in soils containing chromium at levels of 10,400 ppm (James, 1994).

The weathering of iron-bearing minerals such as biotite, hematite, poorly crystalline iron (oxyhydr)oxides, clays and some industrial wastes can liberate Fe(II) ions to solution (Bartlett, 1986; Richard and Bourg, 1991). Ferrous iron is of primary importance in the reduction of Cr(VI) (Kent et al., 1994; Armienta and Quéré, 1995; Davis and Olsen, 1995), and the reaction proceeds as follows (Rai et al., 1988):

$$[3FeO] + 6H^+ + Cr(VI)(aq) = Cr(III)(aq) + 3Fe(III)(aq) + 3H_2O$$

Cr(III) can easily substitute for and/or form solid solutions with Fe(III) in amorphous ferric hydroxide. The typical stoichiometry of the resulting solid phase is $Cr_{0.25}Fe_{0.75}(OH)_3$, and the reaction proceeds according to the following equation (Eary and Rai, 1988):

$$Cr(OH)_2^+ + 3Fe^{3+} + 10H_2O \Leftrightarrow 4\{Cr_{0.25}Fe_{0.75}(OH)_3(s)\} + 10H^+$$

Rai et al. (1986) found that the precipitation of Cr(III) hydroxide and [Fe(III), Cr(III)] hydroxide minerals maintained Cr(III) concentrations in ground water below a level of 0.1 ppm over a pH range of 5 to 10. Hence, [Fe(III), Cr(III)] hydroxide is probably the main Cr(III) solubility-controlling phase in natural environments (Richard and Bourg, 1991).

Ferrous iron need not be in solution to reduce Cr(VI). Reduction may also proceed by the adsorption of Cr(VI) to the surface of Fe(II)-containing minerals, with subsequent electron transfer leading to chromium reduction. Such a process would lead to chromium that was initially weakly adsorbed as Cr(VI) becoming

irreversibly and strongly bound as Cr(III) or a mixed Cr(III)/Fe(III) coprecipitate (Eary and Rai, 1987).

Cr(VI) may also be reduced by organic matter such as simple amino acids (Schroeder and Lee, 1975), or humic and fulvic acids (Goodgame et al., 1984; Boyko and Goodgame, 1986). Intermediate Cr(V) species are produced but decay to Cr(III) in a few days. This form of reduction is favoured under acidic conditions (Stollenwork and Grove, 1985). However, even if rapid reaction occurs in the first few minutes, reduction of Cr(VI) by organics is slower than Cr(III) oxidation (Richard and Bourg, 1991).

The main aqueous Cr(III) species are Cr^{3+}, $Cr(OH)_2^+$, $Cr(OH)^{2+}$, $Cr(OH)_3^0$, and $Cr(OH)_4^-$ (Fig. 1.7; Rai et al., 1986, 1987), and the relative proportions of these species is pH dependent (Calder, 1988):

$$Cr^{3+} + H_2O \Leftrightarrow Cr(OH)^{2+} + H^+$$
$$Cr(OH)^{2+} + H_2O \Leftrightarrow Cr(OH)_2^+ + H^+$$
$$Cr(OH)_2^+ + H_2O \Leftrightarrow Cr(OH)_3^0 + H^+$$
$$Cr(OH)_3^0 + H_2O \Leftrightarrow Cr(OH)_4^- + H^+$$

The Cr^{3+} species is prevalent only at pH below 3.6 (Fig. 1.9), and polymeric Cr(III) species such as $Cr_2(OH)_2^{4+}$, $Cr_3(OH)_4^{5+}$, and $Cr_4(OH)_6^{6+}$ are never significant in natural systems (Rai et al., 1986, 1987).

It is possible that authigenic Cr(III) minerals can exert a significant control on levels of dissolved chromium under moderately oxidising to reducing conditions. Eskolaite ($Cr_2O_3(s)$) and chromite ($FeCr_2O_4(s)$) are possible candidates (Rai et al., 1988), although the former is rare (Rai et al., 1988), and direct precipitation of the latter from solution is not expected at the low temperature of natural systems (Hem, 1977). In a reducing, iron-free environment, Cr(III) precipitates readily to form $Cr(OH)_3(s)$ ($pK_{sp} = 6.8$; Rai et al., 1987). This is thought to be the main solubility-limiting phase in the absence of iron (Richard and Bourg, 1991), and the main aqueous species in its stability field is $Cr(OH)_3(aq)$ (Fig. 1.9). However, as previously discussed, [Fe(III), Cr(III)] hydroxide is probably the main Cr(III) solubility-controlling phase in natural environments (Richard and Bourg, 1991).

Manganese oxides are likely to be responsible for the majority of Cr(III) oxidation in natural aquatic environments. They are present along with the hydrous oxides of iron and aluminium as coatings on mineral grains (Richard and Bourg, 1991; Kent et al., 1994), as crack deposits, or finely disseminated grains (whether or not in relation with bacterial activities) (Richard and Bourg, 1991). The oxidation reaction is thought to occur in three steps (Schroeder and Lee, 1975; Bartlett and James, 1979; Rai et al., 1986; Eary and Rai, 1987):

(1) Adsorption of Cr(III) onto manganese oxide surface sites;
(2) Oxidation of Cr(III) to Cr(VI) by surface Mn(IV);
(3) Desorption of reaction products, Cr(VI) and Mn(II).

The manganese oxide would subsequently decay into solution. The rate of this reaction is related to the amount and surface area of manganese oxides (Schroeder and Lee, 1975; Eary and Rai, 1987). It is initially rapid, but slows after 20-60 minutes, never reaching completion, and it has been suggested that not all the Mn(IV) sites may be accessible to Cr(III) (Rai et al., 1986). Manganese oxides have been shown experimentally to oxidise Cr(III) to Cr(VI) (Eary and Rai, 1987; Johnson and Xyla, 1991). However, the necessity of a solid-phase reaction between either $Cr(OH)_3$ or sorbed Cr(III) species suggests that this reaction is likely to be of little importance in environments low in manganese oxides (Kent et al., 1994; Armienta and Quéré, 1995).

Although oxygen has been shown to oxidise Cr(III) to Cr(VI) under laboratory conditions (Schroeder and Lee, 1975; Nakayama et al., 1981; Rai et al., 1986; Eary and Rai, 1987), the rate of oxidation at room temperature is very low. Thus, Cr(III) is more likely to be involved in faster concurrent reactions such as sorption or precipitation. Hence, the oxidation of Cr(III) by dissolved oxygen is unlikely in soils and aquifers (Richard and Bourg, 1991), and has not been observed in field studies (Kent et al., 1994).

1.3.3.2 Adsorption of Cr(III) and Cr(VI)

Precipitation of Cr(III) from solution either as [Cr(III)/Fe(III)] hydroxide or $Cr(OH)_3(s)$ is favoured under most natural aquatic conditions (Davis and Olsen, 1995). However, under conditions where pH is less than 4, as in some tailings impoundments, Cr(III) concentrations may become high (Calder, 1988). Under such conditions, the cationic Cr(III) species are rapidly, strongly and specifically adsorbed by clay minerals. These minerals are strong adsorbents because they typically have high ion exchange capacities, and pH_{ZPC} (pH of zero point of charge) values of approximately 2-2.5 (Stumm and Morgan, 1981). The adsorption of Cr(III) on silica, which also has a pH_{ZPC} of ~2.5 is shown in Fig. 1.10.

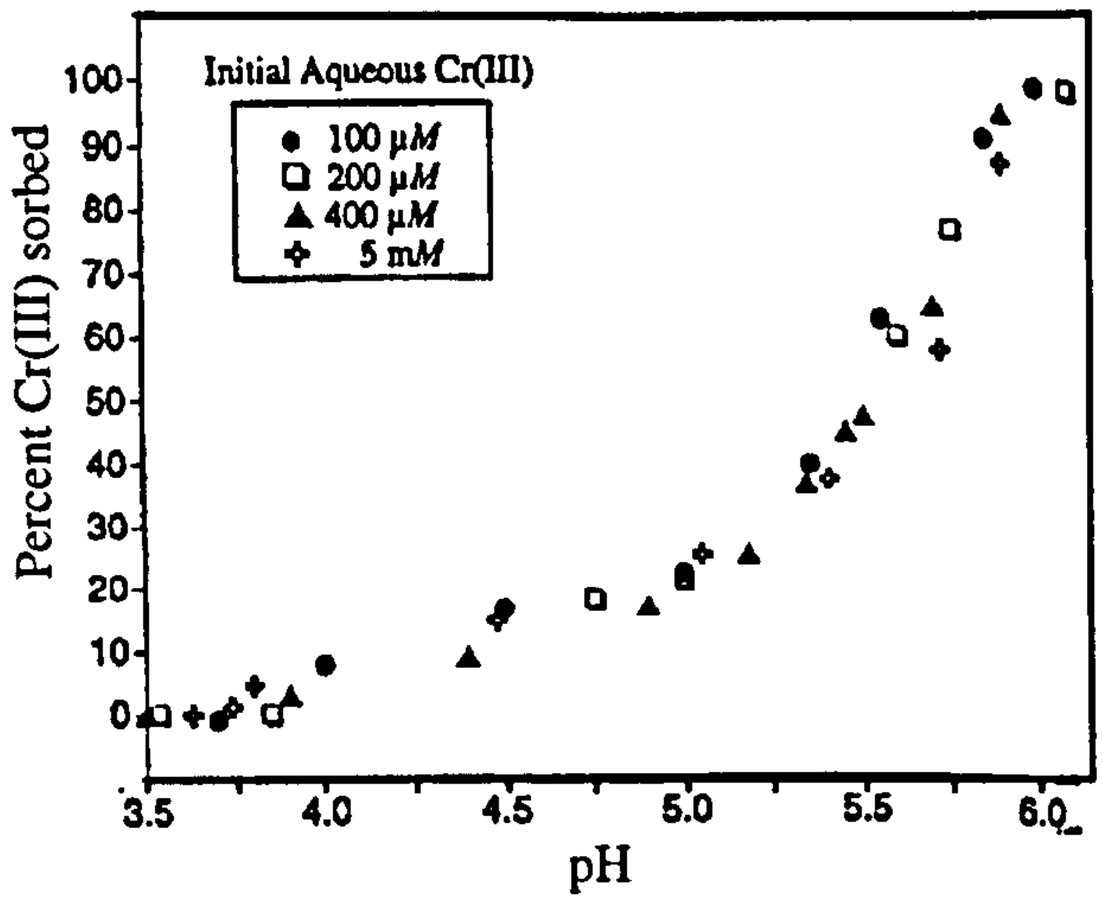

Fig. 1.10. Percent of Cr(III) sorbed as a function of pH at initial aqueous Cr(III) concentrations of 100, 200, 400 and 5000 μM Cr(III), with a silica suspension density of 0.25 gL^{-1}. From Fendorf et al., 1994.

It is clear that the adsorption of Cr(III) increases with pH, reaching 100% by pH 6 (contrast this with the position of the Cd(II) adsorption edges in Fig. 1.5). This is due to the increasingly negative charge of the mineral surface (Rai et al., 1988; Calder, 1988), and Cr(III) is adsorbed so strongly above pH 4 that it is largely immobile (Calder, 1988). Cr(III) adsorption also increases with the solid organic matter content of soils (Pàya Pérez et al., 1988). It decreases when other inorganic cations are in solution as a result of competitive adsorption. It also decreases when dissolved organic ligands are present in solution due to stabilisation of soluble Cr(III)-organic complexes (Richard and Bourg, 1991) (see section 1.3.3.3).

The sorption of chromate anions ($HCrO_4^-$ or CrO_4^{2-}) increases as pH decreases (Fig. 1.11). $HCrO_4^-$ and CrO_4^{2-} are much less strongly sorbed than Cr(III) ions, and are removed from solution most effectively by positively charged surfaces. Since iron, aluminium and manganese oxides have pH_{ZPC} values of 6.7-8.5 (Stumm and Morgan, 1981), they are important adsorbents of Cr(VI) ions. This is illustrated for iron and aluminium oxides in Fig. 1.11, which also shows that the clay minerals are relatively poor sorbents of Cr(VI).

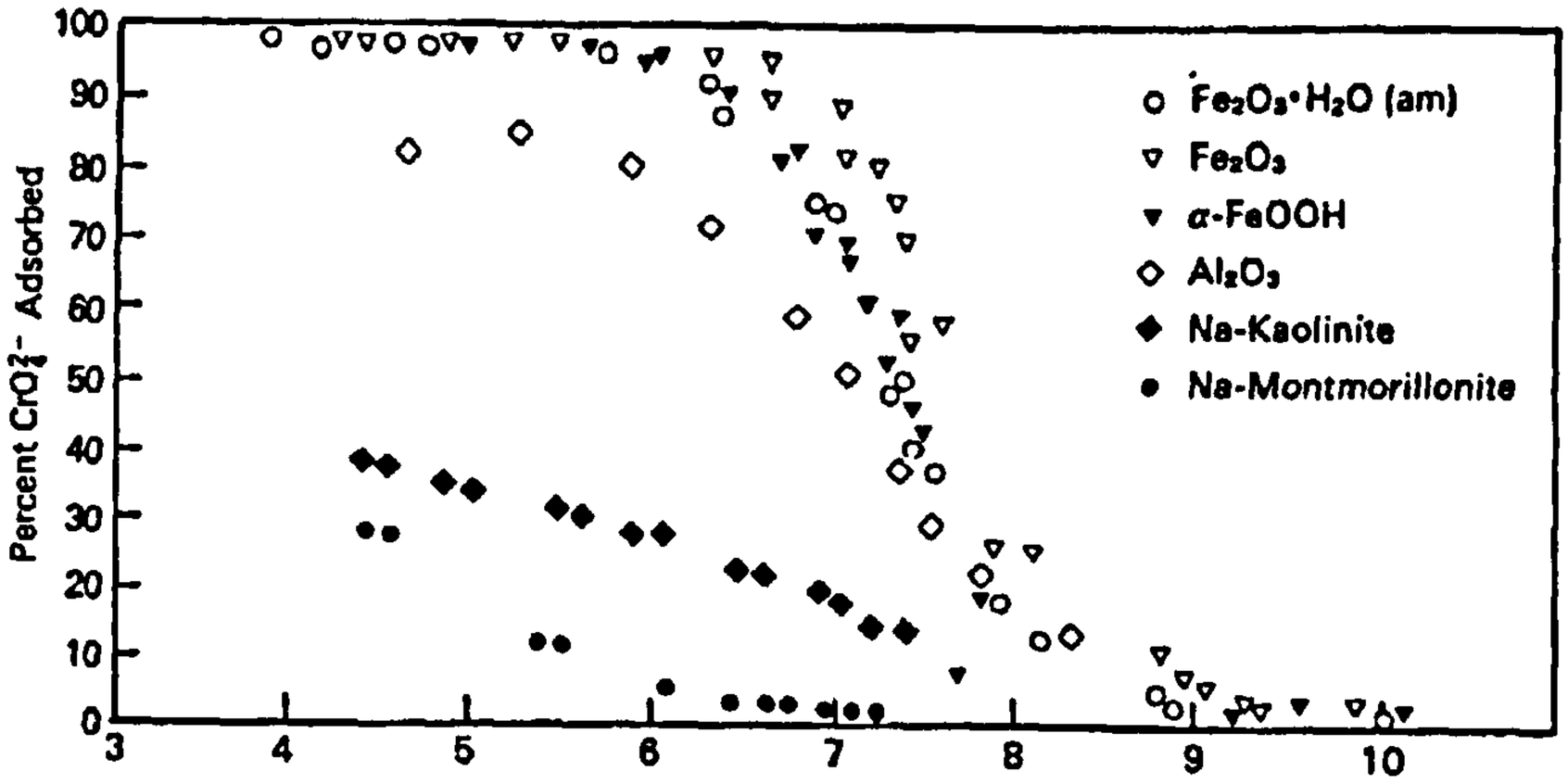

Fig. 1.11. Adsorption of Cr(VI) by different sorbents for a fixed adsorption site concentration. From Rai et al., 1989.

The presence of competing anions such as Cl^-, NO_3^-, SO_4^{2-}, HCO_3^-, $H_2SiO_4^{2}$, phosphate mixtures ($HPO_4^{2-}/H_2PO_4^-$, 1:1) and MoO_4^{2-} can significantly decrease the extent of Cr(VI) adsorption (Stollenwork and Grove, 1985; Music et al., 1986; Rai et al., 1986, 1988; Zachara et al., 1987). Phosphate and sulphate seem to be amongst the most important competing anions encountered in the sub-oxic zone (Kent et al., 1994). However, the co-adsorption of Cr(VI) with major ground water cations (K^+, Ca^{2+}, Mg^{2+}) at millimolar concentrations slightly increases chromate adsorption. This is due to the fact that adsorption of cations increases the positive mineral surface charge. This has the effect of making anion adsorption more favourable at any given pH (Rai et al., 1986). Similarly, chromate adsorption can itself slightly increase the extent of heavy metal adsorption (Cd^{2+}, Co^{2+}, Zn^{2+}) (Benjamin and Bloom, 1981). In systems where metal binding is enhanced by chromate adsorption, Benjamin and Bloom (1981) suggest that a secondary surface phase, such as a Fe-chromate solid may have formed.

Unlike the adsorption of Cr(III) species from solution, Cr(VI) adsorption is quite slow, and its kinetics are not well documented (Richard and Bourg, 1991; Kent et al., 1994). Amacher et al. (1988) suggest that Cr(VI) adsorption proceeds via a two-step reaction. The faster, reversible reaction (probably weak Cr(VI) adsorption) reaches equilibrium within 24 hours, whereas the overall chromium retention reaction fails to reach equilibrium within two weeks. Irreversible or slow reversible reactions such as coprecipitation or internal diffusion have been invoked as an explanation of this behaviour (Amacher et al., 1988). As mentioned earlier, the reduction of adsorbed Cr(VI) to strongly sorbed/coprecipitated Cr(III) would make the adsorption of Cr(VI) strong and 'irreversible'.

However, it is important to remember that in natural environments, Cr(VI) sorption will be highly influenced by the electrostatic conditions imposed by the common major anions which bind to the solid surfaces. Rai et al. (1986) therefore suggest that Cr(VI) adsorption can be expected to be minimal in groundwater and soil. Indeed, Rai et al. (1988) observe that Cr(VI) mobility is decreased only slightly by sorption to amorphous ferric hydroxide, and even less by sorption to clay minerals.

1.3.3.3 Complexation of chromium species

Cr(VI) species are not observed to form complexes with either inorganic or organic ligands (Armienta and Quéré, 1995). However, Cr(III) can form highly soluble complexes in the laboratory with a variety of inorganic ligands such as hydroxyl, sulphate, ammonium, cyanide and sulphocyanide, fluoride and chloride (to a lesser extent) (Richard and Bourg, 1991; Armienta and Quéré, 1995). Organic ligands such as citric acid, diethylenetriamine-pentaacetate (DTPA), fulvic acids and the water-soluble extract of an air-dried soil can also form highly soluble complexes with Cr(III) (Bartlett and Kimble, 1976; James and Bartlett, 1983). Although these complexation reactions are particularly effective under acidic conditions (James and Bartlett, 1983), the complexes remain stable above pH 5.5, at which point all uncomplexed Cr(III) is precipitated or adsorbed (James and Bartlett, 1983). Consequently, complexed Cr(III) may remain mobile in near neutral pH groundwater at relatively high concentrations. Whilst Calder (1988) points out that the presence of Cr(III) complexes has not been documented under field conditions, this may be an artefact of the lack of such data.

1.3.4 The importance of reaction kinetics

Predictive modelling of the transport and fate of redox-sensitive contaminants cannot be based solely on equilibrium thermodynamics, and a knowledge of the relative reaction rates is essential (Kent et al., 1994). This is certainly the case when considering the behaviour of chromium in the environment since (a) Processes such as Cr(III) oxidation by oxygen are secondary in importance to less thermodynamically favourable reactions such as rapid Cr(III) oxidation by Mn(IV); (b) Although the rates of chromium redox reactions are poorly known (Richard and Bourg, 1991), the oxidation of Cr(III) to Cr(VI) is much slower than the reverse reaction; this has implications for the release rate of Cr(VI) from solid mineral/organic surfaces; (c) Although reduction of Cr(VI) by organic material is

feasible, it is even slower than the oxidation of Cr(III) to Cr(VI). As a consequence, the importance of this reaction in the environment is questionable.

Additionally, reactions of chromium during groundwater flow should be considered in the context of a given natural situation. For instance, the reduction of Cr(VI) by Fe(II) from weathering of iron-bearing minerals, which are often concentrated in the finest sediment fraction, may not be significant if the majority of ground water flow is through more porous bands (Davis et al., 1994; Armienta and Quéré, 1995).

1.3.5 Chromium in the environment: Summary

The mobility of chromium is largely determined by its Eh-pH-dependent speciation. However, chemical considerations such as the presence of competing ions and complexing agents are important, as are kinetic considerations.

Cr(III) is expected to be largely immobile in natural systems, since its aqueous concentration is regulated by strong adsorption and a range of low solubility Cr(III) minerals in the neutral to alkaline pH range. Under acidic conditions, adsorption alone is the dominant mechanism limiting Cr(III) mobility. Solubility-limiting precipitation and adsorption reactions can become inhibited in the presence of dissolved ligands such as natural organic matter. Complexes with such material can remain stable up to ~ pH 7, and it is possible that resulting elevated Cr(III) mobility may pose a threat of severe pollution (Richard and Bourg, 1991). Additionally, oxidation of Cr(III) to the more mobile and more toxic Cr(VI) form may occur in the presence of solid manganese oxides.

Under oxidising conditions, the mobility of the Cr(VI) species is largely uninhibited, and Cr(VI) can be transported by groundwater in a largely conservative manner. This means that it is transported at a similar rate to the groundwater flow with very little attenuation. Cr(VI) adsorption to mineral surfaces is relatively weak, and is generally only favoured under neutral to acidic pH conditions. It is decreased by competitive adsorption with common ground water anions. However, reduction to Cr(III) by Fe(II) and dissolved organics with subsequent precipitation, coprecipitation (e.g. Cr,$Fe(OH)_3$(s)) or adsorption of Cr(III) can remove Cr(VI) from solution. This is a seemingly common chain of events because Cr(VI) pollution is generally limited to the vicinity of its source; the majority is reduced to Cr(III).

1.4 AIMS AND OBJECTIVES

It is clear from preceding parts of this chapter that arsenic, cadmium and chromium are all significant contaminants in soil and sediment systems around the world, and that this contamination poses a significant health risk to a huge number of people. The aim of this Ph.D. project is to investigate the fundamental inorganic processes which control the mobility of arsenic, cadmium and chromium in sediments and soils. Performing the literature review that forms the basis of this chapter has allowed me to identify the most important reactions and areas of current uncertainty regarding the behaviour of these three elements. By addressing these problems, I hope to improve our understanding of the processes that lead to 'natural attenuation', which is a phenomenon whereby naturally occurring materials act as a barrier to the migration of contaminants. I also hope to be able to identify situations where natural attenuation should not be relied upon to limit contaminant mobility. I hope that this knowledge will lead to improvements in waste is disposal practice, as well as improvements in the way that contaminated land is currently assessed and remediated.

All of the work presented in this thesis was performed in the laboratory using carefully characterised experimental systems as analogues for natural systems. The experimental systems were purposefully simple in composition. For instance, they did not contain organic material or microbes, both of which are widespread in nature. The reason for this is that whilst the outcome of geochemical reactions involving the three studied elements in nature are often known, the underlying fundamental reaction(s) often are not. In my view, it is pointless to try and evaluate the complex natural reactions as a whole before there is a fundamental understanding of their basic components. Furthermore, it seems logical to me that the complex reactions should be broken down according to the type of chemistry that they involve. Thus, the work that I have performed here amounts to a thorough investigation of some of the most important *inorganic* reactions that exert a control on the mobility of arsenic, cadmium and chromium.

A number of other research groups (notably the Geomicrobiology group in the Department of Earth Sciences, University of Bristol) are currently probing organic and/or microbial aspects of the reactions that I have investigated. Thus, the next logical step would be to combine forces on this research, and perform experiments involving an increasing number of components. This approach promises a full and rigorous understanding of trace metal biogeochemistry, which is the ultimate goal of this type of research.

Below, I outline the specific experimental objectives that are addressed in chapters 3–6.

1.4.1 Cadmium (chapters 3 and 4)

Although cadmium is known to be accumulated by iron and manganese (oxyhydr)oxides in soils and sediments, the fundamental chemical reactions leading to adsorption are poorly constrained. A lack of understanding at such a basic level has hampered the generation of reliable thermodynamic data describing the adsorption process. Thus, a clear aim was to investigate the mechanism by which cadmium sorbed to a range of iron oxyhydroxides and a manganese oxide over a range of pH and surface loading conditions.

1.4.2 Arsenic and chromium (chapters 5 and 6)

Because cadmium exists only in the +2 oxidation state, it's redox chemistry is extremely simple. The same is not true of arsenic and chromium, which commonly exist in the environment in the following oxidation states: As(III), As(V), Cr(III) and Cr(VI). Because these different oxidation states differ markedly in their mobility and toxicity, it is of vital importance that processes leading to changes in oxidation state are recognised and understood. Despite this, relatively little research has been performed in this area.

Changes in redox state commonly result when the contaminant is carried from one geochemical environment into another by groundwater flow and/or when the ambient geochemical conditions change over time whilst contaminant location remains unchanged. In order to investigate the former scenario, solutions of As(V) and Cr(VI) were reacted with suspensions of 'green rust', which is a mixed Fe(II)/Fe(III) oxyhydroxide. This compound a potent reductant that is thought to occur extensively in waterlogged soils and sediments. The latter scenario was simulated by sulphidising a suspension of arsenic-contaminated goethite (α-FeOOH). In both cases, experimental conditions were carefully controlled.

The final objective was to investigate the importance of sorbent ageing on contaminant mobility. This was assessed by monitoring changes in the way that As(V) was sorbed by ferrihydrite (a poorly crystalline iron oxyhydroxide mineral) as it aged into more crystalline forms (goethite and hematite). This reaction is of potentially great importance in assessing the risks posed by heavily contaminated, immature sediments. This is because the ageing of poorly crystalline, high surface area sorbents (such as ferrihydrite) into more crystalline, low(er) surface area

sorbents (such as goethite and hematite) can either lead to contaminant release or the formation of stable coprecipitate minerals.

1.5 REFERENCES

Abd-Elfattah A. and Wada K. (1981) Adsorption of lead, copper, zinc, cobalt and calcium by soils that differ in cation exchange materials. J. Soil. Sci. 32, 271-283.

Ajmal M., Nomani A. A. and Ahmad A. (1984) Acute toxicity of chrome electroplating wastes to microorganisms: adsorption of chromate and chromium(VI) on a mixture of clay and sand. Water, Air, Soil Poll. 23, 119-127.

Alloway B. J. and Jackson A. P. (1991) The behaviour of heavy metals in sewage sludge-amended soils. Sci. Total Environ. 100, 151-176.

Amacher M. C., Selim, H. M. and Iskandar I. K. (1988) Kinetics of chromium(VI) and cadmium retention in soils - a nonlinear multireaction model. Soil Sci. Soc. Am. J. 52, 398-408.

Anderson M. A., Ferguson J. F. and Gavis J. (1976) Arsenate adsorption on amorphous aluminum hydroxide. J. Colloid Interface Sci., 54, 391.

Anderson P. R. and Christensen T. H. (1988) Distribution coefficients of cadmium, cobalt, nickel and zinc in soils. J. Soil Sci. 39, 15-22.

Andreae M. O. amd Klumpp D. K. (1979?) Env. Sci. Technol. 13, 738-740.

Appelo C. A. J. and Potsma D. (1993) *Geochemistry, groundwater and pollution.* Balkema.

Armienta M. A. and Quéré A. (1995) Hydrogeochemical behavior of chromium in the unsaturated zone and in the aquifer of leon valley, mexico. Water, Air, Soil Poll. 84, 11-29.

Asami T., Kubota M. and Orikasa K. (1995) Distribution of different fractions of cadmium, zinc, lead and copper in unpolluted and polluted soils. Water, Air and Soil Poll. 83, 187-194.

Backer, D. E. and Chesnin L. (1975) Chemical monitoring of soils for environmental quality and animal and human health. Adv. Agron. 27, 305-374.

Baes C. F. Jr. and Mesmer R. E. (1977) *The hydrolysis of cations.* John Wiley and Sons, NY. pp.489.

Balistrieri L. S. and Murray J. W. (1982) The adsorption of Cu, Pb, Zn, and Cd on goethite from major ion seawater. Geochim. Cosmochim. Acta 46, 1253-1265.

Bartlett R. J. (1986) Soil redox behaviour. In *Soil Physical Chemistry* (ed. D. L. Sparks), CRC Press, Boca Raton, Florida. pp. 179-207.

Bartlett R. J. and James B. R. (1979) Behaviour of chromium in soils. III. Oxidation. J. Env. Qual. 8, 31-35.

Bartlett R. J. and James B. R. (1988) Mobility and bioavailability of chromium in soils. In *Chromium in the natural and human environments* (eds. J. O. Nriagu and E. Nieboer). John Wiley and Sons, N. Y.

Benjamin M. M. and Bloom N. S. (1981) Effect of strong binding of anionic adsorbates on adsorption of trace metals on amorphous iron oxyhydroxide. In *Adsorption from aqueous solution* (ed. P. H. Tewari). Plenum Press, NY.

Benjamin M. M. and Leckie J. O. (1981) Multiple-site adsorption of Cd, Cu, Zn, and Pb on amorphous iron oxyhydroxide. J. Colloid and Inteface. Sci. 79, 209-221.

Bermond, A. and Bourgeois, S. (1992) Influence of soluble organic matter on cadmium mobility in model compounds and in soils. Analyst 117, 685-687.

Bhumbla D. K. and Keefer R. F. (1994) Arsenic mobilization and bioavailability in soils. In *Arsenic in the environment, Part. 1: Cycling and characterization* (Ed. Nriagu, J. O.). John Wiley and Sons, New York. pp. 51-82.

Bigham J. M., Schwertmann U., Carlson L. and Murad E. (1990) A poorly crystallized oxyhydrosulfate of iron formed by bacterial oxidation of Fe(II) in acid mine water. Geochim. Cosmochim. Acta 54, 2743-2758.

Bowell R. J. (1994) Sorption of arsenic by iron oxides and oxyhydroxides in soils. Applied Geochemistry 9, 279-286.

Bowen H. J. M (1979) *Elemental chemistry of the elements*. Acad. Press, London & N. Y. pp. 60-61.

Bowen H. J. M. (1966) *Trace elements in biochemistry*. Academic Press.

Boyko S. L. and Goodgame D. M. L. (1986) The interaction of soil fulvic acid and Cr(VI) produces relatively long-lived water soluble Cr(V) species. Inorg. Chim. Acta 123, 189-191.

Braman R. S. and Foreback C. C. (1973) Methylated forms of arsenic in the environment. Science 182, 1247-1249.

Branson J. M. and Patrick W. J. (1987) Fixation, transformation, and mobilization of arsenic in sediments. Environ. Sci. Technol. 20, 450-459.

Brookins D. G. (1988) *Eh-pH diagrams for geochemistry*. pp. 56-57. Springer-Verlag, NY.

Brummer G. W., Gerth J. and Barrow N. J. (1988) Reaction kinetics of adsorption and desorption of nickel, zinc and calcium by geothite. I. Adsorption and diffusion of metals. J. Soil. Sci. 39, 37-52.

Calder L. M. (1988) Chromium contamination of groundwater. In *Chromium in the natural and human environments* (eds. J. O. Nriagu and E. Nieboer). John Wiley and Sons, N. Y.

Chatterjee A., Das D., Mandal B. K., Chowdhury T. R., Samanta G. and Chakraborti D. (1995) Arsenic in groundwater in 6 districts of West Bengal, India - The

biggest arsenic calamity in the world. 1. Arsenic species in drinking water and the urine of affected people. Analyst 120, 643-650.

Christensen T. H. (1984) Cadmium soil sorption at low concentrations. 1. Effect of time, cadmium load, pH and calcium. Water, Air, Soil Poll. 21, 105-114.

Collins C.R., Ragnarsdottir K.V., and Sherman D.M. (1999) Effect of inorganic and organic ligands on the adsorption of Cd^{2+} to goethite. Geochim. Cosmochim. Acta. (submitted).

Comans R. N. J. (1987) Adsorption, desorption and isotopic exchange of cadmium on illite: Evidence for complete reversibility. Water Res. 21, 1573-1576.

Cowan C. E., Zachara J. M., and Resch C. T. (1991) Cadmium adsorption on iron oxides in the presence of alkaline earth metals. Environ. Sci. Technol. 25, 437-446.

Das D., Samanta G., Mandall B. K., Chowdry T. R., Chanda C. R., Chowdry P. P., Basu G. K., Chakraborti D. (1996) Arsenic in groundwater in six districts of West Bengal, India. Environmental Geochem. and Health 18, 5-15.

Davis A. and Olsen R. L. (1995) The geochemistry of chromium migration and remediation in the subsurface. Ground Water 33, 759-768.

Davis A. P. and Upadhyaya M. (1996) Desorption of cadmium from goethite (alpha-FeOOH). Water Research 30, 1894-1904.

Davis J. A., Fuller C. C. and Cook A. D. (1987) A model for trace metal sorption processes at the calcite surface: Adsorption of Cd^{2+} and subsequent solid solution formation. Geochim. Cosmochim. Acta 51, 1477-1490.

Deutsch M. (1972) Incidents of chromium contamination of groundwater in Michigan. In *Water quality in a stressed environment* (ed. W. A. Pettyjohn). Burgess Publishing Co., Minneapolis.

Dryssen D. and Wedborg M. (1980) Major and minor element chemical speciation in estuarine waters. In *Chemistry and biochemistry of oceans* (eds. E. Olausson and I. Cato). pp. 71-119. Wiley, Chichester.

Dzomback D. A. and Morel F. M. M. (1990) *Surface complexation modeling: Hydrous ferric oxide*. John Wiley and Sons, NY.

Eary L. E. and Rai D. (1987) Kinetics of Cr(III) oxidation to Cr(VI) by reaction with manganese dioxide. Environ. Sci. Technol. 21, 1187-1193.

Eary L. E. and Rai D. (1988) Chromate removal from aqueous wastes by reduction with ferrous ion. Environ. Sci. Technol. 22, 972-977.

Elkhatib E. A., Bennett O. L. and Wright R. J. (1984) Arsenite sorption and desorption in soils. Soil Sci. Soc. Am. J. 48, 1025-1030.

Elliott H. A., Liberati M. R. and Huang C. P. (1986) Competitive adsorption of heavy metals by soils. J. Env. Qual. 15, 214-219.

Fendorf S. E., Lamble G. M., Stapleton M. G., Kelley M. J. and Sparks D. L. (1994) Mechanism of chromium(III) sorption on silica. 1. Cr(III) surface structure derived by extended X-ray absorption fine structure spectroscopy. *Environ. Sci. Technol.* **28**, 284-289.

Ferguson J. F. and Gavis J. (1972) A review of the arsenic cycle in natural waters. Water Res. 6, 1259-.

Fleischer M. (1972) An overview of distribution patterns of trace elements in soils. Ann. NY Acad. Sci. 199, 6-16.

Fuller C. C. and Davis J. A. (1987) Processes and kinetics of Cd^{2+} sorption by a calcareous aquifer sand. Geochim. Cosmochim. Acta 51, 1491-1502.

Goodgame D. M. L., Hayman P. B. and Hathway D. E. (1984) Formation of water soluble Cr(V) by the interaction of humic acid and the carcinogen Cr(VI). Inorg. Chim. Acta 91, 113-115.

Hahne H. C. H. and Kroontje W. (1973) Significance of pH and chloride concentration on behaviour of heavy metal pollutants: mercury(II), cadmium(II), zinc(II), and lead(II). J. Env. Qual. 2, 444-450.

Hem J. D. (1972) Chemistry and occurence of cadmium and zinc in surface water and groundwater. Water Resources Res. 8, 661-679.

Hering J. G. (1994) Effects of chemical speciation of arsenic on adsorption - implications for arsenic mobility in the environment and removal from drinking-water. Abstracts of papers of the American Chemical Society, Vol.207, no.pt1, pp.210-ENVR.

Hiller D. A. and Brummer G. W. (1995) Electron microprobe studies on soil samples with varying heavy-metal contamination. 1. Methods and analysis of elements in pedogenic oxides. Zeitschrift Fur Pflanzenernahrung Und Bodenkunde 158, 147-156.

Hutchinson T. C. and Meema K. A. (eds.) (1987) *Lead, Cadmium, Mercury and Arsenic in the Environment*. John Wiley and Sons.

Iimura K. (1981) In *Heavy metal pollution in soil of Japan* (Eds. K. Kitagishi and I. Yamane), Jpm. Sci. Soc. Press, Tokyo, pp. 19-26.

James B. R. (1994) Hexavalent chromium solubility and reduction in alkaline soils enriched with chromite ore processing residue. J. Env. Qual. 23, 227-233.

James B. R. and Bartlett R. J. (1983) Behaviour of chromium in soils. VI. Interactions between oxidation-reduction and organic complexation. J. Environ. Qual. 12, 173-176.

Jardine P. M., Weber N. L. and McCarthy J. F. (1989) Mechanisms of dissolved organic carbon sorption on soil. Soil Sci. Am. J. 53, 1378-1385.

Jin T. Y., Lu J. and Nordberg M. (1998) Toxicokinetics and biochemistry of cadmium with special emphasis on the role of metallothionein. Neurotoxicology 19, 529-535.

Johnson B. B. (1990) Effect of pH, temperature, and concentration on the adsorption of cadmium on goethite. *Env. Sci. Technol.* 24, 112-118.

Johnson C. A. and Xyla A. G. (1991) The oxidation of Cr(III) to Cr(VI) on the surface of manganite (γ-MnOOH). Geochim. Cosmochim. Acta 55, 2861-2866.

Kent D. B., Davis J. A., Anderson L. C. D., Rea B. A. and Waite T. D. (1994) Transport of chromium and selenium in the suboxic zone of a shallow aquifer: Influence of redox and adsorption reactions. Water Resources Res. 30, 1109-1114.

Kinniburgh D. G., Jackson M. L. and Syers, J. K (1976) Adsorption of alkaline earth, transition, and heavy metal cations by hydrous oxide gels of iron and aluminium. Soil Sci. Am. J. 40, 796-799.

Krishna Murti C. R., Olade M. A. and Page A. L. (1987) Group Report: Cadmium. In *Lead, cadmium, mercury and arsenic in the environment* (eds. T. C. Hutchinson and K. A. Meema). pp. 35-41. John Wiley and Sons Ltd.

Kuo S. and Jellum J. (1991) Affinity constants and the behaviour of cadmium sorption in some acid soils. Water, Air, Soil Poll. 57-58, 369-376.

Kuo S. and McNeal B. L. (1984) Effects of pH and phosphate on cadmium sorption by ferric oxide. Soil Sci. Am. J. 48, 1040-1044.

Lagerwerff J. V. and Specht A. W. (1970) Contamination of roadside soil and vegetation with Cd, Ni, Pb and Zn. Environ. Sci. Technol. 4, 55-58.

Lamy I., Djafer M. and Terce M. (1991) Influence of oxalic acid on the adsorption of cadmium at the geothite surface. Water, Air, Soil Poll. 57-58, 457-465.

Lamy I., Bourgeois S. and Bermond A. (1993) Soil cadmium mobility as a consequence of sewage sludge disposal. J. Env. Qual. 22, 731-737.

Lehoczky E., Szabo L., Horvath S., Marth P. and Szabados I. (1998) Cadmium uptake by lettuce in different soils. Comm. In Soil Sci. and Plant Anal. 29, 1903-1912.

Lion L. W., Shuler M. L., Hsieh K. M. and Ghiorse W. C. (1988) Trace metal interactions with microbial biofilms. CRC Crit. Rev. Environ. Con. 17, 273-306.

Le Riche H. H. and Weir A. H. (1963) A method of studying trace elements in soil fractions. J. Soil. Sci. 14, 225-235.

Levander O. A. (Ed.) (1977) *Arsenic.* National Academy of Sciences, Washington, DC.

Mandal B. K., Chowdry T. R., Samanta G., Basu G. K., Chowdry P. P., Chanda C. R., Lodh, D., Karan N. K., Dhar R. K., Tamili D. K., Das D., Saha K. C. and

Chakraborti D. (1996) Arsenic in groundwater in seven districts of West Bengal, India - The biggest arsenic calamity in the world. Current Sci. 70, 976-986.

Marin A. R., Masscheleyn P. H. and Patrick W. H. Jr. (1993) Soil redox-pH stability of arsenic species and its influence on arsenic uptake by rice. Plant and Soil 152, 245-253.

Masscheleyn P. H., Delaune R. D. and Patrick W. H. (1991a) Arsenic and selenium chemistry as affected by sediment redox potential and pH. Env. Sci. Technol. 20, 522-527.

Masscheleyn P. H., Delaune R. D. and Patrick W. H. (1991b) Effect of redox potential and pH on arsenic speciation and solubility in a contaminated soil. Env. Sci. Technol. 25, 1414-1419.

Matzat E. and Shiraki K. (1974) Chromium. In *Handbook of geochemistry* (eds. K. Wedepohl et al.). Springer-Verlag, Heidelberg.

McKenzie R. M. (1980) The adsorption of lead and other heavy metals on oxides of manganese and iron. Aust. J. Soil. Sci. 18, 61-73.

McLaughlin M. J., Parker D. R. and Clarke J. M. (1999) Metals and micronutrients - food safety issues. Field Crops Res. 60, 143-163.

Mertz W. (1974) Chromium as a dietary essential of man. In *Trace elemnts metabolism* Vol. 2 (ed. W. G. Hoekstra et al.). pp.185-198. University Park Press, Baltimore.

Moore J. W. and Ramamoorthy S. (1984) *Heavy metals in natural waters: Applied monitoring and impact assessment.* Springer-Verlag. pp. 28-57.

Moore J. N., Ficklin W. H. and Johns C. (1988) Partitioning of arsenic and metals in reducing sulfidic sediments. Environ. Sci. Technol. 22, 432-437.

Naidu R., Bolan N. S., Kookana R. S., and Tiller K. G. (1994) Ionic strength and pH effects on the sorption of cadmium and the surface charge of soils. European J. Soil Sci. 45, 419-429.

Nakayama E., Kuwamoto T., Tsurubo S., Tokoro H. and Fujinaga T. (1981) Chemical speciation of chromium in seawater. 1. Effect of naturally occuring organics materials on the complex formation of Cr(III). Analyt. Chim. Acta 130, 289-294.

Nieboer E. and Jusys A. A. (1988) Biologic chemistry of chromium. In *Chromium in the natural and human environments* (eds. J. O. Nriagu and E. Nieboer). John Wiley and Sons, N. Y.

Nriagu J. O. (1980) Cadmium in the atmosphere and in precipitation. In *Cadmium in the Environment Part 1, Ecological Cycling* (ed. J. O. Nriagu). pp. 71-114. John Wiley and Sons.

Nriagu J. O. (1988) Production and uses of chromium. In *Chromium in the natural and human environments* (eds. J. O. Nriagu and E. Nieboer). John Wiley and Sons, N.Y.

Nriagu, J. O. (ed.) (1994) *Arsenic in the environment, Part. 1: Cycling and characterization.* John Wiley and Sons, New York.

Page A. L., Chang A. C. and El-Amamy M. (1987) Cadmium levels in soils and crops in the United States. In *Lead, cadmium, mercury and arsenic in the environment* (eds. T. C. Hutchinson and K. A. Meema). pp. 119-146. John Wiley and Sons Ltd.

Pàya Pérez A. B. et al. (1988) Sorption of Cr species on soil. In *Heavy metals in the hydrocycle* (eds. M. Astruc and J. N. Lester). Selper, London.

Perlmutter N. M. and Lieber M. (1970) Dispersal of plating wastes and sewage contaminants in groundwaterand surface water, South Farmingdale Massapequa Area, Nassau County, NY. U.S.G.S. Water Supply Paper 1879-G.

Petersen W., Wallmann K., Schroer S., and Schroeder F. (1993) Studies on the adsorption of cadmium on hydrous iron(III) oxides in oxic sediments. Analytica Chimica Acta 273, 323-327.

Pierce M. L. and Moore C. B. (1982) Adsorption of arsenite and arsenate on amorphous iron hydroxide. Water Res. 16, 1247-1253.

Pohland F. G. and Gould J. P. (1986) Codisposal of municipal refuse and industrial-waste sludge in landfills. Water Sci. Technol. 18, 177.

Rai, D., Zachara J. M., Eary L. E., Girvin D. C., Moore D. A., Resch C. T., Sass B. M. and Schmidt R. L. (1986) Geochemical behaviour of chromium species. Final Report EPRI EA-4544. Electric Power Research Institute, Palo Alto, CA.

Rai, D., Sass B. M. and Moore D. A. (1987) Chromium(III) hydrolysis constants and solubility of Cr(III) hydroxide. Inorganic Chem. 26, 345-349.

Rai D., Zachara J. M., Eary L. E., Ainsworth C. C., Amonette J. E., Cowan C. E., Szelmeczka R. W., Resch C. T., Schmidt R. L., Girvin D. C. and Smith S. C. (1988) Chromium reactions in geological materials. Report EPRI EA-5741. Electric Power Research Institute, Palo Alto, CA.

Rai D., Eary L. E. and Zachara J. M. (1989) Environmental chemistry of chromium. Science of the Total Environ. 86, 15-23.

Rai D., Felmy A. R. and Szelmeczka R. W. (1991a) Hydrolysis constants and ion-interaction parameters for Cd(II) in zero to high concentrations of NaOH-KOH and the solubility product of crystalline $Cd(OH)_2$. J. Soln. Chem. 20, 375-390.

Rai D., Felmy A. R. and Moore D. A. (1991b) Thermodynamic model for aqueous Cd^{2+}-$(CO3)^{2-}$ ionic interactions in high-ionic-strength carbonate soutions and the solubility product of crystalline $CdCO_3$. J. Soln. Chem. 20, 1169-1187.

Richard F. C. and Bourg A. C. M. (1991) Aqueous geochemistry of chromium - a review. Water Research 25, 807-816.

Riffaldi R. and Levi-Minzi R. (1975) Title Water, Air, Soil Poll. 5, 79-.

Robinson B. H., Leblanc M., Petit D., Brooks R. R., Kirkman J. H. and Gregg P. E. H. (1998) The potential of *Thlaspi caerulescens* for phytoremediation of contaminated soils. Plant And Soil 203, 47-56.

Robertson F. N. (1975) Hexavalent chromium in the groundwater in Paradise Valley, Arizona. Ground Water 13, 516-527.

Sakata M. (1987) Relationship between adsorption of arsenic(III) and boron by soil and soil properties. Env. Sci. Technol. 21, 1126-1130.

Salt D. E., Pickering I. J., Prince R. C., Gleba D., Dushenkov S., Smith R. D. and Raskin I. (1997) Metal accumulation by aquacultured seedlings of Indian mustard. Environ. Sci. Technol. 31, 1636-1644.

Sanchez-Camazano M., Sanchez-Martin M. J. and Lorenzo L. F. (1994) The content and distribution of cadmium in soils as influenced by the soil properties. Sci. Total Environ. 156, 183-190.

Sanchez-Martin M. J. and Sanchez-Camanzano (1993) Adsorption and mobility of cadmium in natural, uncultivated soils. J. Env. Qual. 22, 737-742.

Schindler P. W. (1967) Heterogeneous equilibria involving oxides, hydroxides, carbonates and hydroxide carbonates. In *Equilibrium concepts in natural water systems* (ed. R. F. Gould). Adv. Chem. Series Vol. 67. Am. Chem. Soc. Washington, DC.

Schmitt H. W. and Sticher H. (1991) Heavy metal compounds in the soil. *In Metals and their compounds in the environment: Occurence, analysis and biological relevance* (ed. E. Merian). pp. 311-331. VCH Publishers.

Schroeder D. C. and Lee G. F. (1975) Potential tranformations of chromium in natural waters. Water, Air, Soil Pollut. 4, 355-365.

Schmidt R. L. (1984) Thermodynamic properties and environmental chemistry of chromium. U. S. Dept. of Energy. Report DE-AC06-76RLD-1830.

Shacklette H. T. and Boerngen J. G. (1984) Element concentrations in soils and other surface materials. U.S.G.S. Professional Paper 1710.

Shuman L. M. (1977) Adsorption of Zn by Fe and Al hydrous oxides as influenced by aging and pH. Soil Sci. Am. J. 41, 703-706.

Smedley P. L., Edmunds W. M. and Pelig-Ba K. B. (1995) Mobility of arsenic in the Obuasi gold-mining area of Ghana: Some impliations for human health. In *Geochemistry and health in developing countries* (eds. Appleton D. et al.).

Spark K. M., Johnson B. B. and Wells J. D. (1995) Characterising heavy-metal adsorption on oxides and oxyhydroxides. Euro. J. Soil Sci. 46, 621-631.

Stollenwork K. G. and Grove D. B. (1985) Adsorption and desorption of hexavalent chromium in an alluvial aquifer near Telluride, Colorado. J. Env. Qual. 14, 150-155.

Stumm W. and Morgan J. J. (1981) *Aquatic Chemistry.* John Wiley and Sons, NY.

Takenaga H. and Aso S. (1975) J. Soil. Sci. Manure, Japan 46, 349-354.

Taylor R. M. and McKenzie R. M. (1966) The association of trace elements with manganese minerals in Australian soils. Aust. J. Soil Res. 4, 29-39.

Tessier A., Rapin F., and Carignan R. (1985) Trace metals in oxic lake sediments; possible adsorption onto iron oxyhydroxides. Geochim. Cosmochim. Acta 49, 183-194.

Tessier A., Fortin D., Belzile N., DeVitre R. R. and Leppard G. G. (1996) Metal sorption to diagenetic iron and manganese oxyhydroxides and associated organic-matter - narrowing the gap between field and laboratory measurements. Geochim. Cosmochim. Acta 60, 387-404.

Tiller K. G., Smith L. H., Merry R. H. and Clayton P. (1987) The dispersal of automotive lead from metropolitan adelaide into adjacent rural areas. Aust. J. Soil. Res. 25, 155-166.

Tipping E. and Hurley M. A. (1992) A unifying model of cation binding by humic substances. Geochim. Cosmochim. Acta 56, 3627-3641.

Turner D. R. (1987) Speciation and cycling of arsenic, cadmium and lead in natural waters. In *Lead, cadmium, mercury and arsenic in the environment* (eds. T. C. Hutchinson and K. A. Meema). John Wiley and Sons Ltd.

Turner D. R., Whitfield M. and Dickson A. G. (1981) The equilibrium speciation of dissolved components in freshwater and seawater at 25°C and 1 atm pressure. Geochim. Cosmochim. Acta 45, 855-881.

Venitt S. and Levy L. S. (1974) Mutagenicity of chromates in bacteria and its relevance to chromate carcinogenesis. Nature 250, 493-495.

Vinogradov A. P. (1959) The geochemistry of rare and dispersed chemical elements in soils, 2nd edn. New York, pp.65-70.

White A. F. and Yee A. (1986) Near surface alkalai diffusion into glassy and crystalline silicates at 25 - 100°C. In ACS Symp. vol. 323 (eds. J. A. Davis and K. F. Hayes).

Woolson E. A. (1977) Weed Sci., 25, 412-416.

World Health Organisation (1993) Guidelines for drinking water quality. Vol. 1. Recommendations, 2nd edn. WHO, Geneva.

Xu H., Allard B. and Grimvall A. (1988) Influence of pH and organic-substance on the adsorption of As(V) on geologic materials. Water, Air, Soil Pollution 40, 293-305.

Xu H., Allard B., Grimvall A. (1991) Effects of acidification and natural organic materials on the mobility of arsenic in the environment. Water, Air, Soil Pollution 57-8, 269-278.

Yan-Chu H. (1994) Arsenic distribution in soils. In *Arsenic in the environment, Pt. 1: Cycling and characterization* (ed. J. O. Nriagu). John Wiley and Sons, New York.

Zachara J. M., Girvin D. C., Schmidt R. L. and Resch C. T. (1987) Chromate adsorption on amorphous iron hydroxide in the presence of major groundwater ions. Env. Sci. Technol. 21, 589-594.

Zhu Y. L., Zayed A. M., Qian J. H., de Souza M. and Terry N. (1999a) Phytoaccumulation of trace elements by wetland plants: II. Water hyacinth. J. Env. Qual. 28, 339-344.

Zhu Y. L., Pilon-Smits E. A. H., Jouanin L. and Terry N. (1999b) Overexpression of glutathione synthetase in Indian mustard enhances cadmium accumulation and tolerance. Plant Physiology 119, 73-79.

Chapter 2

Experimental methods

2.0 INTRODUCTION

This chapter is an overview of the experimental techniques used in the collection and analysis of experimental data in this study.

The majority of aqueous samples were analysed for ppm levels of arsenic, cadmium, chromium, iron, manganese or potassium by inductively-coupled plasma atomic emission spectroscopy (ICP-AES). Inductively-coupled plasma mass spectrometry (ICP-MS) was used to measure aqueous chromium concentrations at ppb levels. Total sulphide concentrations were measured by UV-vis spectrophotometry.

The mineralogy of all solid phases was determined by X-ray diffraction (XRD). Several samples were further characterised by transmission electron microscopy (TEM), electron diffraction (ED) and surface area measurement.

Extended X-ray absorption fine structure (EXAFS) spectroscopy was used to determine the local coordination environment around the 'element of interest' in selected samples. This information provided an insight into how arsenic, cadmium and chromium are adsorbed onto, or incorporated into, a range of minerals. Quantum mechanical calculations were used to predict the idealised geometry of cadmium surface complexes on goethite. This approach was valuable because it provided independent information that was used to guide analysis of the associated EXAFS data.

2.1 DETERMINATION OF DISSOLVED SPECIES

2.1.1 Inductively-Coupled Atomic Emission Spectrometry (ICP-AES)

The majority of aqueous samples were analysed for ppm levels of arsenic, cadmium, chromium, iron, manganese or potassium on a Jobin Yvon JY24 ICP-AES. Table 2.1 details the parameters considered when analysing for these elements. The tabulated detection limits are optimistic, and in reality measurements only became accurate and reproducible above 200 ppb. Some samples could not be analysed by ICP-AES because they were in an unsuitable matrix for this instrument. An example

of this would be digestions for the bulk chemical analysis of chromium-contaminated iron oxyhydroxides (see Chapter 6), which resulted in ppm levels of chromium in ≥ 20 % HCl. These samples had to be diluted so that the matrix was ≤ 5 % HCl, with the consequence that chromium levels fell below the ICP-AES detection limit and into the concentration range more easily measured by ICP-MS.

Table 2.1. Experimental parameters for elements analysed by ICP-AES.

Element	Wavelength (nm)	Detection limit (ppb)	Interferences
Arsenic†	197.262	76.0	Al, V
Cadmium	228.802	2.7	Al, As, Fe, Ni
Chromium	267.716	7.1	Fe, Mn, V
Iron	234.349	10.0	None reported
Manganese	257.610	1.4	Al, Cr, Fe, V
Potassium	766.490	60.0	Ti

† Argon flow must be provided along the beam path in addition to the nitrogen flow used during analysis of all other elements.

The JY24 ICP-AES has a peristaltic pump for the uptake of samples and a Meinhard nebuliser which disperses samples into a fine aerosol. Nitrogen gas is used to carry a portion of this aerosol into the plasma torch where it is dissociated, atomised and ionised. It is the radiation emitted during high to low energy level electron transitions following excitation in the plasma that form the basis of AES measurements. The detection system in the JY24 ICP-AES is composed of an entrance slit that provides a rectangular optical image, followed by a collimating lens or mirror that produces a parallel beam of radiation. A diffraction grating disperses the radiation into its component wavelengths, after which it interacts with a focusing element and then an exit slit which isolates the desired spectral band. Incident radiation is detected by a photomultiplier, and the resulting signal is transferred from the spectrometer to the software by the spectralink. The optics are constantly flushed with nitrogen to keep them clear of debris, and argon is additionally used during the analysis of elements with very low wavelength emission spectra (e.g. arsenic and phosphorus).

Prior to analysis, three or four calibration standards spanning the likely range of analyte concentrations and a pure matrix blank were used to construct the calibration curve. The calibration standards were made up in a 1% v/v HNO_3 matrix; it is important that the matrix has a relatively low ionic strength to avoid deposition of excess dissolved solids as the sample passes through the torch. Samples were

analysed sequentially five times and the resulting values were automatically averaged to provide the reported elemental concentrations, associated standard deviations and relative standard deviations. Samples were re-analysed if the RSD value was greater than 1.5, and reported measurements are accurate to ± 5-10% (Goodman, Pers. Comm.). Ultrapure MilliQ water was passed through the instrument for approximately 30 seconds as a rinse between each sample. Calibration standards were regularly analysed as unknowns during the measurement of a suite of samples to identify unusual instrument behaviour or loss of calibration.

2.1.2 Inductively-Coupled Plasma Mass Spectrometry (ICP-MS)

A VG PlasmaQuad 2+ (VG Elemental, Minford, U.K.) ICP-MS was used to measure aqueous chromium concentrations at ppb levels in samples that could not be analysed by ICP-AES. A calibration curve was constructed during instrument preparation using a set of calibration standards which spanned the expected sample concentration range. In order to compensate for external influences which could artificially alter instrument performance (e.g. power surges or matrix effects), a 100 ppb indium 'internal standard' was added to every calibration standard and sample. Good internal standards are those that will *not* be present in samples, which are relatively unreactive, and which have a similar mass to the elements which are being analysed; indium and gallium are common choices. A pure solution of the 100 ppb indium was analysed during instrument preparation, and count data from all subsequent analyses were normalised against this. A 'blank' consisting of just the matrix (e.g. 1 % v/v HNO_3) was also analysed at this stage and subtracted from each subsequent sample and standard concentration.

During analysis, each sample goes through the following stages: After uptake and nebulisation into a fine aerosol, the aqueous sample is injected into a 6000-10000 K plasma in an argon-cooled glass 'torch' where it is dissociated, atomised and ionised. The sample is then accelerated under vacuum through a series of cones and into quadrupole mass analyser. This consists of four 15mm by 200mm circular rods which are fed with RF potentials, and it acts as a mass filter along the axis of which a stable path only exists for ions of one unique mass at any given time. The mass resolution is determined by the ionic mass / charge ratio, being best when the ratio is high. The raw count data from the mass spectrometer were converted to concentration data using the calibration curve.

During the fully quantitative analyses performed in this study, ^{115}In and ^{52}Cr (which constitutes 76 - 83% of all chromium isotopes) were analysed for. There are no known interferences at either of these masses. Each sample measurement was

sequentially repeated five times and then averaged automatically. The un-averaged raw data was always checked by eye to ensure that there were no irregularities amongst the five repeated measurements. Calibration standards of known concentration were included at regular intervals throughout a sequence of samples to identify any spurious instrument behaviour. Reported concentrations are accurate to the ± 5-10 % level (Kemp, Pers. Comm.).

2.1.3 Sulphide determination by UV-vis spectrophotometry

Total dissolved hydrogen sulphide (H_2S, HS^- and S^{2-}) was determined using a method modified from Cline (1969). The modified method includes a step which rapidly fixes dissolved sulphide in a stable solid form by complexing it with 10% zinc acetate solution. This allows samples to be stored for up to a month at 1-4 °C prior to analysis.

2.1.3.1 Preparation of sulphide standards and instrument calibration

The sulphide standards were prepared in the following manner:

a) A sulphide stock solution was made by dissolving 0.1875 g of $Na_2S \cdot 9H_2O$ in deoxygenated MilliQ water. Note that the sodium sulphide was washed and dried prior to dissolution to rinse off oxidation products.

b) Varying amounts of the sulphide standard (see Table 2.2) were added to seven eppendorfs (Fig. 2.1), and dissolved sulphide was fixed by the addition of 25 µl of 10% zinc acetate solution with thorough mixing.

c) 100 µl of a diamine sulphate/ferric chloride solution (mixed in equal volumes in a 50% v/v HCl matrix) was then added.

d) The total volume in each eppendorf was made to 1 ml with MilliQ water, and colour was allowed to develop for 50 mins. The final volume of reagents in each eppendorf was as shown in Table 2.2:

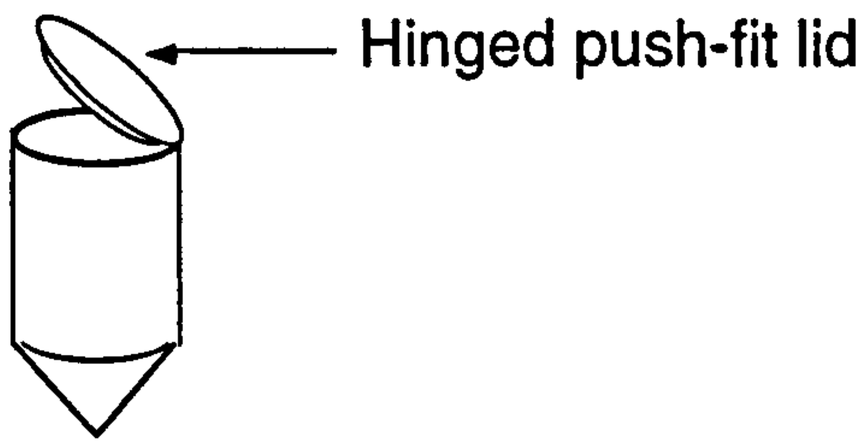

Fig. 2.1 A 2 ml capacity eppendorf. These were used to mix small volumes of sample and reactants.

Table 2.2. Volume of reagents (µl) in UV-vis sulphide standards.

Sulphide standard	10% Zn acetate	Diamine sulphate	MilliQ
0 (blank)	25	100	875
10	25	100	865
25	25	100	850
50	25	100	825
100	25	100	775
150	25	100	725
200	25	100	675

e) Following colour development, 0.208 ml of each solution was withdrawn and made to 5 ml with MilliQ water.

A UV-vis spectrophotometer (CECIL CE292, Cecil Instruments, Cambridge, U.K.) was used to measure colour intensity at 670 nm, after being allowed to warm up for an hour. The instrument was calibrated with the previously prepared sulphide standards, all of which gave absorbance values below 0.92. This is of importance because the colour intensity obeys Beer's Law in this region, ensuring a linear response from the instrument. The detection limit under these conditions is < 10 µM. The excellent agreement between sulphide standard concentrations measured before and after sample analysis indicates the high reproducibility of this method and the low level of instrument drift.

2.1.3.2 Sample preparation and analysis

Sulphide samples were prepared and analysed in the following manner:

a) Immediately after collection, the dissolved sulphide in 1 ml of each supernate was fixed by thorough mixing with 0.25 ml of a 10% zinc acetate solution in an eppendorf. These samples were stored at 1-4 °C and analysed within two weeks of collection.

b) Immediately prior to analysis, 100 µl of each fixed solution was added to 100 µl of freshly mixed diamine sulphate and ferric chloride in a 50% v/v HCl matrix. The total volume of each sample was made to 1 ml with MilliQ water, and the colour was allowed to develop for 50 min.

c) A 0.208 ml subsample of each developed solution was made to 5 ml with MilliQ water and then analysed on the calibrated spectrophotometer.

2.2 MINERALOGICAL CHARACTERISATION

2.2.1 X-ray diffraction

X-ray diffraction is a technique that is widely used to elucidate the composition and structure of different materials. A brief description of the theory behind the technique follows, based on information in Jeffery (1971) and course notes from the 1997 CLRC (Daresbury) 'Synchrotron Radiation School'.

In a diffraction experiment, X-ray photons of a given energy are generated by firing electrons at a metallic target and then using diffraction gratings to ensure that only photons of the desired wavelength are produced. When incident X-ray photons interact with a sample, a certain proportion of them will scatter from the electron density associated with each atom. Photons that interact with different atoms in the sample have to travel different distances before they reach the X-ray detector. The resulting path differences lead to phase changes in the scattered waves, which dependent on how far away from each other and in which direction the different atoms lie with respect to one another. For the most part, interference between the scattered waves is destructive. However, when the phase difference between the scattered waves is equal to an integer multiple of 2π (i.e. they are in phase), there is constructive interference. For a three dimensional crystal, diffraction only occurs when the Laue conditions are satisfied:

$$a^*S = h,\ b^*S = k,\ c^*S = l$$

where a, b and c are vectors describing the crystallographic unit cell; h, k and l are integers and $S = (s_0 - s)/\lambda$, where s_o is the incident beam direction, s is the scattered beam direction and λ is the X-ray wavelength.

It is important to realise that the Laue conditions for diffraction can only be met over a very small range of degrees 2θ (where θ is the angle of X-ray incidence on the sample). This is the reason that X-ray powder diffraction patterns consist of a number of narrow diffraction peaks rising sharply above what is otherwise a low 'background' level of diffraction. The peaks occur at specific values of degrees 2θ, from which the crystallographic d-spacing of minerals in the sample can be determined using the Bragg equation:

$$n\lambda = 2d\sin\theta$$

where λ is wavelength of incident light, d is the distance between atomic planes in the crystal structure, and θ is the angle of X-ray incidence on the sample

Because all minerals have distinct and unique crystallographic structures, knowledge of d-spacing allows determination of sample composition. Furthermore, the width of the peaks can provide some qualitative information about particle size in the sample. This is because the width of the diffraction maximum begins to get measurably larger as the number of unit cells per crystallite drops below 1000. This can be the case with poorly crystalline iron oxyhydroxides such as ferrihydrite. In addition to crystallite size, qualitative information regarding the morphology of crystallites in samples of simple composition can also be gleaned. This is because changes in relative peak intensity in a powder pattern (compared to literature values) can be indicative of inhibited or enhanced growth of certain crystal planes, and hence surface faces. Such changes in crystal morphology can result from the presence of contaminant ions during mineral synthesis or ageing.

Although it is possible to determine the identity of components constituting ≥ 5 per cent by volume in a sample of mixed mineralogy, this method does have limitations. For instance, the ability to differentiate between multiple components in a given sample is dependent on the respective diffraction peaks not overlapping. Indeed, the problem of peak overlap was encountered whilst analysing samples of aged ferrihydrite (see section 5.3.2.2). A potential solution to this problem would have been to use a radiation source with a different wavelength to Cu Kα (such as Co Kα). This would have caused the diffraction peaks to occur at different values of degrees 2θ, thereby reducing the overlap.

In this study, a Philips PW 1800 X-ray diffractometer was used to confirm the identity and purity of all minerals synthesised in the laboratory and to identify the product(s) of phase transformation experiments. This instrument uses a Cu Kα X-ray source which operated at 45 kV/40 mA, and remained at a fixed position whilst the sample was rotated through the required range of degrees 2θ (Fig. 2.2). All scans were from 2 to 70 degrees 2θ, and a step size of 0.02^{o} with a step time of 1 second was used throughout.

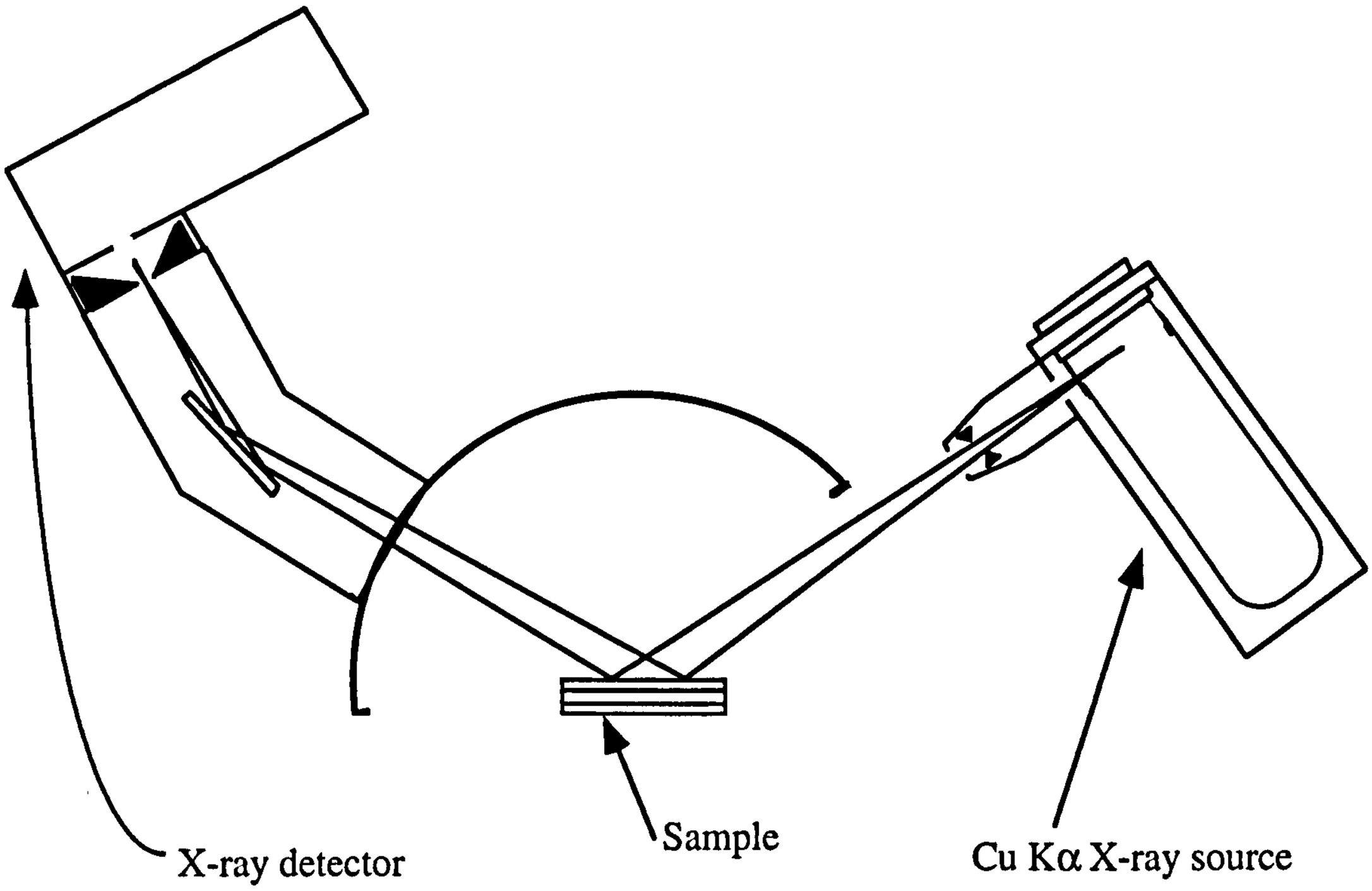

Fig. 2.2 Schematic diagram of Philips PW 1800 powder diffractometer. The sample is rotated during data collection whilst the source and detector remain at fixed positions.

2.2.2 Electron microscopy and electron diffraction

The general crystal morphology of each mineral was examined by transmission electron microscopy (TEM) on a JEOL 100CX TEMSCAN or a Philips EM 430. Samples were prepared by dispersing a fine powder of each mineral in acetone and drying a drop of the resulting suspension onto a slotted copper grid. Both instruments operated in bright-field mode at room temperature, and there was no evidence to suggest radiation damage of the samples under the electron beam. The morphology of goethite was further examined by electron diffraction (ED). See chapter 3 for the results of TEM/ED characterisation of goethite, lepidocrocite, akaganeite and schwertmannite, and chapter 4 for TEM characterisation of cryptomelane.

2.2.3 Surface area determination

The surface area of all minerals used in this study were determined by single point N_2-BET on a Ströhlein area meter in the Department of Chemistry, University of

Bristol. A few millilitres of each mineral stock suspension was air dried at ~40 °C and ground to a fine powder using an agate mortar and pestle. A small amount (0.2 - 0.5 g) of each powdered sample was then outgassed with $N_2(g)$ at room temperature overnight prior to analysis. A trial outgassing at 160 °C resulted in surface area measurements identical to those determined at room temperature, within the analytical of error of $\pm$ 3 $m^2 g^{-1}$. This uncertainty was derived from repeated measurements.

2.2.4 Determination of solid concentration in iron oxyhydroxide stock suspensions

All iron (oxyhydr)oxide stock suspensions were standardised in the following manner. Following homogenisation, 5 ml of each stock suspension was withdrawn and made to 20 ml with 6 M HCl which was then heated to 80 °C for 2 mins. 2 ml of this solution was made to 100 ml with MilliQ water, and ICP-AES was used to determine the concentration of dissolved iron.

2.3 EXTENDED X-RAY ABSORPTION FINE STRUCTURE (EXAFS) SPECTROSCOPY

2.3.1 EXAFS Theory

Much of the information outlined in the following sections on EXAFS spectroscopy was obtained from course notes for the 1997 CLRC (Daresbury) 'Synchrotron Radiation School' and the Daresbury Laboratory web site. Good reviews on the subject are to be found in: Brown et al. (1988), Charlet and Manceau (1993) and Brown et al. (1995).

X-ray absorption spectroscopy (XAS) is the general name for a suite of spectroscopic techniques which are used to derive physical and chemical information about samples by measuring X-ray absorption as a function of wavelength (energy). The basis of XAS is the ejection of electrons from core level bound states that have the following energy hierarchy: K > L > M. The threshold energy required for ejection of an electron from a given bound state (E_b) is specific to a given element, and the spectral features of different elements are significantly different. Because of this, and the fact that EXAFS spectra are weighted averages of all the local environments containing the chosen element (the 'element of interest'), XAFS techniques are as bulk (whole sample) and element-specific.

A typical XAS spectral scan is shown in Fig. 2.3, and it is clear that the spectrum can be divided into three distinct regions.

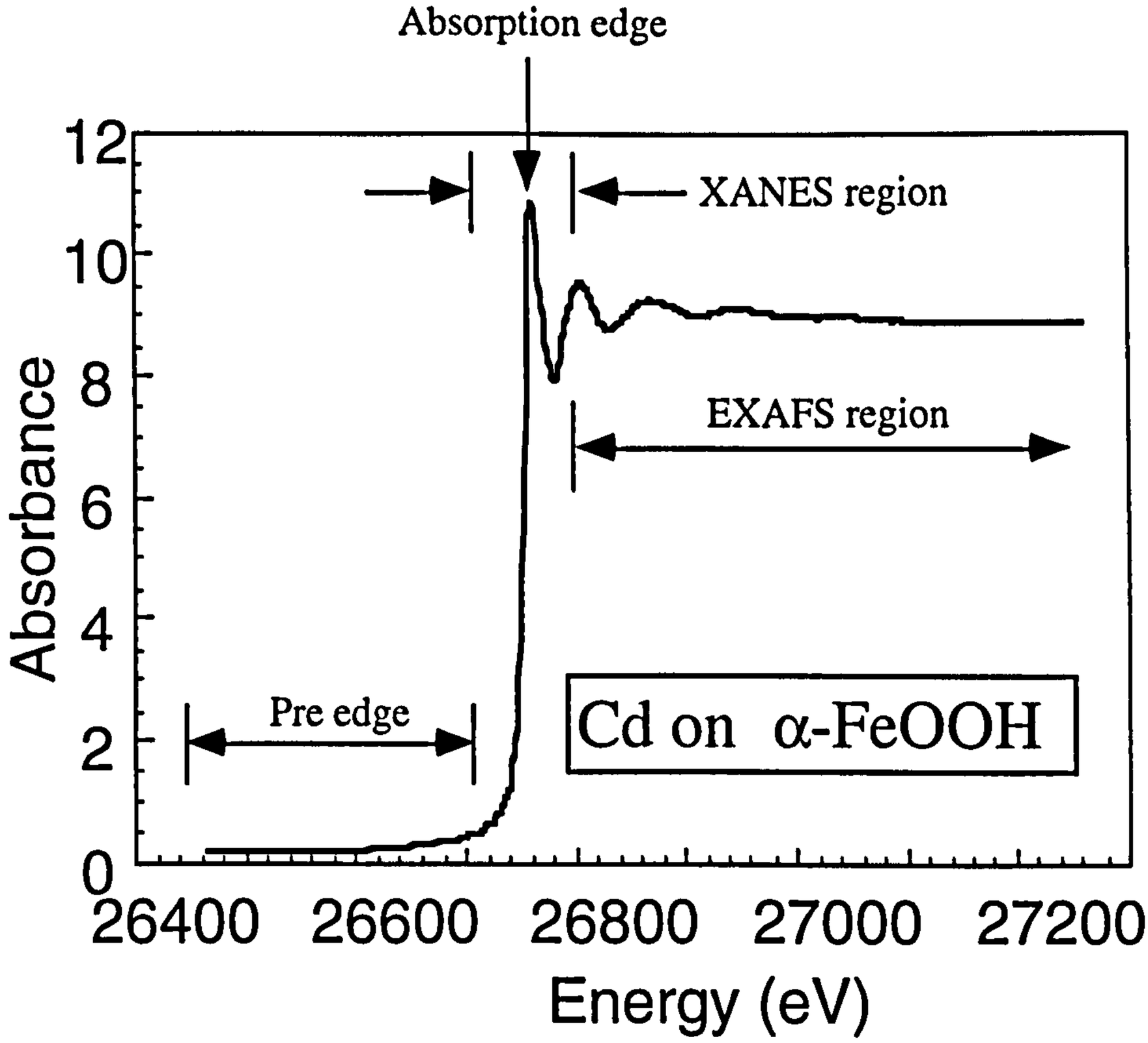

Fig. 2.3. XAFS spectrum of cadmium surface complexes adsorbed on goethite (α-FeOOH).

In the pre-edge region the incident photons have energies less than the binding energy of core level electrons in the element of interest (i.e. $E < E_b$). Electron transitions have low probabilities and no significant absorption occurs in this part of the spectrum (Brown et al., 1988). However, in the X-ray absorption near edge spectroscopy (XANES) region, which runs from just below the absorption edge to about 70 eV above it, absorption does take place because $E \approx E_b$. Thus, electrons can be ejected from a core level (e.g. 1s at the K edge) of the the element of interest into bond, or delocalised, empty states. These electron transitions obey dipole selection rules. For instance, at the K-edge, the final state wave function responsible for the absorption edge discontinuity must have p symmetry. For the first row transition elements, electronic transitions to the empty 3d bond states are possible if these have a certain p character through hybridisation. These 1s –> 3d transitions take place at the bottom of the steeply rising absorption edge, and can give rise to sharp 'pre-edge' features (none are visible in Fig. 2.3). The extent of hybridisation, and hence the strength of the pre-edge feature is at a minimum for centrosymmetric sites and a

maximum for noncentrosymmetric sites. Using this knowledge, the occupancy of a given type of site can be derived quite accurately from XANES data. This technqiue has been used very successfully to assess the composition of transition metal-containing material, such as chromium-contaminated soils (e.g. White and Peterson, 1996).

The XANES region can also provide information about the oxidation state of the element of interest since a positive energy shift of the main absorption edge and of any pre-edge is observed in going from Me^{n+} to $Me^{(n+1)+}$. This positive energy shift is understood conceptually to be due to an increase in the attractive potential of the nucleus on the core level as oxidation number increases. However, the spectral shift is actually due to final state wave functions as well as core level effects. It is because of this that oxidation state is more reliably determined from the energy position of the pre-edge peak than from that of the main absorption edge spectrum in samples of mixed oxidation state.

Note that in this study, preliminary analysis of the main absorption edge (EXAFS) data was performed during data collection from each sample. From this, it was clear that samples in which multiple oxidation states might be expected (e.g. Cr(VI) and As(V) on 'green rust', which is a mixed Fe(II)/Fe(III) oxyhydroxide that is a potent reductant) were in fact dominated by just one oxidation state. Consequently, analysis of the XANES data was deemed unncessary.

In contrast to the origin of XANES, data from the extended X-ray absorption fine structure (EXAFS) spectroscopy region of an XAS spectrum (Fig. 2.3) results from ejection of core level electrons to higher bound or continuum states. Hence, EXAFS can be conceptually viewed as a type of electron diffraction in which the source of electrons lies in the elemtent of interest which is participating in the X-ray absorption process. Ejected photoelectrons radiate away from the central atom in a spherically symmetrical shell which weakly backscatters from the atomic potentials of neighbouring atoms (Fig. 2.4).

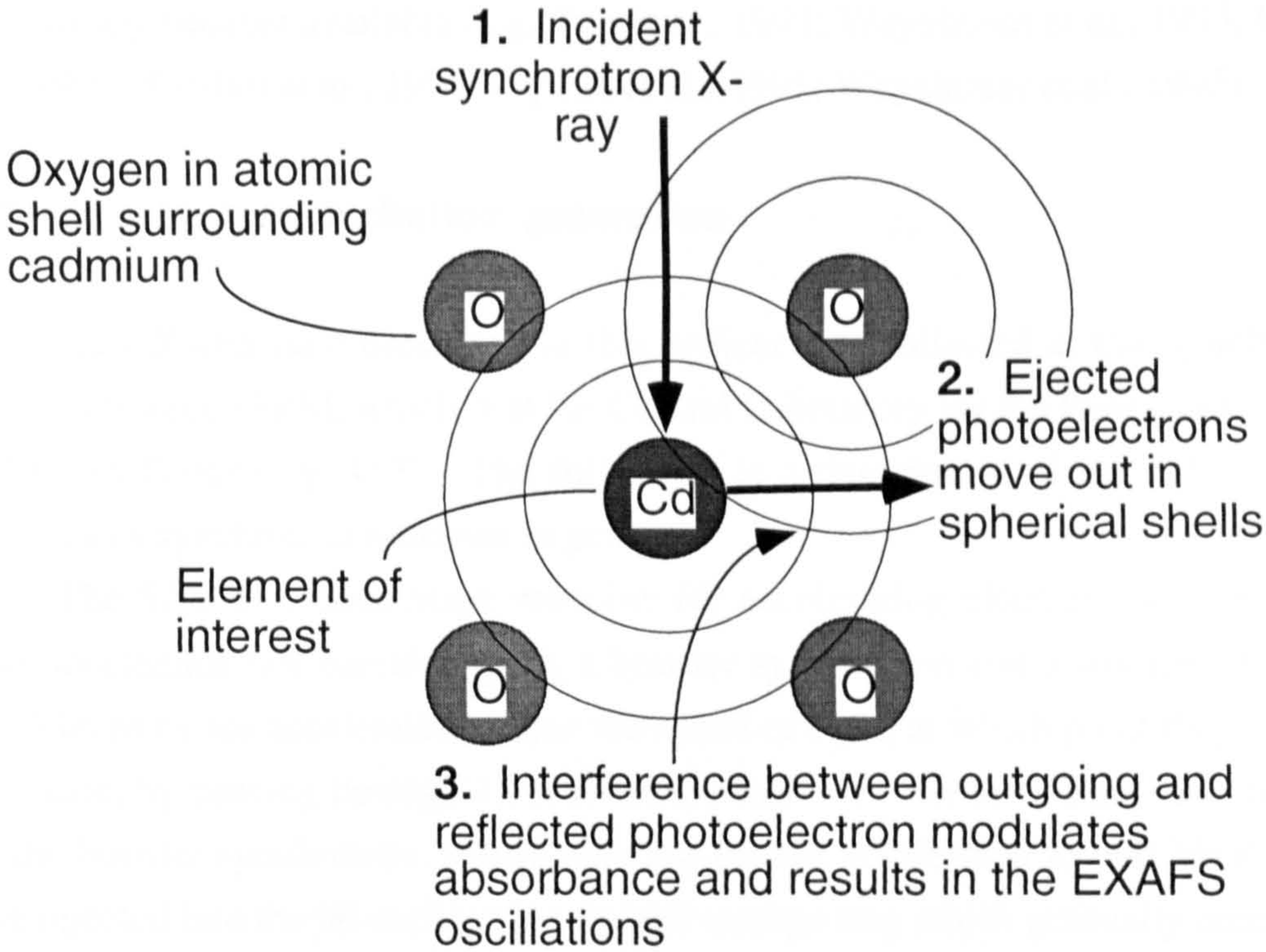

Fig. 2.4 Ejected photoelectrons radiate away from the element of interest (e.g. cadmium) in spherical shells which weakly backscatter from surrounding atomic potentials (e.g. oxygen).

There is interference between the wavefunction of the outgoing photoelectron and that small part of itself which has been scattered back from neighbouring atoms. This influences the probability of absorption of incident photoelectrons, and likewise, the probability of emission of decay fluorescence photons which are produced when the excited atom returns to its ground state. The oscillations resulting from variations in photon absorption above the absorption edge is the EXAFS. The oscillations amount to a only 3–4 % variation with respect to the background, and illustrate why a high resolution X-ray source is required to achieve the necessary signal to noise ratio ($> 10^5$).

EXAFS can be used to determine the localised ($\leq$ 5 Å) coordination environment of a specific element. Importantly, samples can approach conditions found in the environment: the element of interest can be present at concentrations as low as 0.05 wt% (depending on experimental conditions), and since no vacuum is required the samples can contain water (Charlet and Manceau, 1993; Brown et al., 1995). EXAFS can probe no more than a few angstroms from the absorber because of the short mean free path of the ejected photoelectron. However, this is an advantage in that it allows the investigation of systems that possess only short range structural order (Charlet and Manceau, 1993). Thus, EXAFS is particularly suited to the study of trace metals and ligands in solution and their interaction with hydrated mineral surfaces. This fact has been exploited by numerous workers since EXAFS

spectroscopy became available (e.g. Roe et al., 1991; Waychunas et al., 1993; O'Day et al., 1994; Spadini et al., 1994; Papelis et al., 1995; Waychunas et al., 1995).

2.3.2 Synchrotron radiation generation

All EXAFS data presented in this project was collected at the Synchrotron Radiation Source (SRS), which is at the Central Laboratory for the Research Councils (CLRC) in Daresbury, U.K. The following is a description of the SRS and the properties of synchrotron radiation in general.

The SRS is a three-stage machine for accelerating electrons, comprising a linear accelerator (an 'electron gun'), a booster synchrotron and a storage ring (Fig. 2.5). Electrons are accelerated to near the speed of light, at which point they become relativistic, by passing through 11 MeV in the linear accelerator. They then transfer into the booster synchrotron, where they are further accelerated to 600 MeV before being injected into the 96 m diameter circular storage ring which gradually accelerates them to 2 GeV. Here the electrons travel in bunches in a 10^{-7} torr vacuum and pass through sixteen dipole magnets which keep them on their circular path.

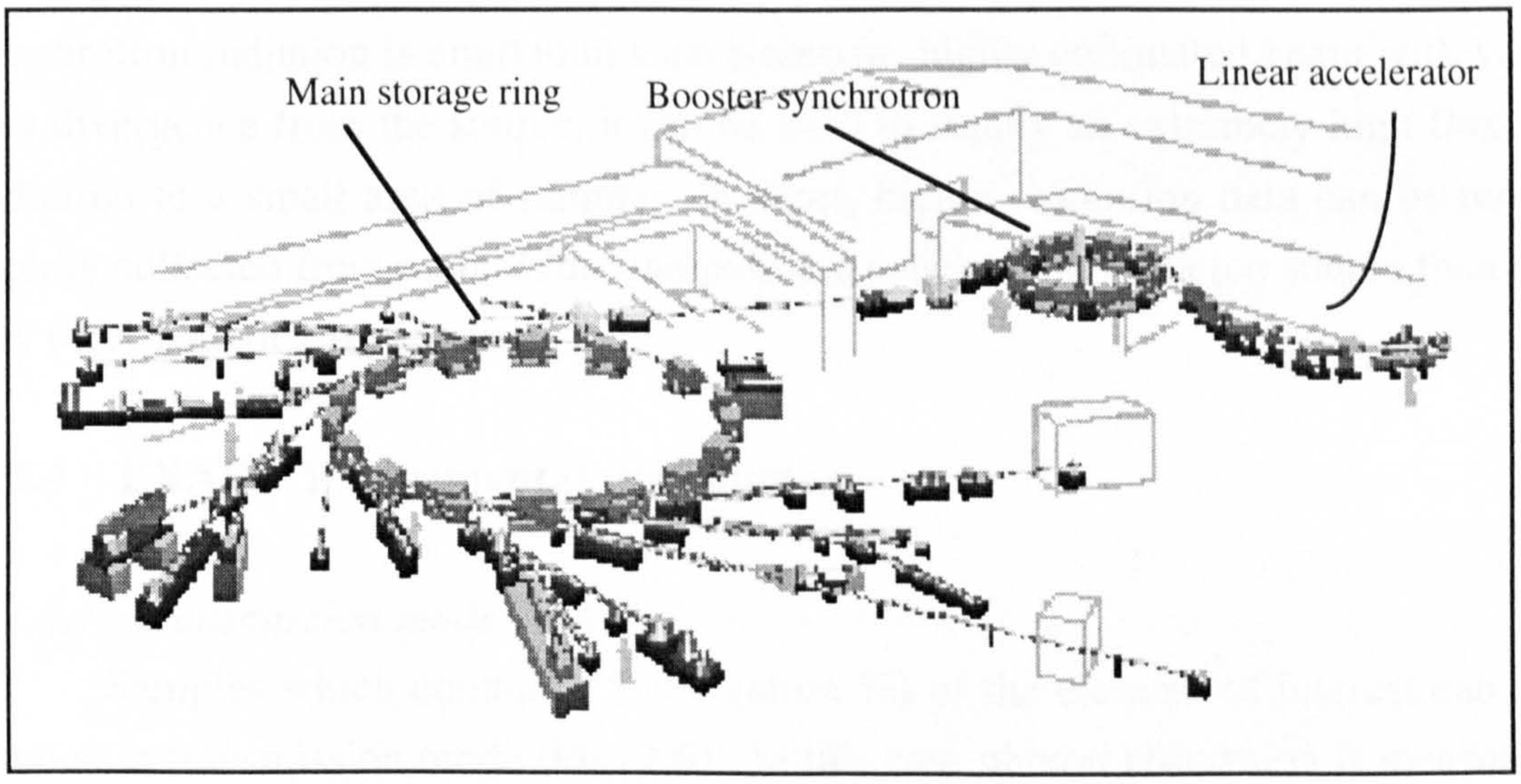

Fig. 2.5 Layout of the synchrotron radiation source at Daresbury. Beamlines leave the main storage ring at a tangent to the path of the electron beam (image from Daresbury Laboratory web page).

As the electrons pass the dipole magnets, their path is deflected and they emit intense beams of light as they are accelerated. This is synchrotron radiation. It emerges at a tangent to the curved storage ring in the form of a narrow (0.3 - 0.5 mm), highly collimated beam rather like a searchlight in front of the emitting particles. Synchrotron radiation with a broad range of energies is emitted from all sixteen dipole magnets in addition to three special magnets known as 'insertion devices', which are

specifically designed to emit high energy X-rays. The data presented in this project was collected from beamlines equipped with insertion devices known as 'wiggler magnets'. These are superconducting magnets which generate extremely high magnetic fields. When the electron beam in the storage ring passes through the wiggler, the high field causes it to effectively take a hairpin bend. The resulting huge acceleration results in the generation of very short wavelength (high energy) synchrotron radiation.

2.3.3 Advantages of synchrotron radiation over conventional lab-based X-ray sources

Synchrotron radiation is between 100 and 10,000 times as intense as conventional lab-based X-ray sources such as rotating anode or sealed tube sources, which are limited by the amount of heat that can be applied to them. Whereas conventional sources produce a monochromatic beam, synchrotron radiation 'white light' is polychromatic, and contains a large part of the electromagnetic spectrum. Monochromatic light of the desired wavelength can be extracted from this spectrum with appropriate beam optics such as monochromators and mirrors. Because synchrotron radiation is emitted in such a narrow, highly collimated beam with very low divergence from the source, it can be used to supply an extremely high flux of radiation to a small area of sample. In short, higher resolution data can be more rapidly collected from more dilute samples at a synchrotron radiation source than on any other type of X-ray source.

2.3.4 EXAFS Experimental techniques

2.3.4.1 Transmission mode EXAFS

Samples which contain ≥ 5 at% (atom %) of the element of interest can be studied in transmission mode (Fig. 2.6). In this case photon absorption is measured as the log of the ratio of the beam intensity before (I_0) and after (I_T) interaction with the sample. The beam intensity is measured in ion chambers that are filled with mixtures of inert gases such that the I_0 and I_T ion chambers absorb 20 % and 80 %, respectively, of the incoming beam intensity.

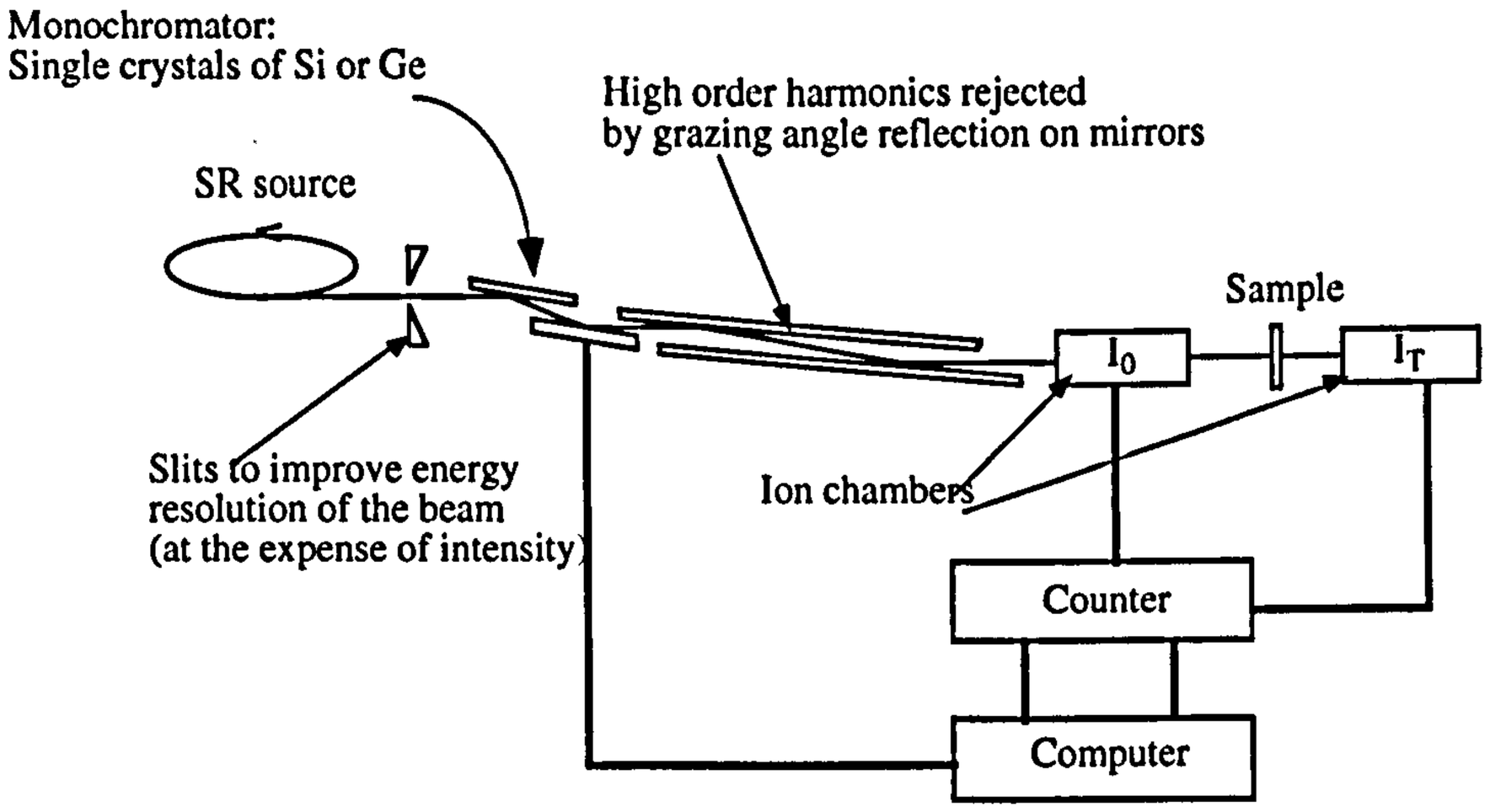

Fig. 2.6. Schematic diagram of experimental setup for transmission mode EXAFS. I_0 and I_T are collected during the spectral scan. The ratio of $\log(I_0:I_T)$ provides a measure of the absorbance, μ.

In this study, transmission mode EXAFS was only used to collect data from standards of known composition, which were used for reference during later curve fitting. These standards were presented to the X-ray beam as a finely ground powder that was evenly spread on layers of Sellotape. These were stacked in multiple layers to achieve a suitable EXAFS signal. Importantly, data were collected from standards under the same experimental conditions as the samples to which they relate. For instance, if sample data were collected in a liquid nitrogen cryostat, reference standard data were also collected at 77 K. This ensured that experimental values derived from standards could legitimately be applied to the 'unknown' samples during data analysis.

2.3.4.2 Fluorescence mode EXAFS

The difference between I_0 and I_T generally becomes too small for useful data analysis when samples contain ≤ 5 at% of the element of interest because there is very little photon absorption. In such a case, data is collected in fluorescence mode, where absorbance is measured as the ratio of $I_F:I_0$ (Fig. 2.7). I_F is the fluorescence signal, due to emission of decay fluorescence photons which are produced when the excited atom returns to its ground state.

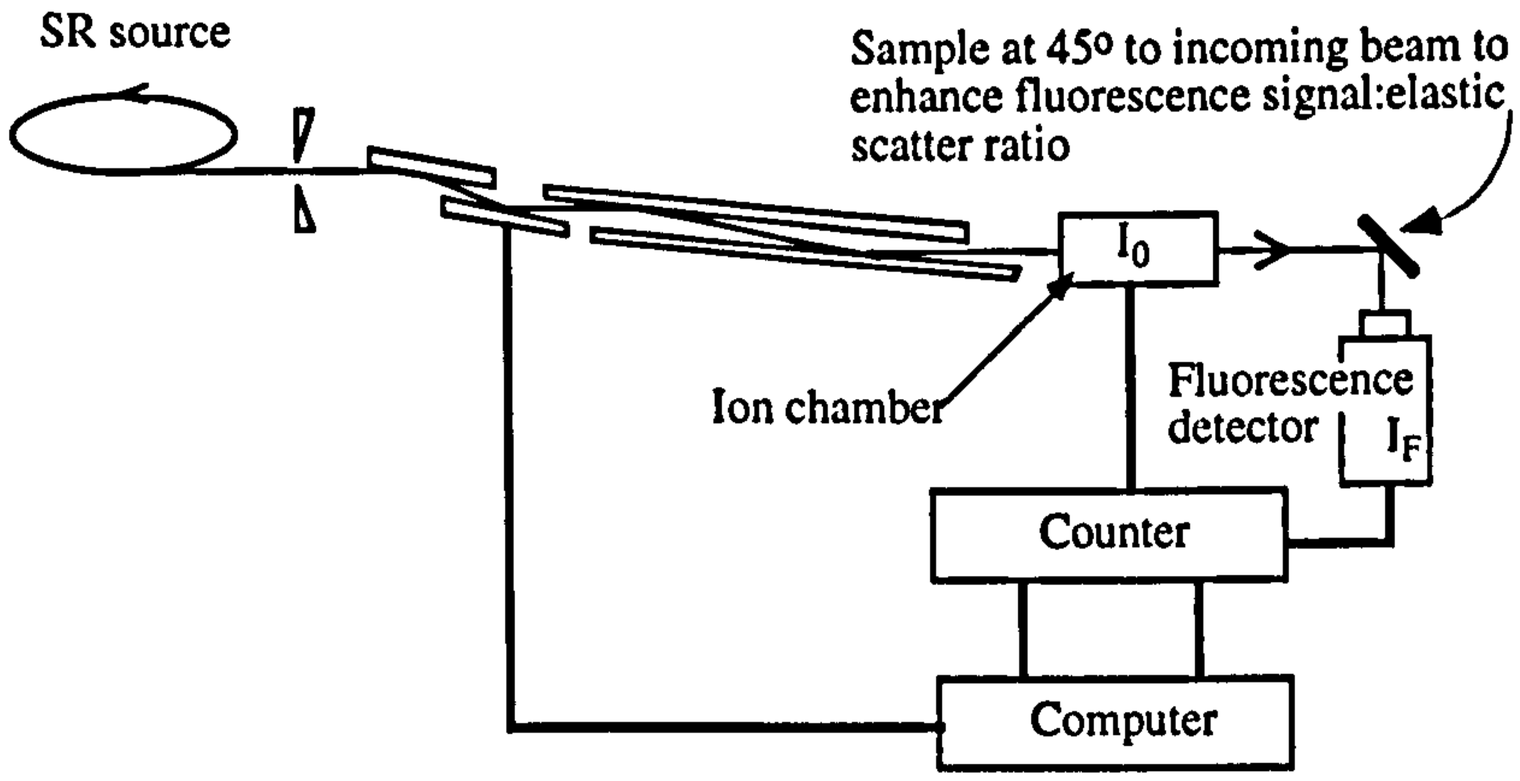

Fig. 2.7. Schematic diagram of experimental setup for fluorescence mode EXAFS. Absorbance is measured as the ratio of I_F to I_0. Note that the sample should be held at 45° to the incoming beam in order to maximise the fluorescence signal : elastic scatter ratio. Elastic scatter can otherwise drown out the fluorescence signal.

The 'adsorption samples' generated in each experiment were presented to the X-ray beam as thick pastes held by Sellotape in 2 mm thick Teflon slides with 4 mm by 15 mm sample slots. In general, air-sensitive samples were stored as pastes frozen in their sample holders and subsequently analysed at 77 K in a cryostat. This proved to be an effective way of avoiding unwanted oxidation. Less delicate samples were stored as either refrigerated or frozen pastes but subsequently analysed at room temperature.

2.3.5 EXAFS formulation, data reduction and analysis

2.3.5.1 EXAFS formulation

The EXAFS equation is used to derive theoretical EXAFS curves from molecular clusters which are representative of those suggested by initial inspection of the EXAFS results. The agreement between experimental and theoretical EXAFS curves, and hence the agreement between real and theoretical clusters, is iteratively refined by specialist software during data analysis. Such modelling allows the determination of the *average* number of atoms surrounding the element of interest, their identity and distance from the central atom, and the associated Debye-Waller factor. Using the plane wave approximation and considering only single scattering of ejected photoelectrons, the contribution to the EXAFS spectrum of the jth atomic shell is formulated as:

$$\chi_j(k) = A_j(k) \sin (2kR_j + \emptyset_{ij}(k))$$

and the whole EXAFS spectrum is obtained by adding each individual contribution:

$$\chi(k) = \Sigma_j \chi_j(k)$$

where $\chi_j(k)$ is the individual atomic pair contribution of the atomic shell j, and k is the modulus of the wavevector of the photoelectron. The phase of $\chi_j(k)$ depends on:

R_j The central atom (i) to backscatterer (j) distance

$\emptyset_{ij}$ (k) The phase shift function, which is characteristic of a given absorber-backscatterer pair. These functions vary monotonically with atomic number. Thus Fe-Fe and Fe-Cr have very similar values of $\emptyset_{ij}$ (k), whilst the phase contrast reaches its maximum between Fe-Fe and Fe-Al since $\emptyset_{Fe\text{-}Fe}$ - $\emptyset_{Fe\text{-}Al}$ is $\approx \pi$.

The amplitude of $\chi_j(k)$ includes the following terms:

$$A(k) = F_j(k) [N_j/kR_j^2] \exp[-2\sigma_j^2k^2 - 2R_j/l(k)]$$

F_j (k) is the backscattering wave amplitude, and is characteristic of the atom present in the jth shell.

N_j is the number of atoms in the jth shell

σ_j is the Debye-Waller factor (mean square of variation in distances from the central atom to the shell under consideration) accounting for the wave damping due to the thermal vibration (σ_T) and the static disorder (σ_S) of atoms. σ_T increases with temperature, and σ_S rises with increasing incoherency of the i-j separation.

l is the electron mean free path (on the order of 5 - 10 Å).

2.3.5.2 Data reduction and analysis

EXAFS data reduction was performed using Daresbury Laboratory software (EXCALIB and EXBACK) (Binsted et al., 1991). EXCALIB was used to calibrate from monochromator position (millidegrees) to eV and sum multiple spectra from individual samples. The start of the EXAFS oscillations was defined and the background absorption was removed using EXBACK. The exact curved wave theory EXAFS analysis programs EXCURV92 or EXCURV98 (Gurman et al., 1984, 1986; Joyner et al., 1987; Gurman, 1988; Binsted et al., 1991, 1992) were then used to generate EXAFS oscillations from a model adsorption cluster which initially consisted of the element of interest surrounded by a suitable number of likely ligands. Least squares refinement was used to fit the theoretical oscillations to experimental data,

causing the cluster to approach the true structure of the adsorption complex. Successive atomic shells were added to the theoretical model until a shell had been assigned to each significant peak in the Fourier Transform (FT) of the EXAFS data. Modelling in this way provided the shell parameters describing the average local structure around the element of interest in each sample.

Joyner tests (Joyner et al., 1987) were performed to ascertain the statistical significance of all new atomic shells during modelling of the EXAFS oscillations. In general only shells which improved the fit between theory and experiment at the 99 % probability level are included in this work. Shells which are significant at the 95 % level of probability are included only under exceptional circumstances. In addition to the Joyner tests, the *R* factor was also used as a guide in data analysis:

$$R_{EXAFS} = \sum_{i} \frac{1}{\sigma}(|\chi_i(k)^{exp} - \chi_i(k)^{theory}|) \times 100\%$$

where σ is the standard deviation of the difference between experimental ($\chi^{experiment}$) and theoretical (χ^{theory}) EXAFS functions over a specified k range. The *R* factor gives a measure of agreement between the experimental and simulated EXAFS functions. For poorly ordered mineral-aqueous systems such as those described here, an *R* value between 20% and 40% indicates an acceptable match between theory and experiment (Dent and Mosselmans, 1992).

EXAFS theory in its simplest form assumes that a single incident photon will interact only with one electron in the element of interest. In practice, interaction with more than one electron can occur, and this results in multiple electron excitations which do not lead to EXAFS oscillations. Photons lost in this way have been accounted for in this study by using a factor known as AFAC in the EXCURV programs. AFAC represents the probability that a photon will excite more than one electron, and thus not result in a contribution to the XAFS oscillations. It was set to range between 0.7 and 0.98 (i.e., 70 - 98% of photons resulting in EXAFS) during all data analysis.

The phase shift functions used in the curve fitting were derived by *ab initio* methods in EXCURV92 and EXCURV98 using Hedin-Lundqvist potentials (Hedin and Lundqvist, 1969) and von Bart ground states. It has been suggested that phase shift functions generated in this way are less accurate than those determined experimentally (Spadini et al., 1994). However, the use of theoretical values is justified by the good agreement between the structure of known standards such as β-$Cd(OH)_2$(s) and scorodite ($FeAsO_4 \cdot 4H_2O$) derived from the EXAFS data using theoretical phase shift functions and published structural data.

2.3.6 EXAFS data display format

EXAFS results are displayed in two formats in this study. The Fourier Transform (FT) plots show the Fourier transform of the EXAFS data (FT of $\chi(k)$) plotted against distance from the element of interest (Å) (Fig. 2.8 a). This type of plot provides the best visual representation of local coordination since each significant peak within 4 Å of the element of interest corresponds to an atomic shell. The EXAFS plots consist of wavenumber (k) ($Å^{-1}$) plotted against the EXAFS function χ, which is weighted by a factor of k^3 ($\chi(k)\cdot k^3$) to enhance oscillations at high k values (Fig. 2.8 b). They are shown since they provide a better representation of the data quality than the FT plots, and because the curve fitting process uses the raw EXAFS data rather than the Fourier transform data. This means that the relative success of curve fitting is best visually assessed by inspecting the EXAFS plots. In both types of plot, the theoretical fit to the data is shown as a bold line whilst the experimental data is shown as a fine line.

It should be noted that only the first peak in each FT plot is corrected for phase-shift effects. Consequently, whilst the experiment and theory curves for the first FT peaks coincide at the true Metal-X distance, the experiment curves for the second, third etc. FT peaks are sometimes displaced from their true Metal-X locations. Any apparent mismatch between experiment and theory in the FT plots is merely an artefact of this, and does not imply a poor fit.

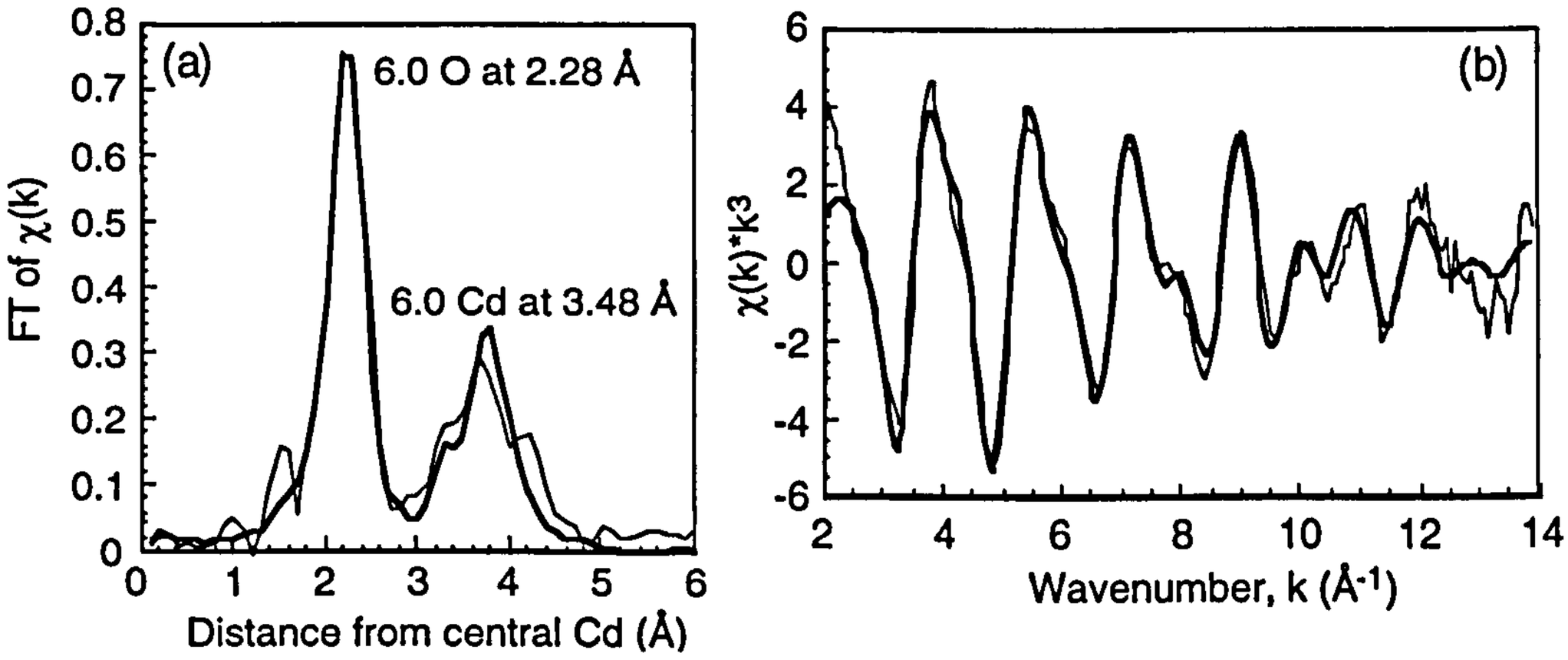

Fig. 2.8. Fourier transform (a) and EXAFS plots (b) from β-$Cd(OH)_2$(s) EXAFS standard.

2.4 *AB INITIO* QUANTUM MECHANICAL PREDICTION OF THE GEOMETRY AND ENERGETICS OF SURFACE COMPLEXES

Density functional theory (DFT) is a quantum mechanical approach that can be used to predict the optimised geometry and total energy of formation of small molecular clusters; surface complexes formed during adsorption are ideal candidates for such treatment. In this context, DFT has proven to be a powerful independent source of information that has assisted evaluation of the EXAFS data. It has previously been used for this purpose by Collins (1997). A cautionary note is that the calculations are performed in the gas phase, with no account taken of solvation effects. Nonetheless, good agreement is found between experimental EXAFS results and certain predicted geometries. This indicates that information derived from *ab initio* quantum mechanical modelling is applicable to the cadmium surface complexes discussed in chapter 3 (Randall et al., 1999).

In this study, the Amsterdam Density Functional Program (ADF 2.0.1; te Velde 1995) was used. Initially, an approximate geometry for each likely adsorption complex was generated based on a consideration of aqueous cadmium speciation and the structure of the iron (oxyhydr)oxide surface. Suitable molecular clusters were developed with the fully hydrated adsorbing ion attached to one or two $Fe(O,OH)_6$ octahedra. These acted as the iron (oxyhydr)oxide substrate. Because the mechanisms of adsorbate attachment were identical to certain types of octahedral linkage in the iron (oxyhydr)oxide bulk structure, it was often possible to generate entire clusters by isolating small parts of an iron (oxyhydr)oxide crystallographic model. This was achieved using the CrystalMaker 2.1.0 computer program (Palmer, 1996). The crystallographic coordinates of each selected cluster were transferred from CrystalMaker into the molecular visualisation package RasMac 2.6 (Sayle, 1996). Using vector addition, the molecular clusters were then supplemented with extra hydrogen atoms so that they approached the expected composition of hydrated surface complexes (Fig. 2.9).

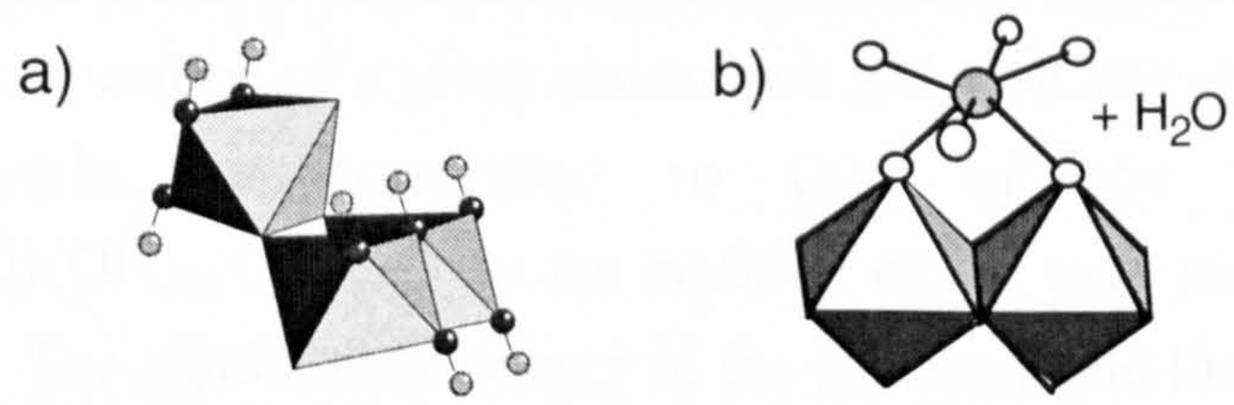

Fig. 2.9. Molecular cluster of three $Fe(O,OH)_6$ octahedra from the goethite bulk structure (a). The same cluster is shown in (b) following adaptation to a hypothetical adsorption complex consisting of a hydrated cadmium ion adsorbed onto two adjacent $Fe(O,OH)_6$ octahedra *via* a double corner sharing mechanism. Ball and stick components of (a) represent hydroxyl groups; oxide groups are not shown.

For each atom, a set of mathematical functions referred to as a basis set was used to define the forms and energies of its associated atomic orbitals. The ADF program uses Slater-type orbitals and the basis sets employed use triple-zeta valence shells with a polarisation function. The first stage of the calculation involved determination of the self-consistent charge density by following the steps outlined below:

1. Solve the Kohn-Sham equations for each atom to get the electron density for each atom (ρ_{atom})
2. Superimpose the ρ_{atom} values to get a first approximation of the charge density of the molecule ($\rho^0_{molecule}$)
3. Given $\rho^0_{molecule}$, solve the Kohn-Sham equation for the molecule to get the molecular orbitals, $\emptyset_i$
4. Given the molecular orbitals, populate them with electrons to get the next approximation of $\rho_{molecule} = \sum n_i \emptyset_i^2$

Steps 3. and 4. were repeated until there was no further change in $\rho_{molecule}$. From the self-consistent charge density, the total energy of the cluster was found, along with the interatomic forces. The next step in the calculation involved moving the atoms by a small increment in order to minimise the interatomic forces, thereby generating a new geometry. Steps 1. to 4. were then repeated with the atoms in their new positions to determine a revised value for the self-consistent charge density.

This whole process was repeated until an optimised geometry had been arrived at and the interatomic forces approached zero. RasMac 2.6 (Sayle, 1996) was then used to visualise the geometry of the optimised cluster and to determine bond angles and interatomic distances.

In addition to predicting optimised geometry, the DFT calculations also determined the total static energy of formation of each cluster from its components in the gas phase. In order to establish an order of relative cluster stability, the composition of the smaller clusters was normalised to that of the largest cluster. For instance, if the composition of a given cluster was $[(H_2O)_3CdFe_2(O)(OH)_6(OH_2)_3]^0$, its energy could be compared to that of the largest cluster $[(H_2O)_5CdFe_2(O)(OH)_6(OH_2)_3]^0$ by the addition of the total static energy of two water molecules. The relative total energy of the clusters could then be calculated by arbitrarily setting the total energy of one cluster to zero, and recalculating values for the other clusters accordingly. This process is detailed further in section 3.2.5.

2.5 REFERENCES

Binsted N., Campbell J. W., Gurman S. J., and Stephenson P. C. (1991) SERC Daresbury Laboratory EXCURV92 program. Daresbury Laboratory, Warrington, U.K.

Binsted N., Strange R. W., and Hasnain S. S. (1992) Restrained refinement. Biochemistry 31, 12117-12125.

Brown G. E. Jr., Calas G., Waychunas G. A., and Petiau J. (1988) X-ray absorption spectroscopy and its applications in mineralogy and geochemistry. In *Spectroscopic Methods in Mineralogy and Geology* (ed. F. Hawthorne). Reviews in Mineralogy Vol. 18, pp. 431-512. Min. Soc. Am.

Brown G. E. Jr., Parks G. A., and O'Day P. A. (1995) Sorption at the mineral-water interface: macroscopic and microscopic perspectives. In *Mineral Surfaces* (eds. D. J. Vaughan and R. A. D Pattrick). pp. 129-183. Chapman and Hall.

Charlet L and Manceau A. (1993) Structure, Formation, and Reactivity of Hydrous Oxide Particles: Insights from X-ray Absorption Spectroscopy. In *Environmental Particles*, Vol. 2 (eds. J. Buffle and H. P. van Leeuwen). IUPAC Environmental Analytical and Physical Chemistry Series. pp. 118-164.

Cline J. D. (1969) Spectrophotometric determination of hydrogen sulphide in natural waters. Limnology and Oceanography 14, 454-458.

Collins C. R. (1997) The geochemistry and structure of surface complexes of Cd^{2+} Hg^{2+}, Sr^{2+}, and Zn^{2+} on goethite: Insights from density functional theory and EXAFS spectroscopy. Ph.D. thesis, University of Bristol.

Dent A. J. and Mosselmans J. F. W. (1992) *A guide to EXBACK, EXCALIB, and EXCURV92.* Daresbury Laboratory, Warrington, U.K.

Gurman S. J. (1988) The small atom approximation theory. J. Phys. C: Solid State Phys. 21, 3699-3717.

Gurman S. J., Binsted N., and Ross I. (1984) Single scattering rapid curved wave theory. J. Phys. C: Solid State Phys. 17, 143-151.

Gurman S. J., Binsted N., and Ross I. (1986) Multiple scattering rapid curved wave theory. J. Phys. C: Solid State Phys. 19, 1845-1861.

Hedin L. and Lundqvist S. (1969) Effects of electron-electron and electron-phonon interactions on the one-electron states of solids. Solid State Phys. 23, 1-181.

Jeffery J. W. (1971) *Methods in X-ray crystallography.* Academic Press.

Joyner R. W., Martin K. J., and Meehan. P. (1987) Some applications of statistical tests in analysis of EXAFS and SEXAFS data. J. Phys. C: Solid State Phys. 20, 4005-4012.

O'Day P. A., Brown G. E. Jr., and Parks G. A. (1994) X-ray absorption spectroscopy of Co(II) multinuclear surface complexes and surface precipitates on kaolinite. J. Colloid Interface Sci. 165, 269-289.

Palmer D. C. (1996) CrystalMaker 2.1.0: Interactive crystallography for MacOS.

Papelis C., Brown G. E. Jr., Parks G. A., and Leckie J. O. (1995) X-ray absorption spectroscopic studies of cadmium and selenite adsorption on aluminium oxides. Langmuir 11, 2041-2048.

Randall S. R., Sherman D. M., Ragnarsdottir K. V. and Collins C. R. (1999) The mechanism of cadmium surface complexation on iron oxyhydroxide minerals. Geochim. Cosmochim. Acta, *in press*.

Roe A. L., Hayes K. F., Chisholm-Brause C. J., Brown G. E. Jr., Parks G. A., Hodgson K. O., and Leckie J. O. (1991) In situ X-ray absorption study of lead ion surface complexes at the goethite-water interface. Langmuir 7, 367-373.

Sayle R. (1996) RasMac Molecular Graphics 2.6.

Spadini L., Manceau A., Schindler P. W., and Charlet L. (1994) Structure and stability of Cd^{2+} surface complexes on ferric oxides. 1. Results from EXAFS spectroscopy. J. Colloid Interface Sci. 168, 73-86.

te Velde G. (1995) Amsterdam Density Functional 2.0.1, Users Guide, Vrije Universiteit, Amsterdam.

Tossell J. A. and Vaughan D. J. (1992) *Theoretical geochemistry - application of quantum mechanics in the earth and mineral sciences.* Oxford Univ. Press.

Waychunas G. A., Rea B. A., Fuller C. C., and Davis J. A. (1993) Surface chemistry of ferrihydrite. 1. EXAFS studies of the geometry of coprecipitated and adsorbed arsenate. Geochim. Cosmochim. Acta 57, 2251-2269.

Waychunas G. A., Davis J. A., and Fuller C. C. (1995) Geometry of sorbed arsenate on ferrihydrite and crystalline FeOOH: Re-evaluation of EXAFS results and topological factors in predicting sorbate geometry, and evidence for monodentate complexes. Geochim. Cosmochim. Acta 59, 3655-3661.

White A. F. and Peterson M. L. (1996) Reduction of aqueous transition metal species on the surfaces of Fe(II)-containing oxides. Geochim. Cosmochim. Acta 60, 3799-3814.

Chapter 3

The Mechanism of Cadmium Surface Complexation on Iron Oxyhydroxide Minerals

3.1 INTRODUCTION

Cadmium is a toxic heavy metal which has become a significant contaminant in many soil and groundwater systems (e.g. Hutchinson and Meema, 1987; Tiller, 1989). The annual flux of cadmium from anthropogenic sources such as mining and smelting operations, waste disposal, and contaminated fertilisers (Hem, 1972; Krishna et al., 1987) is nearly ten times that of all natural sources (Nriagu, 1980). Cadmium is known to bioaccumulate, and the native metal and solutions of its compounds are highly toxic to humans (Jin et al., 1998; Lehoczky et al. 1998). Adsorption from solution onto exposed mineral surfaces has been shown to exert a strong control on the mobility and bioavailability of trace metals such as cadmium in the environment (Krauskopf, 1956; Singh and Subramanian, 1984; Shiller and Boyle, 1987). The iron oxyhydroxides that are used in this study commonly form in the environment as reactive, high surface area secondary minerals resulting from weathering processes. They are often found as crack deposits, as coatings on other less reactive mineral grains (Russell et al., 1975; Coston et al., 1995), or as alteration products on weathering minerals (Walder and Chavez, 1995).

The capacity of iron (oxyhydr)oxides to accumulate contaminants is clearly demonstrated by the fact that trace metal concentrations in soil oxide fractions are often orders of magnitude higher than in bulk soils (Le Riche and Weir, 1963; Taylor and McKenzie, 1966; Hiller and Brummer, 1995). Iron (oxyhydr)oxides are known to accumulate heavy metals by adsorption and/or coprecipitation in rivers and estuaries (Gibbs, 1977; Lion et al., 1982; Johnson, 1986; Zhuang et al. 1994). Studies of metal mobility in lake sediments strongly suggest that cadmium binds directly to the hydroxyl surface groups of iron- and manganese oxyhydroxides such as ferrihydrite and lepidocrocite under near neutral pH conditions (Tessier et al., 1985; 1996). This is the case even in the presence of organic material (Tessier et al., 1985; 1996). Goethite and lepidocrocite have been identified as important mediators of the mobility of a variety of heavy metals including cadmium in acid mine drainage environments (Herbert, 1994; Lin and Herbert, 1997).

Because of the obvious importance of iron (oxyhydr)oxides in attenuating heavy metal transport, many laboratory-based adsorption studies have been performed to investigate this phenomenon (e.g. Davis and Leckie, 1978; Dzombak

and Morel, 1990; Fokkink et al., 1990; Johnson, 1990; Gunneriusson, 1994; Venema et al., 1996b).

Thermodynamic data describing the sorption process are commonly derived using surface complexation models (e.g. Davis and Leckie, 1978; Davis and Kent, 1990; Hayes et al., 1991; Hiemstra and Van Riemsdijk, 1996; Venema et al., 1996a, b). The modelling results are heavily dependent on the accurate chemical and physical representation of surface complexes and the oxide surface (Hayes and Leckie, 1987; Cowan et al., 1991). However, in many cases it seems that the physical representation of a given complex is chosen somewhat arbitrarily, and often without any direct supporting evidence from the samples.

The aim of this study was to clarify the role that inner- or outer sphere adsorption, surface precipitation and/or coprecipitation played in the sorption of aqueous cadmium by a variety of iron oxyhydroxides over a range of pH and cadmium concentrations. The short range structure around sorbed cadmium was probed *in situ* with EXAFS spectroscopy. *Ab initio* quantum mechanical modelling was used to complement and assist EXAFS data interpretation for samples of cadmium adsorbed on goethite. The results provide an enhanced molecular scale description of the fundamental processes leading to adsorption. This new information should lead to an improved understanding of cadmium mobility and attenuation in the environment, and allow quantitative modelling of these processes.

Extended X-ray Absorption Fine Structure (EXAFS) spectroscopy is uniquely suited to determining the *average* coordination environment up to ~4 Å around a given element of interest in poorly ordered materials. Importantly, samples can approach conditions found in the environment: the element of interest can be present at concentrations as low as 0.05 wt% (depending on experimental conditions), and since no vacuum is required the samples can contain water and be at room temperature (Charlet and Manceau, 1993; Brown et al., 1995). These factors have been exploited by numerous workers since EXAFS spectroscopy became available (e.g. Roe et al., 1991; Waychunas et al., 1993; O'Day et al., 1994; Spadini et al., 1994; Papelis et al., 1995; Waychunas et al., 1995).

I chose to study goethite (α-FeOOH), lepidocrocite (γ-FeOOH), akaganeite (β-FeOOH) and schwertmannite ($Fe_{16}O_{16}(OH)_{10}(SO_4)_3 \cdot 10H_2O$) for several reasons. Firstly, all the studied minerals are known to occur to varying degrees in a range of weathering environments (Schwertmann and Cornell, 1991), and the results of this study should therefore have broad applicability. Secondly, each mineral possesses a different proportion of distinct types of surface sites. Studying cadmium adsorption on a number of minerals has thus provided a much better understanding of the relative importance of the different types of surface site than would have been possible by simply varying surface loading on a single mineral. Finally, all four

minerals are relatively stable phases (Schwertmann and Cornell, 1991), and their surface properties do not change over the timescales of EXAFS experiments (hours to days).

3.1.1 Occurrence of goethite, lepidocrocite, akaganeite and schwertmannite in the environment

Goethite is the most common iron oxyhydroxide mineral in nature, and it is known to occur in almost all weathering environments (Schwertmann and Cornell, 1991).

Lepidocrocite has been observed to form in the field *via* oxidation of Fe^{2+} during early diagenesis of lake sediments (Fortin et al., 1993; Tessier et al., 1996). It is known to be the major product resulting from oxidation of Fe^{2+} compounds such as 'green rust' (a mixed Fe^{2+}/Fe^{3+} oxyhydroxide; Schwertmann and Fechter, 1994) and amorphous FeS(s) (Fendorf et al., 1997). Although lepidocrocite is commonly observed in excessively moist soil gleys and pseudogleys (e.g. Schwertmann and Taylor, 1972), it also occurs in better drained calcareous and vertic soils (e.g. Ross and Wang, 1982; Wang et al., 1993). Lepidocrocite can also occur as a major iron (oxyhydr)oxide under acid mine drainage conditions (Herbert, 1995; Karathanasis and Thompson, 1995).

Akaganeite is less common in sediments and soils than either goethite or lepidocrocite. However, it has been recognised as a major iron oxyhydroxide component in some soils and hydrothermal systems (Holm et al., 1983; Chen and Yao, 1995). It has also been identified in marine concretions (Pye, 1988; Alagha et al., 1995) and acid mine drainage environments (Karathanasis and Thompson, 1995).

Schwertmannite is an iron oxyhydroxysulphate mineral which forms through the bacterially mediated oxidation of Fe^{2+} by *Thiobacillus feroxidans* in waters that are rich in sulphate (up to several thousand ppm) (Bigham et al., 1994). It commonly occurs as an ochreous precipitate in environments where acidic waters drain pyritic mines or mine tailings (Karathanasis and Thompson, 1995). However, it has also been recently identified in a stream draining pyritic schists (Schwertmann et al., 1995).

3.1.2 CO_2(g) exclusion during sample preparation

Although the majority of environments outlined above where iron (oxyhydr)oxides can attenuate cadmium transport are open to the atmosphere, all of the adsorption samples were prepared under CO_2(g)-free conditions. The main reason for doing this is that sorption rather than precipitation exerts the major control on trace metal concentrations over a wide range of fresh- and seawater conditions (e.g. Krauskopf, 1956; Singh and Subramanian, 1984; Johnson, 1986; Shiller and Boyle, 1987). Consequently, CO_2(g) was excluded from these experiments to avoid the precipitation of $CdCO_3$(s) (otavite), mindful that previous studies (e.g. Balistrieri and Murray, 1982) have suggested that the presence of dissolved carbonate has little effect on the sorption of cadmium by iron (oxyhydr)oxides.

A further important consideration in excluding CO_2(g) was the way that surface complexation models are currently used. Many attempts to derive thermodynamic data are performed under CO_2(g)-free conditions (e.g. Benjamin & Leckie 1981a; Ainsworth et al., 1994; Lumsdon and Evans, 1994). This is because the calculated intrinsic complexation constants that describe metal adsorption rely on accurately known intrinsic surface acidity constants. These can only be properly determined in the absence of adsorbed carbonate species (Lumsdon and Evans, 1994). Thus, although the results of this study do relate to a simplified system, they are directly applicable to work involving surface complexation models.

3.2 EXPERIMENTAL METHODS

3.2.1 General

All reagents used in this study were analytical grade and labware was acid-washed. Samples, acid/base solutions and stock solutions were prepared using degassed (boiled) MilliQ water to prevent the formation of $CdCO_3$(s). A BDH general purpose combination electrode with an Orion model 720A meter were used to make pH measurements. Calibration ± 0.05 pH units was achieved at room temperature with constantly stirred Whatman NBS grade buffers.

3.2.2 Mineral Preparation and characterisation

Goethite, lepidocrocite and schwertmannite were prepared in the laboratory according to methods reported by Schwertmann and Cornell (1991). Goethite was prepared by hydrolysing a $Fe(NO_3)_3$ solution at pH 12-13 and 70 °C for 60 hours. Plastic labware was used throughout to avoid the danger of the high pH solution leaching silica from glassware. Lepidocrocite was prepared by the oxidation/hydrolysis of a $FeCl_2$ solution at pH 6.7 - 6.9. Schwertmannite was prepared by quickly mixing $FeCl_3$ and Na_2SO_4 solutions at 60°C, and allowing the suspension to cool to room temperature after 12 min. Finally, akaganeite was prepared by briefly boiling a $FeCl_3$ solution and then allowing the suspension to cool to room temperature. Contaminant anions from the synthesis procedures (e.g. NO_3^- and Cl^-) were removed from the resulting mineral suspensions by dialysis against MilliQ water that was frequently changed. This was of particular importance for schwertmannite because transformation to goethite is rapid under high SO_4^{2-} conditions (≥ 1000 ppm), but much slower at low SO_4^{2-} concentrations (Schwertmann and Cornell, 1991).

The identity and purity of the crystalline products was confirmed by X-ray powder diffraction of randomly oriented powder samples. The surface areas of goethite (27 ± 3 m^2g^{-1} and 33 ± 3 m^2g^{-1}; two batches), lepidocrocite (88 ± 3 m^2g^{-1}), akaganeite (65 ± 3 m^2g^{-1}) and schwertmannite (126 ± 3 m^2g^{-1}) were determined by BET surface area analysis following 12 hours of outgassing with $N_2(g)$. The analytical error of ± 3 m^2g^{-1} was determined by repeated measurements. The general crystal morphology of each mineral was examined by TEM and the goethite morphology was further examined by electron diffraction (ED). Goethite crystallites measured approximately 4000 nm long by 150 nm wide. They displayed a characteristic elongate lath-like morphology with a diamond shaped cross-section bounded mainly by the (110) surfaces with little or no contribution from the (100) and (010) surfaces. The chain terminations were bounded by the (021) surfaces which I estimate to comprise ~2 % of the overall crystal surface area. Lepidocrocite crystallites measured approximately 300 nm long by 125 nm wide and displayed the platy morphology (with thickness « width) that is characteristic of this mineral. The ends of the crystallites had a serrated appearance whilst the sides were relatively straight. Akaganeite crystallites were 'cigar-shaped' and measured approximately 100 nm long by 10 nm wide. They were frequently observed to raft together. Schwertmannite crystallites consisted of roughly spherical particles with jagged-looking outlines; these measured approximately 100–1000 nm in diameter.

The goethite and lepidocrocite stock suspensions were stored in closed polypropylene bottles at 4 °C following purging with $N_2(g)$ for ≥ 24 hours to remove

dissolved carbonate species. Akaganeite, schwertmannite and a small amount of goethite were stored as frozen fine powders following air drying at 35 - 40 °C for 24 hours and crushing with an agate mortar and pestle.

3.2.3 Preparation of adsorption samples for EXAFS analysis

The cadmium stock solutions were prepared from $Cd(NO_3)_2 \cdot 4H_2O(s)$. They were acidified to ~pH 4 with a few drops of 1 % v/v HNO_3 and stored at 4 °C in a closed 0.5 L polypropylene flask. Preparation conditions for the adsorption samples are summarised in Table 3.1.

The majority of the samples (61-S to 68-S and 72-S) were prepared in the following manner: Goethite or lepidocrocite stock suspensions (which had previously been placed in an ultrasound bath to break up aggregates), cadmium stock solution, MilliQ water and $NaClO_4 \cdot H_2O$ were added to 500 ml polythene screw top containers to achieve the desired cadmium and sorbent concentrations in a 0.1 M background electrolyte. Sample 47-S was prepared in the same manner but in the absence of the background electrolyte. The pH of the resulting suspensions was manually set to the desired starting value (Table 3.1) with 0.1 or 1.0 M KOH or 1 % v/v HNO_3, whilst CO_2-free conditions were maintained by purging with $N_2(g)$. The sample containers were shaken vigorously at the start of the reaction, and then approximately every 6 hours afterwards. The pH was measured and, if necessary, manually reset to the desired value approximately half way through the 18 hour reaction time.

Table 3.1. Reaction conditions during adsorption sample preparation. Background electrolyte was 0.1 M $NaClO_4$ unless otherwise stated.

Sample	Mineral	Surface area (m^2g^{-1})	[Sorbent] g L^{-1}	[Cd] ppm (initial)	Start pH	Final pH	Wt % Cd	†Surface loading (%)
20-bS‡	Akaganeite	65(3)	13.3	800	7.4	8.0	1.01	52
50-S‡	Schwert-mannite	126(3)	1.0	90	7.0	6.5	2.91	79
43-S (dry)	Goethite	27(3)	4.0	90	7.1	6.5	0.66	79
61-S				50	5.4	5.4	0.39	38
64-S				20	6.6	6.4	0.28	27
65-S	Goethite	33(3)	1.0	50	6.3	6.3	0.54	53
68-S				7	8.2	7.7	0.45	44
70-S				3	9.3	9.3	0.24	24
47-S‡			2.0	90	7.5	6.0	0.74	27
72-S	Lepidocrocite	88(3)	1.0	100	6.5	6.3	1.21	45
73-S			1.0	20	7.0	7.0	0.78	29

Key for Table 3.1:

† Surface loading (a measure of the number of available surface sites occupied by adsorbed cadmium) is calculated on the assumption of a site density of 1.68 sites nm^{-2} for goethite (Lövgren et al., 1990), 1.67 sites nm^{-2} on lepidocrocite (Zhang et al., 1992), and 1.62 sites nm^{-2} on akaganeite (Parida et al., 1997) and schwertmannite.
‡ No background electrolyte.

Samples 70-S and 73-S were prepared as described above except that the suspensions were held in a sealed reaction vessel containing a magnetic stirrer. In both cases, pH was maintained at the required value by a Metrohm 702 Titrino autotitrator using 0.1 M KOH.

Samples 43-S(dry) and 50-S were prepared in the same manner as 61-S to 68-S and 72-S, except that the sorbents were added as dry powders, and 50-S did not have a background electrolyte. Sample 43-S(dry) was air dried at 35 - 40 °C immediately after adsorption was complete. Sample 20-bS was prepared in the absence of a background electrolyte by adding the sorbent as a dry powder to 30 ml of cadmium stock solution in a 50 ml polycarbonate Oak Ridge centrifuge tube. The suspension was constantly purged with $N_2(g)$. The pH was adjusted to the required starting value (Table 3.1) using 0.1 M KOH, and the centrifuge tube was sealed after purging with $N_2(g)$ for a further 15 min. The sample was reacted at 19 ± 2 °C in a rotating tumbler to keep the sorbent in suspension, and pH was measured and reset to the desired value every 12 hours during the 48 hour reaction period.

In all cases, pH was observed to decrease as the sorption reaction proceeded, and the final pH was taken to be that of equilibration. It should be noted that a

maximum of 0.7 ml of acid or base was added to any given sample to achieve the desired pH, and that such additions resulted in minimal changes in total sample volume.

Centrifugation (3000 rpm for 20 - 30 min) was used to separate each reacted suspension into a viscous paste (the 'adsorption sample') and a clear supernate. The supernates were filtered using 0.2 μm cellulose nitrate membrane filters, acidified by addition of 1 % v/v HNO_3, and subsequently analysed for cadmium by either ICP-MS or ICP-AES. The adsorption samples were stored at 1 - 4 °C, and all EXAFS analyses were performed within 72 hours of centrifugation.

3.2.4 Determination of degree of surface loading

The degree of surface loading is an important descriptive parameter for adsorption samples, and its derivation relies heavily on the use of reasonable adsorption site densities. Lövgren et al. (1990) determined a value of 1.68 surface hydroxyl sites per nm^2 on goethite by the addition of excess protons to goethite suspensions. I have used this value to calculate the percentage surface loading of cadmium on the goethite adsorption samples (Table 3.1). Very similar values of 1.67 sites per nm^2 (Zhang et al., 1992) and 1.62 sites per nm^2 (Parida et al., 1997) were used for lepidocrocite and akaganeite, respectively. In this study, schwertmannite was also assumed to possess 1.62 sites per nm^2 because of its supposed structural similarity with akaganeite (Schwertmann and Cornell, 1991).

The site densities used here are consistent with values reported in studies of cation adsorption (e.g. Atkinson et al. 1967). They also agree well with values derived from crystallographic considerations (Pivovarov, 1997) and determinations of the maximum theoretical density of a monolayer of adsorbed cadmium aquo ions (Spark et al., 1995).

3.2.5 *Ab initio* quantum mechanical prediction of the geometry and energetics of adsorption complexes

In this study, *ab initio* Density Functional Theory (DFT) has been used to perform quantum mechanical calculations. These calculations were used to predict the optimised geometry and relative stabilities of four small molecular clusters. Each cluster was representative of a particular type of cadmium surface complex on goethite.

Density Functional Theory as used in the computer code ADF 2.0.1 (te Velde, 1995) was used with a Slater orbital basis set, with triple zeta valence shells and frozen core orbitals (for computational efficiency). The formulae of Vosko et al. (1980) were used for exchange and correlation in the local density approximation and the generalised gradient corrections of Becke (1988) and Perdew (1986) were applied *a posteriori* to the self consistent field step. DFT calculations were performed with a quasi-relativistic correction using core potentials from the computer code Dirac (te Velde, 1995). Clusters containing two iron atoms were spin-constrained to be ferromagnetic.

Initial cluster geometry was based on a consideration of the goethite surface and the likely composition of cadmium surface complexes. Each cluster consisted of two linked $Fe(O,OH)_6$ octahedra with a cadmium aquo complex attached in a way that was representative of a particular adsorption mechanism. The geometry of the iron octahedra was fixed so that it was the same as that in the goethite bulk structure, but no other structural constraint was applied during the calculations. If the iron octahedra were not constrained, they adopted a more relaxed geometry quite different to that expected at the goethite surface.

In addition to predicting geometry, the DFT calculations also determined the total free energy of formation for each cluster. In order to allow these values to be compared relative to each other, the composition of the smaller clusters was normalised to that of the largest cluster by addition of one or two water molecules. The relative total energy of the clusters was then calculated by arbitrarily setting the total energy of one cluster to zero, and recalculating values for the other clusters accordingly.

It should be noted that the total free energy of formation values relate to the formation of clusters from free atoms in the gas phase, with no account taken of solvation effects. Consequently, the resulting energies are large and they are not strictly applicable to the liquid phase. They do nonetheless facilitate the ranking of clusters in terms of relative stability. The good agreement between experimental EXAFS results and certain predicted geometries indicates that information derived from *ab initio* quantum mechanical modelling is applicable to the cadmium surface complexes described here.

3.2.6 EXAFS theory, data collection and analysis

3.2.6.1 General description of EXAFS spectroscopy

An EXAFS spectral scan is obtained by measuring X-ray absorption over a range of photon energies which includes the 'absorption edge' of the element of interest (e.g. Brown et al., 1988; Charlet and Manceau, 1993; Brown et al., 1995). Curve fitting allows the determination of the *average* number (N_j) (± 20 %) of atoms in the jth atomic shell, their distance (R_j) (± 0.02 Å) from the central excited cadmium atom, their identity, and the associated Debye-Waller factor ($2\sigma_j^2$) (e.g. Brown et al., 1988). The latter parameter represents the mean square of variation in distances from the element of interest to the shell under consideration. It accounts for damping of the EXAFS oscillations due to thermal vibration (σ_T) and static disorder (σ_S) within atomic shells (e.g. Brown et al., 1995). The quality of the fit between the experimental and simulated EXAFS functions is represented by the *R* factor:

$$R_{EXAFS} = \sum_i \frac{1}{\sigma}(|\chi_i(k)^{exp} - \chi_i(k)^{theory}|) \times 100\%$$

where σ is the standard deviation of the difference between experimental ($\chi^{experiment}$) and theoretical (χ^{theory}) EXAFS functions over a specified k range. For poorly ordered mineral-aqueous systems such as those described here, an *R* value between 20% and 40% indicates an acceptable match between theory and experiment (Dent and Mosselmans, 1992).

3.2.6.2 Data collection

EXAFS data were collected at the CLRC Synchrotron Radiation Source at Daresbury Laboratory, U.K. Spectra were collected at the cadmium K-edge under room temperature conditions on station 9.2, which is equipped with a double crystal Si (220) monochromator. The storage ring energy was 2.0 GeV and the beam current varied between 130 and 240 mA during data collection. Each adsorption sample was presented to the X-ray beam as a viscous paste held by Sellotape in a 2 mm thick plastic slide with a 4 x 15 mm sample slot. EXAFS data were collected from the adsorption samples during six to ten fluorescence mode scans using a thirteen element Ge diode Canberra detector. EXAFS data were also collected for reference from a β-$Cd(OH)_2$(s) standard in two room temperature transmission mode scans. During all data collection, the monochromator was set to reject 50 % of the incoming beam to minimise higher harmonics in the EXAFS spectra.

3.2.6.3 Data analysis

EXAFS data reduction was performed using Daresbury Laboratory software (EXCALIB and EXBACK) (Binsted et al., 1991). EXCALIB was used to calibrate from monochromator position (millidegrees) to energy (eV) and to average multiple spectra from individual samples. EXBACK was used to define the start of the EXAFS oscillations and perform background subtraction.

The exact curved wave theory EXAFS analysis program EXCURV92 (Gurman et al., 1984, 1986; Joyner et al., 1987; Gurman, 1988; Binsted et al., 1991, 1992) was then used to analyse the EXAFS data. This process involved the comparison of experimental data with theoretical EXAFS oscillations that were derived by EXCURV92 from model clusters. The geometry of these clusters was based on the predicted geometry of the adsorption complexes. For each sample, the cluster that provided the closest initial fit underwent least squares refinement of: Debye-Waller factor, number of atoms per shell, Cd-X distance, and Fermi energy to improve the fit between its theoretical oscillations and the experimental data. This caused the composition and geometry of the model cluster to approach the true structure and chemistry of the adsorption complex. During fitting, any number of the four parameters being refined can be constrained. This facility occasionally proved useful in the early stages of fitting, but all parameters were unconstrained during the final stages of data analysis.

The model clusters initially consisted of only one atomic shell. Successive shells were added to the theoretical model until each significant peak in the Fourier transform of the EXAFS data was accounted for. Statistical tests (Joyner et al., 1987) were performed to ascertain the significance of each new atomic shell, and only those which improved the fit between theory and experiment at the 99 % level of confidence were retained.

Refining theoretical models to find agreement with experimental data in this way provided shell parameters that describe the average local coordination environment around adsorbed cadmium. Care was taken during curve fitting to check that none of the atomic shells could be assigned to the known structure of cadmium solids such as β-$Cd(OH)_2(s)$, γ-$Cd(OH)_2(s)$ or $CdCO_3(s)$.

The phase-shift functions used in the curve fitting were derived by *ab initio* methods in EXCURV92 using Hedin-Lundqvist potentials (Hedin and Lundqvist, 1969) and von Bart ground states. Spadini et al. (1994) have suggested that phase-shift functions generated in this manner are less accurate than those determined experimentally. However, the use of theoretical values is justified by the good agreement between the structure of β-$Cd(OH)_2(s)$ derived from the EXAFS data

using theoretical phase-shift functions (Fig. 3.1) and the published structure of β-$Cd(OH)_2$(s) (Spadini et al., 1994).

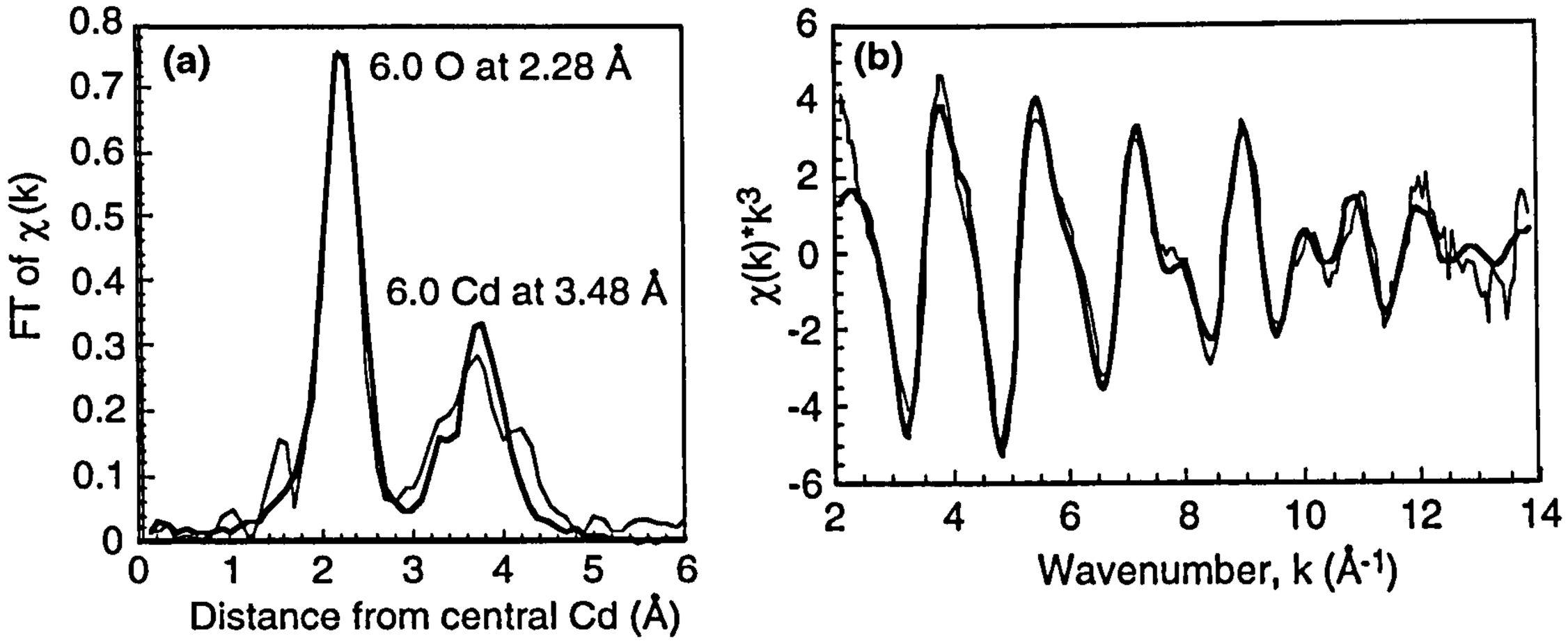

Fig. 3.1. Fourier transform (FT) (a) and EXAFS (b) plots for β-$Cd(OH)_2$(s). The data was analysed using phase-shift functions derived empirically in EXCURV92.

3.2.7 Interpretation of EXAFS data

To a first approximation, the inner sphere complexation of cadmium with iron (oxyhydr)oxide mineral surfaces can be described by the combination of $[Cd(H_2O)_6]^{2+}$ aquo ion octahedra from solution with $Fe(O,OH)_6$ octahedra at the mineral surface. Octahedra can be linked by sharing edges, corners or apices. Because each type of linkage results in a discrete and characteristic Cd-Fe distance, EXAFS spectroscopy can be used to discriminate between the different mechanisms of attachment. For instance, edge sharing between cadmium and ferric iron octahedra results in a Cd-Fe distance of ~3.3 ± 0.1 Å, whilst corner sharing leads to a Cd-Fe distance of ~3.8 ± 0.1 Å (Spadini et al., 1994; Collins et al., 1999). This is known as the 'polyhedral approach' to EXAFS data interpretation (e.g. Combes et al., 1989).

3.3 CADMIUM SORPTION: INNER SPHERE COMPLEXATION VERSUS SURFACE PRECIPITATION

The percentage adsorption of available cadmium from solution by goethite and lepidocrocite was observed to increase dramatically between pH 6 and 8, in agreement with numerous studies of cadmium adsorption onto iron (oxyhydr)oxides (e.g. Kinniburgh et al., 1976; Davis and Leckie, 1978; Leckie et al., 1980; Millward, 1980; Benjamin and Leckie, 1981a, b; Balistrieri and Murray, 1982). This behaviour is explained in terms of the increasingly negative surface charge which develops on amphoteric minerals when surface functional groups deprotonate as pH rises. Significant adsorption of Cd^{2+} occurs below the pH at which there is net zero surface charge (pH_{ZPC}) on lepidocrocite (pH_{ZPC} = 7.3, Zhang et al., 1992) and goethite (pH_{ZPC} = 8.9, Van Geen et al., 1994). The net surface charge is still positive under such conditions, and thus the observed Cd^{2+} adsorption is taken as evidence that this process is thermodynamically favourable (e.g. Lamy et al., 1991). In other words, the chemical (specific) component of the free energy of adsorption is greater than the unfavourable electrostatic component.

The EXAFS results are shown in Figs. 3.1, 3.4, 3.6, 3.7 and 3.9. The experimental data is shown as fine lines and the calculated best fits as bold lines in both the EXAFS plots and the associated Fourier Transform (FT) plots. Each peak in the FT plots corresponds to an atomic shell. It should be noted that only the first peak in each plot is corrected for phase-shift effects. Consequently, whilst the experiment and theory curves for the first FT peaks coincide at the true Cd-X distance, the experiment curves for the second, third etc. FT peaks are sometimes displaced from their true Cd-X locations. Any apparent mismatch between experiment and theory in the FT plots is merely an artefact of this, and does not imply a poor fit. Additionally, it is important to emphasise that curve fitting is performed using the EXAFS data and not the associated Fourier transform data. The best indication of how successful curve fitting has been is thus provided by inspecting the match between theory and experiment in the EXAFS plots and not the FT plots. Table 3.2 summarises the EXAFS results.

Table 3.2. Shell parameters derived from analysis of EXAFS oscillations. Note that values in italics are speculative. N_X is number of atoms in a shell at distance R_X from the central cadmium atom. $2\sigma^2_X$ is the associated Debye-Waller factor. The *R* factor gives a measure of the agreement between experimental and theoretical EXAFS curves. $R < 20\%$ indicates a very good fit whereas $R \leq 40\%$ is acceptable.

Sample	Mineral	Final pH	†Surface loading (%)	N_O	R_O (Å)	$2\sigma^2_O$	N_{Fe}	R_{Fe} (Å)	$2\sigma^2_{Fe}$	*R* (%)
20-bS‡	Akagan-eite	8.0	52	5.5	2.28	0.020	0.8	3.29	0.020	31.9
50-S‡	Schwert-mannite	6.5	79	5.7	2.28	0.020	*0.8*	*3.33*	*0.020*	35.8
43-S (dry)	Goethite	6.5	79	5.8	2.24	0.020	1.4	3.75	0.020	30.4
61-S		5.4	38	6.4	2.26	0.020	1.8	3.77	0.018	36.6
64-S		6.4	27	6.4	2.26	0.020	1.6	3.76	0.020	31.9
65-S	Goethite	6.3	53	6.4	2.25	0.020	1.5	3.75	0.020	23.9
68-S		7.7	44	6.3	2.25	0.020	1.1	3.78	0.020	25.0
70-S		9.3	24	6.0	2.26	0.020	1.5	3.80	0.020	24.0
47-S‡	Lepido-	6.0	27	6.6	2.26	0.020	1.1	3.30	0.018	29.0
72-S	crocite	6.3	45	6.9	2.25	0.020	1.5	3.26	0.020	34.0
73-S		7.0	29	6.8	2.26	0.020	1.4	3.30	0.020	28.2

EXAFS standard	N_O	R_O (Å)	$2\sigma^2_O$	N_{Cd}	R_{Cd} (Å)	$2\sigma^2_{Cd}$	*R*
β-$Cd(OH)_2$(s) (EXAFS experiment)	6.0	2.28	0.016	6.0	3.48	0.024	30.5
β-$Cd(OH)_2$(s) (XRD[1])	6.0	2.34		6.0	3.50		

† Surface loading (a measure of the number of available surface sites occupied by adsorbed cadmium) is calculated on the assumption of a site density of 1.68 sites nm^{-2} for goethite (Lövgren et al., 1990), 1.67 sites nm^{-2} on lepidocrocite (Zhang et al., 1992), and 1.62 sites nm^{-2} on akaganeite (Parida et al., 1997) and schwertmannite.

‡ No background electrolyte.

[1] Spadini et al. (1994).

Data from all adsorption samples and the β-$Cd(OH)_2$(s) standard shows that cadmium is coordinated by an inner atomic shell of approximately six oxygens at a Cd-O distance of 2.24 - 2.28 Å. At least one additional atomic shell containing iron atoms is observed outside the oxygen shell in all the adsorption samples. Since the iron shell(s) occur at a Cd-Fe distance of less than 4 Å, cadmium must adsorb *via* an inner sphere mechanism. The first coordination shell around cadmium therefore consists of terminal -(O,OH) groups at the mineral surface and that part of the solvation shell not lost during adsorption.

There is no evidence of Cd-Cd interactions in data from any of the adsorption samples. This indicates that cadmium did not sorb *via* the precipitation of an ordered crystalline phase such as $Cd(OH)_2$(s) or $CdCO_3$(s). Indeed, the omnipresent nature of the iron shell(s) suggests that the majority of cadmium sorbed by direct

(inner sphere) bonding to the mineral surface. These results are in general agreement with an earlier EXAFS-based study of cadmium sorption on goethite and hydrous ferric oxide by Spadini et al. (1994). However, it should be noted that a minor fraction of cadmium may have sorbed as a poorly ordered precipitate that was not detected. This possibility arises because a high degree of structural disorder can make atom-atom interactions (such as Cd-Cd) very hard to resolve with EXAFS.

3.4 ADSORPTION OF CADMIUM ON GOETHITE

3.4.1 Crystallography and surface chemistry of goethite

Because of its ubiquitous and highly crystalline nature, goethite is the most comprehensively characterised iron oxyhydroxide. It consists of double bands of edge-sharing $FeO_3(OH)_3$ octahedra linked to form 2 x 1 octahedral 'tunnels' which are crossed by hydrogen bonds (Schwertmann and Cornell, 1991). Early work suggested that the (100), (110), (010), and (001) crystal faces (referred space group *P*nma) were dominant (Cornell et al., 1974). However, it has more recently been shown that the (110) surfaces running parallel to the long axis of the laths are dominant whilst the chain terminations are bounded by the much smaller (021) surfaces (Fig. 3.2a). This is true of both natural and synthetic goethites (Smith and Eggleton, 1983; Schwertmann, 1984; Mann et al., 1985; Amouric et al., 1986; Schwertmann and Cornell, 1991; Hiemstra and Van Riemsdijk, 1996).

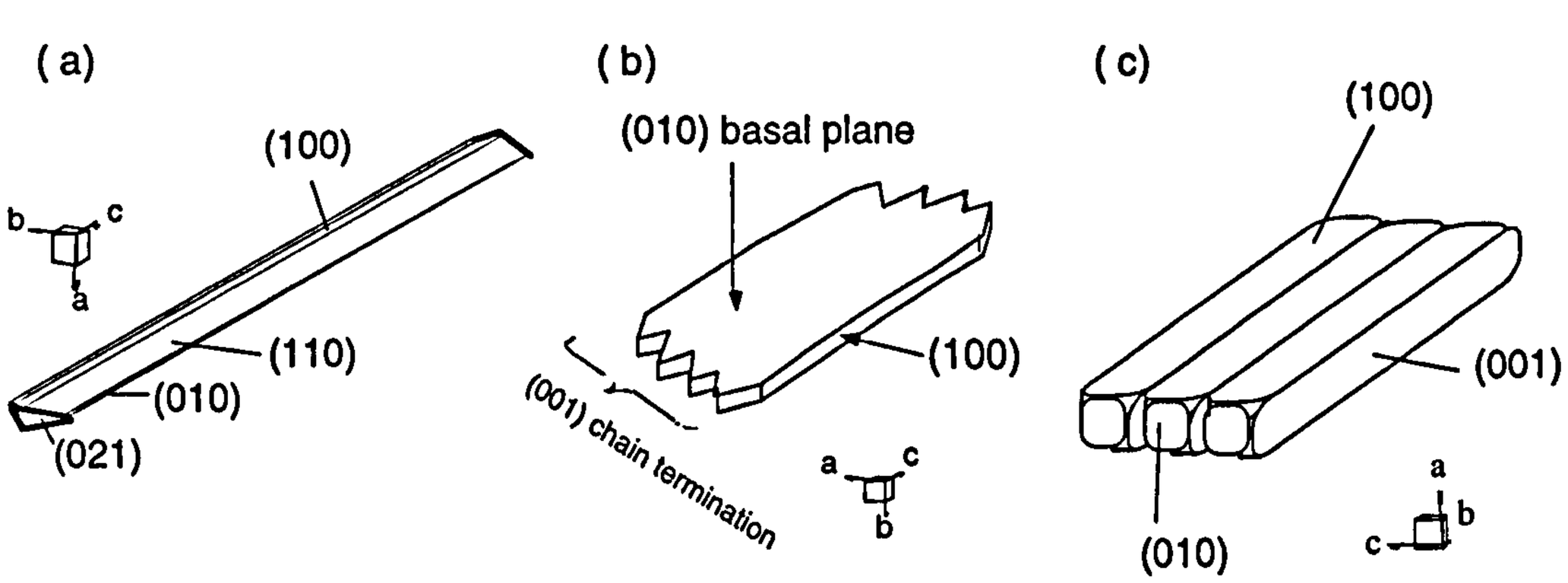

Fig. 3.2. Morphology of (a) goethite, (b) lepidocrocite and (c) akaganeite crystallites. Diagrams not to scale.

Infrared studies suggest that the amphoteric goethite surface is populated by three types of non-equal surface hydroxyl groups that are coordinated to either one, two, or three terminal iron atoms (e.g. Russell et al., 1974; Parfitt et al., 1975;

Russell et al., 1975; Parfitt and Russell, 1977). These are termed **A**-, **C**-, and **B**-type hydroxyls, respectively. They are present on all crystallographic faces parallel to the long axis of the crystallites, and each type of hydroxyl group has a markedly different acidity and reactivity towards adsorbates (Parfitt et al., 1975). The **A**-type hydroxyls are believed to be the most reactive as their oxygen atoms exhibit the lowest coordination number (Parfitt et al., 1977). They appear to be reactive surface sites that are capable of undergoing protonation-deprotonation reactions and complexing ions from solution. **C**-type hydroxyls were occasionally invoked by early workers as being sites for hydrogen bonding of anions (e.g. Parfitt et al., 1975; Russell et al., 1975), but have more recently been shown to be zero charged and essentially inert over a wide pH range (Hiemstra et al., 1989a, b). The **B**-type hydroxyls are also thought to be inert (Parfitt et al., 1977; Spadini et al., 1994).

3.4.2 Results of *ab initio* modelling of cadmium surface complexes on goethite

Ab initio Density Functional Theory (DFT) calculations are restricted to cadmium adsorption on goethite. This is because my most comprehensive EXAFS data set relates to the cadmium-goethite system and because goethite is a highly characterised and commonly used sorbent. Additionally, this modelling approach is novel and the work presented here amounts to a thorough test of its applicability with a good EXAFS data set. Although the *ab initio* modelling approach can be applied to other sorbent - sorbate systems, the results are not transferable between clusters with different geometries or compositions.

Based on likely mechanisms of cadmium adsorption on the goethite surface, the geometry and total static energy of formation of the following molecular clusters was determined: Double corner sharing; single corner sharing; double edge sharing; single edge sharing. The first two offer insight into the structure of cadmium surface complexes on the (110) and (100) surfaces whilst the latter two relate to adsorption on the (021) chain terminations.

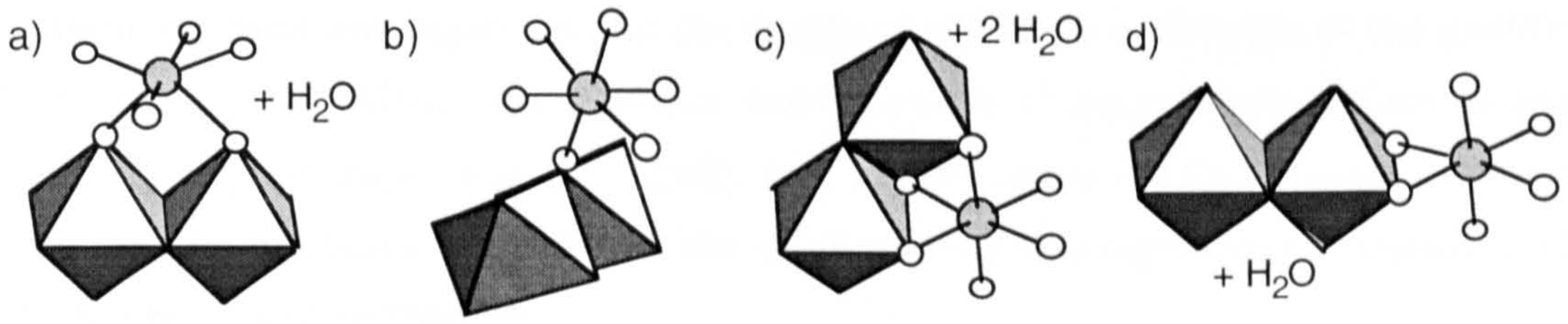

Fig. 3.3. Optimised geometries and relative total energies of formation for Density Functional Theory-optimised clusters representing cadmium adsorption complexes on goethite. The general cluster formula is $[(H_2O)_5CdFe_2(O)(OH)_6(OH_2)_3]^0$ (hydrogen atoms not shown): a) double corner sharing with two **A**-type hydroxyls; b) single corner sharing with one **C**-type hydroxyl (both mechanisms possible on (110) and (100) faces); c) double edge sharing; d) single edge sharing (both mechanisms possible on (021) chain terminations). Note that the energy of the single corner sharing cluster is not reliable because there is strong interaction between the cadmium aquo ion and the singly coordinated hydroxyls of the goethite cluster - see text for details.

The molecular clusters and calculation results are shown in Fig. 3.3. As the polyhedral approach suggests, edge sharing relationships are characterised by significantly shorter Cd-Fe distances (≤ 3.34 Å) than corner sharing relationships (≥ 3.52 Å). However, the Cd-Fe distance observed in the single corner sharing cluster (3.52 Å) is also considerably shorter than that in the double corner sharing cluster (3.76 Å). The polyhedral approach would not predict such a large difference in Cd-Fe distance for linking mechanisms that are outwardly similar; indeed, single- and double corner sharing relationships in the goethite bulk structure do result in identical Fe-Fe distances. This finding underlines the utility of the *ab initio* approach in predicting the true geometry of small molecular clusters. Previously, predictions of surface complex geometry have relied on information derived from the bulk structure of suitable reference compounds. The *ab initio* approach is free of such constraints.

The relative total free energies of formation suggest the following order of increasing cluster stability: double corner (0 kJ mol^{-1}) < single edge (-115 kJ mol^{-1}) < double edge (-309 kJ mol^{-1}). This ranking supports the widely held belief that edge sharing adsorption is more energetically favourable than corner sharing adsorption (e.g. Dzombak and Morel, 1990; Spadini et al., 1994). It also suggests that edge- and corner sharing sites are the 'strong' (high affinity) and 'weak' (low affinity) sites, respectively, in the 'strong site - weak site' approach of Dzombak and Morel's diffuse-layer surface complexation model (1990). Note that the energy of the single corner sharing cluster is not reliable because there is strong interaction

between the cadmium aquo ion and the singly coordinated hydroxyls of the goethite cluster (Fig. 3.3). Whilst this situation does not arise at the goethite surface, it does result in the prediction of an artificially low energy value for this cluster. I do not think that the predicted geometry of the single corner sharing cluster is significantly effected by this phenomenon.

3.4.3 EXAFS results and general discussion for cadmium adsorption on goethite

The EXAFS results for the wet paste goethite adsorption samples covering a range of surface loading and pH conditions are shown in Fig. 3.4 and summarised in Table 3.2. In all cases, a shell of approximately six oxygen atoms is observed at a Cd-O distance of 2.24–2.26 Å, and a shell containing between 1.1 and 1.8 iron atoms is present between 3.75 and 3.80 Å from the central cadmium atom. Note that any observed mismatch between theory and experiment in the FT plots arises because the position of the experimental iron peak is not corrected for phase-shift effects, and does not imply a poor fit. This point is elaborated upon in section 3.3.

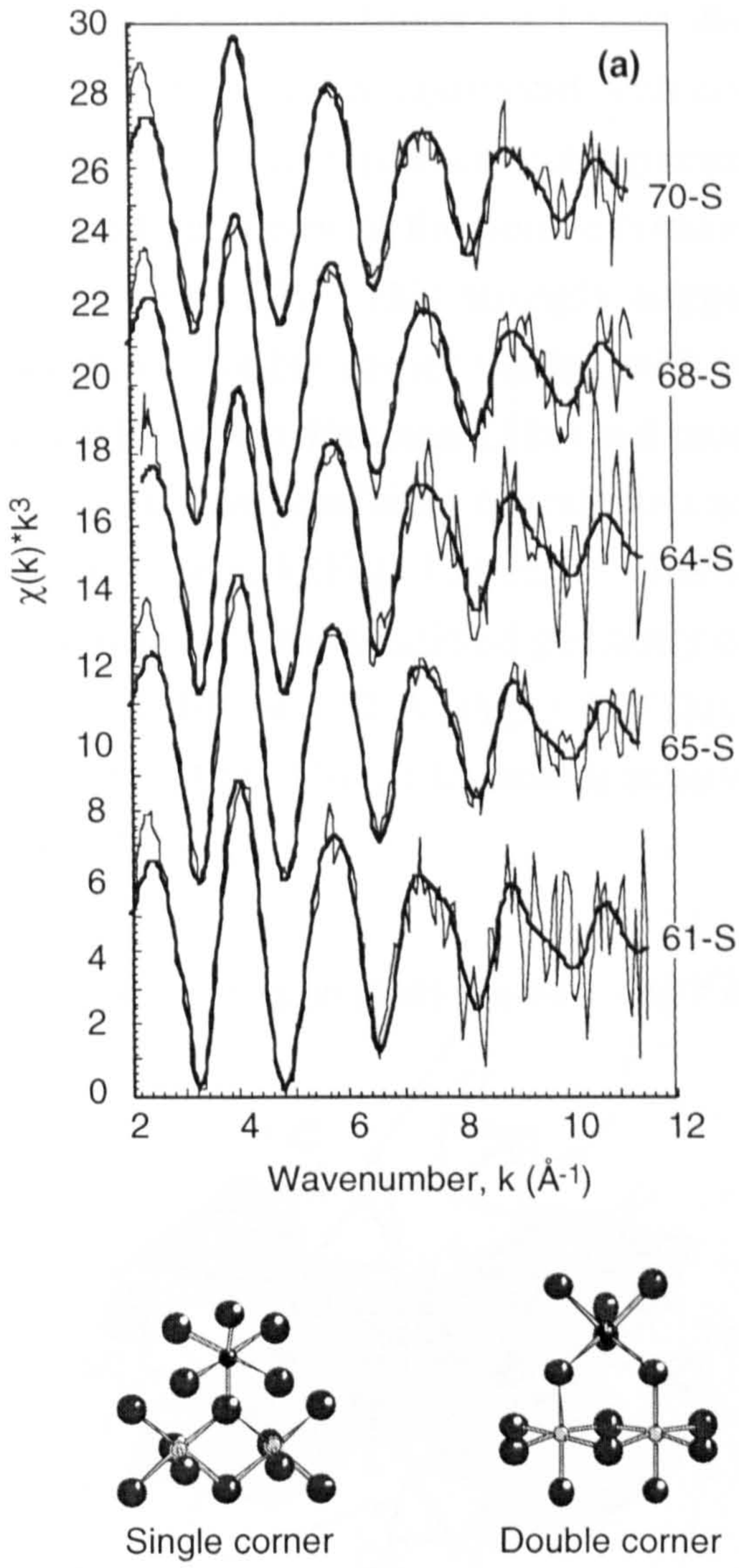

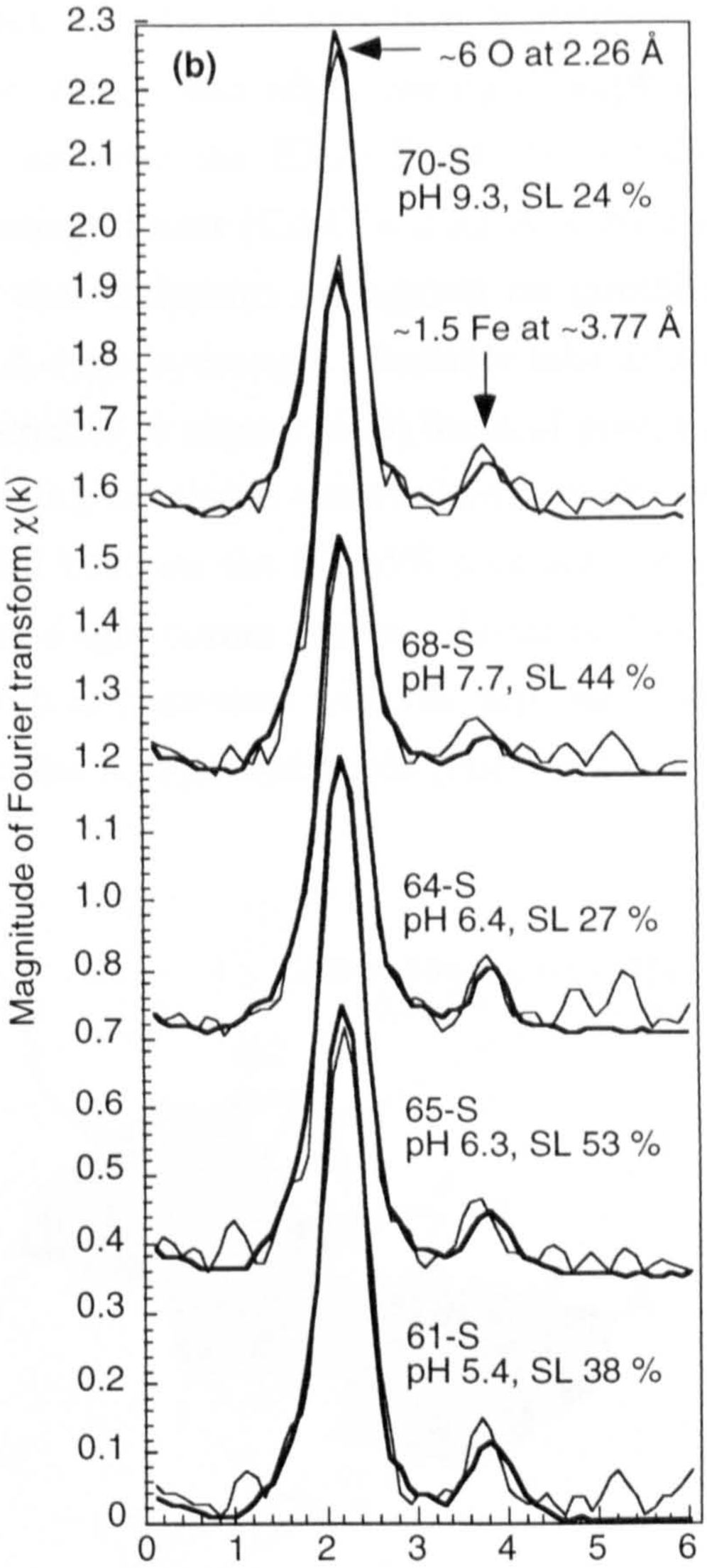

Fig. 3.4. EXAFS (a) and FT (b) plots of cadmium adsorbed on goethite. SL stands for surface loading. The general EXAFS result of six oxygen atoms at 2.24 - 2.26 Å and ~1.5 iron atoms at ~3.77 Å does not change as a function of pH or surface loading. Note that the position of the second peak in the FT plots has not been corrected for phase-shift effects; any apparent mismatch between theory and experiment for the iron FT peak is an artefact of this. The schematic diagrams show a cadmium aquo complex undergoing monodentate single corner sharing adsorption with a **C**-type hydroxyl (left) and bidentate double corner sharing adsorption with two **A**-type hydroxyls (right).

The structure of the adsorption complexes does not alter significantly as a function of pH or surface loading. All observed variation in Cd-O and Cd-Fe distances between samples is very close to the widely accepted experimental error value of ± 0.02 Å (e.g. Brown et al., 1995). The range of iron coordination numbers is quite large, but the samples are not significantly different from each other in this respect because the uncertainty on EXAFS-derived coordination numbers is ± 1.

The observed average Cd-Fe distance of ~3.77 Å and iron coordination numbers (1.1-1.8) are consistent with corner- rather than edge sharing adsorption. Furthermore, there is excellent agreement between the EXAFS results and the predicted geometry of the double corner sharing cluster (Cd-O = 2.22 Å, Cd-Fe = 3.76 Å; Fig. 3.3). This strongly suggests that cadmium adsorption on goethite occurs *via* double corner sharing with two **A**-type hydroxyls. Suitable adsorption sites exist on the dominant (110) and much smaller or absent (100) faces of goethite (Fig. 3.5). The possibility of cadmium adsorbing *via* single corner sharing with one **C**-type hydroxyl (Fig. 3.5) can be discounted because the EXAFS data are not in agreement with the predicted geometry of the single corner sharing cluster (Cd-O = 2.22 Å, Cd-Fe = 3.52 Å; Fig. 3.3). This result is consistent with the supposed low reactivity of the **C**-type hydroxyls relative to the **A**-type hydroxyls (Hiemstra et al., 1989a, b).

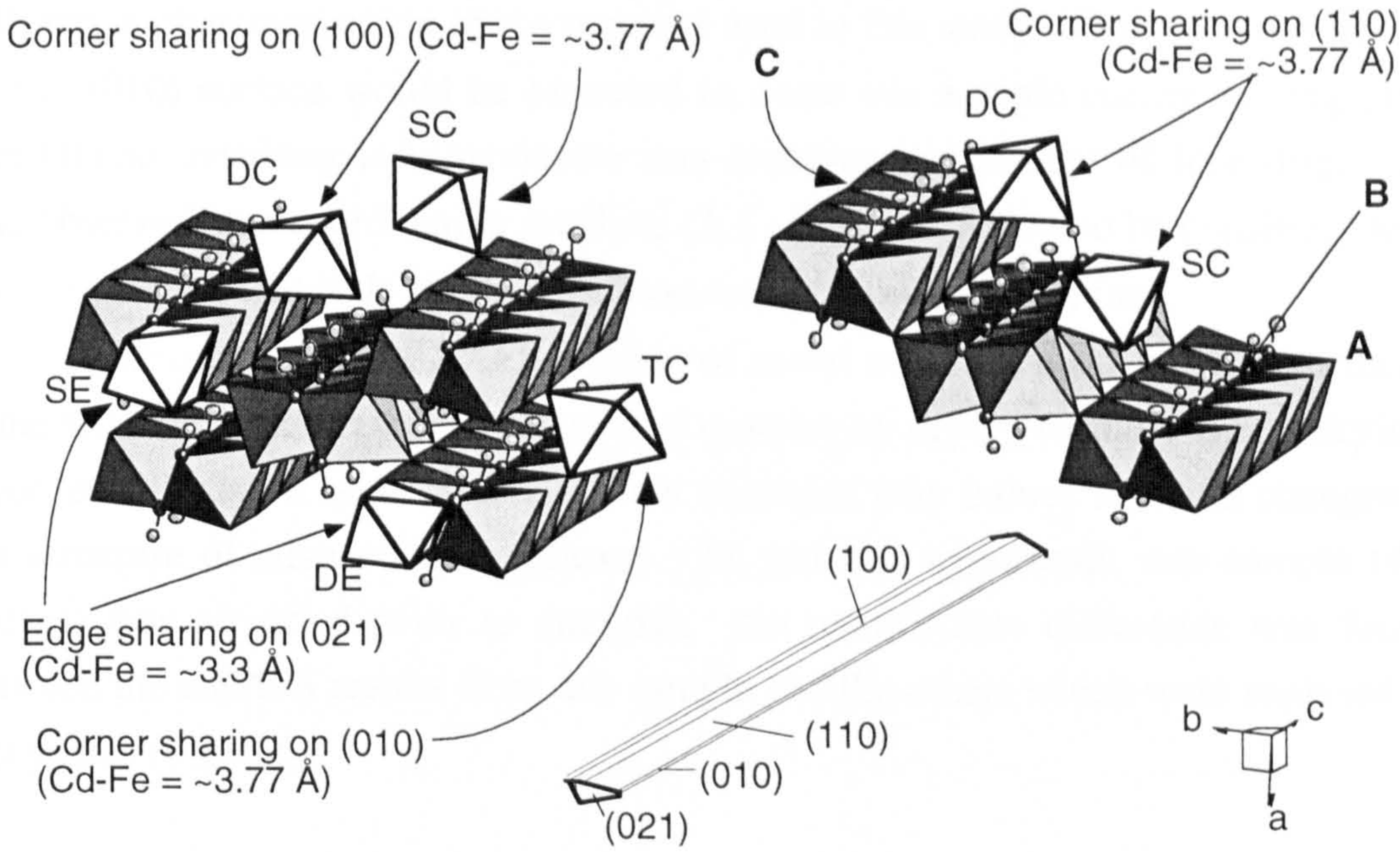

Fig. 3.5. Cadmium adsorbed on goethite has ~1.5 iron nearest neighbours at ~3.77 Å, suggesting adsorption *via* a corner sharing mechanism. Agreement between EXAFS data and the optimised geometry of appropriate molecular clusters suggests that this occurs by bidentate double corner (DC) sharing with singly coordinated **A**-type hydroxyls rather than monodentate single corner (SC) sharing with a **C**-type hydroxyl. There is no evidence for edge sharing adsorption (SE and DE) on the (021) faces; note that these surfaces comprise ~2 % of the total mineral surface area.

It has previously been suggested that the most favourable sites for cadmium adsorption on goethite are the edge sharing sites which are found on (021) faces at the crystal chain terminations (Spadini et al., 1994). Cadmium is expected to favour adsorption on the (021) faces because they are the dominant crystal growth sites and therefore the most reactive crystal surfaces. It is likely that cadmium adsorption on

(021) faces would occur *via* a double edge sharing mechanism (Fig. 3.5). *Ab initio* calculations confirm that surface complexes formed in this way are indeed highly stable (Fig. 3.3).

Spadini et al. (1994) suggest that cadmium adsorption at the edge sharing sites can only be observed by EXAFS at low cadmium surface loadings. This is because the (021) faces comprise only a small fraction of the total crystal surface area; I estimate ~2 % from the morphology of goethite used in this study. *Ab initio* calculations predict short Cd-Fe distances for the single- (Cd-Fe = 3.17 Å) and double (Cd-Fe = 2.87 Å and 3.34 Å) edge sharing clusters (Fig. 3.3). Such short Cd-Fe distances are not observed in the EXAFS data for cadmium on goethite, even when surface loading is as low as 24 %. It is thus clear that an extremely small fraction of total cadmium adsorption occurs at the edge sharing sites.

The (010) faces may contribute to the surface area of the goethite crystals, although they must be small since they were not observed during the electron diffraction characterisation of the material used in this study. Cadmium adsorption on the (010) surface would be expected to occur *via* a triple corner sharing (TC) mechanism, resulting in a maximum iron coordination number of four (Fig. 3.5). The observed iron coordination numbers (1.1 - 1.8) are too low to be consistent with this, suggesting that little or no adsorption occurred on the (010) face.

During previous EXAFS studies of metal adsorption on mineral surfaces, some workers have preserved adsorption samples by drying (usually freeze drying) prior to analysis. It is possible that such treatment may induce artificial changes in the structure of adsorption complexes. To test this hypothesis, one sample (43-S(dry)) was air-dried prior to analysis. No quantifiable difference was found between the EXAFS results from this sample and the others which were analysed as wet pastes (Fig. 3.6).

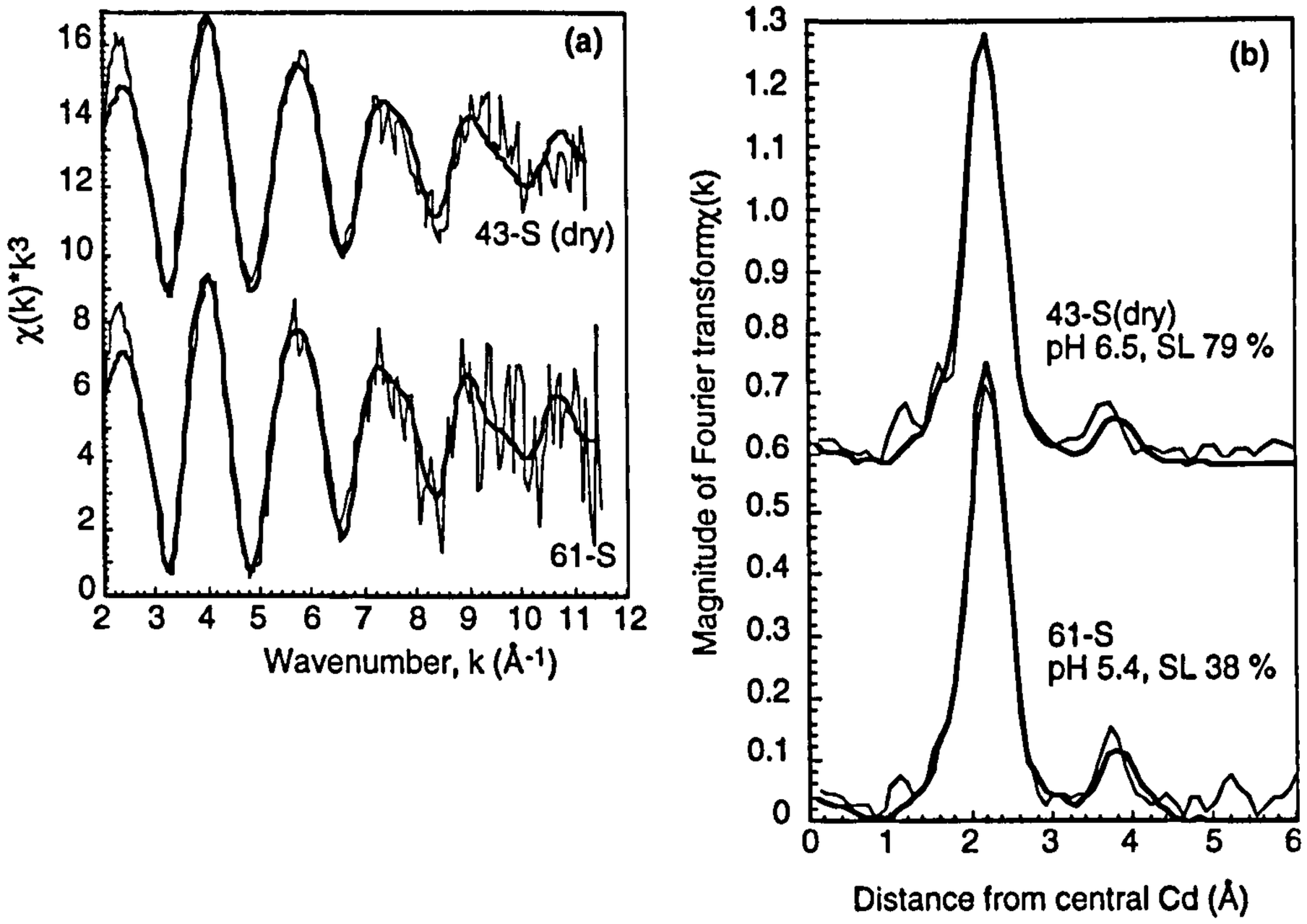

Fig. 3.6. EXAFS (a) and FT (b) plots of cadmium adsorption on goethite as a wet paste (61-S) and as a dry powder (43-S(dry)). SL stands for surface loading. It can be seen that drying does not significantly alter the general EXAFS result for cadmium adsorption on goethite. Note that the position of the second peak in the FT plots has not been corrected for phase-shift effects; any apparent mismatch between theory and experiment for the iron FT peak is an artefact of this.

3.5 ADSORPTION OF CADMIUM ON LEPIDOCROCITE

3.5.1 Crystallography and surface chemistry of lepidocrocite

The lepidocrocite crystal structure is dominated by (010) basal planes parallel to the constituent layers, with smaller (100) planes along the length of the crystallites, and (001) chain terminations (Fig. 3.2b) (e.g. Lewis and Farmer, 1986; Zhang et al. 1992). The (010) plane is populated by a single type of hydroxyl which is coordinated to two terminal iron atoms (Lewis and Farmer, 1986). These are analogous to **C**-type hydroxyls at the goethite surface. Consistent with the low reactivity of goethite **C**-type hydroxyls (Parfitt et al., 1975), the doubly coordinated hydroxyls on the lepidocrocite (010) surface were found to be unreactive towards phosphate (Lewis and Farmer, 1986) and various organic molecules (Bromley et al., 1994). The (100) planes along the sides of the crystallites are populated by triply coordinated oxide ions carrying an excess negative charge of -0.5 (analogous to **B**-type hydroxyls on goethite), and singly coordinated oxide ions carrying a charge of -1.5 (analogous to **A**-type hydroxyls on goethite) (Lewis and Farmer, 1986). The triply coordinated oxide ions are also unreactive to phosphate, whereas the singly

coordinated oxide ions have been invoked as reactive sites which participate in lepidocrocite dissolution (Cornell and Giovanoli, 1988). In their investigation of H^+, Fe^{2+}, and Al^{3+} adsorption on lepidocrocite, Zhang et al. (1992) proposed that both Fe^{2+} and Al^{3+} adsorbed at singly coordinated oxide/hydroxide sites. Although they did not suggest where these might be, it seems likely that the sites in question were located on the (100) surface (c.f., Lewis and Farmer, 1986).

3.5.2 EXAFS results and general discussion for cadmium adsorption on lepidocrocite

The EXAFS results for cadmium adsorbed on lepidocrocite over a range of surface loading and pH conditions are shown in Fig. 3.7 and summarised in Table 3.2. A first shell with approximately six oxygen atoms is present at a Cd-O distance of 2.25 - 2.26 Å, and there is statistical support for only one other atomic shell which contains 1.1 to 1.5 iron atoms (Table 3.2). In this case however, the iron shell is at a Cd-Fe distance of 3.26 - 3.30 Å rather than the 3.75 - 3.80 Å observed for goethite samples; the ~3.28 Å Cd-Fe distance is characteristic of edge sharing adsorption. Note that any observed mismatch between theory and experiment in the FT plots arises because the position of the experimental iron peak is not corrected for phase-shift effects, and does not imply a poor fit. This point is elaborated upon in section 3.3.

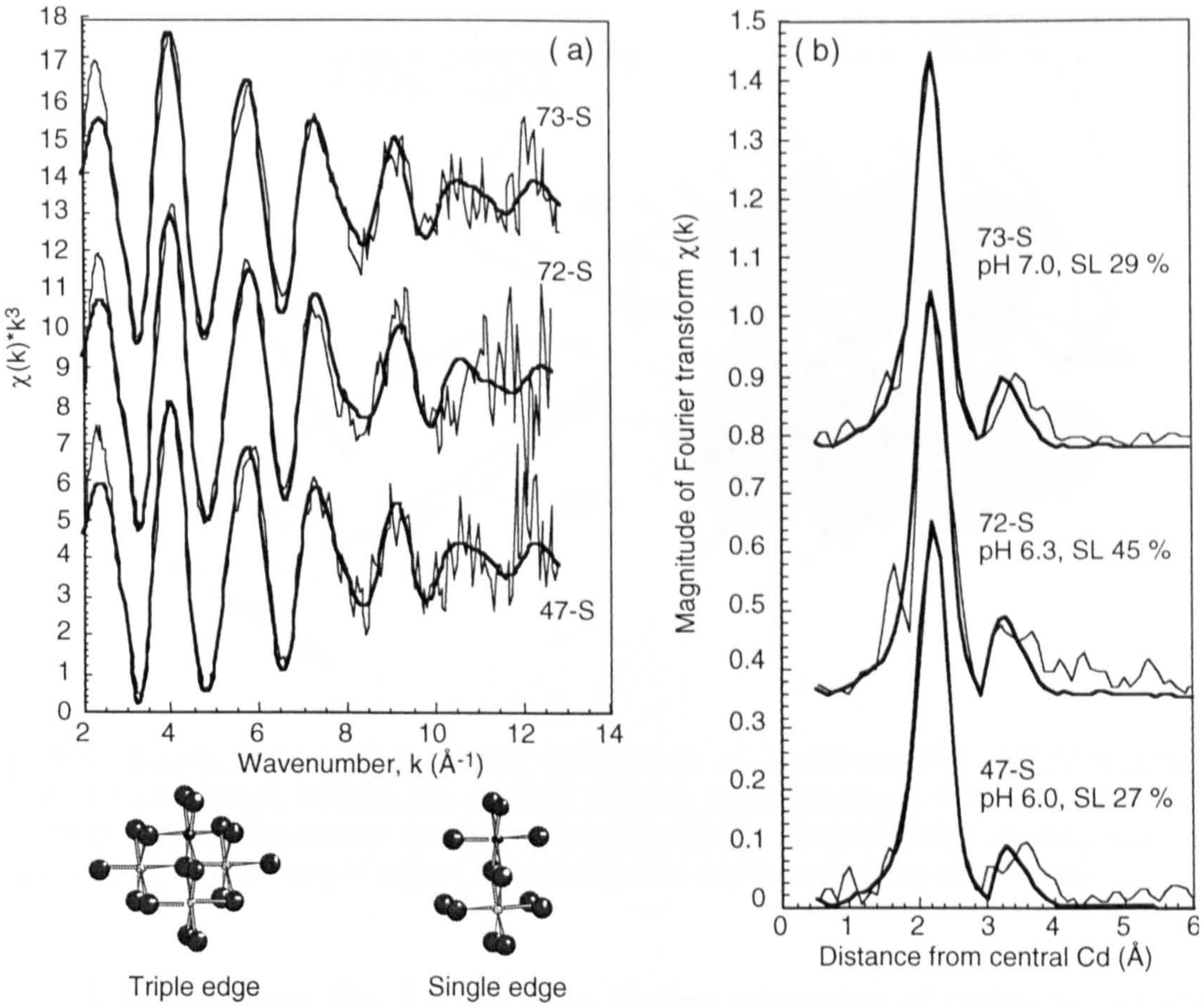

Fig. 3.7. EXAFS (a) and FT (b) plots of cadmium adsorption on lepidocrocite. SL stands for surface loading. The first peak in the FT plot represents the octahedral shell of oxygen atoms around adsorbed cadmium. Although two additional peaks within 4 Å can be seen in the FT plots, there is only statistical support for one additional atomic shell containing 1.1 - 1.5 iron atoms at ~ 3.3 Å. This Cd-Fe distance is characteristic of inner sphere adsorption *via* an edge sharing mechanism. Note that the position of the second peak in the FT plots has not been corrected for phase-shift effects; any apparent mismatch between theory and experiment for the iron FT peak is an artefact of this. The schematic diagrams show a cadmium aquo complex undergoing triple edge- (TE, left) and single edge- (SE, right) adsorption; the small darkly coloured balls represent cadmium in these diagrams.

It is noteworthy that another peak is present at 3.7 - 3.9 Å in the FT plots (Fig. 3.7b), and that its location is suggestive of a corner sharing iron shell. An attempt was made to insert a shell containing 2 iron atoms at 3.8 Å, but Joyner statistical tests (Joyner et al., 1987) provided no support for its presence. However, the sine transform (theory) and sine transform (experiment) curves as well as the Fourier transform (theory) and Fourier transform (experiment) curves from the EXAFS data (not shown) are in phase for the 3.7 - 3.9 Å peak in these samples. This can be taken as qualitative evidence that this peak is real, but that the level of noise in the data prevents its unambiguous identification. Changes in pH (6.0 - 7.0) and surface loading (27 % - 45 %) have no significant effect on the EXAFS results.

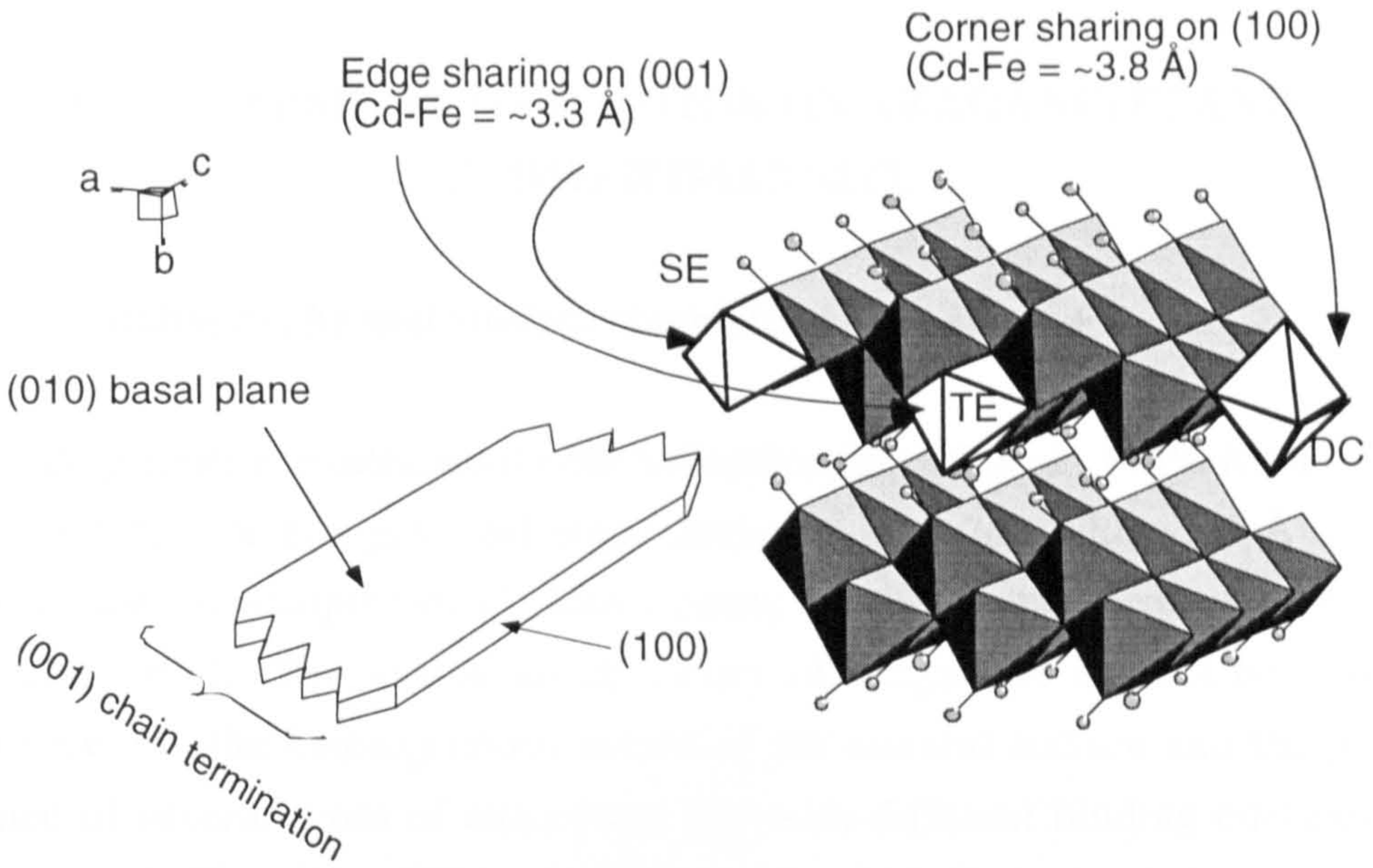

Fig. 3.8. Interpretation of cadmium adsorption on lepidocrocite. EXAFS results show that adsorption occurs *via* an edge sharing mechanism(s), whereas there is no statistical support for corner sharing adsorption (DC). Suitable edge sharing sites for single edge (SE) and triple edge (TE) adsorption are found at the crystal ends.

It is clear from Fig. 3.8 that edge sharing adsorption of cadmium can only occur at the ends of the lepidocrocite crystallites. Likely mechanisms are bidentate single edge (SE) sharing or triple edge (TE) sharing with coordination to four surface hydroxyl groups. These result in maximum possible iron coordination numbers of one and three, respectively. The observed iron coordination numbers (1.1 - 1.5) suggest that adsorption occurs *via* a mixture of the two mechanisms. It is not possible to estimate the contribution of each because of the ± 1 uncertainty associated with the coordination number values.

If corner sharing adsorption does occur at the lepidocrocite surface, it is most likely to take place on the (100) surfaces by double corner sharing between two singly coordinated oxide ions (Fig. 3.8). This mechanism is analogous to that proposed on the (110) and (100) surfaces of goethite. However, the fact that adsorption occurs preferentially at the edge sharing sites supports the idea that the edge- and corner sharing sites are the 'strong' and 'weak' sites of cadmium adsorption, respectively (c.f., Dzmobak and Morel, 1990).

The analysis of a lepidocrocite sample that was prepared in the absence of a swamping background electrolyte (47-S) confirmed that cadmium was inner spherically bound as there is no significant difference in the Cd-Fe distance observed in this sample relative to that from samples which were prepared with a 0.1 M background electrolyte (Fig. 3.7).

3.6. CADMIUM ADSORPTION ON AKAGANEITE AND SCHWERTMANNITE

3.6.1 Crystallography and surface chemistry of akaganeite

Akaganeite is isostructural with hollandite (Bernal et al., 1959; Keller, 1970). The crystallites are elongate and cigar-shaped (Fig. 3.2c), with ~5.0 Å diameter tunnels which are occupied by Cl^- ions running parallel to the needle axis (Post and Buchwald, 1991). The interfacial chemistry of akaganeite has not been studied extensively, but the heterogeneous nature of the mineral surface and the possible existence of several types of adsorption site with different binding energies have been reported (Kanungo, 1994a, b). It has also been suggested that trace metal sorption occurs on this mineral *via* relatively weak monodentate complexation or adsorption of hydrolytic species (MOH^+) in the β-plane, and that adsorption may even occur *via* an outer sphere mechanism (Kanungo, 1994a, b). Bidentate surface complexes $(Fe\text{-}(O,OH))_2\text{-}M$ were discounted because adsorption isotherms could not be adequately modelled when they were considered (Kanungo, 1994a, b). The results of Kanungo (1994a, b) were based on macroscopic observations with no consideration of bulk or surface crystal chemistry, and no attempt was made to identify the oxide or hydroxide groups which might be responsible for sorption.

3.6.2 Crystallography of schwertmannite

Schwertmannite is thought to be structurally similar to akaganeite, the main difference being the occupation of tunnel sites by SO_4^{2-} instead of Cl^- (Schwertmann and Cornell, 1991). This requires significant distortion of the unit cell, which results in poor crystal growth parallel to the needle axis and a characteristic spherical-ellipsoid morphology (Bigham et al., 1994). The authors are not aware of any investigations of the surface chemistry of schwertmannite or its ability to sorb cations.

3.6.3 EXAFS results and general discussion for cadmium adsorption on akaganeite and schwertmannite

Experimental conditions for cadmium adsorption on akaganeite (pH 8.0) and schwertmannite (pH 6.5) are given in Table 3.1. EXAFS results for these samples

are shown in Fig. 3.9 and summarised in Table 3.2. Note that any observed mismatch between theory and experiment in the FT plots arises because the position of the experimental iron peak is not corrected for phase-shift effects, and does not imply a poor fit. This point is elaborated upon in section 3.3.

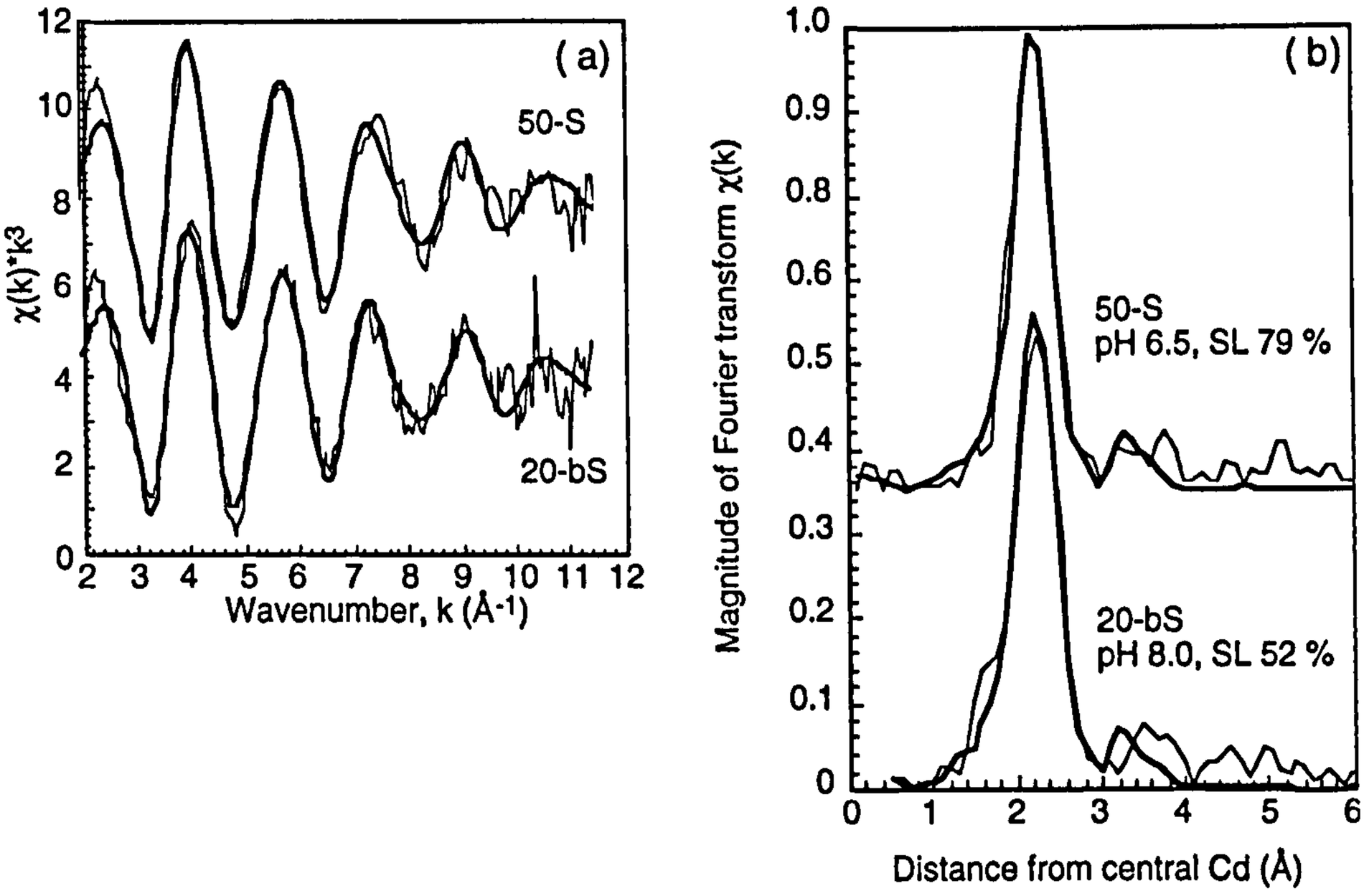

Fig. 3.9. EXAFS (a) and FT (b) plots for cadmium adsorption on akaganeite (20-bS) and schwertmannite (50-S). SL stands for surface loading. Because of ambiguity in the location of the iron coordination shell, all that can be concluded with certainty from these results is that cadmium adsorbs to akaganeite and schwertmannite *via* an inner sphere mechanism. The Cd-Fe separation would be > 4 Å if it were outer spherically bound. Note that the position of the second peak in the FT plots has not been corrected for phase-shift effects; any apparent mismatch between theory and experiment for the iron FT peak is an artefact of this.

For both akaganeite and schwertmannite, the first shell at 2.28 Å contains approximately six oxygen atoms. The FT plots suggest the presence of additional atomic shell(s) between 3.2 and 4.0 Å from the central cadmium atom. Joyner statistical tests (Joyner et al., 1987) show that the inclusion of a 3.3 Å (edge sharing) iron shell in the cadmium on akaganeite sample is justified at the 99 % level of confidence. However, the resulting match between theory and experiment in the FT plot is extremely poor, suggesting that this conclusion may not be entirely valid. An almost identical model describes the cadmium on schwertmannite sample, but there is no statistical support for the presence of the iron shell. However, the sine transform (theory) and sine transform (experiment) curves as well as the Fourier transform (theory) and Fourier transform (experiment) curves are in phase for the 3.3 Å peak in the schwertmannite sample. This can be taken as qualitative evidence that the 3.3 Å peak is real (Mosselmans, pers. comm.). The lack of statistical support for

the 3.3 Å iron shell may thus be a result of the poor experimental data quality for this sample, and this shell is only speculatively included in Table 3.2. The similarity in the results for akaganeite and schwertmannite is notable, and is consistent with the supposed structural similarity between these two minerals. Despite the ambiguity in the EXAFS results, it can be concluded that cadmium adsorbs to akaganeite and schwertmannite *via* an inner sphere mechanism. However, the exact mechanism of adsorption and the type of surface species involved is difficult to determine. These results are in contrast to cadmium sorption on cryptomelane, a manganese- oxide isostructural with both hollandite (Post et al., 1982) and akaganeite. Cryptomelane has been shown to sorb Cd^{2+} *via* ion exchange with H^+ at sites within its structural tunnels at low pH (2) (Chapter 4; Randall et al., 1998).

3.7 IMPLICATIONS OF RESULTS FROM EXAFS AND QUANTUM MECHANICAL MODELLING FOR SURFACE COMPLEXATION MODELS

The results presented here suggest that a single type of corner sharing surface complex is responsible for the vast majority of cadmium adsorption on goethite over the studied surface loading and pH ranges. A similar result follows for lepidocrocite, but the surface complex(es) responsible for the adsorption are of the edge sharing variety. This finding can be used to constrain surface complexation modelling of cadmium adsorption on these minerals to just one type of sorption complex. This assertion is supported by a recent study of the sorption of low concentration (~10^{-6} M) lead, cadmium, zinc and copper onto goethite, which found no support for the existence of 'high affinity' surface sites (Palmqvist et al., 1997). Indeed, Ainsworth et al. (1994) required only the optimised surface complexation constant for the 'low affinity' site rather than constants for both the 'low' and 'high' affinity sites to most effectively model cadmium, cobalt and lead adsorption by fresh hydrous ferric oxide (HFO) using Dzombak and Morel's (1990) diffuse-layer model. The surface complexation constant for the reaction proposed by Ainsworth et al. (1994) is:

$$Fe^wOH^0 + Cd^{2+} \leftrightarrow Fe^wOCd^+ + H^+; \qquad \log K_2^{int} = -1.82$$

Gunneriusson (1994) was also able to model cadmium adsorption on goethite assuming just one type of active surface site, although more than one type of surface complex was required to fit the data. The resulting surface complexation constants, evaluated according to the electrostatic constant capacitance model, are:

$$\equiv FeOH + Cd^{2+} \leftrightarrow \equiv FeOHCd^{2+}; \quad \log \beta^{s}_{0,1,1,0}(\text{int}) = 6.43 \pm 0.05$$

(this value was revised to 5.4 by Palmqvist et al. (1997))

$$\equiv FeOH + Cd^{2+} \leftrightarrow \equiv FeOCd^{+} + H^{+}; \quad \log \beta^{s}_{-1,1,1,0}(\text{int}) = -2.22 \pm 0.05$$

The similarity of the stability constants derived for the deprotonated surface complex on HFO (Ainsworth et al., 1994) and goethite (Gunneriusson, 1994), suggests that cadmium adsorbs to these minerals *via* very similar surface complexation reactions. This would be consistent with the short range structural similarities between HFO and goethite (Charlet and Manceau, 1993). Note that these values are in contrast to those proposed for cadmium adsorption on HFO by Dzombak and Morel (1990), whose diffuse-layer model supports the presence of two surface sites with distinctly different reactivities:

$$Fe^{strong}OH^{0} + Cd^{2+} \leftrightarrow Fe^{strong}OCd^{+} + H^{+}; \quad \log K_{1}^{int} = 0.47$$
$$Fe^{weak}OH^{0} + Cd^{2+} \leftrightarrow Fe^{weak}OCd^{+} + H^{+}; \quad \log K_{2}^{int} = -2.90$$

Thus, there is a lack of evidence for more than one adsorption site on goethite in both the EXAFS data presented here and the macroscopic observations of other workers. Consequently, I propose that the surface complexation constants describing single site adsorption are more accurate than those describing adsorption to two sites of differing affinity.

The use of a single type of adsorption mechanism is likely to become increasingly valid under conditions of competitive adsorption, since such conditions may prevent cadmium from occupying the most favourable sites at the iron oxyhydroxide surface. For instance, the presence of major groundwater/seawater ions in solution has been shown to significantly reduce the adsorption of cadmium and other heavy metals (e.g. Balistrieri and Murray, 1982; Cowan et al., 1991; Petersen et al., 1993; Naidu et al., 1994, Davis and Upadhyaya, 1996), and only a fraction of goethite surface sites are calculated to be 'free' in lakewater and seawater (Sigg and Stumm, 1980; Balistrieri and Murray, 1981). Furthermore, Kinniburgh et al. (1976) have shown that lead, copper, zinc and nickel all adsorb on ferrihydrite more strongly than cadmium. I propose that the EXAFS results reported here for samples with $\geq$ 24 % surface loading are highly applicable to understanding

cadmium adsorption in the presence of major groundwater ions and other heavy metals.

It is thought that the effects of competitive adsorption are best predicted with the use of constants derived from single element adsorption experiments rather than those derived from experiments where there is active competition (Cowan et al., 1991). Consequently, surface complexation constants for the competitive adsorption of cadmium with other ions are not presented.

The results for akaganeite and schwertmannite demonstrate that cadmium adsorbs to these minerals *via* inner sphere mechanism(s). However, these results are less definitive than those for goethite and lepidocrocite.

3.8 CONCLUSIONS

The EXAFS data presented in this paper show that cadmium adsorbs to goethite predominantly *via* a corner sharing mechanism at 'low affinity' sites on the dominant (110) surface. Density functional theory (DFT) calculations and consideration of the likely relative surface hydroxyl group reactivities strongly suggest that this adsorption is achieved by corner sharing with two **A**-type hydroxyls rather than one **C**-type hydroxyl. The EXAFS data provide no evidence for the edge sharing adsorption which previous studies and my quantum mechanical modelling indicate to be energetically favourable over corner sharing adsorption. I suggest that the goethite morphology precludes significant cadmium adsorption at edge sharing sites because these are only present on the crystal ends which are estimated to comprise only ~2 % of the total surface area. Consequently, it seems likely that cadmium adsorption on goethite could be adequately modelled by assuming that bonding occurs only by bidentate corner sharing adsorption. This will be especially true under conditions of moderate to high cadmium surface loading and/or when other competing ions are present in solution. I suggest that the single site surface complexation constants reported by Gunneriusson (1994) and partially revised by Palmqvist et al. (1997) are currently the most reliable for describing cadmium adsorption on goethite:

$$\equiv FeOH + Cd^{2+} \leftrightarrow \equiv FeOHCd^{2+}; \quad \log \beta^{s}_{0,1,1,0}(\text{int}) = 5.4$$

$$\equiv FeOH + Cd^{2+} \leftrightarrow \equiv FeOCd^{+} + H^{+}; \quad \log \beta^{s}_{-1,1,1,0}(\text{int}) = -2.22 \pm 0.05$$

By contrast, edge sharing mechanism(s) are responsible for the majority of cadmium adsorption on lepidocrocite. This mineral has a far greater proportion of edge sharing sites than goethite, and this result confirms the notion that cadmium is

preferentially adsorbed at 'high affinity' edge sharing- rather than 'low affinity' corner sharing sites at the surface of iron oxyhydroxide minerals. The overall mechanism of cadmium adsorption on goethite and lepidocrocite appears to be insensitive to changes in pH and surface loading.

Finally, it has been shown that akaganeite and schwertmannite are capable of sorbing significant amounts of cadmium from solution. Whilst it can be said that this adsorption occurs *via* inner sphere bonding, it has not been possible to unambiguously assign definite adsorption mechanism(s).

The results presented here will assist the modelling of cadmium sorption data and consequently result in improved accuracy of the related thermodynamic data. This should increase our ability to predict and understand the risks posed by cadmium contamination in the natural environment.

3.9 REFERENCES

Ainsworth C. C., Pilon J. L., Gassman P. L. and Van Der Sluys W. G. (1994) Cobalt, cadmium and lead sorption to hydrous iron oxide: Residence time effect. *Soil Sci. Soc. Am. J.* **58**, 1615-1623.

Alagha M. R., Burley S. D., Curtis C. D., and Esson J. (1995) Complex cementation textures and authigenic mineral assemblages in recent concretions from the Lincolnshire Wash (East coast, U.K.) driven by Fe(0) to Fe(II) oxidation. *J. Geol. Soc.* **152**, 157-171.

Amouric M., Baronett A., Nahon D., and Didier P. (1986) Electron microscopic investigations of iron oxyhydroxides and accompanying phases in lateritic iron crust pisolites. *Clays Clay Mineral.* **34**, 45-52.

Atkinson R. J., Posner A. M., and Quirk J. P. (1967) Adsorption of potential-determining ions at the ferric oxide-aqueous interface. *J. Phys. Chem.* **71**, 550-558.

Balistrieri L. S. and Murray J. W. (1981) The surface chemistry of goethite (α-FeOOH) in major ion seawater. *Am. J. Sci.* **281**, 788-806.

Balistrieri L. S. and Murray J. W. (1982) The adsorption of Cu, Pb, Zn, and Cd on goethite from major ion seawater. *Geochim. Cosmochim. Acta* **46**, 1253-1265.

Becke A. D. (1988) Density-functional exchange-energy approximation with correct asymptotic-behaviour. *Phys. Rev. A* **38**, 3098-3100.

Benjamin M. M. and Leckie J. O. (1981a) Multiple-site adsorption of Cd, Cu, Zn, and Pb on amorphous iron oxyhydroxide. *J. Colloid Interface Sci.* **79**, 209-221.

Benjamin M. M. and Leckie J. O. (1981b) Competitive adsorption of Cd, Cu, Zn, and Pb on amorphous iron oxyhydroxide. *J. Coll. Inter. Sci.* **83**, 410-419.

Bernal J. D., Dasgupta D. R., and MacKay A. L. (1959) The oxides and hydroxides of iron and their structural interrelationships. *Clay Min. Bull.* **4**, 15-30.

Bigham J. M., Carlson L., and Murad E. (1994) Schwertmannite, a new iron oxyhydroxysulphate from Pyhasalmi, Finland, and other localities. *Min. Mag.* **58**, 641-648.

Binsted N., Campbell J. W., Gurman S. J., and Stephenson P. C. (1991) *SERC Daresbury Laboratory EXCURV92 program.* Daresbury Laboratory, Warrington, U.K.

Binsted N., Strange R. W., and Hasnain S. S. (1992) Restrained refinement. *Biochemistry* **31**, 12117-12125.

Bromley L. A., Buckley A. M., Chlad M., Davey R. J., Drewe S., and Finlan G. T. (1994) Interactions at the inorganic-organic interface - discriminatory binding of

hydroxybenzenes by lepidocrocite surfaces. *J. Colloid Interface Sci.* **164**, 498-502.

Brown G. E. Jr., Calas G., Waychunas G. A., and Petiau J. (1988) X-ray absorption spectroscopy and its applications in mineralogy and geochemistry. In *Spectroscopic Methods in Mineralogy and Geology* (ed. F. Hawthorne). Reviews in Mineralogy Vol. 18, pp. 431-512. Min. Soc. Am.

Brown G. E. Jr., Parks G. A., and O'Day P. A. (1995) Sorption at the mineral-water interface: macroscopic and microscopic perspectives. In *Mineral Surfaces* (eds. D. J. Vaughan and R. A. D Pattrick). pp. 129-183. Chapman and Hall.

Charlet L. and Manceau A. (1993) Structure, formation, and reactivity of hydrous oxide particles: Insights from X-ray absorption spectroscopy. In *Environmental Particles* (eds. J. Buffle and H. P. van Leeuwen). Environmental Analytical and Physical Chemistry Series Vol. 2, pp. 117-164. Lewis Publishers.

Chen J. C. and Yao Y. C. (1995) Geochemistry of manganese nodules from offshore areas of Mariana Islands and Johnston Island. *J. Southeast Asian Earth Sci.* **11**, 61-70.

Collins C.R., Ragnarsdottir K.V., and Sherman D.M. Effect of inorganic and organic ligands on the adsorption of Cd^{2+} to goethite. *Geochim. Cosmochim. Acta.* (submitted).

Combes J. M., Manceau A., Calas G., and Bottero J. Y. (1989) Formation of ferric oxides from aqueous solutions: A polyhedral approach by X-ray absorption spectroscopy: I. Hydrolysis and formation of ferric gels. *Geochim. Cosmochim. Acta* **53**, 583-594.

Cornell R. M. and Giovanoli R. (1988) Acid dissolution of akaganeite and lepidocrocite - the effect on crystal morphology. *Clays Clay Mineral.* **36**, 385-390.

Cornell R. M., Posner A. M., and Quirk J. P. (1974) Crystal morphology and the dissolution of goethite. *J. Inorg. Nucl. Chemistry* **36**, 1937-1946.

Coston J. A., Fuller C. C., and Davis J. A. (1995) Pb^{2+} and Zn^{2+} adsorption by a natural Al- and Fe-bearing surface coating on an aquifer sand. *Geochim. Cosmochim. Acta.* **59**, 3535-3547.

Cowan C. E., Zachara J. M., and Resch C. T. (1991) Cadmium adsorption on iron oxides in the presence of alkaline earth metals. *Environ. Sci. Technol.* **25**, 437-446.

Davis J. A. and Leckie J. O. (1978) Surface ionization and complexation at the oxide/water interface. 2. Surface properties of amorphous iron oxyhydroxide and adsorption of metal ions. *J. Colloid Interface Sci.* **67**, 90-105.

Davis J. A. and Kent D. B. (1990) Surface complexation modelling in aqueous geochemistry. In *Mineral-Water Interface Geochemistry* (eds. M. F. Hochella and A. F. White). Reviews in Mineralogy Vol. 23, pp. 177-260. Min. Soc. Am.

Davis A. P. and Upadhyaya M. (1996) Desorption of cadmium from goethite (alpha-FeOOH). *Water Research* **30**, 1894-1904.

Dent A. J. and Mosselmans J. F. W. (1992) *A guide to EXBACK, EXCALIB, and EXCURV92.* Daresbury Laboratory, Warrington, U.K.

Dzombak D. A. and Morel F. M. M. (1990) *Surface Complexation Modelling: Hydrous Ferric Oxide.* John Wiley and Sons.

Fendorf S. E., LaForce M. J., Li G. C., and Patterson R. R. (1997) Pulsed-flow kinetic analysis of solid-phase transformations in mineral suspensions using XANES spectroscopy: Oxidation of FeS to γ-FeOOH. *Abstr. Amer. Chem. Soc.* **214**, 34-GEOC (abstr.).

Fokkink L. G. J., Dekeizer A., and Lyklema J. (1990) Temperature dependence of cadmium adsorption on oxides. 1. Experimental observations and model analysis. *J. Colloid Interface Sci.* **135**, 118-131.

Fortin, D., Leppard, G. G., and Tessier, A. (1993) Characteristics of lacustrine diagenetic iron oxyhydroxides. *Geochim. Cosmochim. Acta* **57**, 4391-4404.

Gibbs R. J. (1977) Transport phases of transition metals in the Amazon and Yukon rivers. *Geol. Soc. Amer. Bull.* **88**, 829-843.

Gunneriusson L. (1994) Composition and stability of Cd(II)-chloro and Cd(II)-hydroxo complexes at the goethite (α-FeOOH)/water interface. *J. Colloid Interface Sci.* **163**, 484-492.

Gurman S. J. (1988) The small atom approximation theory. *J. Phys. C: Solid State Phys.* **21**, 3699-3717.

Gurman S. J., Binsted N., and Ross I. (1984) Single scattering rapid curved wave theory. *J. Phys. C: Solid State Phys.* **17**, 143-151.

Gurman S. J., Binsted N., and Ross I. (1986) Multiple scattering rapid curved wave theory. *J. Phys. C: Solid State Phys.* **19**, 1845-1861.

Hayes K. F. and Leckie J. O. (1987) Modeling ionic strength effects on cation adsorption at hydrous iron oxide/solution interfaces *J. Colloid Interface Sci.* **115**, 564-572.

Hayes K. F., Redden G., Ela W., and Leckie J. O. (1991) Surface complexation models: An evaluation of model parameter estimations using FITEQL and oxide mineral titration data. *J. Colloid Interface Sci.* **142**, 448-469.

Hedin L. and Lundqvist S. (1969) Effects of electron-electron and electron-phonon interactions on the one-electron states of solids. *Solid State Phys.* **23**, 1-181.

Hem, J. D. (1972) Chemistry and occurrence of cadmium and zinc in surface water and groundwater. *Water Resources Res.* **8**, 661-679.

Herbert R. B. (1994) Metal transport in groundwater contaminated by acid-mine drainage. *Nordic Hydrology* **25**, 193-212.

Herbert R. B. (1995) Precipitation of Fe oxyhydroxides and jarosite from acidic groundwater. *GFF* **117**, 81-85.

Hiemstra T. and Van Riemsdijk W. H. (1996) A surface structural approach to ion adsorption: The charge distribution (CD) model. *J. Colloid Interface Sci.* **179**, 488-508.

Hiemstra T., van Riemsdijk W. H., and Bolt G. H. (1989a) Multisite proton adsorption modelling at the solid/solution interface of (hydr)oxides: A new approach. I. Model description and evaluation of intrinsic reaction constants. *J. Colloid Interf. Sci.* **133**, 91-104.

Hiemstra T., De Wit J. C. M., and van Riemsdijk W. H. (1989b) Multisite proton adsorption modelling at the solid/solution interface of (hydr)oxides: A new approach. II. Application to various important (hydr)oxides. *J. Colloid Interf. Sci.* **133**, 105-117.

Hiller D. A. and Brummer G. W. (1995) Electron microprobe studies on soil samples with varying heavy metal contamination. 1. Methods and analysis of elements in pedogenic oxides. *Zeitschrift Fur Pflanzenernahrung Und Bodenkunde* **158**, 147-156.

Holm N. G., Dowler M. J., Wadsten T., and Arrhenius G. (1983) β-FeOOH·Cl_n (akaganéite) and Fe1-xO (wüstite) in hot brine from the Atlantis II Deep (Red Sea) and the uptake of amino acids by synthetic β-FeOOH·Cl_n. *Geochim. Cosmochim. Acta* **47**, 1465-1470.

Hutchinson T. C. and Meema K. A. (eds.) (1987) *Lead, Cadmium, Mercury and Arsenic in the Environment*. John Wiley and Sons.

Jin T. Y., Lu J. and Nordberg M. (1998) Toxicokinetics and biochemistry of cadmium with special emphasis on the role of metallothionein. Neurotoxicology **19**, 529-535.

Johnson B. B. (1990) Effect of pH, temperature, and concentration on the adsorption of cadmium on goethite. *Env. Sci. Technol.* **24**, 112-118.

Johnson C. A. (1986) The regulation of trace element concentrations in river and estuarine waters contaminated with acid mine drainage; the adsorption of Cu and Zn on amorphous Fe oxyhydroxides. *Geochim. Cosmochim. Acta.* **50**, 2433-2438.

Joyner R. W., Martin K. J., and Meehan. P. (1987) Some applications of statistical tests in analysis of EXAFS and SEXAFS data. *J. Phys. C: Solid State Phys.* **20**, 4005-4012.

Kanungo S. B. (1994a) Adsorption of cations on hydrous oxides of iron. I. Interfacial behaviour of amorphous FeOOH and β-FeOOH (akaganeite) in different electrolyte solutions. *J. Colloid. Interf. Sci.* **162**, 86-92.

Kanungo S. B. (1994b) Adsorption of Cations on Hydrous Oxides of Iron. III. Adsorption of Mn, Co, Ni, and Zn on β-FeOOH from simple electrolyte solutions as well as from a complex electrolyte solution resembling seawater in major ion content. *J. Colloid. Interf. Sci.* **162**, 103-109.

Karathanasis A. D. and Thompson Y. L. (1995) Mineralogy of iron precipitates in a constructed acid-mine drainage wetland. *Soil Sci. Soc. Amer. J.* **59**, 1773-1781.

Keller P. (1970) Eigenschaften von $(Cl,F,OH)_{<2}Fe_8(O,OH)_{16}$ und akaganéite. *Neues Jahrbuch für Mineralogie Abhandlungen* **113**, 29-49.

Kinniburgh D. G., Jackson M. L., and Syers J. K. (1976) Adsorption of alkaline earth, transition, and heavy metal cations by hydrous oxide gels of iron and aluminium. *Soil Sci. Am. J.* **40**, 796-799.

Krauskopf K. B. (1956) Factors controlling the concentrations of thirteen rare metals in seawater. *Geochim. Cosmochim. Acta* **9**, 1-32B.

Krishna Murti C. R., Olade M. A., and Page A. L. (1987) Group Report: CadmiumIn *Lead, cadmium, mercury and arsenic in the environment* (eds. T. C. Hutchinson and K. A. Meema). pp. 35-41. John Wiley and Sons Ltd.

Lamy I., Djafer M., and Terce M. (1991) Influence of oxalic acid on the adsorption of Cd at the goethite surface. *Water, Air, Soil Poll.* **57-58**, 457-465.

Leckie J. O., Benjamin M. M., Hayes K. F., Kaufman G., and Altmann S. (1980) Adsorption/coprecipitation of trace elements from water with iron oxyhydroxide. *Elect. Pow. Res. Inst. Rept.* **CS-1513**.

Lehoczky E., Szabo L., Horvath S., Marth P. and Szabados I. (1998) Cadmium uptake by lettuce in different soils. *Comm. In Soil Sci. and Plant Anal.* **29**, 1903-1912.

Le Riche H. H. and Weir A. H. (1963) A method of studying trace elements in soil fractions. *J. Soil. Sci.* **14**, 225-235.

Lewis D. G. and Farmer V. C. (1986) Infrared absorption of surface hydroxyl groups and lattice vibrations in lepidocrocite (γ-FeOOH) and boehemite (γ-AlOOH). *Clay Minerals* **21**, 93-100.

Lin Z. X. and Herbert R. B. (1997) Heavy metal retention in secondary precipitates from a mine rock dump and underlying soil, Dalarna, Sweden. *Environ. Geol.* **33**, 1-12.

Lion L. W., Altmann R. S., and Leckie J. O. (1982) Trace metal adsorption characteristics of estuarine particulate matter: Evaluation of the contribution of Fe/Mn and organic surface coatings. *Env. Sci. Technol.* **16**, 660-666.

Lövgren L., Sjöberg S. and Schindler P. W. (1990) Acid/base reactions and Al(III) complexation at the surface of goethite. *Geochim. Cosmochim. Acta* **54**, 1301-1306.

Lumsdon D. G. and Evans L. J. (1994) Surface complexation model parameters for goethite (α-FeOOH). J. Colloid Interface Sci. **164**, 119-125.

Mann S., Cornell R. M., and Schwertmann U. (1985) The influence of aluminium on iron oxides: XII. High-resolution transmission electron microscopic (HRTEM) study of aluminous goethites. *Clay Minerals* **20**, 255-262.

Millward G. E. (1980) The adsorption of cadmium by iron (III) precipitates in model estuarine solutions. *Environ. Technol. Lett.* **1**, 394-399.

Naidu R., Bolan N. S., Kookana R. S., and Tiller K. G. (1994) Ionic strength and pH effects on the sorption of cadmium and the surface charge of soils. *European J. Soil Sci.* **45**, 419-429.

Nriagu J. O. (1980) Cadmium in the atmosphere and in precipitation. In *Cadmium in the Environment Part 1, Ecological Cycling* (ed. J. O. Nriagu). pp. 71-114. John Wiley and Sons.

O'Day P. A., Brown G. E. Jr., and Parks G. A. (1994) X-ray absorption spectroscopy of Co(II) multinuclear surface complexes and surface precipitates on kaolinite. *J. Colloid Interface Sci.* **165**, 269-289.

Palmqvist U., Ahlberg E., Lövgren L., and Sjöberg S. (1997) In situ voltammetric determinations of metal ions in goethite suspensions: Single metal ion systems. *J. Colloid Interface Sci.* **196**, 254-266.

Papelis C., Brown G. E. Jr., Parks G. A., and Leckie J. O. (1995) X-ray absorption spectroscopic studies of cadmium and selenite adsorption on aluminium oxides. *Langmuir* **11**, 2041-2048.

Parfitt R. L. and Russel J. D. (1977) Adsorption on hydrous oxides. IV. Mechanisms of adsorption of various ions on goethite. *J. Soil Sci.* **28**, 297-305.

Parfitt R. L., Russell J. D., and Farmer V. C. (1975) Confirmation of the surface structures of goethite (α-FeOOH) and phosphated goethite by infrared spectroscopy. *J. Chem. Soc. Fara. Trans. I.* **72**, 1082-1087.

Parfitt R. L., Fraser A. R., and Farmer V. C. (1977) Adsorption on hydrous oxides. III. Fulvic acid and humic acid on goethite, gibbsite, and imogolite. *J. Soil Sci.* **128**, 245-257.

Parida K. M., Gorai B., Das N. N., and Rao S. B. (1997) Studies on ferric oxide hydroxides. 3. Adsorption of selenite (SeO_3^{2-}) on different forms of iron oxyhydroxides. *J. Colloid Interface Sci.* **185**, 355-362.

Perdew J. P. (1986) Density-functional approximation for the correlation energy of the inhomogeneous electron gas. *Phys. Rev. B* **33**, 8822-8824.

Petersen W., Wallmann K., Schroer S., and Schroeder F. (1993) Studies on the adsorption of cadmium on hydrous iron(III) oxides in oxic sediments. *Analytica Chimica Acta* **273**, 323-327.

Pivovarov S. (1997) Surface structure and site density of the oxide-solution interface*J. Colloid Interface Sci.* **196**, 321-323.

Post J. E. and Buchwald V. F. (1991) Crystal structure refinement of akaganeite. *Amer. Mineral.* **76**, 272-277.

Post J. E., Von Dreele R. B., and Buseck P. R. (1982) Symmetry and cation displacements in hollandites: Structure refinements of hollandite, cryptomelane, and priderite. *Acta Crystallogr.* **B38**, 1056-1065.

Pye K. (1988) An occurrence of akaganeite (β-FeOOH·Cl) in recent oxidised carbonate concretions, Norfolk, England. *Min. Mag.* **52**, 125-126.

Randall S. R., Sherman D. M., and Ragnarsdottir K. V. (1998) An EXAFS investigation of cadmium sorption on cryptomelane (KMn_8O_{16}). *Chem. Geol.* **151**, 95-106.

Roe A. L., Hayes K. F., Chisholm-Brause C. J., Brown G. E. Jr., Parks G. A., Hodgson K. O., and Leckie J. O. (1991) In situ X-ray absorption study of lead ion surface complexes at the goethite-water interface. *Langmuir* **7**, 367-373.

Ross G. J. and Wang C. (1982) Lepidocrocite in a calcareous, well-drained soil. *Clays Clay Mineral.* **30**, 394-396.

Russell J. D., Parfitt R. L., Fraser A. R., and Farmer V. C. (1974) Surface structures of gibbsite, goethite, and phosphated goethite. *Nature* **248**, 220-221.

Russell J. D., Paterson E., Fraser A. R., and Farmer V. C. (1975) Adsorption of carbon dioxide on goethite (α-FeOOH) surfaces, and its implications for anion adsorption. *J. Chem. Soc. Faraday Trans.* **71**, 1623-1630.

Schwertmann U. (1984) The influence of aluminium on iron oxides: IX. Dissolution of Al-goethites in 6M HCl. *Clay Minerals* **19**, 9-19.

Schwertmann U. and Taylor R. M. (1972) The transformation of lepidocrocite to goethite. *Clays. Clay Mineral.* **20**, 151-158.

Schwertmann U. and Cornell R. M. (1991) *Iron oxides in the laboratory: Preparation and characterization.* VCH Publishers.

Schwertmann U. and Fechter H. (1994) The formation of green rust and its transformation to lepidocrocite. *Clay Min.* **29**, 87-92.

Schwertmann U., Bigham J. M., and Murad E. (1995) The 1st occurrence of schwertmannite in a natural stream environment. *European J. Mineral.* **7**, 547-552.

Shiller A. M. and Boyle E. A. (1987) Variability of dissolved trace metals in the Mississippi River. *Geochim. Cosmochim. Acta* **51**, 3273-3277.

Sigg L. and Stumm W. (1981) The interaction of anions and weak acids with the hydrous geothite (α-FeOOH) surface. Colloids and Surfaces **2**, 101-117.

Singh S. K. and Subramanian V. (1984) Hydrous Fe and Mn oxides - Scavengers of heavy metals in the aquatic environment. CRC Crit. Rev. Environ. Control 14. 33-90.

Smith K. L. and Eggleton R. A. (1983) Botryoidal goethite: A transmission electron microscope study. *Clays Clay Mineral.* **31**, 392-396.

Spadini L., Manceau A., Schindler P. W., and Charlet L. (1994) Structure and stability of Cd^{2+} surface complexes on ferric oxides. 1. Results from EXAFS spectroscopy. *J. Colloid Interface Sci.* **168**, 73-86.

Spark K. M., Johnson B. B. and Wells J. D. (1995) Characterizing heavy-metal adsorption on oxides and oxyhydroxides. European J. Soil Sci. **46**, 621-631.

Taylor R. M. and McKenzie R. M. (1966) The association of trace elements with manganese minerals in Australian soils. *Aust. J. Soil Res.* **4**, 29-39.

Tessier A., Rapin F., and Carignan R. (1985) Trace metals in oxic lake sediments; possible adsorption onto iron oxyhydroxides. *Geochim. Cosmochim. Acta.* **49**, 183-194.

Tessier A., Fortin D., Belzile N., DeVitre R. R., and Leppard G. G. (1996) Metal sorption to diagenetic iron and manganese oxyhydroxides and associated organic-matter - narrowing the gap between field and laboratory measurements. *Geochim. Cosmochim. Acta* **60**, 387-404.

te Velde G. (1995) Amsterdam Density Functional 2.0.1, Users Guide, Vrije Universiteit, Amsterdam.

Tiller K. G. (1989) Heavy metals in soils and their environmental significance. In *Advances in Soil Science* Vol. 9 (ed. B. A. Stewart). pp. 113-142.

Van Geen A., Robertson A. P., and Leckie J. O. (1994) Complexation of carbonate species at the goethite surface: Implications for adsorption of metal ions in natural waters. *Geochim. Cosmochim. Acta* **58**, 2073-2086.

Venema P., Hiemstra T., and Van Riemsdijk W. H. (1996a) Comparison of different site binding models for cation sorption: description of pH dependency, salt dependency, and cation-proton exchange. *J. Colloid Interface Sci.* **181**, 45-59.

Venema P., Hiemstra T., and Van Riemsdijk W. H. (1996b) Multisite adsorption of cadmium on goethite. *J. Colloid Interface Sci.* **183**, 515-527.

Vosko S. H., Wilk L., and Nusair M. (1980) Accurate spin-dependent electron liquid correlation energies for local spin density calculations: a critical analysis. *Canadian J. Phys.* **58**, 1200-1204.

Walder I. F. and Chavez W. X. (1995) Mineralogical and geochemical behavior of mill tailing material produced from lead-zinc skarn mineralization, Hanover, Grant County, New Mexico, U.S.A. *Environ. Geol.* **26**, 1-18.

Wang H. D., White G. N., Turner F. T. and Dixon J. B. (1993) Ferrihydrite, lepidocrocite, and goethite in coatings from East Texas vertic soils. *Soil Sci. Soc. Am. J.* **57**, 1381-1386.

Waychunas G. A., Rea B. A., Fuller C. C., and Davis J. A. (1993) Surface chemistry of ferrihydrite. 1. EXAFS studies of the geometry of coprecipitated and adsorbed arsenate. *Geochim. Cosmochim. Acta* **57**, 2251-2269.

Waychunas G. A., Davis J. A., and Fuller C. C. (1995) Geometry of sorbed arsenate on ferrihydrite and crystalline FeOOH: Re-evaluation of EXAFS results and topological factors in predicting sorbate geometry, and evidence for monodentate complexes. *Geochim. Cosmochim. Acta* **59**, 3655-3661.

Zhang Y, Charlet L., and Schindler P. W. (1992) Adsorption of protons, Fe(II), and Al(III) on lepidocrocite (γ-FeOOH). *Colloids and Surfaces* **63**, 259-268.

Zhuang Y. Y., Allen H. E., and Fu G. M. (1994) Effect of aeration of sediment on cadmium-binding. *Environ. Toxicol. Chem.* **13**, 717-724.

Chapter 4

An EXAFS Investigation of Cadmium Sorption on Cryptomelane (KMn_8O_{16})

4.1 INTRODUCTION

Cadmium is a toxic heavy metal which has become a significant contaminant in many soils and aquifers. Its mobility in the environment is known to be strongly inhibited by sorption on Fe and Mn (hydr)oxides (e.g., Krauskopf, 1956; Singh and Subramian, 1984; Shiller and Boyle, 1987). Mn oxide minerals exist in many different forms in nature, ranging from the sheet structures of birnessite and buserite to the tunnel structures of hollandite and todorokite (Potter and Rossman, 1979; Golden et al., 1987; Manceau and Combes, 1988). Interconversions between the different forms are possible, providing an important feature of this class of compound (Giovanoli, 1976). Mn oxides are often associated with large amounts of iron. They occur widely as poorly crystalline dark brown to black segregations on the surfaces of solid particles, in cracks or veins, or in the form of nodules (Greenland and Hayes, 1983). Although they usually comprise only a minor constituent of the bulk, they can have a considerable effect on some soil properties (McKenzie, 1972) because they have large reactive surface areas and participate in both adsorption (e.g. Gadde and Laitinen, 1974) and ion exchange (e.g. Golden et al., 1986) reactions. Mn oxides tend to have lower pH of zero point of charge (pH_{ZPC}) values (~pH 2 - 4) than iron (hydr)oxide minerals (~pH 6 - 9) (Healey et al., 1966; McKenzie, 1981), and are consequently capable of adsorbing cations under relatively low pH conditions (Gadde and Laitinen, 1974; McKenzie, 1989). Many trace metals (Ni, Mo, Cr, Co, V, Cu and Zn) in soils are known to be strongly associated with Mn oxides (Burns, 1976; Crowther et al., 1983), and thus these minerals are clearly important in the regulation of soil toxicity and the bioavailability of essential nutrients (Adams et al., 1969). The minerals themselves can be an important source of nutrient Mn, but can also contribute to Mn toxicity in many plants under waterlogged or extremely acidic conditions (Golden et al., 1986).

In an extensive survey Chukhrov and Gorshkov (1981) found that the most commonly occurring Mn mineral in soil profiles was vernadite (δ-MnO_2), followed by birnessite ($(Na,Ca,K)Mn_7O_{14}\cdot 3H_2O$), cryptomelane, ($KMn_8O_{16}$), todorokite, ($(Ca,Na,K)(Mg,Mn^{2+})Mn_5O_{12}\cdot xH_2O$) and hausmannite ($Mn_3O_4$). Cryptomelane is known to be the major Mn oxide in certain lateritic weathering profiles (Parc et al., 1989; Ostwald, 1992; Vasconcelos et al., 1994; Ruffet et al., 1996), where it

commonly forms by authigenic precipitation (Vasconcelos et al., 1994). The presence of cryptomelane is documented in weathered ultramafic rocks (Llorca and Monchoux, 1991). It has also been identified as an important vein and/or fracture-lining Mn mineral in volcanic tuffs (such as that at the proposed Yucca Mountain high-level nuclear waste repository) (Carlos et al., 1993), in rocks surrounding granites (Nakashima and Imaoka, 1991), and in fault zones and related karsts in marbles (Nimfopoulos and Pattrick, 1991). The K-bearing nature of Mn oxides such as cryptomelane has been exploited in dating the progression of oxidation fronts during weathering and pedogenic processes using K-Ar and $^{40}Ar/^{39}Ar$ dating methods (Vasconcelos et al., 1992, 1994; Lippolt and Hautmann, 1995; Dammer et al., 1996; Ruffet et al., 1996; Henocque et al., 1997).

Cryptomelane has the hollandite structure (see below), in which there are ~4.6 Å tunnels (Vicat et al., 1986). In natural cryptomelane the tunnel sites are occupied primarily by K^+, although variable amounts of other cations (commonly Sr^{2+}, Ba^{2+}, Na^+, Pb^{2+}) and water are also present (Post et al., 1982). The tunnel sites in isomorphous minerals are primarily occupied by Ba^{2+} (hollandite), and Pb^{2+} or Na^+ (coronadite and manjiroïte, respectively) (Post et al., 1982).

A number of studies have been performed to investigate the sorption of alkali and alkaline earth cations (Tsuji and Abe, 1985; Tsuji and Komarneni, 1993b; Feng et al., 1995) and transition metals (McKenzie, 1970, 1980; Tsuji and Komarneni, 1993a) on cryptomelane. However, with the exception of McKenzie (1971, 1980), these studies have all utilised the H^+-form of cryptomelane (generated by washing the K^+-form with nitric acid) since it has a higher exchange capacity than the K^+ form. The results from the alkali and alkaline earth studies show charge balancing ion exchange of metals for H^+ (Tsuji and Abe, 1985) and changes in the cryptomelane lattice parameters (Tsuji and Komarneni, 1993b; Feng et al., 1995) that are consistent with ion exchange within the tunnels. This ion exchange displays a selectivity for cations with an effective ionic radius of ~1.4 Å (Tsuji and Abe, 1985; Tsuji and Komarneni, 1993a; Feng et al., 1995). Such selectivity has been invoked by Tsuji and Komarneni (1993a) as evidence that several divalent transition metal ions (Pb, Mn, Co, Cu, Hg, Cd, Zn, Ni) are sorbed within the tunnels of H^+-cryptomelane (via charge balancing ion exchange with H^+). The selective ion exchange properties of cryptomelane have proved useful, and the application of this material as an ionic sieve has been demonstrated by several workers (Tsuji and Abe, 1985; Bilewicz and Fuks, 1993; Elabsy et al., 1993; Elnaggar et al., 1993; Tsuji and Komarneni, 1993a). The sorption of Co^{2+} from seawater and tapwater onto H^+-cryptomelane is shown to result in a drop in supernate pH (Tsuji and Komarneni, 1993a), whilst sorption of Cu on the K^+-cryptomelane (McKenzie, 1970) is reported

to lead to an initial release of K to solution (although the majority of this is subsequently readsorbed).

The aim of this study was to investigate the interaction of aqueous Cd^{2+} with the K^+ form of cryptomelane. I found that this mineral was able to sorb up to two thirds of the available Cd^{2+} from solution at pH as low as 2.0. The uptake of such a large amount of Cd^{2+} at very low pH was unexpected, given the fact that the pH_{ZPC} of this material is reported to be 4.5 ± 0.5 (Healey et al., 1966). I felt that Cd^{2+} sorption by ion exchange at tunnel sites rather than adsorption on the amphoteric external surface of cryptomelane might explain some of this unexpected sorption capacity. Extended X-ray Absorption Fine Structure (EXAFS) spectroscopy was used to determine the local coordination environment of sorbed Cd, and thus identify its location and speciation on or within the cryptomelane structure. EXAFS has previously been successfully applied to the determination of metal coordination in other Mn minerals (e.g., Manceau et al., 1987, 1990, 1992). However, it has never before been used to identify the location of metals sorbed onto a mineral with the hollandite structure. The results presented here clarify the mechanism by which cryptomelane sorbs Cd at low pH, and have implications for the mobility of Cd in the environment and for the use of cryptomelane in K-Ar dating techniques.

4.2 THE STRUCTURE OF CRYPTOMELANE

The hollandite type structure was first solved by Byström and Byström (1950), and has subsequently been further refined by a number of workers (Cadée and Verschoor, 1978; Sinclair et al., 1980; Post et al., 1982; Miura, 1986; Vicat et al., 1986; Manceau and Combes, 1988; Rossouw et al., 1992). It consists of double chains of edge-sharing MnO_6 octahedra that share corners with each other (Fig. 4.1a). This results in a framework structure containing ~4.6 Å tunnels. These are parallel to the c-axis of the unit cell (referred to tetragonal space group *I* 4/*m*) (Post et al., 1982; Vicat et al., 1986).

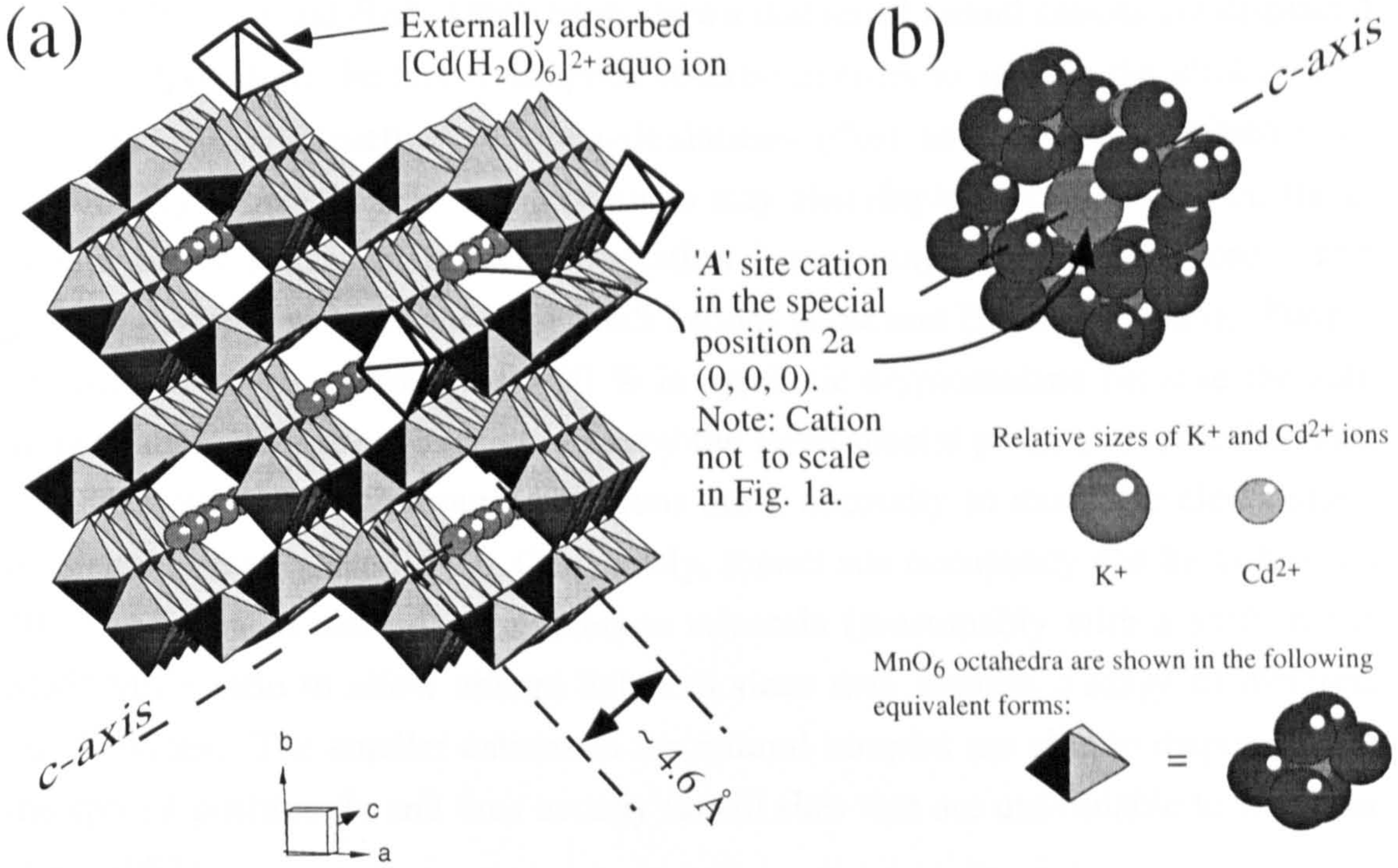

Fig. 4.1. The cryptomelane structure contains ~4.6 Å tunnels running parallel to the crystallographic c-axis (a). The ***A*** type cation K^+ (r_{ionic} = 1.38 Å) is large enough to reside in the ideal tunnel cation position (special position 2a (0, 0, 0)) where it coordinates with eight equidistant O^{2-} ions (b). The smaller Cd^{2+} ion (r_{ionic} = 0.95 Å) has to displace along the c-axis and towards the tunnel walls to achieve its ideal Cd-O separation and the Cd-Mn separation derived from the EXAFS results. Externally adsorbed Cd (unshaded octahedra in (a)) can only coordinate with 1 to 2 MnO_6 octahedra (shaded), whilst that in the tunnels can coordinate with up to eight Mn atoms (b). Note that (a) and (b) are to the same scale with the exception of the tunnel cations, which are not to scale in (a).

Synthetic Mn oxides with the hollandite structure have the general formula $\boldsymbol{A}_{0\text{-}2}(Mn^{4+}, Mn^{3+})_8O_{16}$ (Post and Burnham, 1986). The Mn cations are in octahedral coordination with oxygen, and form the framework of the mineral, whilst the mono- or divalent ***A*** cations (K^+ alone in synthetic cryptomelane) occupy the tunnel positions (Post and Burnham, 1986). The inclusion of lower-valence (< +4) cations such as Mn^{3+} in the octahedral sites is essential to offset the positive charge of the tunnel cations (Post and Burnham, 1986).

It is thought that the tunnel cations coordinate with structural O^{2-} in the tunnel walls, and that the resulting cation-O^{2-} bond distance will be the same as that observed in crystalline solids (Post et al., 1982). K^+ (r_{ionic} 1.38 Å, Shannon, 1976) and Ba^+ (r_{ionic} 1.35 Å, Shannon, 1976) are large enough to reside in the ideal tunnel cation site at the special position 2a (0, 0, 0) (this nomenclature gives the atomic positions in fractional coordinates). In this position they are at the centre of a cavity formed by eight equidistant O atoms which lie at the corners of a distorted prism (Post et al., 1982) (Fig. 4.1b). Several structural refinements (Post et al., 1982; Vicat

et al., 1986; Post and Bish, 1989) have shown that small tunnel cations are displaced from (0, 0, 0) along the tunnel direction (c-axis) in order to achieve the ideal cation-O^{2-} separation. Structure energy calculations (Post and Burnham, 1986) have additionally shown that the smaller cations may also displace orthogonally off the c-axis to better satisfy their ideal separation from tunnel wall oxygen ions. The greatest displacements occur with small cations (Post and Burnham, 1986). Tunnel site occupancy is approximately 30 % in synthetic cryptomelane because the sole tunnel cation (K^+) is only able to occupy the large special position 2a, and because vacancies between neighbouring K^+ ions are a necessity to minimise electrostatic repulsion (Vicat et al., 1986). Conversely, tunnel site occupancy can be as high as 50 % to 75 % in natural cryptomelane minerals (presumably with a shift in the Mn^{4+}:Mn^{3+} ratio to allow charge balance) since they contain a range of different sized cations. The smaller cations in the natural samples are able to displace from the special position 2a and thus occupy tunnel sites that are unavailable to K^+ (Post et al., 1982).

Many of the structural refinements (Post et al., 1982; Vicat et al., 1986; Post and Bish, 1989) and structure energy calculations (Post and Burnham, 1986) show that there is an element of disorder on the position of the tunnel cations. Post and Burnham (1986) have shown that the minimum energy tunnel cation positions are a function of the arrangement of the octahedral cations in the framework of hollandite minerals. These workers also showed that the different arrangements of octahedral +3 and +4 cations have very similar energies, and are therefore likely to occur in a random distribution in any one sample (Post and Burnham, 1986). As a result, there will also be a random distribution of the associated tunnel cation positions (Post and Burnham, 1986). Further disorder may also result from the electrostatic repulsion between neighbouring tunnel cations (Sinclair et al. 1980; Vicat et al., 1986), which is weak but significant, and greatest for divalent cations (Post and Burnham, 1986). These results cast light on the location of Cd sorbed on cryptomelane.

4.3 EXTENDED X-RAY ABSORPTION FINE STRUCTURE SPECTROSCOPY BACKGROUND

Extended X-ray absorption fine structure (EXAFS) spectroscopy is a bulk element-specific technique that can be used to determine the *average* coordination environment up to ~ 4 Å around an element of interest (Cd in this case) in poorly ordered samples. EXAFS measurements can often be performed on wet pastes (*in situ*), and for elements present at relatively low concentrations (> 0.05 wt%, depending on experimental conditions). No long range order is required in the

sample, which can be in a liquid, amorphous, or crystalline state (e.g., Brown et al., 1988, 1995; Charlet and Manceau, 1993). Thus, EXAFS is particularly suited to the study of trace metal interactions with minerals and inorganic ligands in solution.

An EXAFS spectral scan is obtained by measuring X-ray absorption over a range of photon energies which includes the 'absorption edge' of the element of interest (e.g. Brown et al., 1988, 1995; Charlet and Manceau, 1993). Curve fitting allows the determination of the *average* number (N_j) (± 20%) of atoms in the j atomic shell, their distance (R_j) (± 0.02 Å) from the central excited Cd atom, their identity, and the associated Debye-Waller factor (σ_j) (e.g., Brown et al., 1988, 1995; Charlet and Manceau, 1993). The latter parameter represents the mean square of variation in distances from the element of interest to the shell under consideration. It accounts for damping of the EXAFS oscillations due to the thermal vibration (σ_T) and the static disorder (σ_S) of atoms in atomic shells (e.g., Brown et al., 1988, 1995; Charlet and Manceau, 1993). The *R* factor is a goodness of fit parameter which is used in the curve fitting process. For poorly ordered mineral-aqueous systems such as the one described here, an *R* value of between 20 and 40 indicates an acceptable match between theory and experiment (Dent and Mosselmans, 1992). A significant consideration is that EXAFS only provides unique answers for a system that involves 2, and at best 3, well defined coordination environments for the element of interest. As the number of different sites exceeds this value it becomes increasingly difficult to resolve individual atomic shells (Charlet and Manceau, 1993).

EXAFS results are commonly displayed in two forms: The k^3-weighted EXAFS data ($\chi(k)\cdot k^3$) is plotted against wavenumber (k) ($Å^{-1}$) in the EXAFS spectrum. In the radial distribution function (RDF) the Fourier transform of the EXAFS data (FT of $\chi(k)$) is plotted against distance from the central Cd atom (Å). The RDF often provides the best visual representation of coordination around the element of interest, since each peak in the spectrum corresponds to an atomic shell. However, the corresponding EXAFS spectrum is often shown because this provides a better representation of data quality than the RDF. In both types of plot, theory is shown as a bold line whilst experimental data is shown as a fine line.

4.4 MATERIALS AND METHODS

All reagents used in this study were analytical grade, and all labware was acid-washed. The Cd stock solution and the adsorption sample were prepared with boiled MilliQ® water to prevent the formation $CdCO_{3(s)}$ (otavite). Un-degassed MilliQ® water was otherwise used throughout. pH measurements were made with a BDH® general purpose combination pH electrode in combination with an Orion®

model 720A pH meter. pH calibration to ± 0.05 pH units was achieved at room temperature with constantly stirred Whatman® NBS grade buffers (1.677 ± 0.005 and 4.001 ± 0.005 at 20 °C). The adsorption sample used in the EXAFS experiment was prepared under CO_2-free conditions (see below).

4.4.1 Cryptomelane preparation and characterisation

Cryptomelane was synthesised via a method detailed by McKenzie (1971): 158.0 g of $KMnO_4$ (Aldrich®) were added to 2.5 litres of boiling MilliQ® water in a 3 L Pyrex® beaker. Two moles of 11.6 M HCl (Fisher®) was slowly added to the permanganate solution in a dropwise fashion. The suspension was vigorously stirred and boiled for a further ten minutes, resulting in a brown precipitate. This was cleaned by repeated cycles of centrifugation and resuspension in MilliQ® water and then air dried at 35 - 40 °C. An agate mortar and pestle was used to grind the crystalline product to a fine powder. The identity of the powder was confirmed as cryptomelane by X-ray diffraction of a randomly oriented powder sample using Cu Kα radiation on a Philips PW 1800 X-ray powder diffractometer. The XRD powder pattern of dry cryptomelane (Fig. 4.2) exhibits relatively well defined peaks and a low background. This is in agreement with the Joint Committee on Powder Diffraction Standards card 20-908, and the XRD data obtained for cryptomelane by previous workers (McKenzie, 1971; Chen et al., 1986; Golden et al., 1986). However, following rehydration (24 hr in MilliQ® water) there was a broadening of the peaks and a growth in background, indicating a significant increase in disorder (Fig. 4.2). This may result from chain width disorder, such as that observed in hollandite and romanechite (Turner and Busek, 1979), and cryptomelane (Chen et al., 1986).

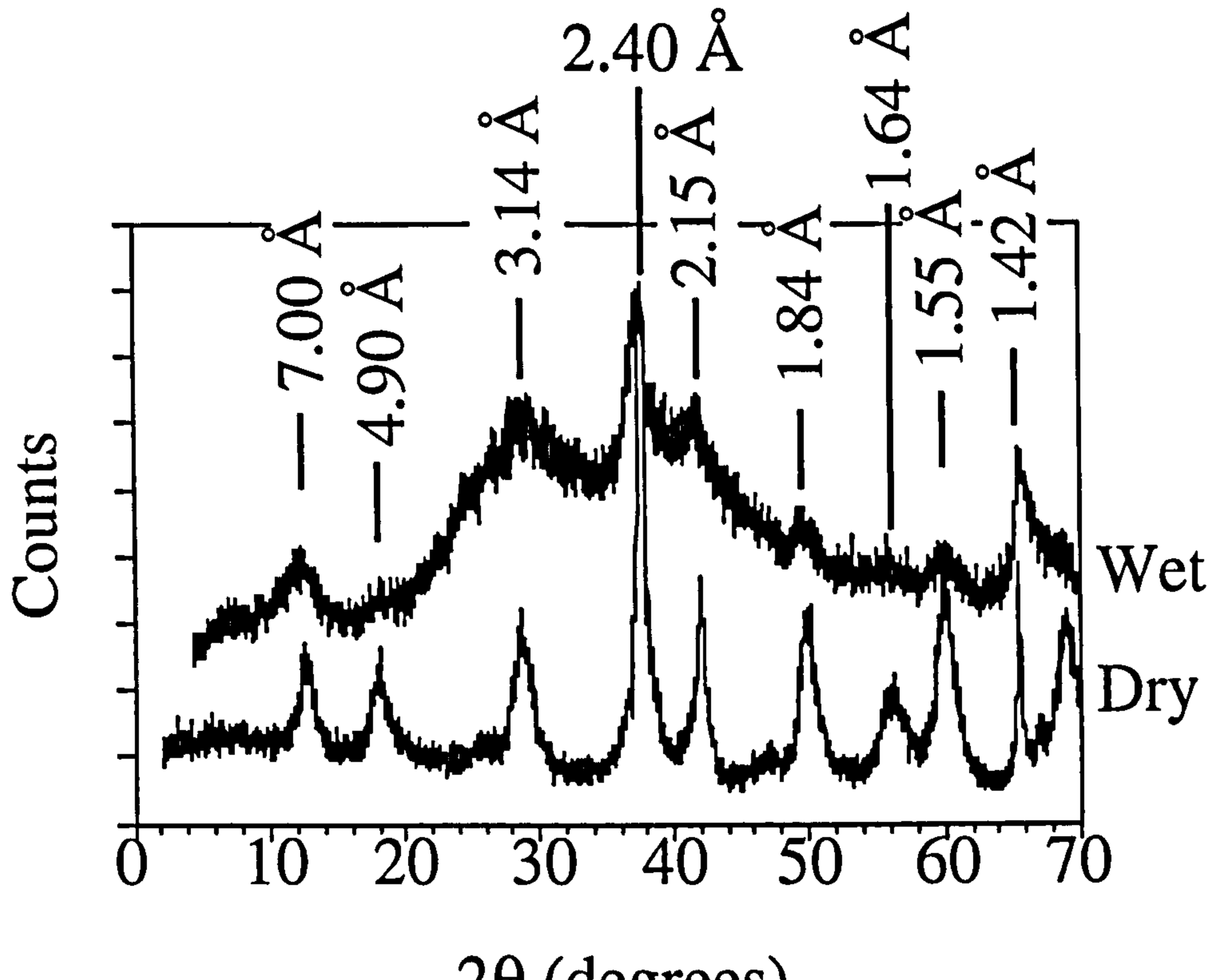

Fig. 4.2. Cu Kα powder pattern (0.02° step, 45 kV/40 mA) of the synthetic cryptomelane that was used to prepare the EXAFS adsorption sample. Note that the well defined peaks in the dry material (Dry) broaden significantly following hydration (Wet). This peak broadening and the rise in background suggests significant structural disorder in the hydrated form.

The N_2-BET surface area of the laboratory produced cryptomelane was 115 m^2g^{-1}, as determined on a Ströhlein area meter following 12 hr of outgassing with $N_2(g)$. It should be noted that because nitrogen is likely to be able to penetrate the tunnels to some extent, some fraction of the total surface area may correspond to tunnel surfaces. A TEM photomicrograph (JEOL 100CX TEMSCAN) (Fig. 4.3) shows cryptomelane to have a fibrous morphology, which is characteristic of the hollandite-type minerals (DeGuzman et al., 1994). The molar ratio of K:Mn in the synthetic cryptomelane was confirmed as 1:8 following total dissolution in concentrated HCl and analysis by ICP-AES.

Whilst the average oxidation state of Mn was not measured in the synthetic cryptomelane used in this study, a value of 3.80 has been reported for a similar material (DeGuzman et al., 1994).

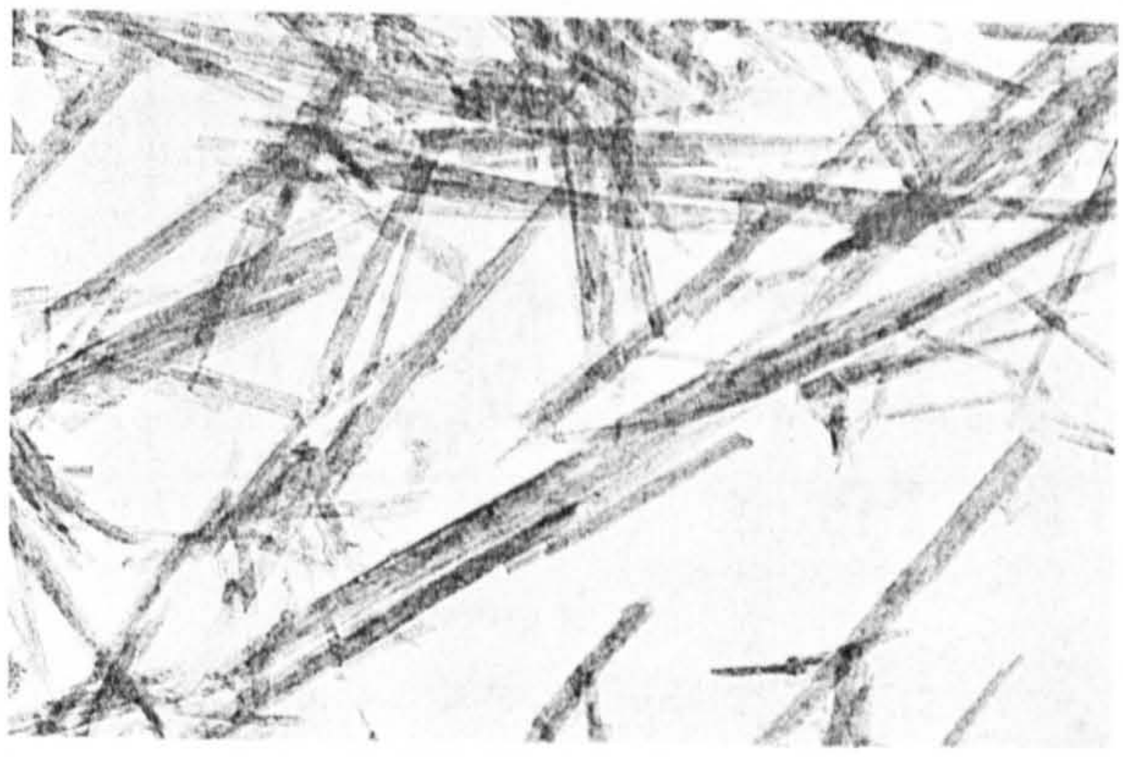

Fig. 4.3. TEM photomicrograph of synthetic cryptomelane, showing the acicular morphology which is characteristic of Mn oxides with the hollandite structure. The crystallites are elongate along the c-axis, and measure approximately 1-1.5 μm in length.

4.4.2 Preparation of the cryptomelane adsorption sample for EXAFS analysis

The cryptomelane adsorption sample used in the EXAFS experiment was prepared in the following manner: A 874 ppm Cd stock solution was prepared by dissolving an appropriate amount of $Cd(NO_3)_2 \cdot 4H_2O(s)$ (Fluka®) in CO_2-free MilliQ® water. This was acidified to ~pH 4 with a few drops of 1 % v/v HNO_3 (Fisher®), and stored in a closed 0.5 L polypropylene flask. A 30 ml aliquot of this solution was placed into a 50 ml polycarbonate Oak Ridge® centrifuge tube. The pH of this solution was adjusted to 2.5 by a manual addition of 0.1 M HNO_3 (Fisher®) whilst purging dissolved CO_2 from the solution with $N_2(g)$. Finely powdered cryptomelane (800 mg) was then added to the stock solution in the centrifuge tube. After purging with $N_2(g)$ for a further 15 min the centrifuge tube was sealed. The sample was reacted at 19 ± 2 °C for 48 hr in a rotating tumbler to keep the cryptomelane in suspension. The final pH was 2.0. Centrifugation (3000 rpm, 10 min) was used to separate the suspension into a wet paste (the 'adsorption sample') and its supernate. The supernate was decanted and then acidified by exactly 50 % dilution with 1 % v/v HNO_3 (Fisher®). The dilution-corrected concentrations of Cd and K in the acidified supernate were 300.6 ppm (ICP-MS, VG Elemental PlasmaQuad2+) and 2.64 ppm (ICP-AES, Jobin Yvon JY 24)), respectively. The adsorption sample was estimated to contain 2.15 wt% Cd (from the difference in Cd concentration before and after reaction with 800 mg of cryptomelane) and 50 - 60 wt% supernate (from the difference in weight of a similar sample before and after 12 hr of air drying at 35 - 40 °C). The adsorption sample was transported to Daresbury

laboratory as a wet paste in the polycarbonate Oak Ridge® centrifuge tube. EXAFS analysis was performed within 48 hr of centrifugation.

4.4.3 EXAFS data collection and interpretation

EXAFS data were collected at the CLRC Synchrotron Radiation Source (SRS) at Daresbury Laboratory, U.K. Spectra were collected at the Cd K-edge under room temperature conditions on station 9.2, which is equipped with a harmonic-rejecting double crystal Si (220) monochromator. The storage ring positron energy was 2.0 GeV, and the beam current varied between 130 and 240 mA. The adsorption sample was presented to the X-ray beam as a wet paste held by Sellotape® in a 2 mm thick plastic slide with a 4 x 15 mm sample slot. Although the adsorption sample contained approximately 50–60 wt% supernate, I have determined that less than 6 % of the EXAFS signal originated from Cd in the liquid fraction. EXAFS data were collected in six 30 min fluorescence mode scans during which no attempt was made to maintain CO_2-free conditions. EXAFS data were also collected from β-$Cd(OH)_{2(s)}$ (Fluka®) in two room temperature transmission mode scans. This material was used as a reference standard in later curve fitting.

EXAFS data reduction was performed using native Daresbury Laboratory software packages (EXCALIB and EXBACK) (Dent and Mosselmans, 1992). The EXAFS oscillations were simulated with the Daresbury curved wave theory EXAFS analysis program EXCURV92 (Gurman et al., 1984, 1986; Joyner et al., 1987; Gurman, 1988; Binsted et al., 1991, 1992). Modelling in this way provided the average shell parameters describing the local structure around the central excited Cd atom. Joyner tests (Joyner et al., 1987) were performed to ascertain the statistical significance of Cd and K atomic shells which I attempted to insert around the central Cd atom during modelling of the EXAFS oscillations.

The phase shift functions used in the curve fitting were derived from theory in EXCURV92. It has been suggested that phase shift functions generated in this way are less accurate than those determined experimentally (Spadini et al., 1994). However, the use of theoretical values is justified by the good agreement between the structure of β-$Cd(OH)_2$(s) derived from the EXAFS data using theoretical phase-shift functions (Fig. 4.4) and the published structure of β-$Cd(OH)_2$(s) (Spadini et al., 1994).

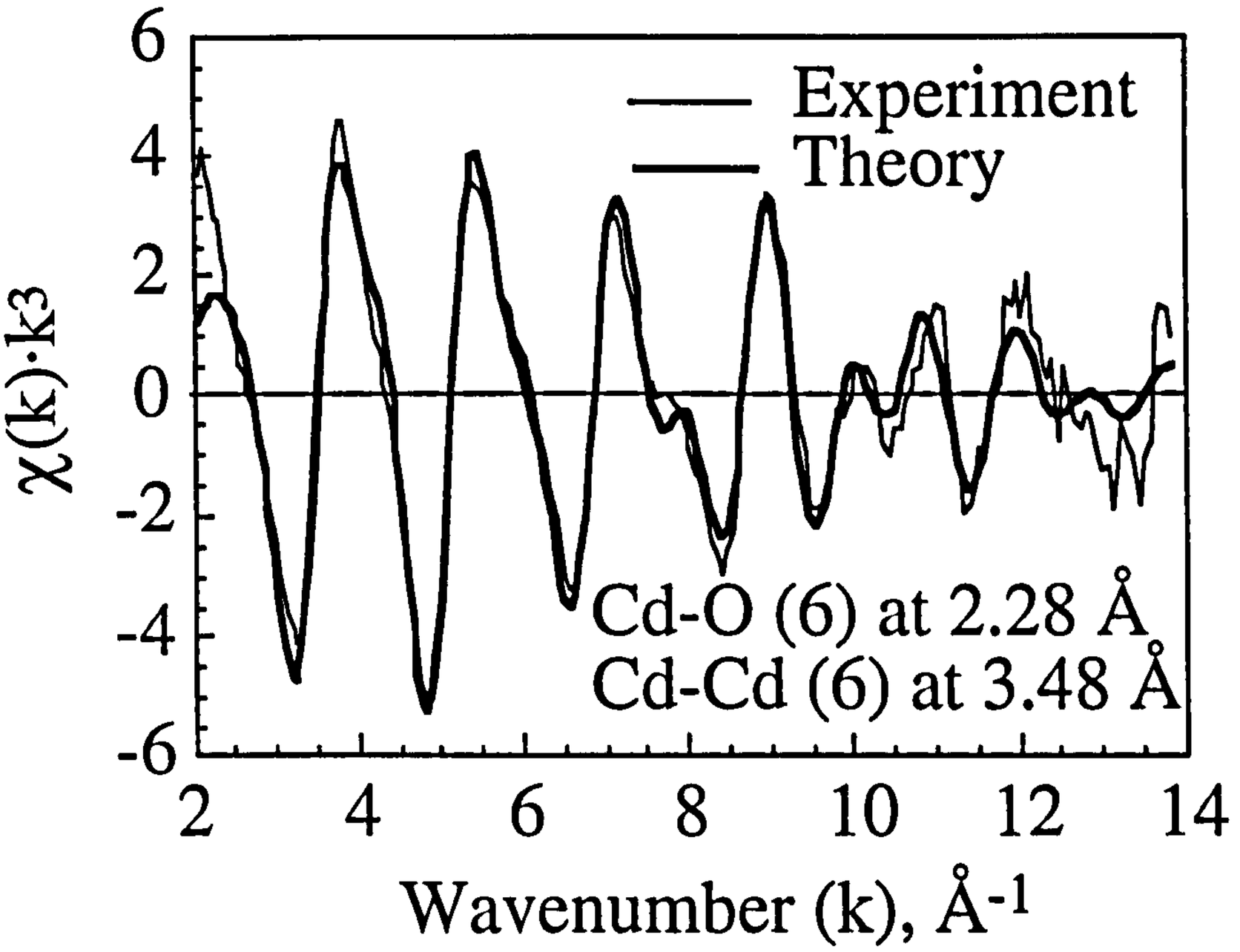

Fig. 4.4. EXAFS spectrum and theoretical curve fit for β-$Cd(OH)_{2(s)}$. The simulation was performed using the known structure of β-$Cd(OH)_{2(s)}$ and theoretical phase shift functions derived with the EXAFS simulation package EXCURV92. The subsequent use of theoretical phase shift functions in the analysis of EXAFS data from the cryptomelane adsorption sample is justified by the goodness of fit between experiment and theory shown here.

4.4.4 CrystalMaker simulations

The interactive crystallography software package CrystalMaker (2.1.0) (Palmer, 1996) was used to simulate the effect on Cd-O and Cd-Mn separations and coordination numbers of displacing Cd from the special position 2a. Crystallographic data from DeGuzman et al. (1994) was used to construct a model of cryptomelane in CrystalMaker. Various displacements were then applied to the location of Cd in the tunnels by altering the fractional coordinates describing the tunnel cation location. A bond search was performed around Cd in each of the new tunnel positions to find the number of surrounding Mn and O atoms and the associated interatomic distances. Results from various displacements were compared with the distance and coordination number values from analysis of the EXAFS data to help clarify the location of sorbed Cd.

4.5 RESULTS AND DISCUSSION

Although the sample which was examined by EXAFS was prepared at low pH (2.0), 66% of available Cd^{2+} was removed from solution to produce a sample containing 2.15 wt% Cd. This is equivalent to a surface site loading of ~21%, assuming a sorption site density for Cd on cryptomelane of 4.8 sites nm^{-2} (McKenzie, 1981) over the measured surface area of 115 m^2g^{-1}.

The aqueous speciation of Cd is dominated by the divalent aquo cation $[Cd(H_20)_6]^{2+}$ under the prevailing experimental conditions (Brookins, 1988), and cryptomelane ($pH_{ZPC} = 4.5 \pm 0.5$, Healey et al., 1966) is likely to have a net positive surface charge at pH 2.0. Intuitively, little Cd sorption would be expected at this pH. However, other weakly hydrolysed cations (such as Cu, Co, Ni, Pb, Zn etc.) are known to be specifically adsorbed by Mn oxides below their respective pH_{ZPC}'s (McKenzie, 1989). As a consequence, the strong uptake of Cd^{2+} by cryptomelane at pH 2.0 cannot be taken as evidence for sorption into the tunnel sites rather than onto the external surface.

However, the high coordination number of Mn atoms around sorbed Cd (4.9 ± 1.0 Mn at 3.65 Å, Fig. 4.5a and b, Table 4.1) cannot be explained by externally adsorbed Cd alone. By analogy with my recent EXAFS investigation of Cd adsorption on iron hydroxide minerals (Randall et al., 1996a,b, 1999), Cd adsorbed on the external surface of cryptomelane is expected to be in direct coordination with only 1 to 2 Mn atoms (Fig. 4.1a). In practice the effects of static and thermal disorder at the surface will reduce the average coordination number still further (Charlet and Manceau, 1993). Since the EXAFS spectrum represents an average of all of the coordination environments which Cd occupies in the sample (Brown et al., 1988, 1995; Charlet and Manceau, 1993), the high Mn coordination number of 4.9 suggests that the majority of sorbed Cd is within the tunnel structure at pH 2.0. Additionally, the small Cd-Mn separation (3.65 Å) indicates that this sorption occurs via an inner sphere mechanism as the Cd-Mn separation would be » 5 Å if an outer sphere mechanism had been involved.

Table 4.1. EXAFS shell parameters for β-$Cd(OH)_{2(s)}$ reference standard and cryptomelane adsorption sample.

Sample	pH	Surface loading	N_O	R_O (Å)	$2\sigma^2_O$	N_{Cd}	R_{Cd} (Å)	$2\sigma^2_{Cd}$	*R*
β-$Cd(OH)_{2(s)}$	--	--	6.0[b] ± 1.2	2.28 ± 0.02	0.016	6.0[b] ± 1.2	3.48 ± 0.02	0.024	30.5
	pH	Surface loading	N_O	R_O (Å)	$2\sigma^2_O$	N_{Mn}	R_{Mn} (Å)	$2\sigma^2_{Mn}$	*R*
Cryptomelane	2.01	~21%[a]	6.5 ± 1.3	2.24 ± 0.02	0.019	4.9 ± 1.0	3.65 ± 0.02	0.019	33.6

[a] Derived using a sorption site density for Cd on cryptomelane of 4.8 sites nm^{-2} (McKenzie, 1981).
[b] Value held constant during fit.

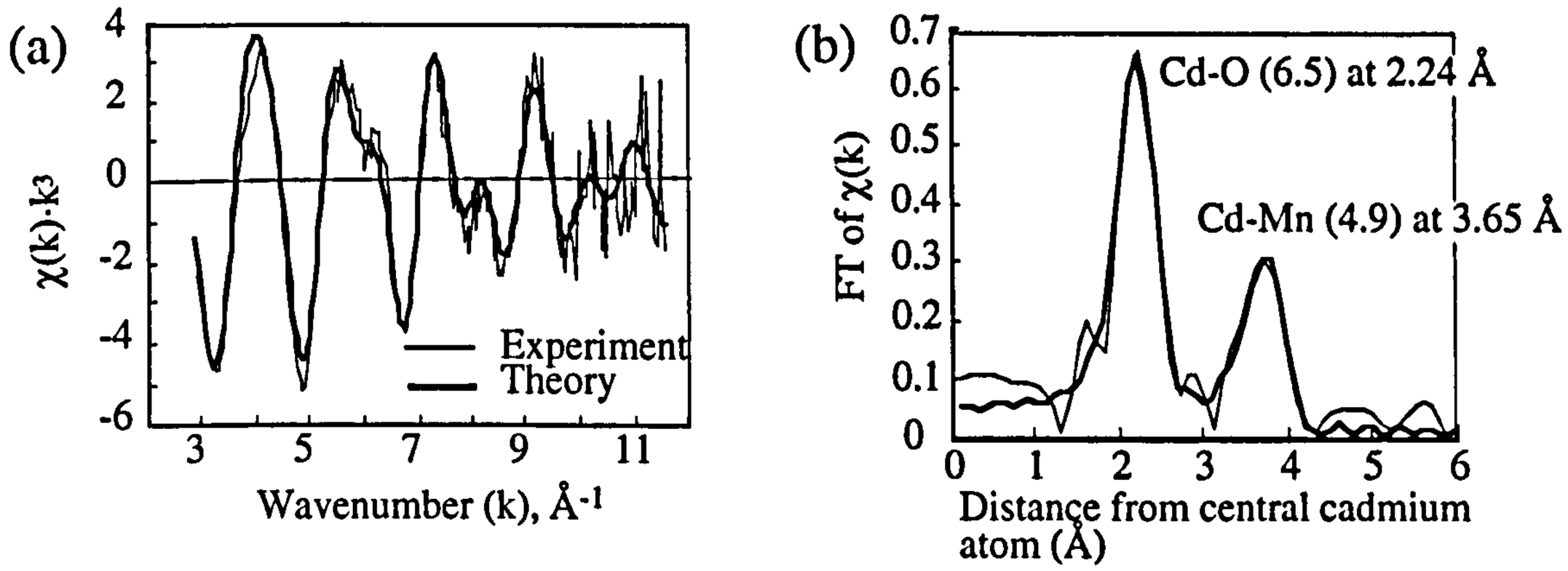

Fig. 4.5. EXAFS spectrum (a) and RDF (b) of the local environment of Cd sorbed on cryptomelane at pH 2.0. The coordination environment around sorbed Cd (4.9 ± 1.0 Mn at 3.65 ± 0.02 Å) strongly indicates that the majority of sorbed Cd is inside the tunnels, and that it is displaced from the ideal tunnel cation position (special position 2a (0, 0, 0)). The oxygen coordination environment around cadmium (6.5 ± 1.3 O at 2.24 ± 0.02 Å) is consistent with this, but also suggests that sorbed Cd is partly hydrated.

The CrystalMaker simulations show that Cd in the special position 2a would be surrounded by four Mn atoms within a radius of 4 Å. Note that EXAFS results become increasingly ambiguous at a distance of over 4 Å from the element of interest in poorly ordered systems (Charlet and Manceau, 1993). When Cd is displaced from this position, as is necessary for the average Cd-Mn separation to approach 3.65 Å, the CrystalMaker results suggest that the number of Mn atoms within 4 Å can increase to as much as eight. These Mn atoms are present at a range of Cd-Mn separations, the average of which is 3.65 Å. It is likely that individual Mn peaks are not observed in the RDF (Fig. 4.5a) because of disorder in the cryptomelane structure, and the inability of EXAFS to resolve individual atomic shells when the atoms in a given shell occur over a range of distances.

On the basis of simulations that I performed with CrystalMaker, Cd in the special position 2a (0, 0, 0) would be expected to coordinate with eight equidistant

tunnel wall O^{2-} ions at 2.85 Å. Although one oxygen coordination shell containing 6.5 ± 1.3 O atoms is observed in the EXAFS results (Fig. 4.5, Table 4.1), it is only 2.24 Å from the central Cd atom. This is further evidence that Cd is not present at the special position 2a. In order to achieve a Cd-O separation of 2.24 Å, Cd must displace from (0, 0, 0) along the c-axis and orthogonally off it towards the tunnel walls. In such a situation only 2 - 4 of the 6.5 O atoms observed at 2.24 Å could be accounted for by tunnel wall O^{2-} ions. It is possible that the remainder are due to coordination with free water in the tunnels. This would mean that Cd in the tunnels exists in a partly hydrated form. It has been suggested that Li^+ is sorbed in cryptomelane tunnels with its solvation shell at least partly intact (Feng et al., 1995), and it is possible that the same is also true of Cd insertion into the tunnels. As is the case with Mn, the range of Cd-O distances that would be expected to result from the displacement of Cd from the special position 2a are not observed in the EXAFS results (Fig. 4.5a). This is again explained by the fact that EXAFS cannot resolve the large number of different Cd-O distances that are likely to result from such a displacement. This is especially true in the case of an atom such as O, which provides a relatively weak contribution to the EXAFS spectrum because it has a low mass.

Although only a very small amount of K was released from cryptomelane to solution during Cd sorption, the Joyner statistical tests (Joyner et al., 1987) indicate that there is no support for the presence of a K shell within 4 Å of Cd (at the 5 % level of probability). However, this result is unsurprising since only 30 % of the tunnel sites are likely to be occupied by K in fresh cryptomelane (Vicat et al., 1986), and electrostatic repulsion between the cations would tend to maximise their separation. It should also be noted that Joyner tests provide no support for a Cd shell within 4 Å of the central Cd atom (at the 5 % level of probability). The absence of such a shell indicates that Cd was not sorbed in the form of a precipitate such as $Cd(OH)_2(s)$ or $CdCO_3(s)$.

The EXAFS results strongly indicate the existence of Cd within the structural tunnels in cryptomelane. Tunnel Cd is certainly displaced from the special position 2a, but the resolution of the data is not good enough to identify a unique tunnel position. The inability of EXAFS to resolve individual sorption sites in this case results in part from the disorder which is known to occur on the location of tunnel cations (Post et al., 1982; Post and Burnham, 1986; Vicat et al., 1986; Post and Bish, 1989). Whilst this disorder is significant in dry samples, Fig. 4.2 demonstrates that it is even greater in wet paste samples such as that analysed by EXAFS in this study.

The sorption of Cd^{2+} (r_{ionic} 0.95 Å, Shannon, 1976) into the cryptomelane tunnels at pH 2.0 is somewhat unexpected given that cryptomelane is thought to exhibit a strong preference for cations with an effective ionic radius of ~1.4 Å (Tsuji

and Komarneni, 1993b; Feng et al., 1995). However, a previous Rietveld structural refinement of Ni^{2+}, Fe^{2+}, and Cu^{2+} sorbed on cryptomelane has shown that these cations are located in the tunnels (Yin et al., 1994). Furthermore, it should be noted that many of the previous ion exchange studies used cryptomelane-type Mn oxide which contains H^+ rather than K^+ as the tunnel cation (Tsuji and Abe, 1985; Tsuji and Komarneni, 1993a,b; Feng et al., 1995), and that the selectivities of these two forms may be different. The sorption of Cd^{2+} into the tunnel sites is likely to allow a more effective balancing of the negative charge on the cryptomelane structure because the relatively small Cd^{2+} ion can occupy sites that are unavailable to K^+. It may therefore be energetically favourable. If so, this could help to explain why so much Cd was apparently sorbed in the structural tunnels which were at least partially filled with K.

Since the supernate from the EXAFS adsorption sample contained very little K (2×10^{-6} moles K released during sorption of 1.6×10^{-4} moles Cd), Cd^{2+} did not exchange for K^+. If the average oxidation state of Mn in the synthetic cryptomelane used in the study is 3.8 (by analogy with the similar material used by DeGuzman et al., 1994), the chemical formula would be $K(Mn^{4+}_{6.4}, Mn^{3+}_{1.6})O_{16}$. This has a charge deficit of -0.6, which could be satisfied by 0.6 mole H^+ ions in the tunnels in addition to K^+. Thus, Cd^{2+} may have exchanged for H^+ rather than K^+. This mechanism is plausible because the drop in pH during sorption (0.5 pH units) indicates that 2.05×10^{-4} moles H^+ were liberated to solution during the sorption of 1.6×10^{-4} moles Cd^{2+}. This suggests a near charge-balancing exchange of Cd^{2+} for H^+, when the uncertainty of pH measurement is taken into account.

4.6 CONCLUSION

The results of this study show that cryptomelane is an effective sorbent of Cd at very low pH levels (2.0). EXAFS results indicate that Cd sorption at pH 2.0 occurs predominantly at tunnel sites in the cryptomelane structure. This process may be energetically favourable if it allows a more effective balancing of the negative structural charge on cryptomelane. The limited release of the predominant tunnel cation (K^+) during Cd sorption indicates that Cd^{2+} exchanges for H^+ ions, which are likely to be in the tunnels in addition to K^+. This conclusion is supported by the lowering of pH during Cd sorption. This is an important result for K-Ar dating techniques which use natural cryptomelane, because the possibility of K replacement by competing cations would increase dating uncertainties.

Sorbed Cd is displaced from the ideal tunnel cation position (special position 2a (0, 0, 0)) in order to achieve a separation of 2.24 Å from the tunnel wall O^{2-} ions

with which it is coordinated. EXAFS results show that Cd has a complete octahedral solvation shell, but this cannot be due to tunnel wall O^{2-} ions alone. It is possible that tunnel Cd is also partly coordinated with free water in the tunnels in order to complete its solvation shell.

Although this study suggests that Cd is able to sorb at tunnel sites in cryptomelane, structural disorder and the likely existence of a number of different sorption sites mean that EXAFS is unable to identify unique sorption sites. I intend to perform band structure calculations in order to resolve some of the remaining uncertainty on the location of sorbed Cd.

4.7 REFERENCES

Adams, S. N., Honeysett J. L., Tiller, K. G., and Norrish, K., 1969. Factors controlling the increase of cobalt in plants following the addition of cobalt fertilizer. Aust. J. Soil Res., 7: 29-42.

Bilewicz, A. and Fuks, L., 1993. New selective adsorbents for ammonium ions -regeneration of dialysate in portable artificial kidney. Chemia Analityczna, 38: 331-338.

Binsted, N., Campbell, J. W., Gurman, S. J., and Stephenson, P. C., 1991. SERC Daresbury Laboratory EXCURV92 program.

Binsted, N,. Strange, R. W., and Hasnain, S. S., 1992. Restrained refinement. Biochemistry, 31: 12117-12125.

Brookins, D. G, 1988. Eh-pH Diagrams for Geochemistry. Springer-Verlag, NY. pp. 56-57.

Brown, G. E., Calas, G., Waychunas, G. A., Petiau, J., 1988. X-ray absorption spectroscopy and its applications in mineralogy and geochemistry. In: F. Hawthorne (Editor), Spectroscopic Methods in Mineralogy and Geology. Reviews in Mineralogy, 18. Mineralogical Society of America, Washington, DC. pp. 431-512.

Brown, G. E., Jr., Parks, G. A., and O'Day, P. A., 1995. Sorption at the mineral-water interface: macroscopic and microscopic perspectives. In: D. J. Vaughan, and R. A. D Pattrick (Editors), Mineral Surfaces. Chapman and Hall. pp. 129-183.

Burns, R. G., 1976. The uptake of Co onto ferromanganese nodules, soils, and synthetic manganese (IV) oxides. Geochim. Cosmochim. Acta, 40: 95-102.

Byström, A. and Byström, A. M., 1950. The crystal structure of hollandite, the related manganese oxide minerals, and α-MnO_2. Acta Crystallogr., 3: 146-154.

Cadée, M. C. and Verschoor G. C., 1978. Barium tin chromium oxide, a new hollandite phase. Acta Crystallogr., B34: 3554-3558.

Carlos, B. A., Chipera, S. J., Bish, D. L., and Craven, S. J., 1993. Fracture-lining manganese oxide minerals in silicic tuff, Yucca Mountain, Nevada, USA. Chem. Geol., 107: 47-69.

Charlet, L. and Manceau, A., 1993. Structure, formation, and reactivity of hydrous oxide particles: Insights from X-ray absorption spectroscopy. In: J. Buffle and H. P. van Leeuwen (Editors), Environmental Analytical and Physical Chemistry Series. Vol. 2: Environmental Particles. Lewis Publishers. pp. 117-164.

Chen, C. C., Golden, D. C., and Dixon, J. B, 1986. Transformation of synthetic birnessite to cryptomelane - An electron microscopic study. Clays Clay Mineral., 34: 565-571.

Chukhrov, F. V. and Gorschkov, A. I., 1981. Iron and manganese oxide minerals in soils. Trans. R. Soc. Edinburgh, Earth Sci., 72: 195-200.

Crowther, D. L., Dillard, J. G., and Murray, J. W., 1983. The mechanism of Co(II) oxidation on synthetic birnessite. Geochim. Cosmochim. Acta, 47: 1399-1403.

Dammer, D., Chivas, A. R., and McDougall, I., 1996. Isotopic dating of supergene manganese oxides from the Groote Eylandt deposit, Northern Territory, Australia. Econ. Geol. Bull. Soc. Econ. Geol., 91: 386-401.

DeGuzman, R. N., Shen, Y.-F., Neth, E. J., Suib, S. L., O'Young, C.-L., Levine, S., and Newsam, J. M., 1994. Synthesis and characterization of octahedral molecular-sieves OMS-2 having the hollandite structure. Chem. Material., 6: 815-821.

Dent, A. J. and Mosselmans, J. F. W., 1992. A guide to EXBACK, EXCALIB, and EXCURV92. CLRC Daresbury Laboratory internal document.

Elabsy, M. A., Elnaggar, I. M., Hamid, M. M. A., Aly, H. F., 1993. Separation of uranium from thorium on cryptomelane-type hydrous manganese-dioxide. J. Radioanal. Nucl. Chem. Articl., 172: 145-153.

Elnaggar, I. M., Elabsy, M. A., Abdelhamid, M. M., and Aly, H. F., 1993. Sorption behavior of uranium and thorium on cryptomelane-type hydrous manganese dioxide from aqueous solution. Solv. Extract. Ion Ex., 11: 521-540.

Feng, Q., Kanoh, H., Miyai, Y., and Ooi., K., 1995. Alkali-metal ions insertion/ extraction reactions with hollandite-type manganese oxide in the aqueous-phase. Chem. Material., 7: 148-153.

Gadde, R. R. and Laitinen, H. A., 1974. Studies of heavy metal adsorption by hydrous iron and manganese oxides. Anal. Chem., 46: 2022-2026.

Giovanoli R., 1976. Vom Hexaquo-Mangan zum Mangan-Sediment. Reaktionssequenzen feinteiliger fester Mangan-oxihydroxide. Chimia, 30: 102-103.

Golden D. C., Dixon J. B., and Chen C. C., 1986. Ion exchange, thermal transformations, and oxidising properties of birnessite. Clays Clay Miner., 34: 511-520.

Golden, D. C., Chen, C. C., and Dixon, J. B., 1987. Transformation of birnessite to buserite, todorokite, and manganite under mild hydrothermal treatment. Clays Clay Mineral., 35: 271-280.

Greenland, D. J. and Hayes, M. H. B., 1983. The Chemistry of Soil Constituents. Wiley, Chichester. pp. 143-145.

Gurman, S. J., 1988. The small atom approximation theory. J. Phys. C: Solid State Phys., 21: 3699-3717.

Gurman, S. J., Binsted, N., and Ross, I., 1984. Single scattering rapid curved wave theory. J. Phys. C: Solid State Phys., 17: 143-151.

Gurman, S. J., Binsted, N., and Ross, I., 1986. Multiple scattering rapid curved wave theory. J. Phys. C: Solid State Phys., 19: 1845-1861.

Healey, T. W., Herring, A. P., and Fuerstenau, D. W., 1966. The effect of crystal structure on the surface properties of a series of manganese dioxides. J. Colloid Interface Sci., 21: 435-444.

Henocque, O., Ruffet, G., Colin, F., and Feraud, G., 1997. The $^{40}Ar/^{39}Ar$ dating of supergene minerals as a new investigation tool of lateritic dynamics. Abs. Supplement 1, Abs. of European Union of Geosciences 9, Terra Nova, 9. Cambridge, Cambridge, U.K, pp. 583.

Joyner, R. W., Martin, K. J., and Meehan. P., 1987. Statistical significance tests. J. Phys. C., 20: 4005-4012.

Krauskopf, K. B., 1956. Factors controlling the concentrations of thirteen rare metals in seawater. Geochim. Cosmochim. Acta, 9: 1-32B.

Lippolt, H. J. and Hautmann, S., 1995. $^{40}Ar/\beta^{39}Ar$ ages of Precambrian manganese ore minerals from Sweden, India and Morocco. Mineralium Deposita, 30: 246-256.

Llorca, S. and Monchoux, P., 1991: Supergene cobalt minerals from New Caledonia. Canadian Mineral., 29: 149-161.

Manceau, A., and Combes, J. M., 1988. Structure of Mn and Fe oxides and oxyhydroxides: A topological approach by EXAFS. Phys. Chem. Mineral. 15: 283-295.

Manceau, A., Llorca, S., and Calas, G., 1987. Crystal chemistry of cobalt and nickel in lithiophorite and asbolane from New Caledonia. Geochim. Cosmochim. Acta, 51: 105-113.

Manceau, A., Buseck, P. R., Miser, D., Rask, J., and Nahon, D., 1990. Characterization of Cu in lithiophorite from a banded Mn ore. Amer. Mineral., 75: 490-494.

Manceau, A., Gorshkov, A. I., and Drits, V. A., 1992. Structural chemistry of Mn, Fe, Co, and Ni in manganese hydrous oxides. 2. information from EXAFS spectroscopy and electron and X- ray-diffraction. Amer. Mineral., 77: 1144-1157.

McKenzie, R. M., 1970. The reaction of cobalt with manganese dioxide minerals. Aust. Journ. Soil. Res., 8: 97-106.

McKenzie, R. M., 1971. The synthesis of birnessite, cryptomelane, and some other oxides and hydroxides of manganese. Mineral. Mag., 38: 493-502.

McKenzie, R. M., 1972. The sorption of some heavy metals by the lower oxides of manganese. Geoderma, 8: 29-35.

McKenzie, R. M., 1980. The adsorption of lead and other heavy metals on oxides of manganese and iron. Aust. J. Soil. Res., 18: 61-73.

McKenzie, R. M., 1981. The surface charge of manganese dioxides. Aust. J. Soil. Res., 19: 41-50.

McKenzie, R. M., 1989. Manganese oxides and hydroxides. In: J. B. Dixon and S. B. Weed (Editors), Minerals in Soil Environments (2nd edn.). Soil. Sci. Am., Wisconsin. pp. 439-465.

Miura, H., 1986. The crystal structure of hollandite. Mineralogical Journ., 13: 119-129.

Nakashima, K. and Imaoka, T., 1991. K-rich cryptomelane from Mt. Kumogi area, Shimane Prefecture, Southwest Japan. Neues Jahrb. Mineral.-Monatsh. 113-128.

Nimfopoulos, M. K. and Pattrick, R. A. D., 1991. Mineralogical and textural evolution of the economic manganese mineralization in Western Rhodope Massif, N. Greece. Mineral. Mag., 55: 423-434.

Ostwald, J., 1992. Genesis and paragenesis of the tetravalent manganese oxides of the Australian continent. Econ. Geol. Bull. Soc. Econ. Geol., 87: 1237-1252.

Palmer, D. C., 1996. CrystalMaker 2.1.0. Interactive Crystallography for MacOS. Cambidge University Technical Services.

Parc, S., Nahon, D., Tardy, Y., and Vieillard, P., 1989. Estimated solubility products and fields of stability for cryptomelane, nsutite, birnessite, and lithiophorite based on natural lateritic weathering sequences. Amer. Mineral., 74: 466-475.

Post, J. E. and Burnham, C. W., 1986. Modeling tunnel-cation displacements in hollandites using structure-energy calculations. Amer. Mineral., 71: 1178-1185.

Post, J. E. and Bish, D. L., 1989. Rietveld refinement of the coronadite structure. Amer. Mineral., 74: 913-917.

Post, J. E., Von Dreele, R. B., and Buseck, P. R., 1982. Symmetry and cation displacements in hollandites: Structure refinements of hollandite, cryptomelane, and priderite. Acta Crystallogr., B38: 1056-1065.

Potter, R. M. and Rossman, G. R., 1979. The tetravalent manganese oxides: identification, hydration, and structural relationships. Amer. Mineral., 64: 1199-1218.

Randall, S. R., Sherman, D. M., and Ragnarsdottir, K. V., 1996a. Cadmium adsorption on hydrous metal oxides: An EXAFS investigation of the mechanisms. Geol. Soc. Amer. 1996 AGM, Abs. with Programs, vol. 28 (7). Geol. Soc. Amer., Boulder, CO. pp. A-518.

Randall, S. R., Sherman, D. M., Ragnarsdottir, K. V., and Robbins, R. A., 1996b. An EXAFS investigation of the structure of cadmium surface complexes on hydrous iron oxides and birnessite. European Union of Geosciences 9, Abs. Supplement 1 (Terra Nova vol. 9). Cambridge, Cambridge, U.K, pp. 560.

Randall S. R., Sherman D. M., Ragnarsdottir K. V. and Collins C. R., 1999. The mechanism of cadmium surface complexation on iron oxyhydroxide minerals. Geochim. Cosmochim. Acta, *in press*.

Rossouw, M. H., Liles, D. C., Thackeray, M. M., David, W. I. F., and Hull, S., 1992. Alpha manganese dioxide for lithium batteries: A structural and electrochemical study. Matt. Res. Bull., 27: 221-230.

Ruffet, G., Innocent, C., Michard, A., Feraud, G., Beauvais, A., Nahon, D., and Hamelin, B., 1996. A geochronological $^{40}Ar/^{39}Ar$ and $^{87}Rb/^{87}Sr$ study of K-Mn oxides from the weathering sequence of Azul, Brazil. Geochim. Cosmochim. Acta, 60: 2219-2232.

Shannon, R. D., 1976. Revised effective ionic radii and systematic studies of interatomic distances in halides and chalcogenides. Acta. Cryst., A32: 751-767.

Shiller, A. M. and Boyle, E. A., 1987. Variability of dissolved trace metals in the Mississippi River. Geochim. Cosmochim. Acta, 51: 3273-3277.

Sinclair, W., McLaughlin, G. M., and Ringwood, A. E., 1980. The structure and chemistry of a barium titanite hollandite-type phase. Acta Crystallogr., B36: 2913-2918.

Singh, S. K. and Subramian, V., 1984. Hydrous Fe and Mn oxides. Scavengers of heavy metals in the aquatic environment. CRC Crit. Rev. Environ. Control, 14: 33-90.

Spadini, L., Manceau, A., Schindler, P. W., and Charlet, L., 1994. Structure and stability of Cd^{2+} surface complexes on ferric oxides. 1. Results from EXAFS spectroscopy. J. Colloid Interface Sci., 168: 73-86.

Tsuji, M. and Abe, M., 1985. Synthetic inorganic ion-exchange materials. XXXVIII. Acid-base properties of a cryptomelane-type hydrous manganese (IV) oxide and some chromatographic applications. Bull. Chem. Soc. Japan, 58: 1109-1114.

Tsuji, M. and Komarneni, S., 1993a. Selective exchange of divalent transition metal ions in cryptomelane-type manganic acid with tunnel structure. J.Materials Res., 8: 611-616.

Tsuji, M. and Komarneni, S., 1993b. Powder X-ray-diffraction study of a cryptomelane-type manganic acid and its alkali cation-exchanged forms. J.Materials Res., 8: 3145-3150.

Turner, S. and Busek, P. R., 1979. Manganese oxide structures and their intergrowths. Science, 203: 456-458.

Vasconcelos, P. M., Becker, T. A., Renne, P. R., and Brimhall, G. H., 1992. Age and duration of weathering by $^{40}K/^{40}Ar$ and $^{40}Ar/^{39}Ar$ analysis of potassium-manganese oxides. Science, 258: 451-455.

Vasconcelos, P. M., Renne, P. R., Brimhall, G. H., and Becker, T. A., 1994. Direct dating of weathering phenomena by $^{40}Ar/^{39}Ar$ and K-Ar analysis of supergene K-Mn Oxides. Geochim. Cosmochim. Acta, 58: 1635-1665.

Vicat, J., Fanchon, E., Strobel, P., and Tran Qui, D., 1986. The structure of $K_{1.33}Mn_8O_{16}$ and cation ordering in hollandite-type structures. Acta Crystallogr., B42: 162-167.

Yin, Y. G., Xu, W. Q., DeGuzman, R., Suib, S. L., O'Young, C. L., 1994. Studies of stability and reactivity of synthetic cryptomelane-like manganese oxide octahedral molecular-sieves. Inorg. Chem., 33: 4384-4389.

Chapter 5

The fate of As(V) during early diagenetic processes

5.1 INTRODUCTION

5.1.1 The environmental chemistry of arsenic

Arsenic has long been recognised as a toxin and carcinogen and arsenic poisoning can result in the development of skin and other cancers (Mandal et al., 1996). In recognition of these potential health risks, the recommended maximum drinking water limit for arsenic is 10 ppb (WHO, 1993).

Elevated levels of arsenic can result from anthropogenic activities such as mining, the use of arsenical pesticides, application of fertilisers, irrigation, dust, the burning of fossil fuels and the disposal of industrial and animal wastes (Nriagu, 1994). However, terrains rich in sulphide-bearing strata can also display elevated levels of arsenic in surface water and groundwater due to sulphide oxidation (Nriagu, 1994). The concentration of arsenic is increased by accumulation during weathering processes and translocation in colloidal fractions (Iimura, 1981). Hence, arsenic levels in shales (14.5 ppm on average; Bhumbla and Keefer, 1994), sediments (100-300 ppm; Branson and Patrick, 1987) and soils (7.2 ppm, Bhumbla and Keefer, 1994) are enriched relative to the 1.8 ppm crustal average (Iimura, 1981).

In general, the speciation, solubility, mobility, bioavailability and toxicity of arsenic depends on its oxidation state. Hence, an understanding of the Eh - pH dependent transformations between various species is essential to our knowledge of its behaviour in the environment (Masscheleyn et al., 1991). The majority of naturally occurring arsenic is inorganic. Aqueous speciation is dominated by the As(V) oxyanions $H_2AsO_4^-$ and $HAsO_4^{2-}$ under oxidising conditions (Grossl et al., 1997) and the neutral As(III) species $H_3AsO_3^0$ under more reducing conditions (Fig. 1.1) (Masscheleyn, 1991b; Grossl et al., 1997). The As(III) species is far more toxic (Ferguson and Gavis, 1972), soluble and mobile (Deuel and Swoboda, 1972; Pierce and Moore, 1982) than the arsenate species, which are strongly adsorbed by iron oxyhydroxides (Livesey and Huang, 1981; Aggett and Roberts 1986; Moore et al., 1988; Belzile and Tessier, 1990; Fuller et al., 1993; Waychunas et al., 1993; Sullivan and Aller, 1996; Sun and Doner, 1996).

5.1.2 The effect of ferrihydrite ageing on arsenic mobility

Poorly crystalline iron oxyhydroxides such as ferrihydrite are generally the first solid phases to form during the oxidation of Fe(II) under environmental conditions. Ferrihydrite commonly exists in iron-containing springs, drainage lines, lake oxide precipitates, ground water and stagnant-water soils, river sediments and, in the oceans, deep sea crusts and manganese nodules (Schwertmann and Cornell, 1991). It is also an extremely important sorbent under acid mine drainage environments (Moore et al., 1991). Furthermore, iron oxyhydroxides such as ferrihydrite which form at the oxic-anoxic boundary in sediments constitute a very effective barrier against upwards diffusing arsenic that is released in the iron reduction zone (Petersen et al., 1995). Arsenic often becomes enriched in upper oxic sediment layers as a consequence of this (Petersen et al., 1995), even when background levels of arsenic are very low (Farmer and Lovell, 1986).

Ferrihydrite, otherwise known as hydrous ferric oxide (HFO), is metastable, and over time it can age into more crystalline minerals *via* a number of pathways. For instance, it has been observed to transform into hematite (under near neutral pH conditions) and goethite (under relatively strong acidic or alkaline conditions) in the laboratory (Schwertmann and Murad, 1983). Goethite appears to be the common ageing product in the field (Tuhela et al., 1997).

Ferrihydrite typically exhibits a very high reactive surface area and it can accumulate large amounts of arsenic by adsorption (Aggett and O'Brien, 1985; Aggett and Roberts, 1986; Fuller and Davis, 1989; Belzile and Tessier, 1990; Fuller et al., 1993; Petersen et al., 1995; Guo et al., 1997) and coprecipitation (Wilson and Hawkins, 1978; Mok et al., 1988). The fate of adsorbed and coprecipitated contaminants upon ageing of ferrihydrite is unclear; they could simply remain adsorbed as surface complexes or they may be incorporated into the bulk crystal structure. In this case, they could only be released upon dissolution of the host mineral. Conversely, they could be expelled from the crystal structure and desorbed during ageing, in which case their mobility and bioavailability would be vastly increased. This is a possibility because amorphous iron (oxyhydr)oxides such as ferrihydrite have a much higher arsenic sorption capacity per unit mass than crystalline ageing products such as goethite (Bowell, 1994).

Whether or not a contaminant ion is coprecipitated into the structure of a mineral, expelled to solution or simply remains adsorbed on the mineral surface has obvious implications for contaminant mobility. However, the effect of a range of secondary processes on contaminant mobility also depends heavily on the physical location of the contaminant. For instance, the reduction of aqueous As(V) can occur *via* both abiotic and biotic mechanisms, whereas the reduction of As(V) that is

sorbed on ferrihydrite can only be achieved by microbes and proceeds many times slower than that of As(V)(aq) (Zobrist et al., 1998). Processes resulting in the reduction of adsorbed As(V) can lead to the release of arsenic to solution because As(III) is less strongly adsorbed by iron (oxyhydr)oxides than As(V) (Bowell, 1994). Thus, an understanding of how the speciation and location of sorbed arsenic changes as ferrihydrite ages is clearly of importance when predicting the long-term risks posed by contaminated sediments. Such knowledge is also of use in improving water treatment processes which currently use iron (oxyhydr)oxides to remove arsenic from wastewater such as that produced in acid mine drainage environments (Shokes and Moller, 1999).

5.1.3 The influence of 'green rust' on arsenic mobility

'Green rusts' are green-blue Fe(II)-Fe(III) hydroxides which were first identified as corrosion products of steel and iron water pipes (Stampfl, 1969). They are postulated to be intermediate phases in the formation of iron (oxyhydr)oxides such as goethite, lepidocrocite and magnetite *via* the oxidation of Fe(II) under reducing and weakly acidic to weakly alkaline conditions (Schwertmann and Fechter, 1994). Importantly, they can also form during the reductive dissolution of existing Fe(III) (oxyhydr)oxides (Hansen et al., 1994; Schwertmann and Fechter, 1994), and Frederickson et al. (1998) have shown that green rust formation can occur during dissimilatory reduction of hydrous ferric oxide by a groundwater bacterium. The mottling often observed in gleyed soil horizons and the grey-green colour in the uppermost layers of some lake and marine sediments has been attributed to the presence of mixed valence minerals such as green rust (Buurman, 1980; Newman, 1987). However, green rust has only been positively identified in recent times (Trolard et al., 1997) because the extreme air-sensitivity of this mineral has made its isolation and characterisation difficult.

Green rust minerals possess the pyroaurite-sjögrenite structure consisting of sheets of $Fe(II)(OH)_6$ in which some of the Fe(II) is replaced by Fe(III) (Taylor, 1973) (Fig. 5.1). This results in a positive layer charge which is balanced by the inclusion of anions such as Cl^-, CO_3^{2-}, and SO_4^{2-} between the layers (Feitknecht and Keller, 1950; Bernal et al., 1959; Stampfl, 1969; Brindley and Bish, 1976). The resulting green rusts are termed GR1(Cl^-), GR2(CO_3^{2-},), and GR2(SO_4^{2-}). Although GR1 and GR2 both have hexagonal close packed structures, GR1 is assigned a rhombohedral space group whereas GR2 is assigned a hexagonal one (Bernal et al., 1959). Sulphate and carbonate are the most commonly reported interlayer anions in

nature, and the sulphate form of green rust has the general formula $Fe_y^{(II)}Fe_x^{(III)}(OH)_{3x+2y-2z}(SO_4)_z$ (Schwertmann and Fechter, 1994).

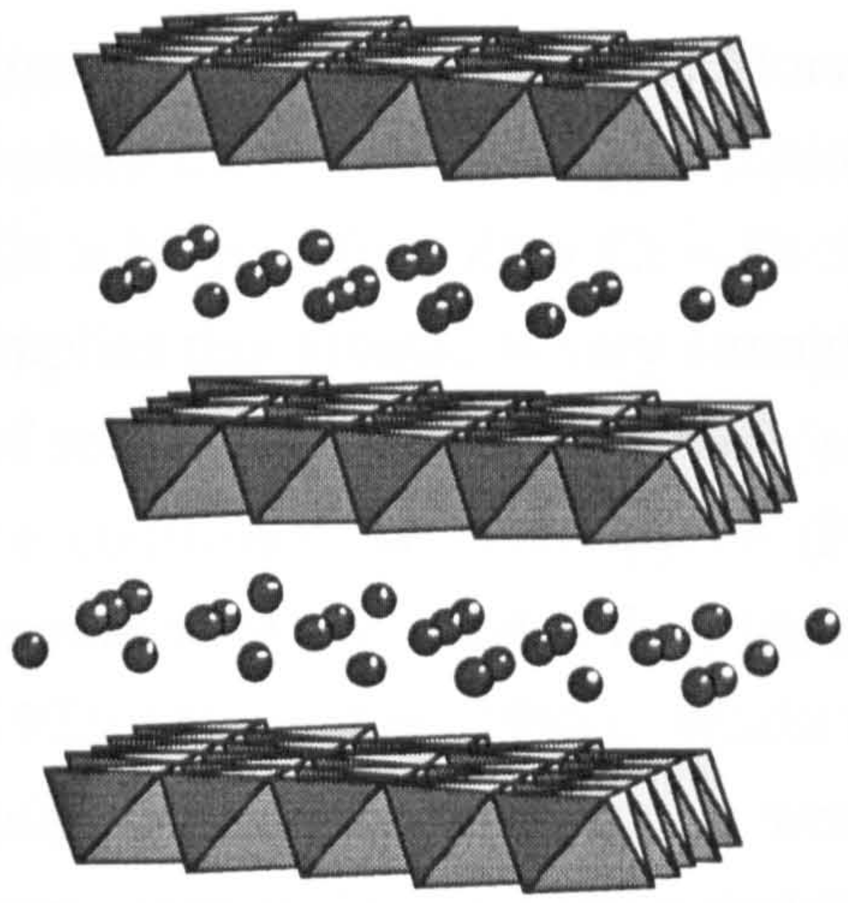

Fig. 5.1. The crystal structure of green rust compounds consists of layers of $Fe(II)(OH)_6$ in which some of the Fe(II) is replaced by Fe(III). These alternate with layers of anions (SO_4^{2-}, CO_3^{2-} and Cl^-) and water which bind the $Fe(OH)_6$ layers via hydrogen bonding The pyroaurite-type structure, which green rust shares, is shown here. The diagram was drawn with CrystalMaker 2.1.0 (Palmer, 1996) using data from Allmann (1968).

Green rusts are of potentially great importance to trace metal mobility in the environment. This is partly because their characteristically poor crystallinity results in a very high reactive surface area, but mainly because of their mixed valence. The presence of Fe(II) in the structure means that green rust can potentially act as a very effective reductant of transition elements such as As(V). The reduction of As(V) following adsorption on green rust would probably lead to the desorption of the more toxic As(III) because this is less strongly adsorbed than As(V) (Bowell, 1994).

To date, relatively few studies of the interaction of trace groundwater components with green rust have been performed. In one investigation, Se(VI) was observed to be reduced directly to Se(0) following adsorption, and more rapidly to Se(0) *via* a Se(IV) intermediate following co-precipitation into the interlayer anion sites (Myneni et al., 1997). Hansen et al. (1994, 1996) have also shown that sulphate green rust is capable of reducing nitrate to ammonium. Importantly, the rates of abiotic selenium and nitrate reduction by green rust were comparable to those achieved *via* microbial pathways (Myneni et al., 1997).

5.1.4 The effect of iron oxyhydroxide sulphidisation on arsenic mobility

Microbially-mediated reactions in anoxic sediments commonly result in the production of large amounts of hydrogen sulphide (Luther and Morse, 1998). The onset of such conditions leads to the reductive dissolution of oxide and silicate minerals (Moore et al., 1988; Canfield, 1989; Masscheleyn et al., 1991). Ferrous iron derived from the reduction of oxides and silicates reacts with dissolved sulphide to produce authigenic acid-volatile iron monosulphides (AVS) (FeS_x; $0.9 < x < 1.5$),

and ultimately pyrite (FeS_2) (Goldhaber and Kaplan, 1974, 1980; Howarth and Jørgensen, 1984). Iron sulphides are very strong scavengers of many trace elements, and they exert the dominant control on contaminant mobility under reducing conditions (Huerta-Diaz and Morse, 1990, 1992; Zhuang et al., 1994). The general pattern for the extent of pyritisation of trace metals is: Hg > As = Mo > Cu > Fe > Co > Ni >> Mn > Zn > Cr = Pb > Cd (Huerta-Diaz and Morse, 1990, 1992). This implies that arsenic is very strongly associated with pyrite following sulphidisation of sediments. However, it has also been suggested that arsenic concentrations may be controlled by arsenopyrite (FeAsS) or authigenic arsenic sulphides such as orpiment (As_2S_3) and realgar (AsS) rather than iron sulphides (Ferguson and Gavis, 1972; Moore et al., 1988). Whilst the majority of research has focused on the role of sulphides in sediments, recent work suggests that authigenic sulphides may also be important in limiting trace metal mobility in soils (Brennan and Lindsay, 1996; Hesterberg et al., 1998).

Although the mobility of arsenic is limited by sorption onto iron-(oxyhydr)oxides or iron sulphides under steady state conditions, aqueous trace metal concentrations can increase dramatically during the reductive dissolution of (oxyhydr)oxides (Korte, 1991; Stumm et al., 1990; Petersen et al., 1995) or the oxidation of sulphides (Zhuang et al., 1994). These reactions are known to take place during the early diagenesis of sediments and dredging activity/storm events, respectively. Under such conditions, there is the possibility that significant amounts of arsenic could be transported away from the site of contamination, and pose a risk to human health. It is clearly of importance that we understand these reactions so that the potential release of contaminants can be predicted. This is especially true when it is realised that external factors such as seasonal changes in groundwater level or reservoir water depth can cause the reduction/oxidation reactions to occur on a repeating, cyclical basis (Moore et al., 1988).

5.1.5 Aims

Because arsenic is such a common and significant contaminant in many soil and groundwater systems, it is essential that the reactions controlling its mobility and bioavailability are understood. This is true over both short- (e.g. adsorption and complexation reactions) and long (e.g. incorporation into mineral structures or release to solution as minerals age) timescales. This chapter describes a series of experiments that have been performed to investigate changes in arsenic speciation and mobility during:

a) adsorption onto ferrihydrite which was subsequently aged to goethite and/or hematite;
b) interaction with a pre-existing green rust phase and during coprecipitation with green rust, with the subsequent oxidation of both forms to lepidocrocite (γ-FeOOH);
c) the sulphidisation of goethite (α-FeOOH) that was contaminated with adsorbed arsenate.

The results have direct applications in assessing the risks posed by contaminated sediments. They should also prove useful in developing wastewater treatment technologies since As_2S_3(am) precipitation is a technique currently used to remove arsenic from waste streams (Robins, 1985).

5.2 EXPERIMENTAL METHODS

5.2.1 General

All reagents used in this study were analytical grade and labware was acid-washed. An Orion model 720A meter was used to make pH measurements with a Willhelm-type reference electrode - glass pH electrode pairing (both from both Sentek Ltd.) during the green rust experiments. The same meter was used with a glass combination electrode (Sentek Ltd.) during the ferrihydrite ageing and goethite sulphidisation experiments. Calibration ± 0.05 pH units was achieved at room temperature with constantly stirred Whatman NBS grade buffers. The As(V) stock solution was prepared from $Na_2HAsO_4 \cdot 7H_2O$ and was stored at 4 °C in a closed amber-coloured HDPE bottle.

5.2.2 Preparation of As(V) on ferrihydrite ageing samples

5.2.2.1 Preparation of pure ferrihydrite

Ferrihydrite was prepared by neutralising 500 ml of a 0.2 M ferric nitrate solution with 1M KOH according to the method reported by Schwertmann and Cornell (1991). Approximately 360 ml of KOH was required to bring the solution to pH 7.5; the last 20 ml was added in a dropwise fashion with constant checking of pH. The resulting deep brown slurry was rinsed clean of contaminant anions (e.g. NO_3^-) by repeated centrifugation and re-suspension in fresh MilliQ water. The clean suspension was allowed to age for 24 hours at room temperature prior to being used.

5.2.2.2 *Ageing of As(V)-contaminated ferrihydrite*

One litre of a thoroughly mixed 20 g L^{-1} ferrihydrite stock suspension was divided equally (by weight) between four 1 litre amber HDPE screw-top containers. The containers were amber-coloured to reduce the risk of unwanted photoredox reactions. 750 ml - X ml of MilliQ with a 0.1 M $NaClO_4$ background electrolyte was then added to each container. X is the volume of 990 ppm As(V) stock solution that, when added, made the total volume of each sample 1000 ml. X = 0, 12.5, 62.5 and 125 ml in samples 'No As-HFO', 'low As-HFO', 'Med. As-HFO' and 'High As-HFO', respectively.

The transformation of ferrihydrite to hematite occurs via an internal dehydration/rearrangement process (Fischer and Schwertmann, 1975). Conversely, goethite is formed by dissolution of the precursor followed by nucleation and growth of the more crystalline phase (Fischer and Schwertmann, 1975). The relative proportion of goethite and hematite in the final product is strongly dependent on pH. Hematite is dominant between pH 5.5 and pH 9, whereas goethite is dominant under higher and lower pH conditions (Schwertmann and Murad, 1983). Because goethite is the most commonly occurring iron (oxyhydr)oxide in temperate climates (Schwertmann and Cornell, 1991), experimental conditions were tailored so that this mineral was the dominant ageing product. It was hoped that reducing the number of variables in this way would assist interpretation of the EXAFS results.

The pH of each suspension was set to 4 with 10% v/v HNO_3 immediately after the As(V) stock solution was added. The system was then allowed to equilibrate at room temperature for two hours; Wilkie and Hering (1996) have previously established that this is long enough for the removal of 100% of available As(V) from solution between pH 4 and 8. After equilibration, the samples were placed in a 60 ± 3°C oven and aged for a total of 1076.5 hours. It is important to note that the mechanisms of ferrihydrite ageing to goethite and hematite are not temperature dependent between 25°C and 70°C (Fischer and Schwertmann, 1975; Cornell and Schwertmann, 1979; Schwertmann and Murad, 1983). Hence, whilst ageing at elevated temperatures has allowed us to accelerate the process, the results are still applicable to low temperature systems.

The pH of all samples decreased as the reactions proceeded, with the rate of pH decrease greatest in 'No As-HFO' and lowest in 'High As-HFO'. The pH of each sample was manually buffered on a frequent basis to keep it within 0.3 pH units of pH 4 for the duration of the reaction. This was achieved by the judicious addition of small amounts of 5M KOH every 2-3 days near the start of the ageing period, and 1M KOH every 4-5 days subsequently. Immediately prior to each pH buffering cycle, approximately 40 ml of well mixed suspension was collected from each sample in brim-full screw-top polypropylene centrifuge tubes. Carbonate has been

shown to have a minor influence on As(V) sorption by (Wilkie and Hering, 1996), or coprecipitate with, ferrihydrite (Fuller et al., 1993), and no attempt was made to exclude CO_2(g) during the ageing process.

Progressive changes in the colour of the suspensions from deep brown to an increasingly yellow ochre ('No As-HFO') or red-yellow ochre (Low and Medium As-HFO) indicated that mineralogical transformations were taking place. The colour of 'High As-HFO' changed little from its initial deep brown colour.

Centrifugation (3000 rpm for 20 - 60 min) was used to separate each reacted suspension into a clear supernate and a viscous paste (the 'adsorption sample') which was frozen prior to analysis. It is interesting to note that the ease of sample settling during centrifugation increased with arsenic content. The supernates were filtered using 0.2 μm cellulose nitrate membrane filters and analysed for arsenic within 24 hours of collection on a Jobin-Yvon JY-24 ICP-AES. Determinations of aqueous arsenic concentration by this technique are often reported to involve a hydride generation step. This was not deemed necessary here as a pilot study showed that our ICP-AES was capable of returning accurate and repeatable determinations of arsenic concentration from a range of standards. It was, however, necessary to constantly flush the instrument optics with argon in addition to the normal nitrogen flow during arsenic analyses. The concentration of dissolved iron was also measured by ICP-AES in a number of samples to check for dissolution of the iron oxyhydroxide during ferrihydrite ageing.

X-ray diffraction was used to determine the mineralogy of the aged samples. XRD slides were prepared by air-drying a water-based suspension of each sample onto small glass discs which were placed in aluminium sample holders during analysis. The relative diffraction peak intensities were used to determine the relative proportion of goethite and hematite in mixed mineralogy samples.

5.2.3 Preparation of As(V)-ferrihydrite 'coprecipitate' ageing samples

A further ferrihydrite sample was generated at pH 4, but this time arsenic was present during the hydrolysis and precipitation of Fe(III) so that the effect that this had on the form of sorbed arsenic and the mineralogy of the ageing product could be investigated. This sample is termed 'pH 4 As-HFO coprecipitate', and it was prepared in the following manner: Forty grams of $Fe(NO_3)_3 \cdot 9H_2O$ was dissolved in 500 ml of MilliQ water that had a 0.1 M $NaClO_4$ background electrolyte and contained 30 ml of a 1340 ppm As(V) stock solution. This mixture was brought to pH 7.5 by the rapid addition of 310 ml of 1M KOH with the subsequent dropwise addition of a further 20 ml. The resulting deep brown slurry was made to 1 litre with

MilliQ water in an amber coloured screw-top container, and its pH was set to 4.0 by the addition of a small volume of 10 % v/v HNO_3. After an equilibration period of approximately 1 hour, a sample was collected from the well mixed suspension in a brim-full 40 ml screw-top polypropylene centrifuge tube, and the remainder of 'pH 4 As-HFO coprecipitate' was aged in an oven at 60 ± 3°C for a total of 886 hours. The pH of 'pH 4 As-HFO coprecipitate' decreased as ageing proceeded, but at such a high rate that it was impossible to prevent its pH from occasionally dropping approximately one unit below the desired value (pH 4) between buffering cycles. Buffering was achieved by the judicious addition of small amounts of 5M KOH every 2-3 days near the start of the ageing period, and 1M KOH every 4-5 days subsequently. Immediately prior to each pH buffering cycle, approximately 40 ml was collected from the well mixed sample. As with the 'As-HFO' samples, no attempt was made to exclude $CO_2(g)$ during the ageing process. Centrifugation, aqueous sample analysis and adsorption sample storage was conducted in the same manner as for the other 'As-HFO' samples. 'pH 4 As-HFO coprecipitate' samples were also characterised by XRD.

5.2.4 Arsenic interaction with green rust

5.2.4.1 Preparation of green rust with adsorbed As(V) ('As-GR' sample series)

The method of Schwertmann and Fechter (1994) was followed to prepare sulphate green rust ($GR2(SO_4^{2-})$) with the expected approximate bulk formula $Fe^{(II)}_2Fe^{(III)}(OH)_5(SO_4)$. Light was excluded from all samples during preparation and analysis to prevent unwanted photoredox reactions. Sample preparation took place in a 500 ml straight-sided polythene beaker. This contained a magnetic follower and was capped by an airtight PVC lid with holes for pH electrodes, gas inlet/outlet ports and sample ports (Fig. 5.2). Sample details are summarised in Table II of the appendix.

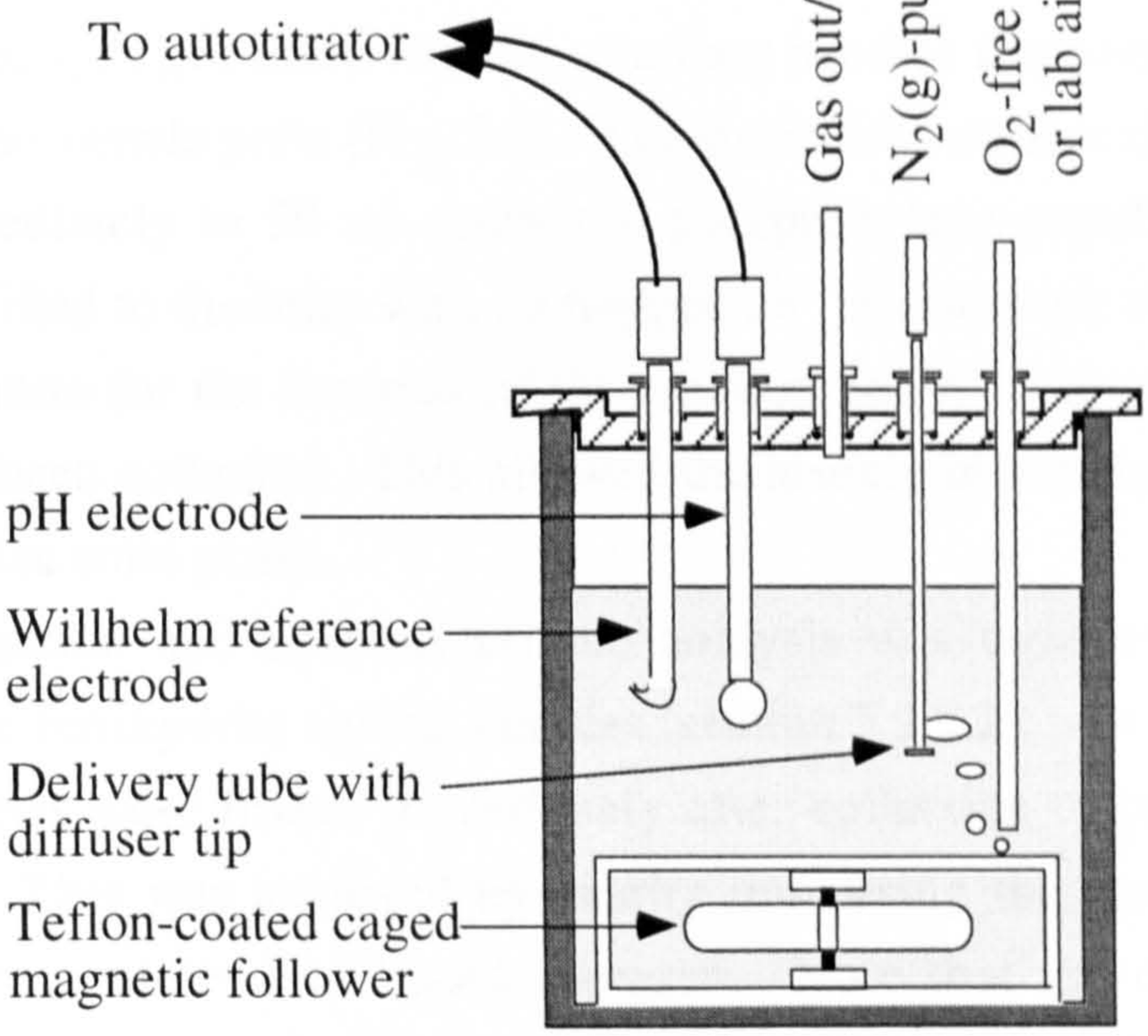

Fig. 5.2. Reaction vessel used to prepare samples of green rust to which As(V) was added after formation ('As-GR' sample series) and prior to nucleation ('As-GRCO' series). The total volume of the reaction vessel was 500 ml, and it was wrapped in aluminium foil at all times to exclude light which may have otherwise caused unwanted photoredox reactions. The 1 M NaOH was supplied by a Metrohm 718 pH-stating titrator; it was stored in a plastic reagent bottle prior to delivery to the reaction vessel to prevent possible leaching of silica from the walls of a glass reagent bottle.

Initially, 370 ml of MilliQ water was added to the beaker and purged with N_2(g) for 48 hours to remove dissolved oxygen prior to the addition of 20.57 g of $FeSO_4 \cdot 7H_2O$. The resulting light green solution was continually purged with N_2(g) whilst the pH was raised from an initial value of ~3.4 to pH 7.0 over a 15 minute period by the addition of CO_2/N_2-free 1.0 M NaOH from a Metrohm 718 pH-stat titrator. Once pH 7.0 was reached, the N_2(g) flow was replaced with laboratory air supplied by a small pump *via* an open ended 4 mm ID glass tube. The light green solution started to darken in colour and become more turgid as soon as air flow began, and passed through consecutive dark green-blue, ochre-green and finally bright orange stages over a period of approximately 6 hours. Because the oxidation/hydrolysis reaction liberates protons, the 718 titrator was required to constantly add 1.0 M NaOH throughout the reaction to maintain pH at 7.0 ± 0.1. The rate of base addition was high for the first ~100 minutes of reaction (~0.6

ml/min), but subsequently decreased to a much lower and constant value of ~0.03 ml/min.

The dark green suspension was first sampled after 50 minutes, and 14.7 ml of a 1340 ppm As(V) stock solution was then added. Further samples were collected periodically throughout the course of the 18 hour reaction. Sampling was achieved with 20 ml plastic syringes fitted with 50 mm long needles that were used to pierce rubber septa in the sample ports (Fig. 5.2). The suspension collected in this way was transferred immediately to 50 ml screw-top polypropylene copolymer centrifuge tubes that were filled to the brim with no trapped air. These were stored in the dark at room temperature for the duration of the reaction and then centrifuged after the last sample had been collected. This allowed the arsenic in solution ample time to equilibrate with the solid phase.

Centrifugation and aqueous sample analysis was conducted in the same manner as for the ferrihydrite ageing samples (section 5.2.2.2). All of the green rust adsorption samples were frozen immediately after collection to prevent oxidation during storage. This was achieved by briefly immersing the centrifuge tubes in which they were contained in liquid nitrogen. Note that the concentration of dissolved iron was also measured by ICP-AES in all samples to establish the relationship between levels of dissolved arsenic and iron as a function of reaction time.

X-ray diffraction was used to determine the mineralogy of all samples. The XRD slides were prepared by air-drying a glycerol-based suspension of each sample onto small glass discs. The glycerol-based suspension was generated by quickly mixing a drop of each green rust sample with a small amount of glycerol. This resulted in a viscous paste which protected the air-sensitive samples against oxidation during XRD analysis (Hansen et al., 1994). Note that there was no significant difference in diffraction patterns collected from a fully oxidised sample with and without the glycerol matrix (see section 5.3.3.2). Comparison of the relative intensity of observed green rust and lepidocrocite diffraction peaks allowed a qualitative assessment of the rate of green rust oxidation.

The reproducibility of the green rust preparation method was verified by generating a set of duplicate samples and analysing them by XRD. The results from both sets of samples were in good agreement.

5.2.4.2 Preparation of green rust with coprecipitated As(V) ('As-GRCO' sample series)

A series of green rust samples were prepared and progressively oxidised in the presence of As(V) using exactly the same method that was used to prepare the 'As-GR' sample series, with the exception that the As(V) stock solution was added

prior to, rather than after, the nucleation of green rust from solution. Samples were first collected 1 hour after green rust formation commenced, and then periodically throughout the 18 hour reaction. Sample collection and treatment was exactly the same as detailed in section 5.2.4.1.

5.2.5 Sulphidisation of As(V)-contaminated goethite

5.2.5.1 Sample preparation

A 41.5 g L^{-1} goethite stock suspension was prepared according to the method detailed in section 5.2.6.1. Approximately 125 ml of this stock suspension was added to the reaction vessel shown in Fig. 5.3 and made to a total volume of 1.0 L with MilliQ water with a 0.1 M $NaClO_4$ background electrolyte. A pipette was then used to add 20.0 ml of a 1340 ppm As(V) stock solution to the reaction vessel, and the pH of the As(V)-goethite suspension was subsequently buffered from ~pH 8.5 to pH 6.0 by the addition of a small amount of 10% HNO_3. After 5 minutes at pH 6.0, two 20 ml samples (GS2 and GS bulk chem.) were collected using 20 ml plastic syringes with 50 mm stainless steel tips.

Following equilibration at pH 6.0 ± 0.1 for approximately 2 days, sample GS3 was collected as per GS2. After a further day of equilibration at pH 6.0 ± 0.1, the suspension began to be purged with $H_2S(g)$. This was delivered to the closed reaction vessel in a nitrogen carrier gas following generation by the slow addition of 10% HCl to a stirred ~1M HNaS solution in a roundbottom flask (Fig. 5.3). The HCl was fed by a Metrohm 721 autotitrator at a rate of 0.5 ml min^{-1} for the first 4 hours and 0.1 ml min^{-1} subsequently. Purging with hydrogen sulphide caused the pH of the suspension to drop from 6.0 to a stable value of 5.2 ± 0.1 over a 4 hour period. Although the suspension was still an ochre yellow colour after 2 hours of hydrogen sulphide flow, it had turned deep olive green-black when sample GS4 was collected (as per GS2) after 4.5 hours. It is interesting to note that very brief exposure to air caused the deep olive green-black suspension to revert to its previous ochre yellow colour at this stage in the sulphidisation.

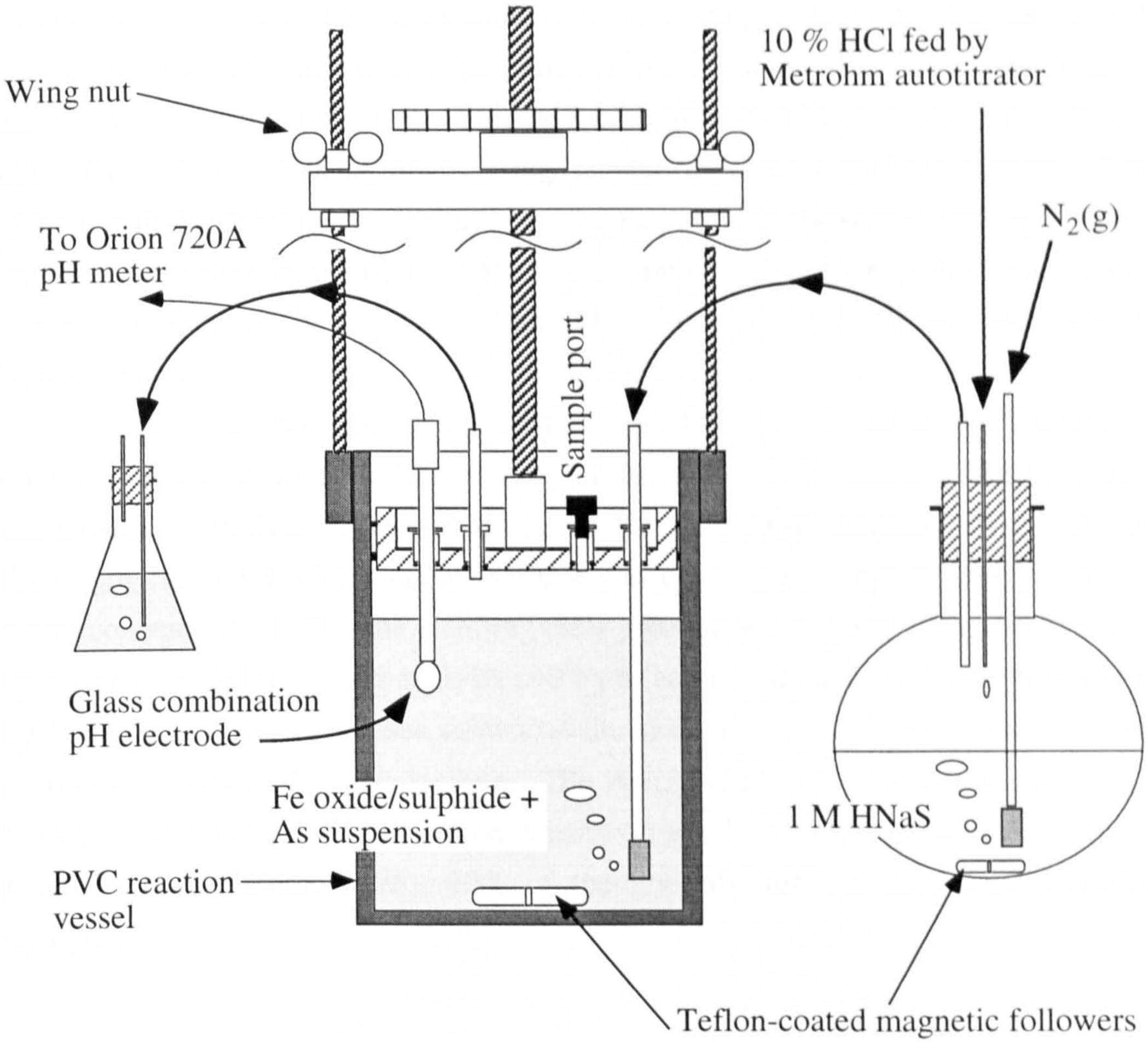

Fig. 5.3. Experimental apparatus used to sulphidise As(V)-contaminated goethite. The lid of the reaction vessel is on a central threaded shank, and was moved down (by turning the large knurled wheel) each time samples were taken to ensure that subsequent samples could be collected and that the electrode remained submerged. Rubber O-rings under all threaded plugs and around the lid ensured that the reaction vessel was gas-tight at all times. H_2S(g) was generated by the slow dropwise addition of 10 % HCl to a ~ 1 M HNaS solution, and transferred to into the reaction vessel in an O_2-free N_2(g) carrier gas. Outlet gas was fed through a small conical flask of water to prevent atmospheric oxygen entering the reaction vessel through the outlet gas pipe. Diagram is not to scale; reaction vessel brim-full volume is ~ 1.5 L.

Centrifugation, aqueous sample analysis (dissolved arsenic and iron concentration), adsorption sample storage (freezing) and characterisation (XRD) of samples GS2 to GS9 was performed in the same manner as for the green rust samples (section 5.2.4.1). Total dissolved hydrogen sulphide (H_2S, HS^- and S^{2-}) was also determined in samples GS4 to GS9 by a method modified from Cline (1969) (see section 2.1.3 for further information). Samples were collected in duplicate (except for GS4 and GS6) with minimal exposure to oxygen. Dissolved sulphide was chemically fixed by mixing each 1 ml sample with 0.25 ml of a 10% zinc acetate solution, thereby allowing samples to be stored safely prior to analysis. During analysis, a UV-vis spectrophotometer (CECIL CE292, Cecil Instruments,

Cambridge, U.K.) was used to measure colour intensity at 670 nm. The instrument was calibrated with previously prepared sulphide standards, all of which gave absorbance values below 0.92. This was of importance because colour intensity obeys Beer's Law in this region, ensuring a linear response from the instrument. The detection limit under these conditions is < 10 μM. There was excellent agreement between sulphide standard concentrations measured before and after sample analysis, indicating the high reproducibility of this method and the low level of instrument drift.

Sample 'GS bulk chem.' was not frozen. It was analysed within 2 hours of collection to ascertain the bulk chemistry of the initial As(V)-contaminated goethite suspension. Analysis was performed in the following manner: 5 ml of the thoroughly mixed 'GS bulk chem.' sample was dissolved in approximately 5 ml of warm concentrated HCl. The resulting clear solution was diluted with MilliQ water by a factor of 20 for arsenic analysis and by a factor of 2000 for iron analysis (both by ICP-AES). These analyses show that the suspension initially consisted of 29.6 ppm arsenic and 5.05 g L^{-1} goethite. The As/(As+Fe) ratio was thus 6.89 x 10^{-3}. Using a maximum As(V) adsorption density on goethite of 1.58 sites nm^{-2} (derived from Sun and Doner, 1996), 90% of the goethite surface sites were initially occupied.

5.2.6 Preparation of EXAFS reference standards

A number of samples were prepared from highly characterised starting materials for use as the EXAFS standards. The data collected from these standards was used for reference whilst analysing EXAFS data from the 'unknown' samples.

5.2.6.1 As(V) on goethite, hematite and lepidocrocite

Goethite was prepared by hydrolysing a ferric nitrate solution at pH 12-13 and 70 °C for 60 hours (Schwertmann and Cornell, 1991). Plastic labware was used throughout to avoid the danger of the high pH solution leaching silica from glassware. The ochre yellow precipitate was collected by centrifugation and cleaned by dialysis against frequently changed MilliQ water for one week. The general crystal morphology was examined by TEM and electron diffraction. Goethite crystallites measured approximately 4000 nm long by 150 nm wide. They displayed a characteristic elongate lath-like morphology with a diamond shaped cross-section bounded mainly by the (110) surfaces with little or no contribution from the (100) and (010) surfaces. The chain terminations were bounded by the (021) surfaces which are estimated to comprise ~2 % of the overall crystal surface area (Fig. 3.2).

Hematite was prepared by hydrolysis of ferric nitrate (Schwertmann and Cornell, 1991). Two litres of 0.002 M HNO_3 in a Duran flask was heated to 98 °C in an oven. Precisely 16.6 g of un-hydrolysed $Fe(NO_3)_3 \cdot 9H_2O$ were then added with vigorous stirring to generate a 0.02 M Fe(III) solution. The closed Duran flask was then held at 98 °C for seven days, after which the bright red precipitate was collected and washed by repeated centrifugation and re-suspension in fresh MilliQ water.

Lepidocrocite was prepared by the oxidation/hydrolysis of a $FeCl_2$ solution at pH 6.7 - 6.9 (Schwertmann and Cornell, 1991). The product was collected and cleaned using the method described above for goethite. Transmission electron microscopy showed the crystallites to measure approximately 300 nm long by 125 nm wide, displaying the platy morphology (with thickness « width) that is characteristic of this mineral. The ends of the crystallites had a serrated appearance whilst the sides were relatively straight.

Each cleaned mineral suspension was stored as a refrigerated stock suspension prior to use. The identity and purity of the crystalline products was confirmed by X-ray powder diffraction of randomly oriented powder samples. Additionally, the surface area of goethite (34 ± 3 $m^2 g^{-1}$), hematite (20 $m^2 g^{-1}$) and lepidocrocite (88 ± 3 $m^2 g^{-1}$) was determined by BET surface area analysis following 12 hours of outgassing with $N_2(g)$. The analytical error of $\pm$ 3 $m^2 g^{-1}$ was determined by repeated measurements.

Immediately prior to preparation of the EXAFS reference standards, aliquots of the goethite, hematite and lepidocrocite stock suspensions were air dried at ~50°C for 48 hours. The dry material was then crushed with an agate mortar and pestle. In all cases, precisely 0.50 g of the resulting fine powder was weighed out into 370 ml of MilliQ water with a 0.1 M $NaClO_4$ background electrolyte. The added mineral powders were thoroughly dispersed by a combination of stirring and treatment in an ultrasound bath, and were allowed to re-hydrate over a 24 hour period. Subsequently, 0.93 ml of a 1340 ppm As(V) stock solution was added to the goethite suspension, and 1.12 ml of the same stock solution was added to the hematite and lepidocrocite suspensions with stirring. The goethite and hematite suspensions were equilibrated at pH 3.9 ± 0.05 under ambient temperature and atmospheric conditions for 24 hours with the use of a Metrohm 718 pH stat titrator containing 0.1 M HNO_3. The same conditions and equipment were used during equilibration of the lepidocrocite suspension, except that pH was maintained at 7.0 ± 0.05 by the addition of 0.1 M NaOH from the titrator.

It should be noted that a maximum of 0.7 ml of HNO_3 or NaOH was added to any sample to achieve the desired pH, and that such additions resulted in minimal changes in total sample volume. Centrifugation, aqueous sample analysis and solid sample storage was conducted in the same manner as for the ferrihydrite ageing

samples. Percentage surface loading values, which describe the proportion of available surface sites occupied by adsorbed arsenic, were calculated using a surface site density for As(V) on goethite of 1.58 sites nm^{-2} derived from Sun and Doner (1996).

5.2.6.2 Mineral reference standards

Samples of orpiment (As_2S_3) and scorodite ($FeAsO_4 \cdot 2H_2O$) were obtained from University of Bristol, Department of Earth Sciences, courtesy of Dr. Liz Loeffler. The samples were ground to a fine powder in an agate mortar and pestle that was part-filled with acetone to keep dust down. Small drops of the acetone-based suspension were dried onto glass discs, and subsequently analysed by XRD to confirm the mineralogy of each sample. The remainder of the powdered samples was spread into a fine coating on layers of Sellotape. The coated layers of tape were subsequently made into EXAFS samples by cutting them up and stacking them one on top of the other.

5.2.7 EXAFS theory, data collection and analysis

5.2.7.1 General description of EXAFS spectroscopy

An EXAFS spectral scan is obtained by measuring X-ray absorption over a range of photon energies which includes the 'absorption edge' of the element of interest (e.g. Brown et al., 1988, 1995; Charlet and Manceau, 1993). Curve fitting allows determination of the *average* number (N_j) (± 20 %) of atoms in the jth atomic shell, their distance (R_j) (± 0.02 Å) from the central excited cadmium atom, their identity, and the associated Debye-Waller factor ($2\sigma_j^2$) (e.g. Brown et al., 1988). The latter parameter represents the mean square of variation in distance between the element of interest and the shell under consideration. It accounts for damping of the EXAFS oscillations due to thermal vibration (σ_T) and static disorder (σ_S) within atomic shells (e.g. Brown et al., 1995). The quality of the fit between the experimental and simulated EXAFS functions is represented by the *R* factor:

$$R_{EXAFS} = \sum_i \frac{1}{\sigma}(|\chi_i(k)^{exp} - \chi_i(k)^{theory}|) \times 100\%$$

where σ is the standard deviation of the difference between experimental ($\chi^{experiment}$) and theoretical (χ^{theory}) EXAFS functions over a specified k range. For poorly ordered mineral-aqueous systems such as those described here, an *R* value between

20% and 40% indicates an acceptable match between theory and experiment (Dent and Mosselmans, 1992).

5.2.7.2 Data collection

EXAFS data were collected at the CLRC Synchrotron Radiation Source at Daresbury Laboratory, U.K. Spectra were collected at the arsenic K-edge (11.8667 keV) on station 16.5. Data from the aged As-HFO samples and the associated As(V) on goethite/hematite reference standards was collected under room temperature conditions. However, data from the green rust and goethite sulphidisation samples and the As(V) on lepidocrocite reference standard was collected at 77 K to minimise the risk of oxidation. Station 16.5 is equipped with a water cooled, harmonic rejecting double crystal Si (311) monochromator and a 1.2m long plane mirror which is bent to provide vertical focusing. Because the focusing mirror minimised higher harmonics in the EXAFS spectra, it was not necessary to detune the monochromator during data collection. The storage ring energy was 2.0 GeV and the beam current varied between 130 and 240 mA during data collection. Each adsorption sample was presented to the X-ray beam as a viscous paste held by Sellotape in a 2 mm-thick Teflon slide with a 4 x 15 mm sample slot. EXAFS data were collected from the samples and goethite/hematite/lepidocrocite standards during four to six fluorescence mode scans using an Ortec 30-element solid state detector. EXAFS data were also collected from the EXAFS reference standards scorodite ($FeAsO_4 \cdot 2H_2O$) and orpiment (As_2S_3) in three room temperature transmission mode scans. Both minerals were presented to the X-ray beam as a finely ground powder that was evenly spread on layers of Sellotape. These were stacked one atop of the other to achieve a suitable EXAFS signal.

5.2.7.3 Data analysis

EXAFS data reduction was performed using Daresbury Laboratory software (EXCALIB and EXBACK) (Binsted et al., 1991). EXCALIB was used to calibrate from monochromator position (millidegrees) to energy (eV) and to average multiple spectra from individual samples. EXBACK was used to define the start of the EXAFS oscillations and perform background subtraction.

The exact curved wave theory EXAFS analysis program EXCURV98 (Gurman et al., 1984, 1986; Joyner et al., 1987; Gurman, 1988; Binsted et al., 1991, 1992) was used to analyse the EXAFS data. This process involved the comparison of experimental data with theoretical EXAFS oscillations that were derived by EXCURV98 from model clusters. The geometry of these clusters was based on knowledge of the likely arsenic coordination environment in each sample. In all

cases, the cluster that provided the closest initial fit underwent least squares refinement of: Debye-Waller factor, number of atoms per shell, As-X distance, and Fermi energy to improve the fit between its theoretical oscillations and the experimental data. This caused the composition and geometry of the model cluster to approach the true structure and chemistry of the adsorption complex. The value of some parameters were held constant in the early stages of fitting, but all parameters were normally unconstrained during the final stages of data analysis. The model clusters initially consisted of only one atomic shell. Successive shells were added to the theoretical model until each significant peak in the Fourier transform of the EXAFS data was accounted for. Statistical tests (Joyner et al., 1987) were performed to ascertain the significance of each new atomic shell, and only those which improved the fit between theory and experiment at the 99% level of confidence were retained.

Refining theoretical models to find agreement with experimental data in this way provided shell parameters that describe the average local coordination environment around adsorbed arsenic. Care was taken during curve fitting to check whether any of the atomic shells could be assigned to the known structure of arsenic-containing solids such as scorodite ($FeAsO_4 \cdot 2H_2O$).

The phase-shift functions used in the curve fitting were derived by *ab initio* methods in EXCURV98 using Hedin-Lundqvist potentials (Hedin and Lundqvist, 1969) and von Bart ground states. The use of theoretical values is justified by good agreement between the structures of scorodite and orpiment derived from EXAFS data in this study using theoretical phase-shift functions (Fig. 5.4) and the published data from these minerals (Kitahama et al., 1975; Helz et al., 1995).

5.2.8 Interpretation of EXAFS data

To a first approximation, the inner sphere complexation of As(V) with iron (oxyhydr)oxide mineral surfaces can be described by the combination of $Fe(O,OH)_6$ octahedra at the mineral surface and $H_2AsO_4^-$ tetrahedra from solution. These can be linked by sharing edges, corners or apices. Because each type of linkage results in a discrete and characteristic As-Fe distance, EXAFS spectroscopy can be used to discriminate between the different mechanisms of attachment. For instance, single edge sharing between arsenic and ferric iron octahedra results in an As-Fe distance of ~2.8 ± 0.1 Å, double corner sharing leads to an As-Fe distance of ~3.3 ± 0.1 Å, and single corner sharing results in a As-Fe distance of 3.6 ± 0.1 Å (Waychunas et al., 1993; Manceau, 1995). This is known as the 'polyhedral approach' to EXAFS data interpretation (e.g. Combes et al., 1989).

5.3 RESULTS AND DISCUSSION

5.3.1 EXAFS reference standards

EXAFS data from the EXAFS reference standards are shown in Fig. 5.4 and summarised in Table 5.1.

Table 5.1. EXAFS results from EXAFS reference standards. CN_X is number of atoms in a shell at distance R_X (Å) from the central cadmium atom. $2\sigma^2_X$ (Å^2) is the associated Debye-Waller factor. The *R* factor gives a measure of the agreement between experimental and theoretical EXAFS curves. $R < 20\%$ indicates a very good fit whereas $R \leq 40\%$ is acceptable.

Sample	$R_{As\text{-}O}$	CN_O $2\sigma^2_O$	$R_{As\text{-}S}$	CN_S $2\sigma^2_S$	$R_{As\text{-}Fe1}$	CN_{Fe1} $2\sigma^2_{Fe1}$	$R_{As\text{-}Fe2}$	CN_{Fe2} $2\sigma^2_{Fe2}$	*R* factor
Scorodite $FeAsO_4 \cdot 2H_2O$	1.68	4.0 *0.004*	-	-	3.38	3.9 *0.013*	-	-	25.1
As(V) on goethite 36.6% SL 0.24 wt%	1.69	4.0 *0.004*	-	-	2.85	0.8 *0.019*	3.31	1.5 *0.011*	22.0
As(V) on hematite 0.29 wt%	1.69	4.0 *0.005*	-	-	2.86	1.1 *0.020*	3.32	1.1 *0.014*	20.0
As(V) on lepidocro. 17.4% SL 0.3 wt%	1.69	4.0 *0.003*	-	-	-	-	3.32	1.7 *0.011*	22.0
Orpiment As_2S_3	-	-	2.29	2.9 *0.005*	3.20 **As-As**	1.0 **As** *0.016*	3.56 **As-As**	2.4 **As** *0.020*	21.2

Notes:

† % SL = percentage surface loading, which describes the proportion of available surface sites occupied by adsorbed arsenic. These values were calculated using a maximum surface site density for As(V) of 1.58 sites nm^{-2} on goethite derived from Sun and Doner (1996).

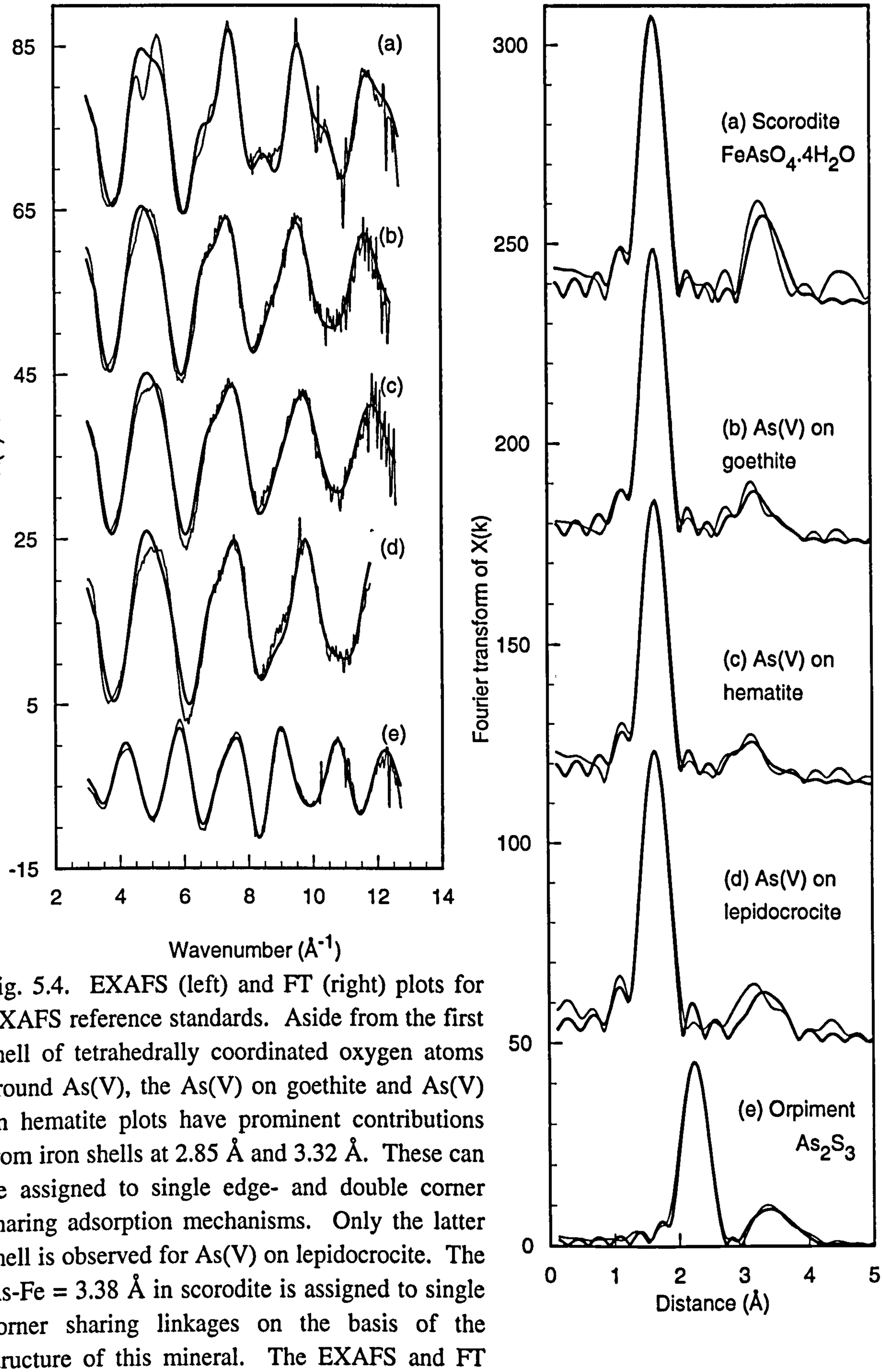

Fig. 5.4. EXAFS (left) and FT (right) plots for EXAFS reference standards. Aside from the first shell of tetrahedrally coordinated oxygen atoms around As(V), the As(V) on goethite and As(V) on hematite plots have prominent contributions from iron shells at 2.85 Å and 3.32 Å. These can be assigned to single edge- and double corner sharing adsorption mechanisms. Only the latter shell is observed for As(V) on lepidocrocite. The As-Fe = 3.38 Å in scorodite is assigned to single corner sharing linkages on the basis of the structure of this mineral. The EXAFS and FT plots for orpiment are distinctly different, with a S shell at 2.29 Å and As shells at 3.20 and 3.56 Å.

The spectra from all samples except orpiment are dominated by a shell of four oxygen atoms at a distance of 1.69 Å from the central As(V) atom. The low Debye-Waller factors (0.003 - 0.005 $Å^2$) for this shell are an indication of its rigidity. Beyond the oxygen shell, iron shells at As-Fe distances of 2.85 - 2.86 Å and 3.31 - 3.32 Å are clearly visible in the As(V) on goethite and As(V) on hematite FT plots. On the basis of geometrical considerations, these are assigned to (bidentate) single edge- and (bidentate) double corner sharing adsorption mechanisms (Fig. 5.5). There is no evidence for (monodentate) single corner sharing adsorption, which has a characteristic As-Fe distance of 3.65 Å (Waychunas et al., 1993). Bidentate arsenate site attachment should be strongly favoured thermodynamically and kinetically over monodentate attachment because of the greater strength of the bidentate chemical bonding, and the likelihood that any monodentate arsenate can add a bond and become bidentate (Waychunas et al., 1993). Thus, it is possible that monodentate adsorption is not observed because the sorption capacity of the more favourable bidentate adsorption sites is not exceeded at the studied surface loading levels.

The observed interatomic distances and coordination numbers are in good agreement with previous studies of As(V) adsorption on goethite, which identified As-Fe distances of 2.80 Å - 2.83 Å (Manceau, 1995) and 3.29 Å (Waychunas et al., 1993). There has, however, been some debate in the literature as to the importance of the 2.80 - 2.83 Å (edge sharing) shell. Waychunas et al. (1993, 1995) find little or no EXAFS evidence for its existence, and argue that arsenate tetrahedra would have to be deformed in order to achieve single edge adsorption. Conversely, Manceau (1995) provides good EXAFS evidence for the adsorption of significant amounts of arsenate at the edge sharing sites; the results presented here are in strong agreement with the latter view.

Although the fits for As(V) on goethite and As(V) on hematite yield very similar numbers, the ratio of CN_{Fe1} to CN_{Fe2} is higher in the case of hematite. This suggests that single edge sharing adsorption is more important in this sample than it is in the case of As(V) on goethite.

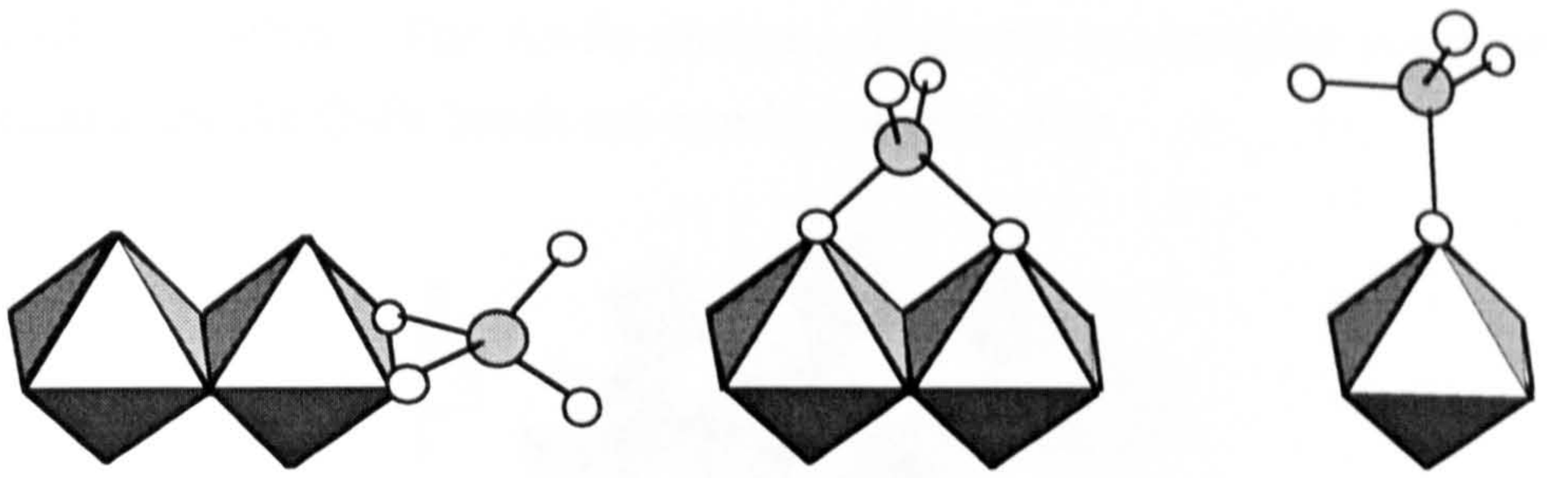

Fig. 5.5. Mechanism of arsenate attachment on $Fe(O,OH)_6$ octahedra. The associated interatomic distances are for As(V) adsorbing to $Fe(III)O_6$ octahedra, and will be slightly longer for As(V) adsorption on $Fe(II)O_6$ octahedra. As-Fe distances are from Waychunas et al. (1993) and Manceau (1995).

The dominant iron shell contribution in As(V) on lepidocrocite is at an As-Fe distance of 3.32 Å (Fig. 5.4 d), indicating that As(V) predominantly adsorbs to this mineral via a double corner sharing mechanism. Inclusion of a shell containing 1.0 iron atom at 2.85 Å does improve the agreement between theory and experiment in the FT plot. Since it does not, however, lead to a statistically significant improvement in the quality of the fit to the EXAFS data, the 2.85 Å shell is not included in the final fit (Table 5.1).

Thus, arsenate adsorbs to all of the EXAFS reference standards by forming inner sphere bonds with hydroxyl groups at the mineral surface. This is consistent with the findings of previous spectroscopic studies (e.g. Waychunas et al., 1993, 1995; Hsia et al., 1994; Manceau, 1995; Sun and Doner, 1996; Fendorf et al., 1997) and wet chemistry studies (e.g. Grossl and Sparks, 1995). The results of a pressure-jump relaxation study also support the suggestion that As(V) bonds to iron (oxyhydr)oxides by forming inner sphere complexes (Grossl et al., 1997).

Aside from the tetrahedral oxygen shell, the scorodite ($FeAsO_4 \cdot 2H_2O$) spectra are dominated by a single iron shell at an As-Fe distance of 3.38 Å. This is in good agreement with the As-Fe distance of 3.358 Å derived by Kitahama et al. (1975) using XRD, and gives us confidence that the phase shifts (derived by *ab initio* methods in EXCURV98) used during EXAFS data analysis are accurate. The As-Fe distance of 3.38 Å is assigned to single corner linkages between arsenate tetrahedra and FeO_6 octahedra, on the basis of the known crystal structure of this mineral (Fig. 5.6). Single corner sharing with a linear bond through the apices of FeO_6 octahedra and arsenate tetrahedra should yield the greatest possible As-Fe distance (Fig. 5.5); Waychunas et al. (1993) suggest that this is 3.65 Å for As(V)

adsorbed on goethite. The As-Fe distance observed in scorodite is not as large as this because the As-O-Fe bonds are non-linear (Fig. 5.6).

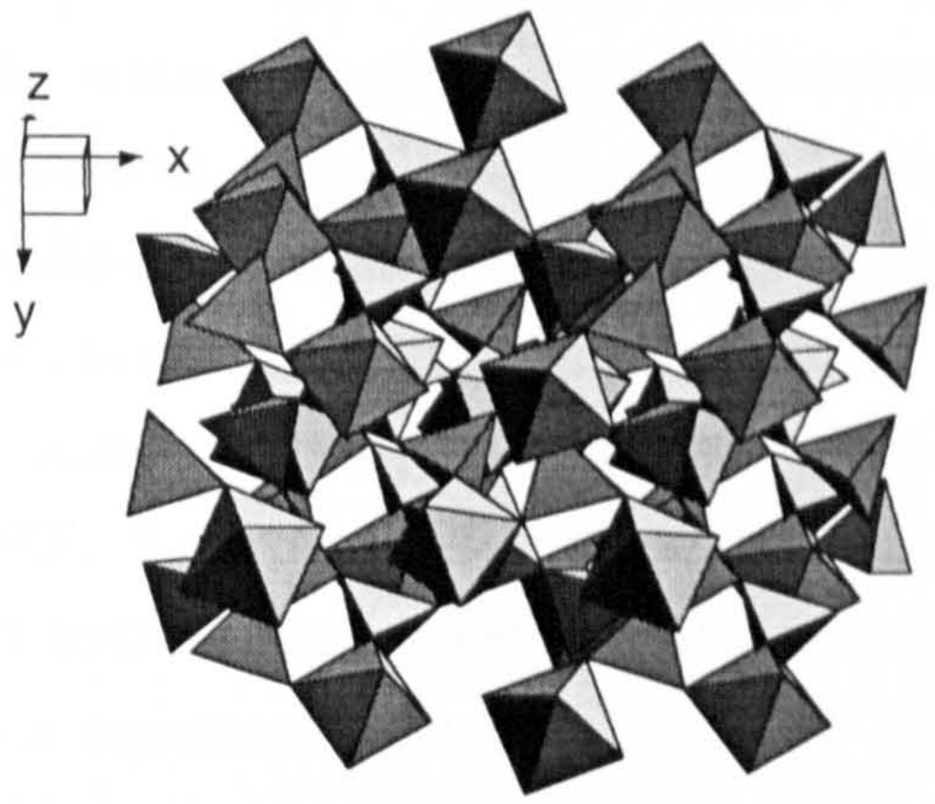

Fig. 5.6. The crystal structure of scorodite ($FeAsO_4 \cdot 2H_2O$). Diagram created in CrystalMaker 2.1.0 (Palmer, 1996) using data from Kitahama et al. (1975).

The orpiment EXAFS data and its Fourier transform (Fig. 5.4 e) are distinctly different to those from adsorbed As(V) (Fig. 5.4 a-d). The most prominent feature of the data is a shell of three sulphur atoms at an As-S distance of 2.29 Å, outside which there are arsenic shells at As-As distances of 3.20 Å and 3.56 Å (Table 5.1). The interatomic distances and coordination numbers derived from this data are in good agreement with the findings of a previous EXAFS study of this mineral (Helz et al., 1995). This gives us further confidence that the phase shifts used during EXAFS data analysis are correct.

5.3.2 Ageing of arsenic-contaminated ferrihydrite

5.3.2.1 Chemical observations from ageing of arsenic-contaminated ferrihydrite

Iron was not released to solution during ageing of any arsenic-contaminated ferrihydrite (As-HFO) sample. More importantly, there was no release of arsenic to solution during ageing. This indicates that even though the iron oxyhydroxide sorbents were becoming increasingly crystalline (see section 5.3.2.2), with a concomitant decrease in reactive surface area highly likely (Fuller et al., 1993), the sorption capacity for As(V) was not exceeded. To put this into perspective, let us assume that all of the ferrihydrite in 'Low As-HFO', 'Med. As-HFO' and 'High As-HFO' had aged into goethite with a surface area of 30 $m^2\,g^{-1}$. If this were the case, the percentage of available surface sites occupied by As(V) in these three samples would be 48%, 238% and 478%, respectively. The lack of As(V) release is almost certainly a result of the fact that 'High As-HFO', and 'Med. As-HFO' to a lesser

extent, underwent incomplete transformation during the 1076.5 hour reaction time (see section 5.3.2.2). It may also be due in part to the low pH of the system (~pH 4) which favours As(V) sorption. These findings differ from those of Fuller et al. (1993), who observed the release of arsenic during the room temperature ageing of an As(V)-HFO coprecipitate at ~pH 8. It also differs markedly from my findings during the ageing of Cr(III)-contaminated ferrihydrite at pH 12.9, where a constant release of chromium was observed (Chapter 6).

All sample supernates tended to become more acidic as ageing proceeded. The pH of 'No As-HFO', 'Low As-HFO', 'Med. As-HFO' and 'High As-HFO' decreased at a rate of 0.1 to 0.3 units per day near the start of the reaction. This rate gradually decreased to a constant value of 0.01 to 0.1 units per day after about twenty days, presumably as the ferrihydrite precursor was progressively reacted away. The rate of pH decrease always followed the same order: 'No As-HFO' > 'Low As-HFO' > 'Med. As-HFO' > 'High As-HFO'. This, combined with the fact that the colour change after 1076.5 hour of ageing was greatest in 'No As-HFO' and least in 'High As-HFO', suggests that the measured rate of pH decrease was a reasonable indicator of reaction rate.

The rate of pH decrease in the 'pH 4 As-HFO coprecipitate' sample was always greater than in all other As-HFO samples. It was initially 0.45 units per day and decreased to a constant value of ~0.15 units per day after twenty days. This sample had an As/(As+Fe) ratio very similar to that of 'Low As-HFO' (0.0054 and 0.0033, respectively). Consequently, the difference in the rate of pH change suggests that the reaction in 'pH 4 As-HFO coprecipitate' proceeded in a slightly different manner to that in the other As-HFO samples.

5.3.2.2 X-ray diffraction results from ageing of arsenic-contaminated ferrihydrite

X-ray diffraction powder patterns from the goethite and hematite EXAFS reference standards are shown in Fig. 5.7 (a) and (b) for comparison with data from the As-HFO ageing products (Fig. 5.7 c-g). Peak positions and relative intensities in Fig. 5.7 (a) and (b) are in good agreement with JCPDS cards 29-713 (goethite) and 13-534 (hematite), respectively.

The diffraction peaks in powder patterns from the 'No As-HFO' series of samples can almost exclusively be assigned to goethite (Fig. 5.7 c). The two non-goethite peaks are relatively weak and can be assigned to hematite, indicating the presence of trace amounts of this mineral. This is to be expected since previous studies have shown that the product of ferrihydrite ageing at pH 4 is 95% goethite and 5% hematite (Schwertmann and Murad, 1983).

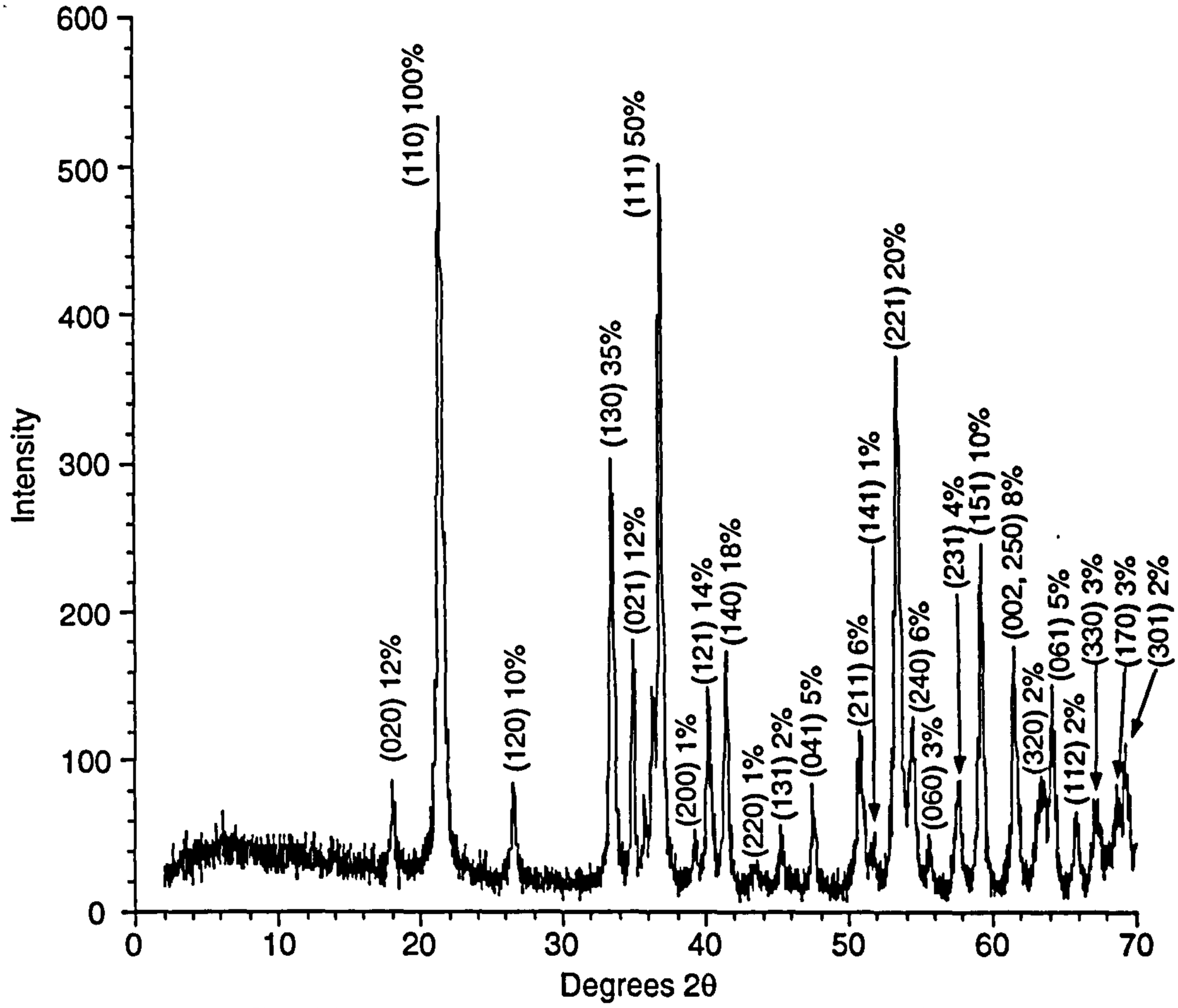

Fig. 5.7 a. Goethite XRD reference standard. Numbers in parentheses are published relative peak intensity values.

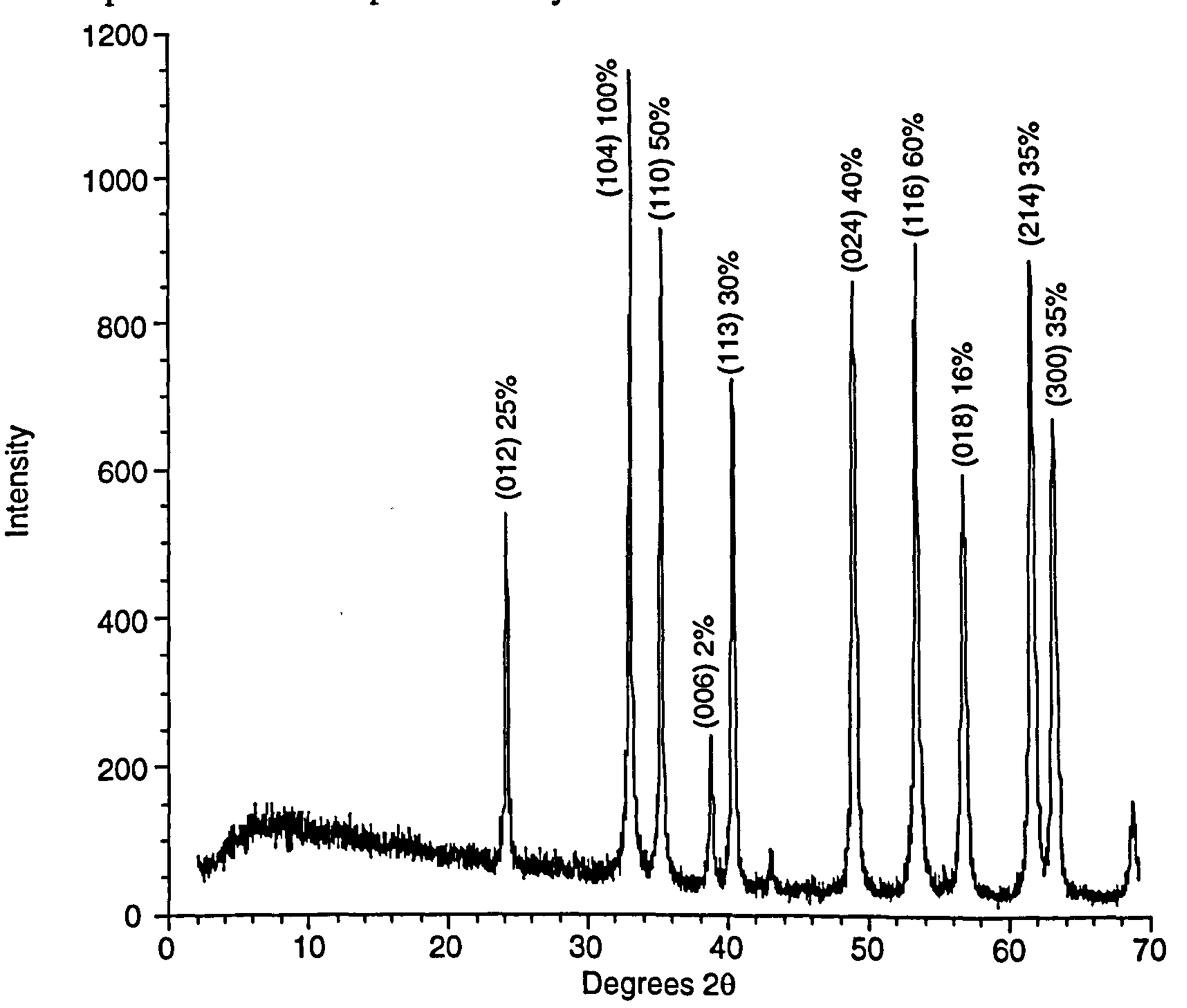

Fig. 5.7 b. Hematite XRD reference standard. Numbers in parentheses are published relative peak intensity values.

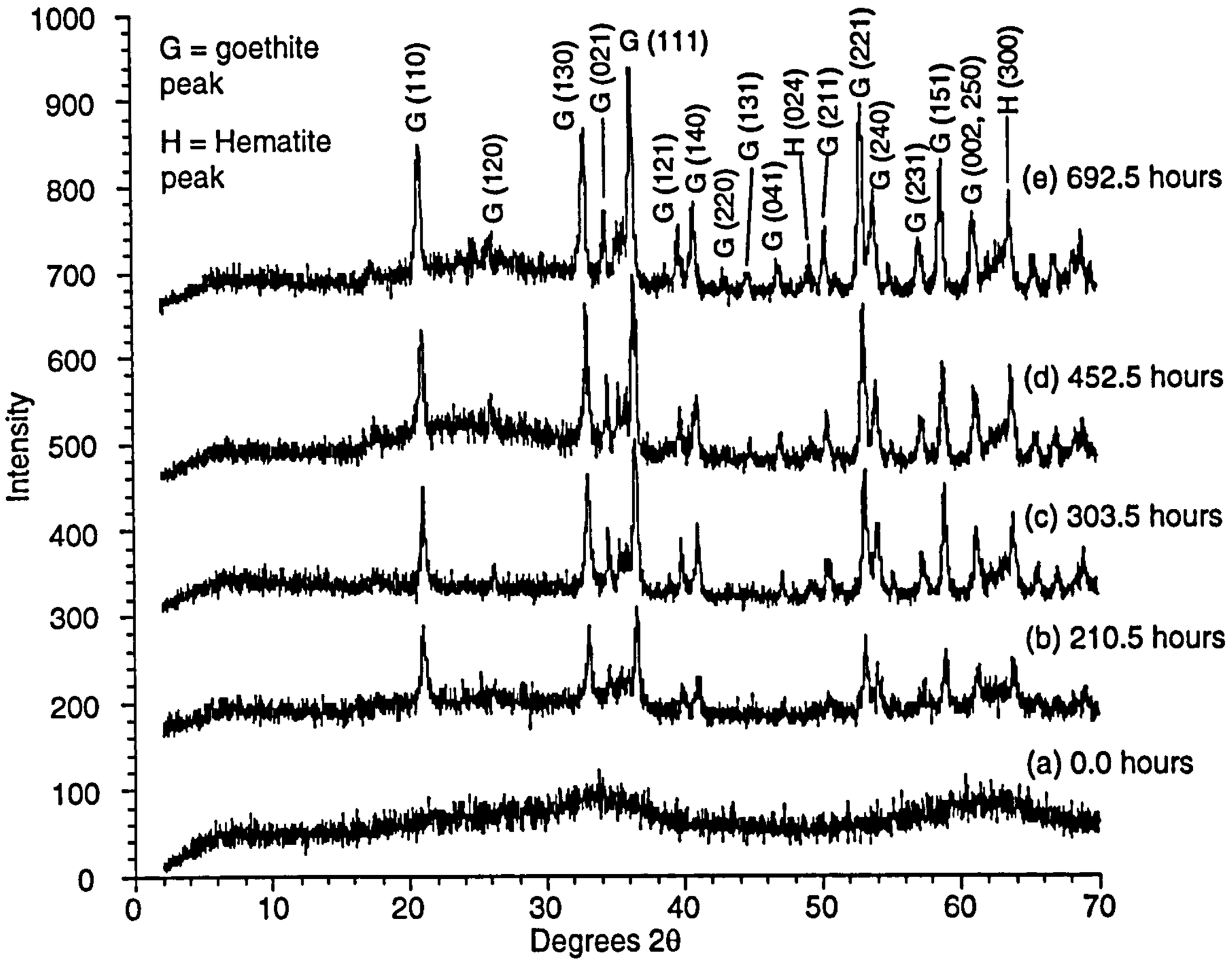

Fig. 5.7 c. XRD powder patterns from As(V)-free ferrihydrite (No As-HFO) samples collected on (a) 27/6, (b) 6/7, (c) 10/7, (d) 16/7 and (e) 26/7/98 after ageing at 60±3°C.

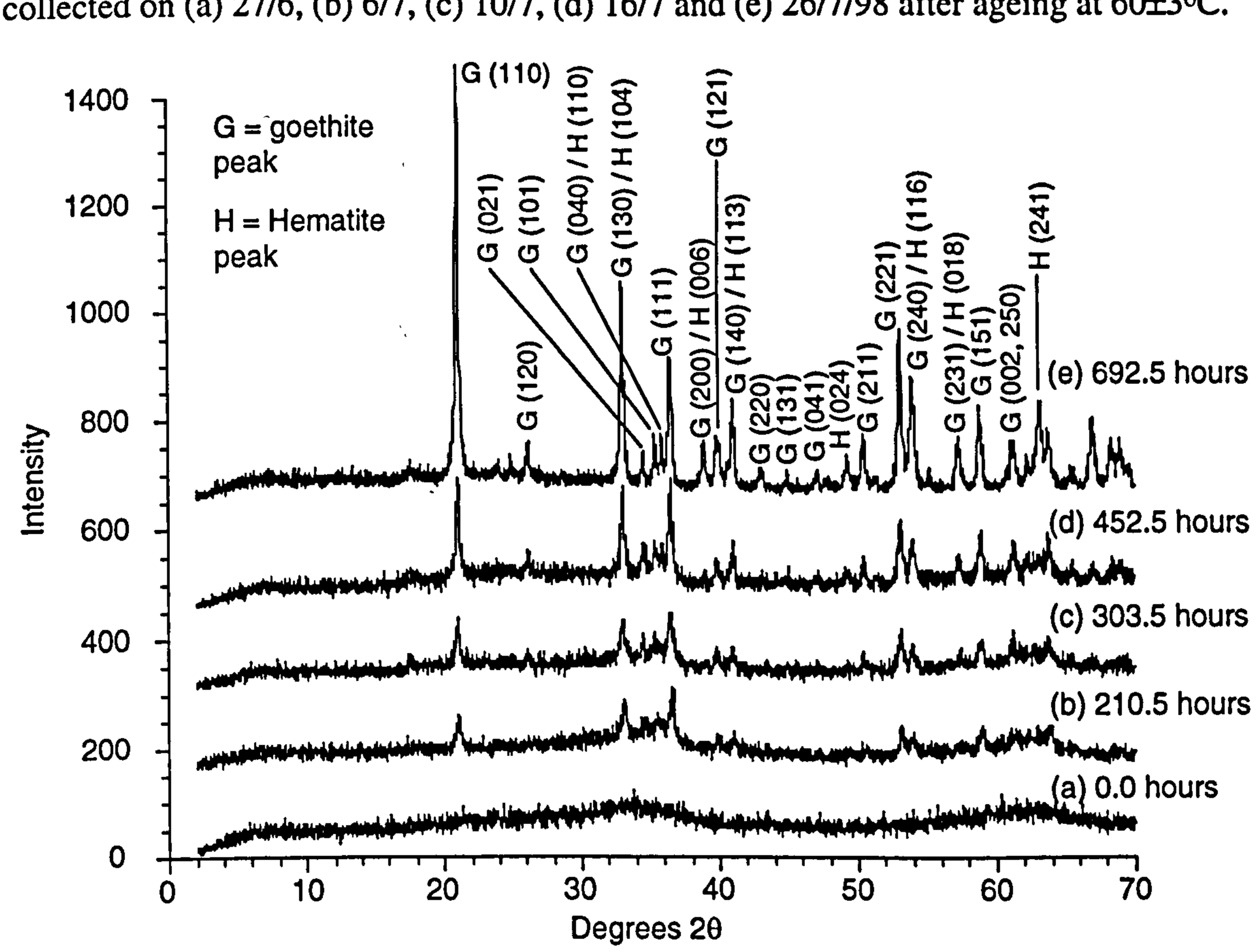

Fig. 5.7 d. XRD powder patterns from ferrihydrite samples with As/As+Fe = 0.0033 (Low As-HFO) collected on (a) 27/6, (b) 6/7, (c) 10/7, (d) 16/7 and (e) 26/7/98 after ageing at 60±3°C.

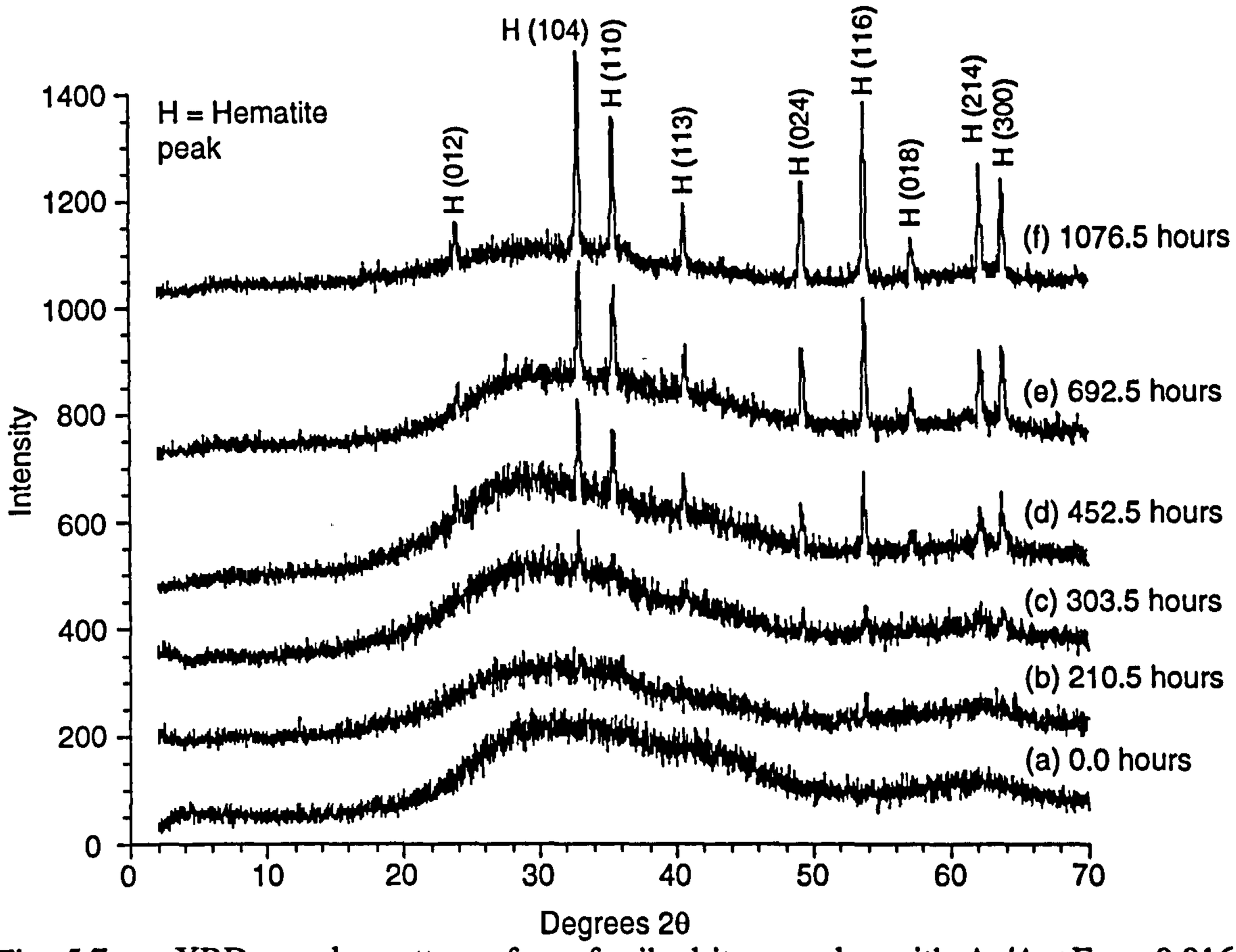

Fig. 5.7 e. XRD powder patterns from ferrihydrite samples with As/As+Fe = 0.016 (Med. As-HFO) collected on (a) 27/6, (b) 6/7, (c) 10/7, (d) 16/7, (e) 26/7 and (f) 11/8/98 after ageing at 60±3°C.

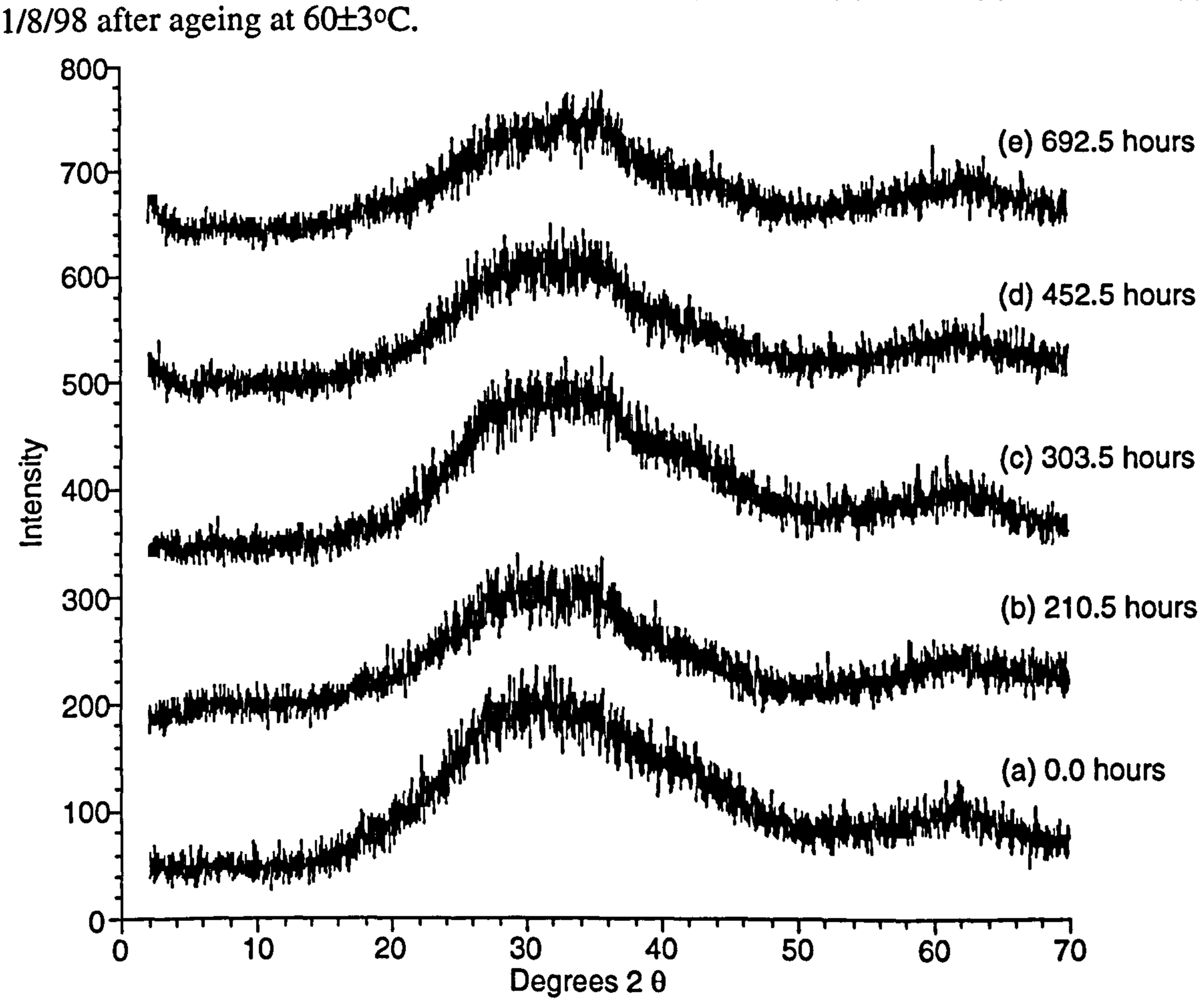

Fig. 5.7 f. XRD powder patterns from ferrihydrite samples with As/As+Fe = 0.032 (High As-HFO) collected on (a) 27/6, (b) 6/7, (c) 10/7, (d) 16/7 and (e) 26/7/98 after ageing at 60±3°C.

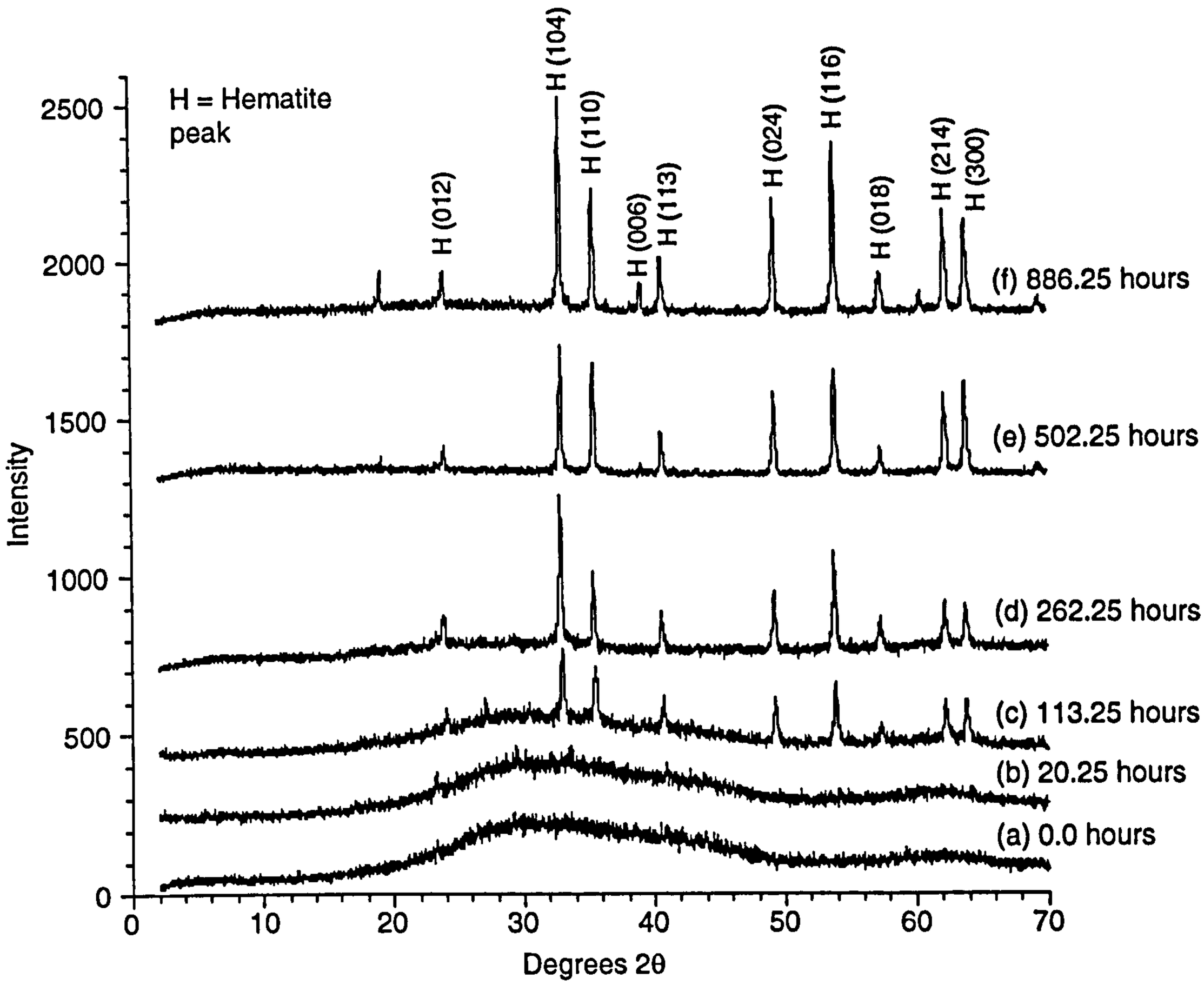

Fig. 5.7 g. XRD powder patterns from ferrihydrite samples which were nucleated in the presence of As(V) to yield a solid with As/As+Fe = 0.0054 ('pH 4 As-HFO coprecipitate'), and collected on (a) 5/7, (b) 6/7, (c) 10/7, (d) 16/7, (e) 26/7 and (f) 11/8/98 after ageing at 60±3°C.

In contrast to the 'No As-HFO' powder patterns, those from the 'Low As-HFO' sample series (As/(As+Fe) = 0.0033) contain several hematite peaks (Fig. 5.7 d). However, the low intensity of these relative to goethite-only peaks such as the (110) and (111) suggests that hematite still comprises a relatively small component of these samples. Exactly how small is hard to say because several of the most diagnostic goethite and hematite diffraction peaks coincide, and it is impossible to tell how much each mineral is contributing to the intensity of a given peak. Notwithstanding this, a reasonable estimate of the composition of the final ageing product is 80-90% goethite and 10-20% hematite. This would be consistent with the fact that the final colour of the 'Low As-HFO' suspension was largely ochre yellow (goethite) with a tinge of red (hematite).

Increasing As/(As+Fe) by a factor of five from 0.0033 to 0.016 ('Med. As-HFO'; Fig. 5.7 e) dramatically reduces the goethite content of the final ageing product to below levels detectable by XRD (≤ 5 vol%). All of the diffraction peaks in the 'Med. As-HFO' powder pattern can be assigned to hematite, but broad humps are still visible between 30-50 degrees 2θ and 60-70 degrees 2θ, even after 1076.5 hours of ageing. These coincide with the broad humps that are characteristic of the 2-line ferrihydrite starting material (Schwertmann and Cornell, 1991) (see time 0.0 hours in Fig. 5.7 e), and suggest that significant amounts of ferrihydrite remain at the end of the ageing process. This finding is important because it explains how the As(V) sorption capacity of 'Med. As-HFO' was not exceeded during ageing. If all of the ferrihydrite had aged to hematite, the bulk surface area of the sample would have decreased to a point where arsenic would probably have been released to solution.

Increasing As/(As+Fe) still further to 0.032 effectively arrests the ageing process altogether (Fig. 5.7 f). It is clear that there is no development of any crystalline phase. This again explains how 'High As-HFO' was able to hold onto its high As(V) loading.

It is evident that the presence of As(V) during nucleation has a significant effect on the rate at which the ageing process proceeds. It is also clear from Fig. 5.7 (g) that it exerts a significant influence on the product of the ageing process. Although the As/(As+Fe) value for 'pH 4 As-HFO coprecipitate' (0.0054) is only slightly larger than that for 'Low As-HFO' (0.0033), the 'pH 4 As-HFO coprecipitate' ageing product consists entirely of hematite, whereas that from 'Low As-HFO' contains just 10-20% hematite. In addition to this, the diffraction peaks in 'pH 4 As-HFO coprecipitate' are very sharp and the background is very low, unlike that of 'Med. As-HFO'. This indicates that >90% of the available ferrihydrite has aged into hematite. If this is the case and it is assumed that the resulting hematite has a surface area of 30 $m^2 g^{-1}$, the percentage surface loading is 86%. It is likely that no arsenic was released to solution during the ageing of 'pH 4 As-HFO coprecipitate' because

the sorption capacity was not exceeded. It should be pointed out that increased hematite content of 'pH 4 As-HFO coprecipitate' does not arise simply from the fact that it was aged at a slightly lower pH than the other As-HFO samples (section 5.2.3); even at pH 3 the product of ferrihydrite ageing is expected to be 88% goethite and 12% hematite (Schwertmann and Murad, 1983).

In summary, increasing levels of As(V) have two major effects on the ageing of arsenic-contaminated ferrihydrite. Firstly, increasing arsenic content favours the formation of hematite over goethite, all other conditions being equal. Secondly, the rate of reaction decreases significantly as As/(As+Fe) increases, and is effectively arrested at a value of 0.032.

The first observation is explained by the fact that hematite forms via internal dehydration and rearrangement whilst goethite forms via dissolution and re-precipitation (Fischer and Schwertmann, 1975). At a given pH, the former mechanism is favoured by clumping of particles. Since the ease of sample settling during centrifugation was observed to increase with arsenic content, it seems likely that As(V) facilitates the necessary aggregation of ferrihydrite particles. A mechanism was proposed for this by Waychunas et al. (1996).

The second observation is partly explained by the fact that arsenate binuclear surface complexes are highly effective at inhibiting both the reductive (e.g. by H_2S) and non-reductive dissolution of iron (oxyhydr)oxides such as goethite (Biber et al., 1994). This phenomenon is due to (1) the large activation energy which must be overcome to simultaneously detach two surface metal centres and to (2) the lack of additional surface protonation when uncharged binuclear or multinuclear complexes are formed (Biber et al., 1994). It is also partly explained by the fact that As(V) is known to poison the growth of iron oxyhydroxides by blocking crystal growth sites (Waychunas et al., 1996). Whilst dissolution and crystal growth both become increasingly retarded with rising arsenic levels, it is noteworthy that crystal growth is significantly inhibited even when arsenic surface loading is well below monolayer coverage (Waychunas et al., 1996).

Finally, the point at which As(V) is introduced to the system also has an effect on the mineralogy of the final ageing product. 'Low As-HFO' and 'pH 4 As-HFO coprecipitate' had very similar As/(As+Fe) ratios and were aged under near identical conditions. Despite this, the former aged into 80-90% goethite/10-20% hematite whilst the latter aged into 100% hematite.

Phenomena very similar to those observed here for arsenate have previously been observed for phosphate. This is not surprising since these two oxyanions share a very similar chemistry. Indeed, strong competitive adsorption has been observed between these two species on model iron oxyhydroxides (Manning and Goldberg, 1996) and soils (Melamed et al., 1995).

5.3.2.3 EXAFS results from ageing of arsenic-contaminated ferrihydrite

The EXAFS and FT plots from 'Low As-HFO' samples collected after 0, 210.5, 692.5 and 1076.5 hours of ageing and a 'Med. As-HFO' sample collected after 210.5 hours are shown in Fig. 5.8 (a). The associated EXAFS data is summarised in Table 5.2. All samples have a shell of iron atoms at 2.79 - 2.87 Å which can be assigned to single edge sharing adsorption on ferrihydrite and the goethite that it ages into (Fig. 5.5). The two least aged samples (0.0 hours and 210.5 hours) additionally have a shell of iron atoms at 3.30 - 3.31 Å, which is consistent with bidentate corner sharing adsorption across the apices of adjacent ferric octahedra (Fig. 5.5). Although the XRD data shows that 'Low As-HFO' contains little or no goethite after 0.0 and 210.5 hours of ageing, the fits to the EXAFS data from these two early samples are very similar to that for the As(V) on goethite reference standard (Table 5.2). This is not surprising because the local structure of ferrihydrite is very similar to that of goethite and akaganeite (β-FeOOH) (Manceau and Combes, 1988; Combes et al., 1989; Shinoda et al., 1994).

After 692.5 hours of ageing the 3.30 -3.31 Å iron shell is replaced by another at 2.95 - 2.96 Å, and following 1076.5 hours of oxidation, a third iron shell appears at 3.48 Å. Indeed, there is an indication in the FT plot after 692.5 hours of ageing that the 3.48 Å is already starting to develop at this stage in the reaction (Fig. 5.8 a).

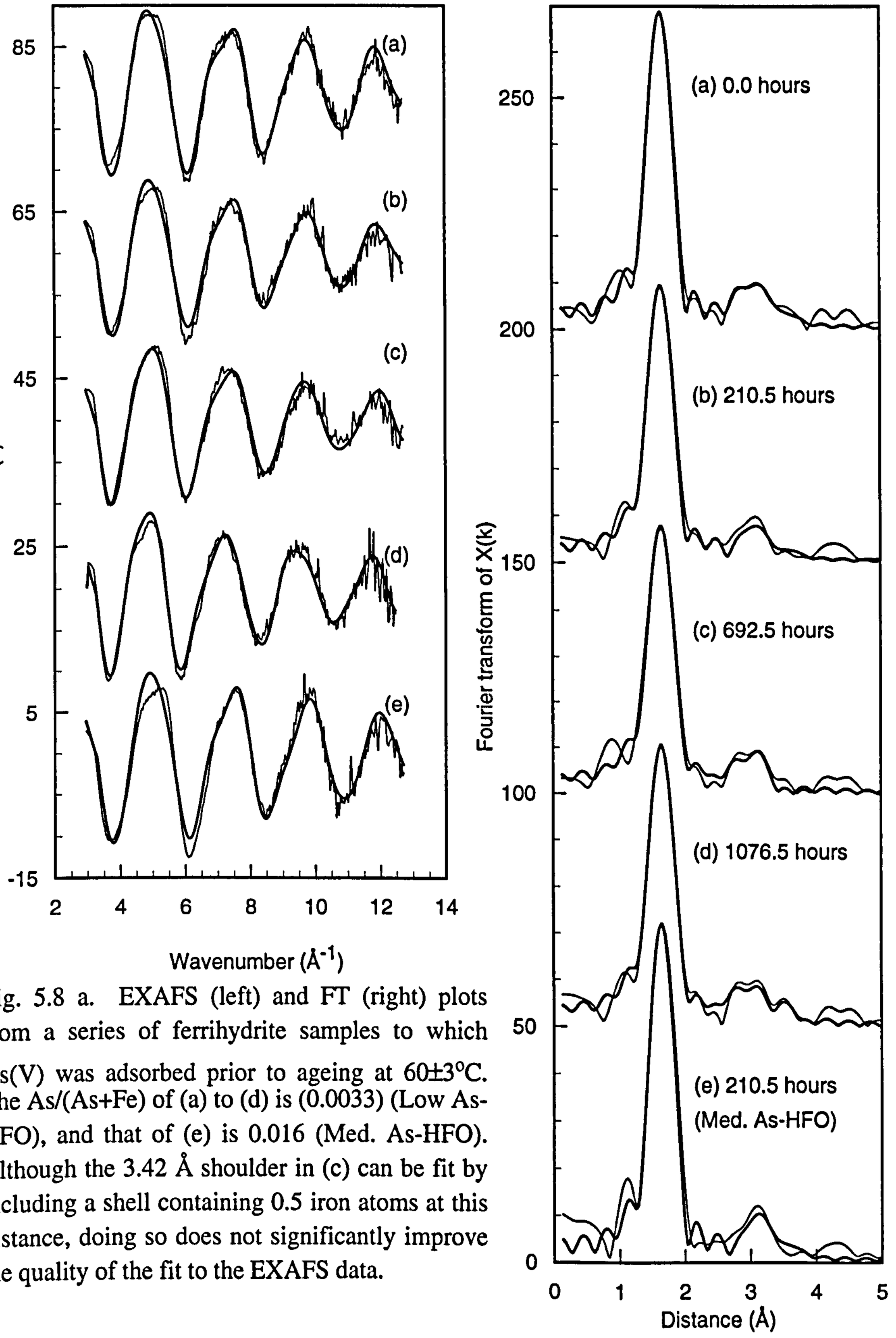

Fig. 5.8 a. EXAFS (left) and FT (right) plots from a series of ferrihydrite samples to which As(V) was adsorbed prior to ageing at 60±3°C. The As/(As+Fe) of (a) to (d) is (0.0033) (Low As-HFO), and that of (e) is 0.016 (Med. As-HFO). Although the 3.42 Å shoulder in (c) can be fit by including a shell containing 0.5 iron atoms at this distance, doing so does not significantly improve the quality of the fit to the EXAFS data.

Table 5.2. EXAFS results from 'Low As-HFO', 'Med. As-HFO' and 'pH 4 As-HFO coprecipitate' samples and EXAFS standards. CN_X is number of atoms in a shell at distance R_X (Å) from the central cadmium atom. $2\sigma^2_X$ (Å^2) is the associated Debye-Waller factor. *R* gives a measure of the agreement between experimental and theoretical EXAFS curves. $R < 20\%$ indicates a very good fit whereas $R \leq 40\%$ is acceptable. Note that the Debye-Waller factors for the iron shells were constrained to 0.011 Å^2 during the final stages of fitting to allow the associated coordination numbers to be compared between samples. The freely refined Debye-Waller factors generally fell in the range 0.009 to 0.013 Å^2.

Reaction time	$R_{As\text{-}O}$	CN_O $2\sigma^2_O$	$R_{As\text{-}Fe1}$	CN_{Fe1} $2\sigma^2_{Fe1}$	$R_{As\text{-}Fe2}$	CN_{Fe2} $2\sigma^2_{Fe2}$	$R_{As\text{-}Fe3}$	CN_{Fe3} $2\sigma^2_{Fe3}$	*R* factor
'Low As-HFO' As/(As+Fe) = 0.0033									
0.0 hr	1.69	4.0 *0.006*	2.84	0.7 *0.011*	3.30	0.9 *0.011*	-	-	19.8
210.5 hr	1.69	3.9 *0.007*	2.87	0.5 *0.011*	3.31	0.6 *0.011*	-	-	22.3
692.5 hr	1.69	4.0 *0.008*	2.79	1.1 *0.011*	2.95	1.2 *0.011*	-	-	22.0
1076.5 hr	1.69	4.1 *0.008*	2.79	1.3 *0.011*	2.96	1.3 *0.011*	3.48	0.6 *0.011*	20.8
Medium As-HFO As/(As+Fe) = 0.016									
210.5 hr	1.68	4.1 *0.005*	2.87	0.6 *0.011*	3.30	0.9 *0.011*	-	-	24.4
'pH 4 As-HFO coprecipitate' As/(As+Fe) = 0.0054									
0.0 hr	1.69	4.1 *0.005*	2.74	0.8 *0.011*	2.90	1.2 *0.011*	3.33	0.9 *0.011*	19.0
113.25 hr	1.70	4.1 *0.006*	2.87	1.5 *0.011*	3.01	0.8 *0.011*	3.36	0.9 *0.011*	23.8
502.25 hr	1.69	4.1 *0.006*	2.80	1.6 *0.011*	2.97	1.6 *0.011*	3.46	0.8 *0.011*	19.2
886.25 hr	1.69	4.1 *0.008*	2.79	1.3 *0.011*	2.96	1.3 *0.011*	3.48	0.6 *0.011*	20.8

Table 5.2 continued.

Sample	% SL† (wt % As)	EXAFS standards $R_{As\text{-}O}$	$CN_{As\text{-}O}$ $2\sigma^2_{As\text{-}O}$	$R_{As\text{-}Fe1}$	$CN_{As\text{-}Fe1}$ $2\sigma^2_{As\text{-}Fe1}$	$R_{As\text{-}Fe2}$	$CN_{As\text{-}Fe2}$ $2\sigma^2_{As\text{-}Fe2}$	*R* factor
As(V) on goethite	36.6 (0.24)	1.69	4.0 *0.004*	2.85	0.8 *0.019*	3.31	1.5 *0.011*	22.0
As(V) on hematite	(0.29)	1.69	4.0 *0.005*	2.86	1.1 *0.020*	3.32	1.1 *0.014*	20.0
Scorodite $FeAsO_4 \cdot 2H_2O$	-	1.68	4.0 *0.004*	3.38	3.9 *0.013*	-	-	25.1

Notes:

† % SL = percentage surface loading, which describes the proportion of available surface sites occupied by adsorbed arsenic. These values were calculated using a maximum surface site density for As(V) of 1.58 sites nm^{-2} on goethite derived from Sun and Doner (1996).

The XRD data from 'Low As-HFO' (Fig. 5.7 d) shows that a significant amount of ageing from ferrihydrite (the presence of which is indicated by the high background and low diffraction peak intensity) to crystalline goethite occurred between 210.5 hours and 692.5 hours. This would have been accompanied by a decrease in surface area, and therefore the number of available surface sites (Fuller et al., 1993). It seems likely that this change caused the occupation of the less energetically favourable single corner sharing sites (section 5.3.1, Fig. 5.5.), which manifest themselves as the 3.48 Å peak. This As-Fe distance is not as great as that suggested by Waychunas et al. (1993) for single corner sharing adsorption of As(V) on goethite (3.65 Å). It is, however, still consistent with single corner sharing because an As-Fe distance of 3.38 Å is observed for this mechanism in scorodite.

The origin of the 2.95 - 2.96 Å shell is more problematic, and it has not been documented in previous studies of As(V) adsorption on iron oxyhydroxides. The low iron coordination numbers (1.1 - 1.3) indicate that the As(V) atoms associated with this shell are bound at mineral surface sites rather than sorbed within the mineral structure. Furthermore, the relatively short As-Fe distance is suggestive of an edge sharing adsorption mechanism. What is not clear is how this differs from the edge sharing mechanism which has already been identified as the source of the 2.79 - 2.87 Å As-Fe relationship.

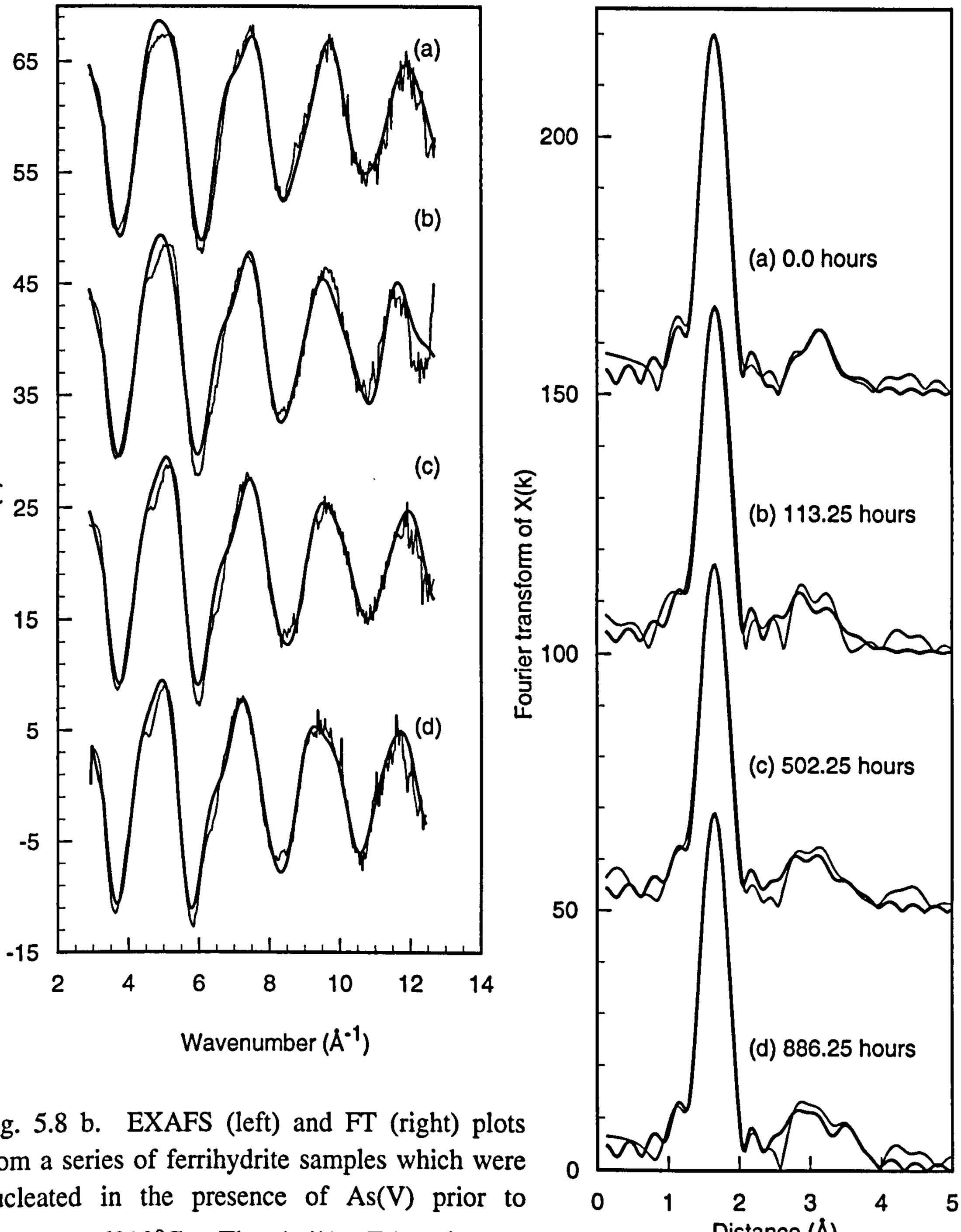

Fig. 5.8 b. EXAFS (left) and FT (right) plots from a series of ferrihydrite samples which were nucleated in the presence of As(V) prior to ageing at 60±3°C. The As/(As+Fe) ratio was 0.0054 ('pH 4 As-HFO coprecipitate' sample series).

The 'Med. As-HFO' sample in Fig. 5.8 (a) contained five times as much As(V) as the 'Low As-HFO' samples shown in the same plot. However, the EXAFS results from 'Med. As-HFO' after 210.5 hours of ageing are essentially identical to those from 'Low As-HFO' after 0.0 hours and 210.5 hours of ageing. This simply illustrates that increasing the arsenic loading does not cause the adsorption mechanism to change. EXAFS data was not collected from any 'High As-HFO' samples.

The EXAFS and FT plots for the 'pH 4 As-HFO coprecipitate' series of samples are shown in Fig. 5.8 b, and the associated data is summarised in Table 5.2. All samples have iron shells at 2.74 - 2.87 Å and 2.90 - 3.01 Å. As with the As-Fe contributions at similar distances in 'Low As-HFO', these shells are consistent with adsorption via single edge sharing mechanisms.

In addition to the shells at 2.74 - 2.87 Å and 2.90 - 3.01 Å, the two least aged samples of 'pH 4 As-HFO coprecipitate' (0.0 hours and 113.25 hours) have a third iron shell at 3.33 - 3.36 Å. As with the 'Low As-HFO' series, this is thought to correspond to bidentate corner sharing adsorption across the apices of adjacent ferric octahedra. Sometime between 113.25 and 502.25 hours of ageing, this relationship is replaced by another which results in an iron shell at 3.46 - 3.47 Å. It is likely that this has a similar origin to the 3.48 Å shell observed in the 'Low As-HFO' series. Namely, mineralogical transformations during ageing cause a decrease in surface area. In turn, this results in the occupation of relatively unfavourable single corner sharing adsorption sites as the sorption capacity of the more energetically favourable sites is exceeded.

5.3.2.4 Ageing of As(V)-contaminated ferrihydrite - Summary

Whilst there are early differences between the EXAFS results from the 'pH 4 As-HFO coprecipitate' and 'Low As-HFO' ageing series, the As(V) sorption environment is ultimately the same regardless of whether the adsorption or coprecipitate route is followed (Table 5.2). A similar finding was made by Waychunas et al. (1993) for As(V) adsorbed by and 'coprecipitated' with ferrihydrite. This is despite the indication from macroscopic chemical observations that the ageing reaction proceeded in a slightly different manner in the 'pH 4 As-HFO coprecipitate' series than it did in the other As-HFO samples (section 5.3.2.1).

The observed iron coordination numbers (0.5 - 1.6) strongly indicate that sorbed As(V) remained bound in external surface complexes throughout the ageing process in all As-HFO samples, even the 'pH 4 As-HFO coprecipitate' series. If it had truly been coprecipitated with iron and/or formed a solid, the iron coordination numbers would have been in the region 3 - 4; As(V) in scorodite is surrounded by a shell of four iron atoms at 3.38 Å (Fig. 5.4 (a), Table 5.2). The fact that there are

As-Fe interactions at several distances in 'pH 4 As-HFO coprecipitate' but just one distance in scorodite is further evidence that little if any arsenic coprecipitated in this form.

It is interesting to note that whilst the EXAFS results from the most aged 'Low As-HFO' samples and all 'pH 4 As-HFO coprecipitate' samples are similar to each other, they are distinctly different from the As(V) on goethite, lepidocrocite and hematite reference standards. This is the case despite the fact that XRD shows the bulk product of the ageing process to be goethite and/or hematite (Fig. 5.7 d, e and g). This observation is best explained by invoking As(V) poisoning as the cause of structural deformation that is limited to the surface of the ageing products. This explains how a novel As(V) coordination environment can develop whilst the bulk ferrihydrite ageing product is pure goethite and/or hematite.

Irrespective of how arsenic is bound, the finding that As(V) exists mainly in sorbed form during ageing is in very good agreement with the field findings of Voigt et al. (1996). These workers find that arsenic exists in predominantly sorbed form in contaminated land and even in soils that have been chemically 'fixed' during remediation efforts. They also find no direct evidence for the formation of arsenate minerals (Voigt et al., 1996).

The experimental work presented here and field studies such as that by Voigt et al. (1996) have one important conclusion: The aqueous concentration of arsenic in oxic, iron-rich sediments and soils will depend on the equilibrium between species in solution and those that are adsorbed. Equilibrium with authigenic As(V)-containing solids such as scorodite and other arsenates will be of minor importance. This is especially true since scorodite is only stable under acidic conditions (Foster et al., 1998).

5.3.3 The interaction of As(V) with green rust

5.3.3.1 Chemical observations from the interaction of As(V) with green rust

Levels of dissolved iron and arsenic recorded during the growth and oxidation of a series of green rust samples with As(V) added after ('As-GR' series; Fig. 5.9 a) and before ('As-GRCO' series; Fig. 5.9 b) green rust nucleation are shown below.

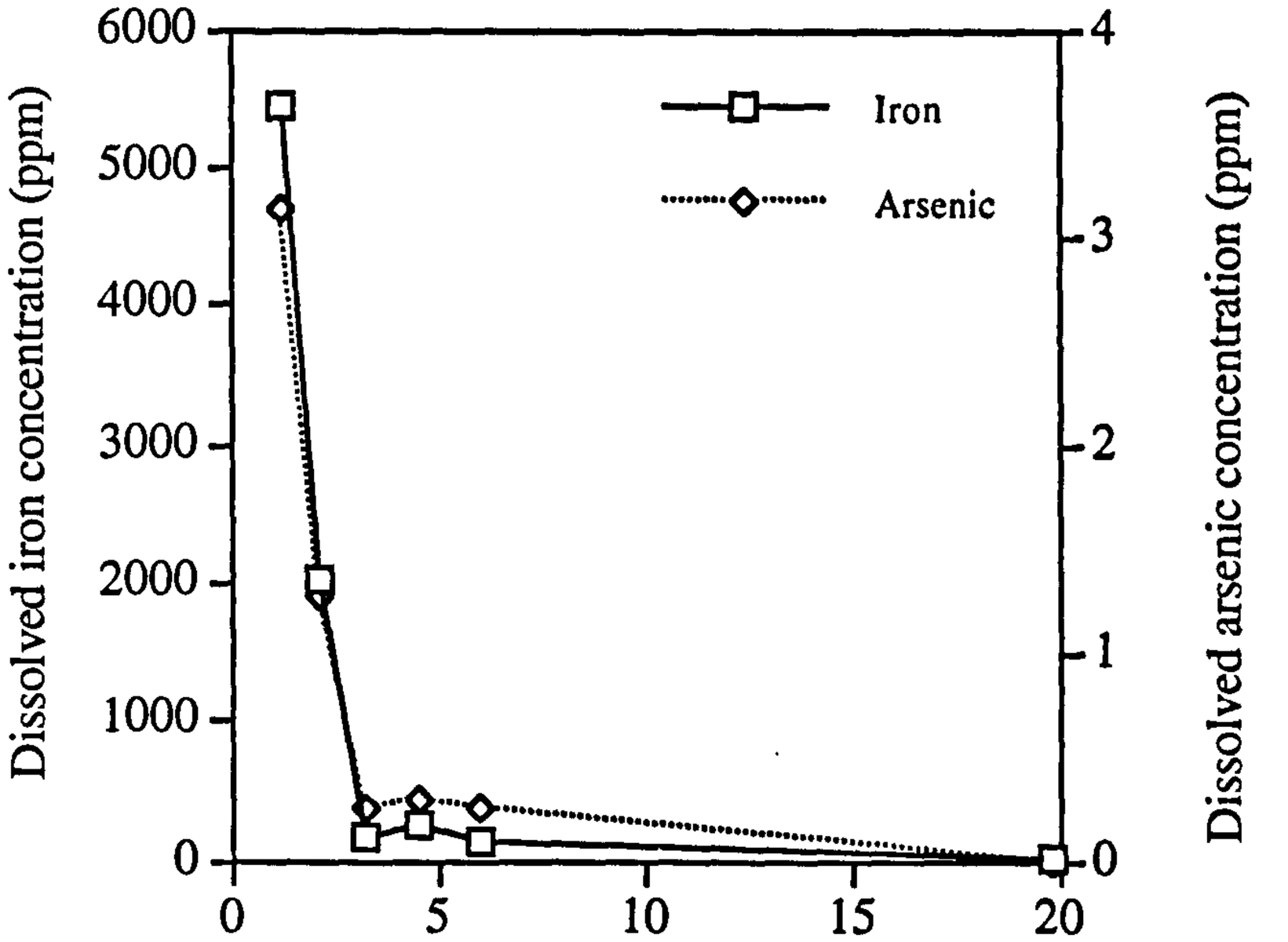

Fig. 5.9 a. Changes in dissolved iron and arsenic concentrations during the formation and oxidation of green rust with adsorbed As(V) ('As-GR' sample series).

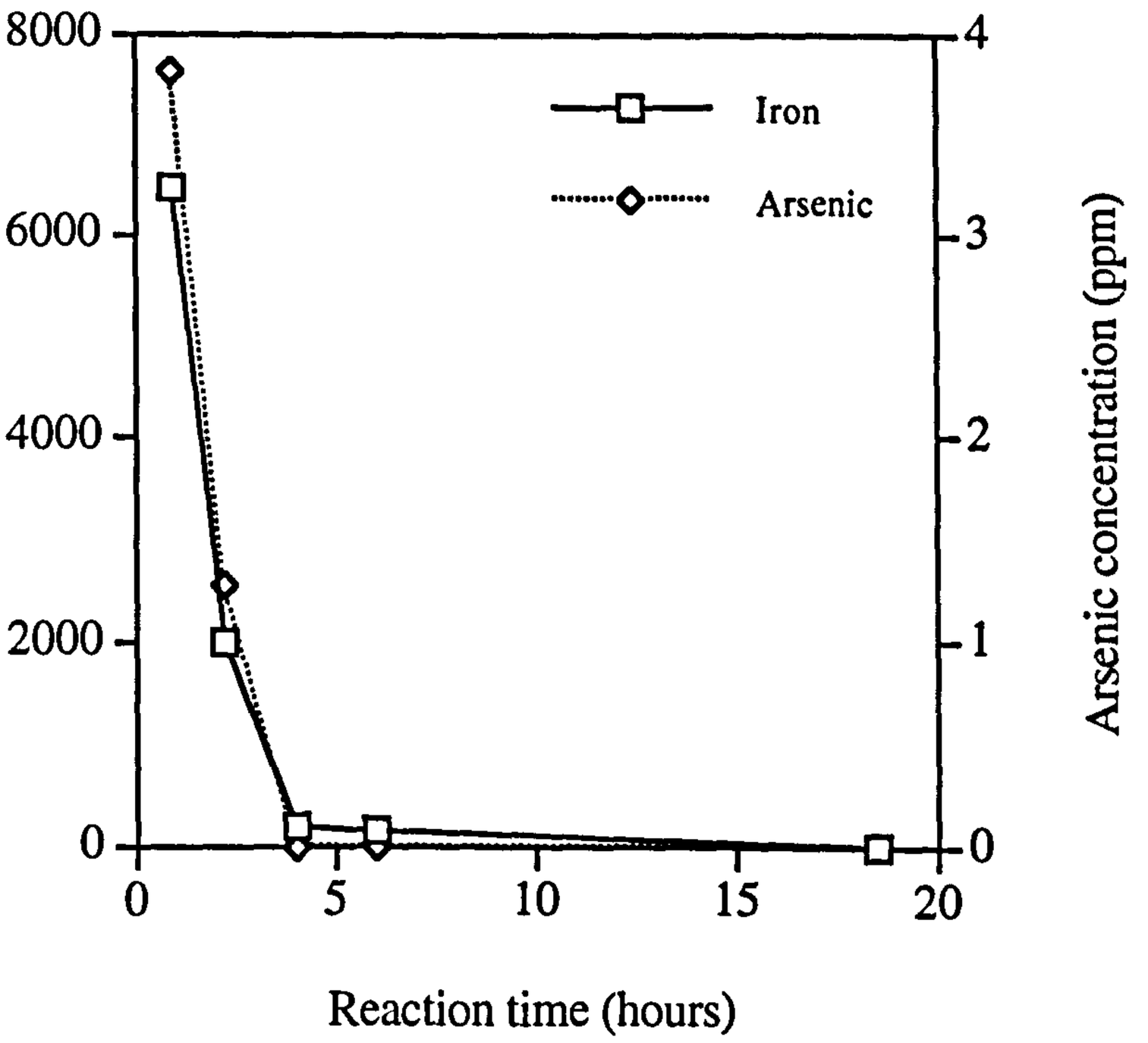

Fig. 5.9 b. Changes in dissolved iron and arsenic concentrations during the formation and oxidation of green rust that was nucleated in the presence of As(V) ('As-GRCO' sample series).

Initial levels of dissolved iron are high in both cases, but represent only 40-50% of total iron in the system (11200 ppm if all dissolved). By comparison, initial levels of dissolved arsenic are relatively low; only 6-8% of total available arsenic remains in solution one hour after the start of the reaction. This suggests that even when 40-50% of total iron is in solution, that which is in a solid form (as green rust) is capable of sorbing 92-94% of available arsenic.

There are a number of notable differences between Fig. 5.9 (a) and (b). Firstly, initial levels of dissolved iron and arsenic are higher in the 'As-GRCO' series of samples than the 'As-GR' series despite the fact that both systems were identical in composition. Secondly, whilst the concentration of both analytes drops most rapidly in the 'As-GR' series, the lowest concentrations following 4 hours of oxidation are recorded in the 'As-GRCO' series. This indicates that arsenic is most effectively removed from solution by coprecipitation with green rust rather than sorption onto pre-existing surfaces.

Secondly, a small temporary increase in both arsenic and iron concentrations after 4.5 hours of oxidation is observed in Fig. 5.9 (a). Although the changes in concentration are relatively small, they are likely to be 'real' because the same effect is observed for both analytes. They may be a consequence of the phase change between green rust and lepidocrocite. XRD results (section 5.3.3.2) suggest that the phase transformation starts after around three hours of oxidation, but it is clear that the highest proportion of co-existing green rust and lepidocrocite is found after 4.5 hours of oxidation. It therefore seems likely that the small increase in dissolved iron and arsenic concentrations occurred at the same time as the greatest amount of green rust oxidation was taking place.

No perturbation in dissolve iron and arsenic concentrations is observed for the 'As-GRCO' series. This could be explained by invoking a slight difference in the arsenate adsorption mechanism between the two sample series. A second possibility is that the sampling density was not sufficiently high in the 'As-GRCO' series to pick up the perturbation. However, this is unlikely to be the explanation because whilst XRD results for the 'As-GRCO' series show that significant amounts of green rust and lepidocrocite co-exist after 4.0 and 6.0 hours of oxidation (section 5.3.3.2), no corresponding increase in either iron or arsenic concentrations is observed in Fig. 5.9 (b).

An important final observation is that, notwithstanding the small perturbation in dissolved arsenic and iron concentrations observed in Fig. 5.9 (a), arsenic concentrations remained very low in both series following the first 3-4 hours of reaction, and ultimately fell below detectable limits. This suggests that As(V) was not reduced to As(III) by the green rust. If it had been, dissolved arsenic levels

would have been expected to remain measurable and possibly even increase because As(III) is not as strongly adsorbed as As(V) (Bowell, 1994). This point is discussed further in section 5.3.3.3.

5.3.3.2 X-ray diffraction results from the interaction of As(V) with green rust

The XRD results from the 'As-GR' sample series are shown in Fig. 5.10 (a).

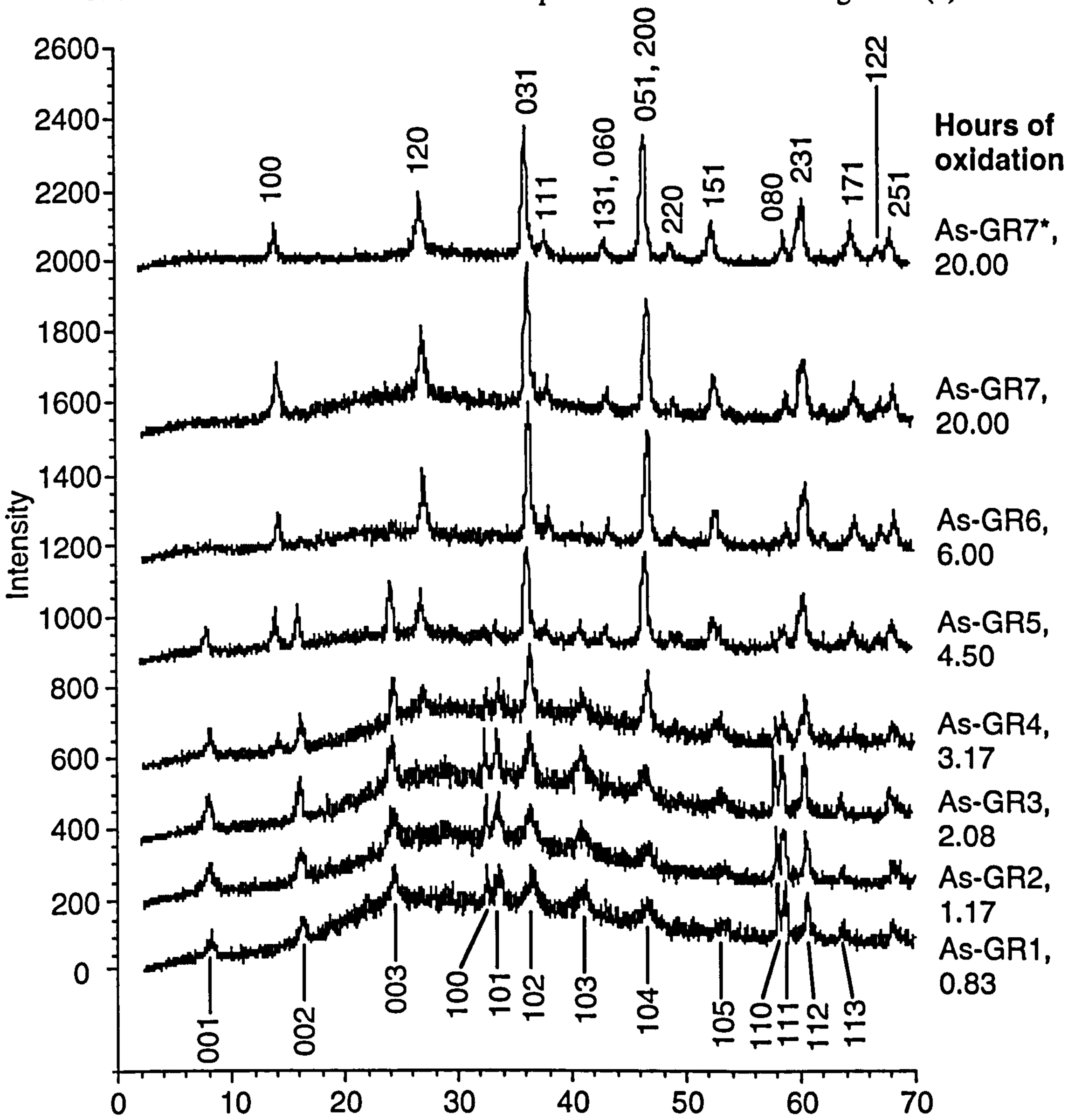

Fig. 5.10 a. XRD results from the progressive oxidation of green rust with adsorbed As(V) ('As-GR') to lepidocrocite at pH 7±0.05. Green rust and lepidocrocite peak indexing from Vins et al. (1987) and JCPDS card 8-98, respectively. Sample As-GR7* is identical to As-GR7 except that the sample was made up using a water-based paste rather than a glycerol-based smear. All other green rust XRD samples were made up in a glycerol matrix to prevent oxidation during analysis. The As-GR7 and As-GR7* powder patterns are identical, indicating that the use of a glycerol medium does not introduce artefacts into the data.

The characteristic (001), (002) and (003) lines of sulphate green rust (GR2(SO_4^{2-})) can be clearly seen in the data from sample As-GR1. These lines correspond to crystallographic plane spacings of 11.2 Å, 5.58 Å and 3.77 Å (Vins et al., 1987). All other peaks in As-GR1 can also be assigned to GR2(SO_4^{2-}), and there is no evidence for the presence of magnetite (Fe_3O_4). The (001), (002) and (003) peaks become slightly more intense and sharper over the first 4.5 hours of oxidation (up to As-GR5) but are absent after 6.0 hours (As-GR6). A similar pattern is observed for other less intense green rust peaks such as the (100), (101) and (103). These observations suggest that whilst green rust is being lost from solution due to oxidation, that which remains becomes increasingly crystalline as it ages.

After 3.2 hours of oxidation (As-GR4), the (100) and (120) peaks of lepidocrocite start to develop. Since they co-exist with the remaining green rust peaks and there is no evidence for an intermediate phase, it seems likely that green rust oxidises directly into lepidocrocite. Other lepidocrocite peaks, such as the (031) and (051, 200), also grow strongly at the same time as the (100) and (120) peaks. It should be noted, however, that both the (031) and (051, 200) lepidocrocite lines have identical d-spacings to the green rust (102) (2.48 Å) and (104) (1.94 Å) lines. This cannot be taken as evidence for the existence of green rust in the most oxidised sample (As-GR7) for two reasons: Firstly, the most diagnostic (001), (002) and (003) green rust lines are absent from the As-GR7 powder pattern, and secondly the lines in question can more easily be assigned to lepidocrocite.

After 6.0 hours of oxidation, all green rust has been oxidised. Thereafter, the lepidocrocite peaks simply become more intense, presumably as a result of an increase in crystallinity with ageing. There is no evidence for the development of other mineral phases. Although the peaks in As-GR7 are well defined, they are two to three times less intense than those recorded from a pure lepidocrocite XRD standard (data not shown). This suggests that the material in As-GR7 is not highly crystalline. This is a possibly because the system contained As(V), which has been shown to poison the growth of ferrihydrite (Waychunas et al., 1993, 1996).

Finally, it is important to note that the use of glycerol as an anti-oxidation coating did not introduce any artefacts into the XRD data. This was proven by analysing the most oxidised sample with (As-GR7) and without (As-GR7*) glycerol.

The XRD results for the 'As-GRCO' sample series are shown in Fig. 5.10 b.

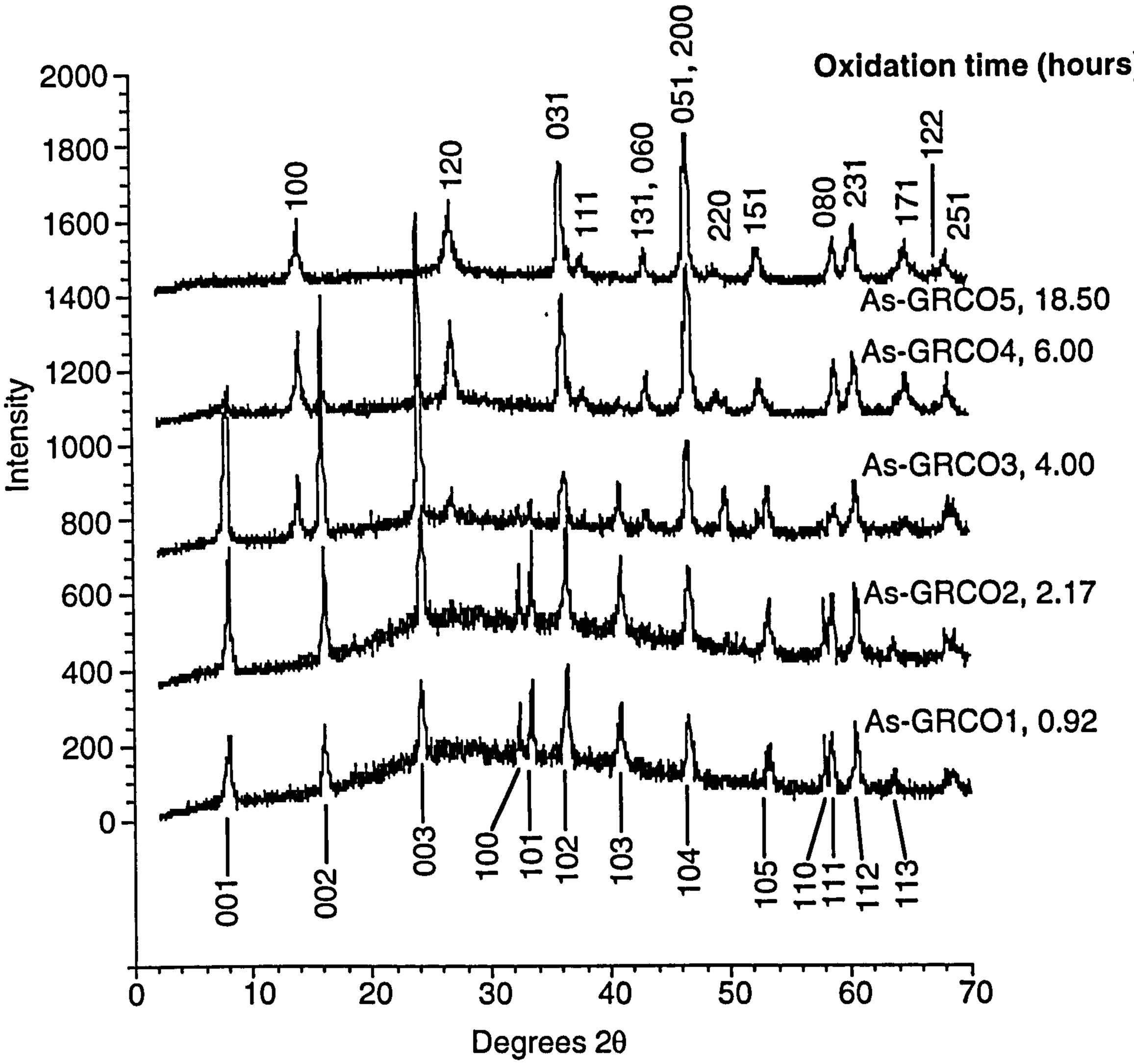

Fig. 5.10 b. XRD results from the progressive oxidation at pH 7±0.05 of green rust that was nucleated in the presence of As(V) ('As-GRCO'). Green rust and lepidocrocite peak indexing from Vins et al. (1987) and JCPDS card 8-98, respectively.

In general, the results are very similar to those from the 'As-GR' series of samples; all peaks in As-GRCO1 can be assigned to sulphate green rust whilst all those in the final oxidation product (As-GRCO5) can be assigned to lepidocrocite. Increases in diffraction peak intensity suggest that the green rust is becoming more crystalline as it ages, and the coexistence of lepidocrocite and green rust diffraction peaks between 4.00 and 6.00 hours of oxidation indicates that green rust is oxidising directly into lepidocrocite.

There is, however, one notable difference: It is evident that the green rust diffraction peaks in the 'As-GRCO' series are much more intense than those in the 'As-GR' series. This is a clear indication that nucleating green rust in the presence of As(V) increases its crystallinity. The relatively low intensity of the green rust

diffraction peaks in Fig. 5.10 (a) is consistent with the 'As-GR' crystallites being very small, whereas the reverse appears to be true of those from the 'As-GRCO' series. Any differences in green rust diffraction peak intensity do not carry over into the final oxidation products since the powder patterns from samples As-GR7 and As-GRCO5 are essentially identical.

Finally, it is apparent that a small amount of green rust persists after 6.00 hours of oxidation in the 'As-GRCO' series (As-GRCO4) whilst it is absent from the 'As-GR' series at this stage in the reaction. This may be a result of the higher crystallinity of green rust in the 'As-GRCO' series. It may, however, simply be due to a slight difference in reaction conditions between the two sample series.

5.3.3.3 EXAFS results from the interaction of As(V) with green rust

The arsenic K-edge EXAFS results from the 'As-GR' and 'As-GRCO' series of samples are shown in Fig. 5.11 and summarised in Table 5.3.

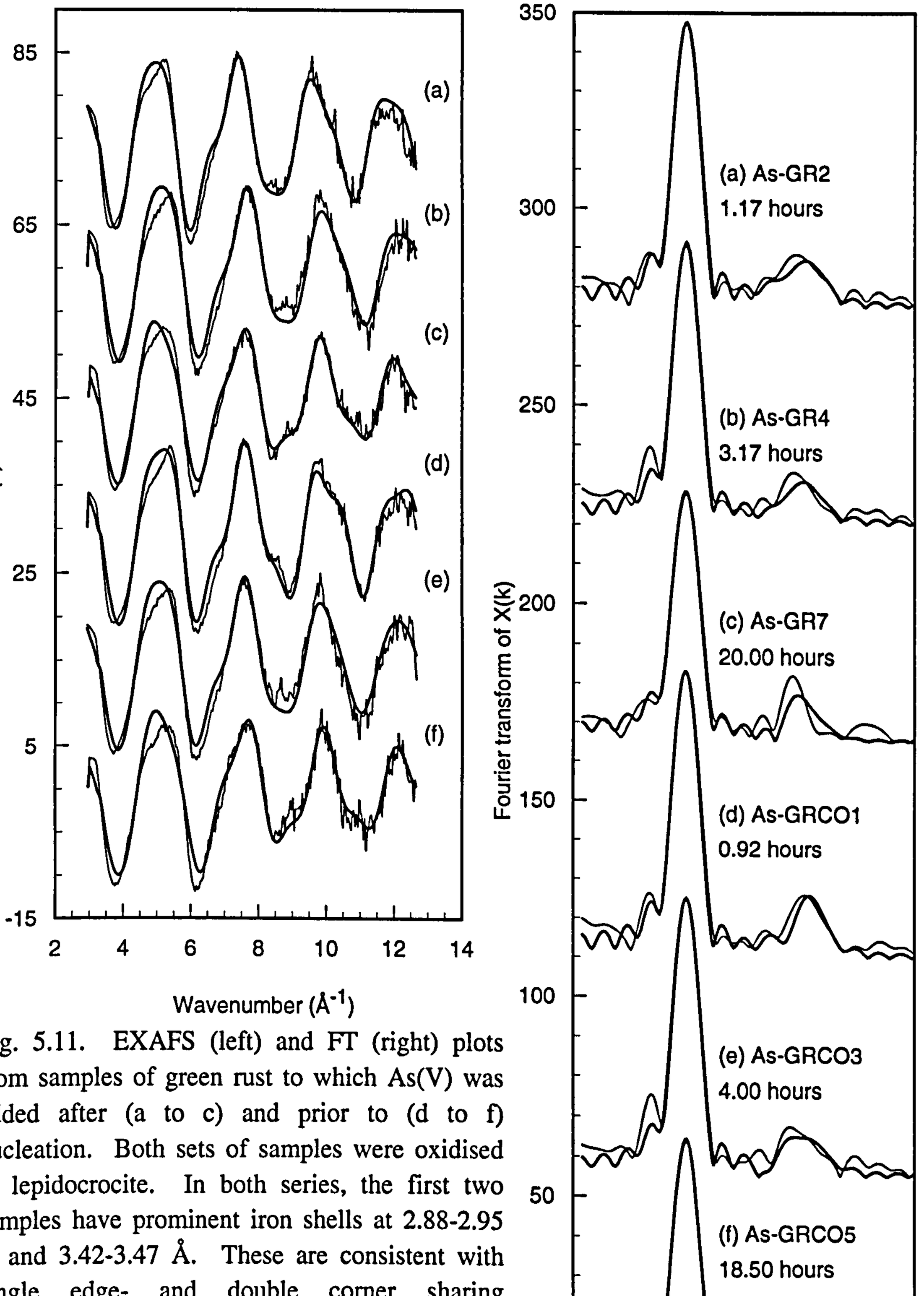

Fig. 5.11. EXAFS (left) and FT (right) plots from samples of green rust to which As(V) was added after (a to c) and prior to (d to f) nucleation. Both sets of samples were oxidised to lepidocrocite. In both series, the first two samples have prominent iron shells at 2.88-2.95 Å and 3.42-3.47 Å. These are consistent with single edge- and double corner sharing adsorption on a ferrous hydroxide-bearing mineral. The oxidised samples (c and f) have just one iron shell at 3.36 Å, which is due to double corner sharing adsorption on Fe(III). Importantly, there is no evidence for the reduction of As(V) to As(III).

Table 5.3. EXAFS results from As(V) on green rust and As(V)-green rust coprecipitate samples. CN_X is number of atoms in a shell at distance R_X (Å) from the central cadmium atom. $2\sigma^2_X$ (Å^2) is the associated Debye-Waller factor. The *R* factor gives a measure of the agreement between experimental and theoretical EXAFS curves. $R < 20\%$ indicates a very good fit whereas $R \leq 40\%$ is acceptable.

Sample	Reaction time (hr)	$R_{As\text{-}O}$	CN_O *$2\sigma^2_O$*	$R_{As\text{-}Fe1}$	CN_{Fe1} *$2\sigma^2_{Fe1}$*	$R_{As\text{-}Fe2}$	CN_{Fe2} *$2\sigma^2_{Fe2}$*	*R* factor
As-GR2	1.17	1.69	3.9 *0.004*	2.90	1.1 *0.019*	3.42	1.7 *0.011*	20.7
As-GR4	3.17	1.69	4.1 *0.005*	2.91	0.9 *0.019*	3.42	1.5 *0.011*	25.2
As-GR7	20.00	1.69	3.8 *0.006*	3.36	1.6 *0.011*	-	-	22.0
As-GRCO1	0.92	1.69	4.0 *0.004*	2.88	0.8 *0.019*	3.45	2.5 *0.012*	22.0
As-GRCO3	4.00	1.70	4.0 *0.005*	2.95	0.7 *0.019*	3.47	1.9 *0.017*	25.7
As-GRCO5	18.50	1.69	3.9 *0.006*	3.36	1.5 *0.009*	-	-	27.2

EXAFS reference standard

Sample	% SL† *(wt % As)*	$R_{As\text{-}O}$	CN_O *$2\sigma^2_O$*	$R_{As\text{-}Fe1}$	CN_{Fe1} *$2\sigma^2_{Fe1}$*	$R_{As\text{-}Fe2}$	CN_{Fe2} *$2\sigma^2_{Fe2}$*	*R* factor
As(V) on lepidocrocite	17.4 *0.3*	1.69	4.0 *0.003*	3.32	1.7 *0.011*	-	-	22.0

Notes:

† % SL = percentage surface loading, which describes the proportion of available surface sites occupied by adsorbed arsenic. These values were calculated using a maximum surface site density of 1.58 sites nm^{-2} on goethite derived from Sun and Doner (1996).

The most striking and important feature of these EXAFS results is that arsenic exists as arsenate (4 oxygen atoms at an As-O distance of 1.69-1.70 Å) in all samples. There is no evidence to suggest the formation of the more mobile As(III) species, which is characterised by a shell of 3.0 oxygen atoms at an As-O distance of 1.79 Å (Manning et al., 1998). This is in contrast to my finding that green rust instantaneously reduces aqueous Cr(VI) and sorbs it as a Cr(III) hydroxide

precipitate whilst oxidising green rust to magnetite (Chapter 6). The absence of As(III) cannot be explained by its oxidation during EXAFS analysis. This assertion is supported by the fact that there were never any differences between multiple EXAFS spectra that were collected from any one given sample over a period of hours. Manning et al. (1998) have previously proven this point during their EXAFS and XANES analysis of As(III) adsorbed on goethite.

Using data compiled by Krauskopf and Bird (1995), the overall electrode potential (E^0) for the reaction:

$$2Fe^{2+} + H_3AsO_4 = 2Fe^{3+} + HAsO_2$$

is +0.20. The fact that this value is positive indicates that the reaction should not take place simultaneously (Krauskopf and Bird, 1995). However, structural Fe(II) is a much stronger reducing agent than Fe(II)(aq) (White and Peterson, 1996), and the overall electrode potential for the reaction:

$$2Fe(OH)_2 + H_3AsO_4 = 2Fe(OH)_3 + HAsO_2$$

is -1.12, suggesting that the reaction should take place spontaneously (Krauskopf and Bird, 1995). It is therefore very interesting that it appears not to. Since both the 'As-GR' and 'As-GRCO' samples were equilibrated at room temperature for no more than 24 hours, it is possible that As(V) reduction did not occur for kinetic reasons. Unfortunately, this cannot be proven because no kinetic data for the reaction between solid phase Fe(II) and aqueous As(V) has been published. One final piece of evidence to support the notion that As(V) was not reduced by green rust is that no mineralogical changes were observed in the first few hours of reaction, and those which occurred in the latter stages can easily be assigned to air oxidation of green rust. Compare this result with the instantaneous oxidation of green rust to magentite by Cr(VI) (Chapter 6) and the fact that Se(VI) (Myneni et al., 1997) and nitrite (Hansen et al., 1994) are known to oxidise green rust to magnetite/lepidocrocite and goethite, respectively.

The first two samples from both the 'As-GR' and 'As-GRCO' series have iron shell contributions at 2.88-2.95 Å and 3.42-3.47 Å. These are entirely consistent with single edge- and double corner adsorption on $Fe(II)O_6$ octahedra in a manner analogous to As(V) adsorption on $Fe(III)O_6$ octahedra (Fig. 5.5). The As-Fe distances observed in the green rust system are slightly larger than those observed in the As(V)-goethite or As(V)-ferrihydrite systems because Fe(II)-O bonds are 0.13 Å longer than Fe(III)-O bonds (Wehrli, 1990).

The XRD results clearly show that lepidocrocite was co-existing with green rust when both As-GR4 and As-GRCO3 were collected (section 5.3.3.2). Consequently, it is noteworthy that the EXAFS results from these two samples suggest adsorption on Fe(II) (oxyhydr)oxide (green rust) rather than Fe(III) (oxyhydr)oxide (lepidocrocite); this observation indicates that green rust oxidation has to occur before arsenic can become adsorbed by lepidocrocite.

The As(V) coordination environment remains identical in the 'As-GR' and 'As-GRCO' series following complete oxidation of green rust to lepidocrocite. However, it is now characterised by just one As-Fe interaction (Fig. 5.11 c and f; Table 5.3). This occurs at an As-Fe distance of 3.36 Å, which suggests that adsorption occurs *via* bidentate double corner sharing between the apices of adjacent $Fe(III)O_6$ octahedra (Fig. 5.5). The coordination environment observed in As-GR7 and As-GRCO5 is very similar to that in the As(V) on lepidocrocite EXAFS reference standard (Fig. 5.4, Table 5.3). This result is interesting because the As(V) coordination environment on the As-HFO ageing products (goethite and/or hematite) is distinctly different to that observed for the As(V) on goethite and hematite EXAFS reference standards (section 5.3.2.4).

With two exceptions, the iron shell coordination numbers fall in the range 0.7 to 1.7. This strongly suggests that As(V) remained adsorbed in surface complexes throughout the formation and oxidation of green rust, and that it did not form a coprecipitate and/or solid solution with iron. The coordination numbers in the 3.45-3.47 Å shells of As-GRCO1 and As-GRCO3 are slightly greater at 1.9-2.5, but even these are not high enough to suggest true coprecipitation with green rust. Furthermore, the increased coordination numbers cannot be explained by As(V) incorporation into the green rust interlayer sites. This is because the observed As-Fe distance (3.45-3.47 Å) is considerably smaller than the 4.3 Å SO_4^{2-}-Fe distance in green rust (distance derived from crystallographic model shown in Fig. 5.1).

5.3.4 Sulphidisation of As(V)-contaminated goethite

5.3.4.1 Chemical observations from the sulphidisation of As(V)-contaminated goethite

Changes in the concentration of dissolved iron, arsenic and total sulphide ($H_2S + HS^- + S^{2-}$) as a function of time during the sulphidisation of As(V)-contaminated goethite are shown in Fig. 5.12.

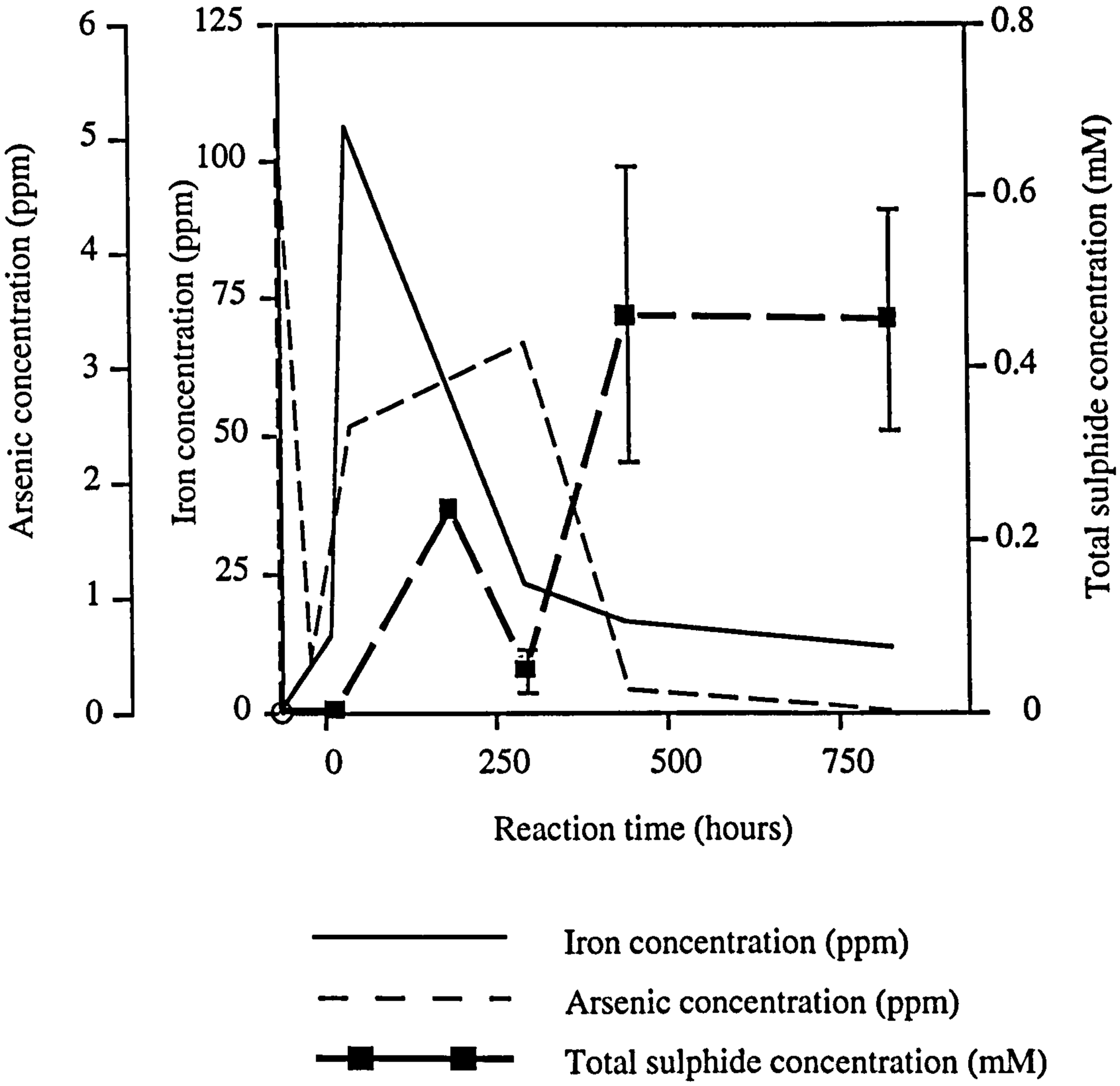

Fig. 5.12. Changes in the aqueous concentration of arsenic, iron and total sulphide ($H_2S + HS^- + S^{2-}$) during the sulphidisation of As(V)-contaminated goethite. The supply of $H_2S(g)$ started at t = 0.0 hours. It is clear that steady state conditions are achieved after approximately 500 hours. The last three sulphide data points represent averages of concentration values recorded from duplicate samples. The error bars represent the actual sample concentrations.

The initial spike in arsenic concentrations marks the time at which it was added to the reaction vessel, and it is clear that it was rapidly adsorbed by goethite. Hydrogen sulphide gas flow started at t = 0.0 hours, and sample GS4 was collected 4.5 hours after this. Although dissolved sulphide remains below detectable limits at this stage in the reaction, increases in the levels of aqueous iron and arsenic indicate that the reductive dissolution of goethite has begun. Maximum dissolved iron concentrations of 105 ppm (1.9×10^{-3} M) are recorded after 29 hours of sulphidisation (GS5). Although this concentration is high relative to values recorded in reducing sediments, it should be noted that it represents just 3% of total iron in the system. In this system, levels of dissolved iron are most likely to be regulated by equilibrium with goethite under oxic conditions and iron sulphide(s) under reducing,

sulphide-rich conditions. Consequently, the peak in iron concentrations after 29 hours probably represents the point in time when the availability of solubility-limiting solid phases was at a minimum. Between 29. 0 (GS5) and 287.5 (GS7) hours of sulphidisation, dissolved iron concentrations fall sharply to ≤ 25 ppm and continue to decline more slowly thereafter. This observation is consistent with the formation of a solubility-limiting iron sulphide phase which is stable under the new conditions, and XRD data supports this hypothesis (section 5.3.4.2).

Although arsenic concentrations do rise sharply at the same time as iron concentrations, they do not peak until after 287.5 hours of sulphidisation (GS5). This may be because adsorbed As(V) stabilised the FeOOH surface against dissolution, causing the As(V)-contaminated goethite to be the last FeOOH fraction to undergo dissolution. Indeed, Biber et al. (1994) have clearly shown that binuclear surface complexes (such as those formed by As(V) on goethite; see EXAFS results in section 5.3.4.3) are highly effective at stabilising iron (oxyhydr)oxides against reductive dissolution. A similar phenomenon was observed during the ageing of As(V)-contaminated ferrihydrite (section 5.3.2.2).

Between 287.5 (GS5) and 434.5 (GS7) hours of sulphidisation, arsenic concentrations undergo a dramatic decrease to ≤ 0.4 ppm, and fall below detectable limits after 816.5 hours. As in the case of iron, this behaviour is consistent with the development of a new solubility-limiting phase. This is likely to be an iron and/or arsenic sulphide mineral; see section 5.3.4.3 for further discussion. Petersen et al. (1995) suggest that arsenic should be relatively mobile under sulphidic conditions as a result of the supposed instability of its sulphides. In contrast to this, it is noteworthy that only 10% of the available 29.6 ppm of arsenic was released to solution during sulphidisation. Whilst this suggests that arsenic remained relatively immoble, it is important to realise that any arsenic that remained in solution following the onset of sulphidisation (Fig. 5.12) was most likely to be in the mobile and toxic As(III) form.

The pattern of changes in dissolved sulphide concentrations are entirely consistent with the reductive dissolution of FeOOH and the subsequent formation of iron sulphide(s). As stated previously, levels of dissolved sulphide were initially below detectable limits even when increases in dissolved arsenic and iron indicated that sulphidisation had started. At this stage in the reaction, it is likely that all available sulphide was being used to attack the FeOOH phase. The first peak in sulphide concentrations occurred 174.0 hours after sulphidisation started (GS6). This is at the point when dissolved iron concentrations were starting to decrease, and it seems likely that more sulphide was being added to the system than was required for the reductive dissolution of remaining FeOOH. However, levels of dissolved sulphide underwent a decrease between 174.0 hours and 287.5 hours (GS7), at the

same time as the final sharp decrease in iron concentration was occurring. Because XRD evidence indicates that mackinawite ($Fe_{1+x}S$) is forming at this stage in the reaction (section 5.3.4.2), it is reasonable to assume that available sulphide was being consumed during the growth of this mineral. After dissolved iron (and arsenic) concentrations had reached low and relatively stable levels (after 434.5 hours), dissolved sulphide concentrations increased once more, this time to a constant value of around 0.45 mM. This level of dissolved sulphide compares favourably with concentrations found in sedimentary environments, which vary but are generally less than $5.0x10^{-3}$ M (Stanton and Goldhaber, 1991). Note that the last three sulphide data points represent averages from duplicate samples, and the associated error bars represent the actual sample concentrations. Whilst the first (lower concentration) sample of each duplicate was exposed to the lab atmosphere for up to 60 seconds before fixing in zinc acetate, the second (higher concentration) sample was collected much more rapidly. The difference in recorded concentrations may thus be due to greater loss of sulphide due to volatilisation in the first than the second sample. The disparity between duplicate sample concentrations is unlikely to have an instrumental origin since analysis of standards as unknowns before and after the samples demonstrated the high reproducibility of this method.

5.3.4.2 X-ray diffraction results from the sulphidisation of As(V)-contaminated goethite

The XRD results from samples collected during the progressive sulphidisation of As(V)-contaminated goethite are shown in Fig. 5.13.

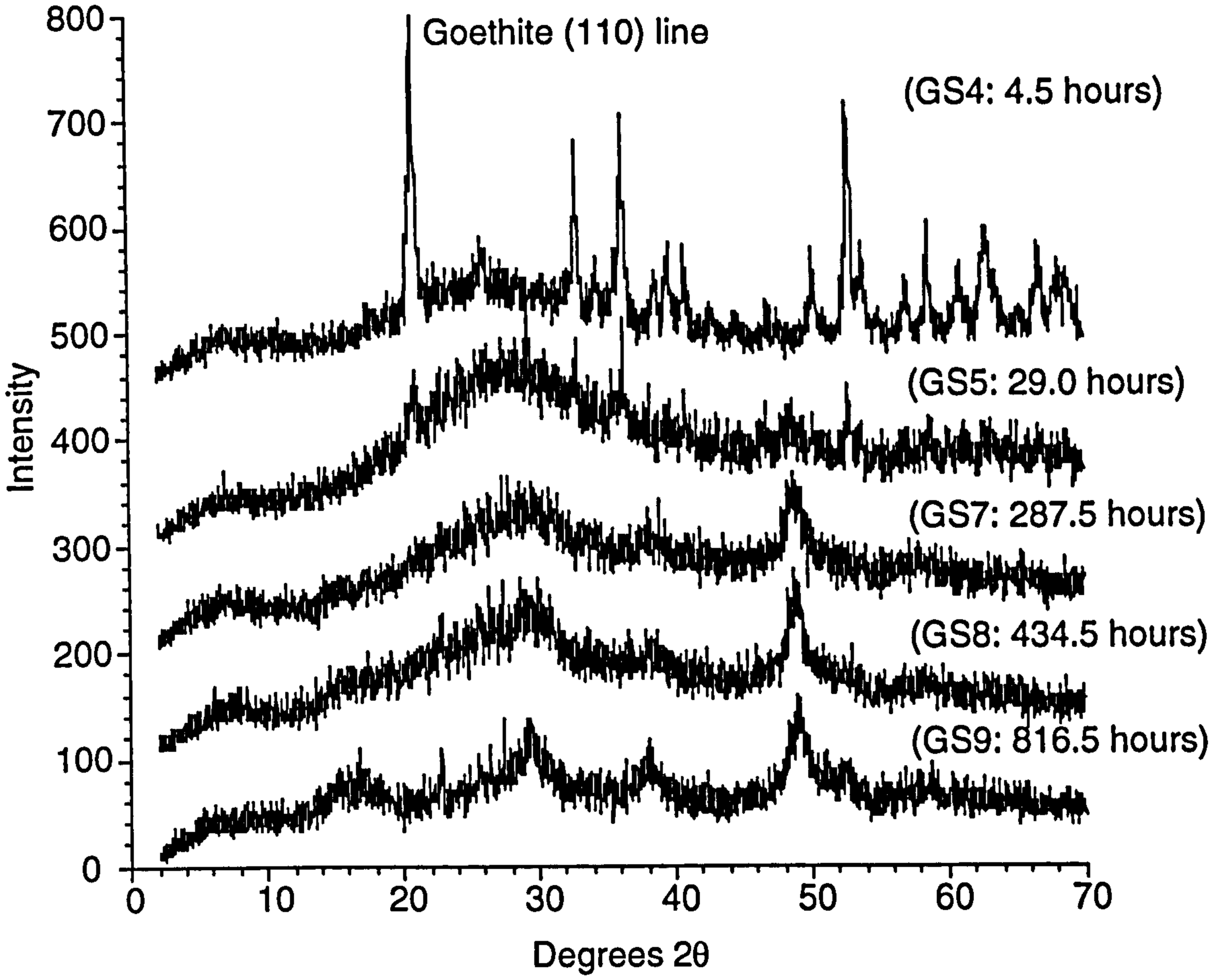

Fig. 5.13. XRD results from the sulphidisation of As(V)-contaminated goethite (GS4) to poorly crystalline mackinawite ($Fe_{1+x}S$) (JCPDS card 15-37) (GS9) at pH 5.2±0.1.

Sample GS4 was collected 4.5 hours after the flow of $H_2S(g)$ had started. The positions and relative intensities of the peaks are identical to those of pure goethite, although the absolute intensities are relatively low. For instance, the (110) line in (GS4) has an intensity of ~300 whereas the intensity of the same line in a sample of pure goethite (Fig. 5.7 a) is 550. This is qualitative evidence that reductive dissolution started very shortly after $H_2S(g)$ supply began, and is consistent with the presence of increasing amounts of iron in solution at this time (Fig. 5.12). Twenty-nine hours after H_2S flow began (GS5), only traces of the most intense goethite peaks remained, and a new 1.86 Å peak started to develop along with a broad hump between 20-30 degrees 2θ. The presence of only one new peak suggests the presence of minimal crystalline solubility-limiting phases, with a correspondingly high dissolved iron concentration when GS5 was collected (Fig. 5.12).

Following 287.5 hours of sulphidisation (GS7), all trace of the goethite precursor had disappeared and the 1.86 Å peak had grown considerably. A new ~2.37 Å peak also started to develop and the 20-30 degrees 2θ hump started to gain

some structure. This trend continued through GS8 (434.5 hours). The final product (GS9, 816.5 hours) was characterised by prominent 1.86 Å, 2.37 Å and 3.05 Å peaks and a more diffuse ~5.3 Å contribution. The intensity and position of these peaks suggest that the sulphidisation product is an acid volatile sulphide (AVS) mineral called mackinawite ($Fe_{1+x}S$) (JCPDS card 15-37). The relatively poor crystallinity of this material is indicated by the width and low absolute intensity of these peaks. Comparison with published XRD tables shows that GS9 does not contain any pyrite (FeS_2), marcasite (FeS_2), greigite (Fe_3S_4) or arsenopyrite (FeAsS).

Previous work has shown that the first iron sulphide phase to form under anoxic sedimentary environments is amorphous iron sulphide (FeS(am)) (Berner, 1967). This initial precipitate develops incipient long-range order in a matter of days, and transforms into poorly crystalline mackinawite quite rapidly under both abiotic (e.g. Rickard, 1995) and microbially-mediated conditions (Herbert et al., 1998). However, transformation to a well crystallised form of this mineral can take up to two years at 25°C (Rickard, 1995). Consequently, poorly crystalline mackinawite is likely to exert a strong control on the concentrations of dissolved ferrous iron and sulphide in reducing sediments (Herbert et al., 1998), although its presence is hard to confirm because it commonly occurs as a finely dispersed precipitate and as a coating on other minerals (Morse and Cornwell, 1987).

It appears that the abiotic method used to achieve goethite sulphidisation in this study successfully replicated the mineralogical changes expected during the early development of natural sedimentary iron sulphides. Although a number of studies have shown that disordered mackinawite is a precursor phase to pyrite formation (Schoonen and Barnes, 1991; Stanton and Goldhaber, 1991; Wilkin and Barnes, 1996, 1997; Rickard, 1997; Rickard and Luther, 1997), the formation of pyrite is not expected within the time frame of this experiment.

5.3.4.3 EXAFS results from the sulphidisation of As(V)-contaminated goethite

The arsenic K-edge EXAFS results from GS3 (pre-sulphidisation), GS4, GS8 and GS9 are shown in Fig. 5.14 and summarised in Table 5.4.

Table 5.4. EXAFS results from As(V)-goethite and its sulphidisation products. CN_X is number of atoms in a shell at distance R_X (Å) from the central cadmium atom. $2\sigma^2_X$ (Å^2) is the associated Debye-Waller factor. The *R* factor gives a measure of the agreement between experimental and theoretical EXAFS curves. $R < 20\%$ indicates a very good fit whereas $R \leq 40\%$ is acceptable.

Sample Sulphidis-ation time	R_{As-O}	CN_O $2\sigma^2 o$	R_{As-S}	CN_S $2\sigma^2 s$	R_{As-Fe1}	CN_{Fe1} $2\sigma^2 Fe1$	R_{As-Fe2}	CN_{Fe2} $2\sigma^2 Fe2$	*R* factor
GS3	1.69	4.1	-	-	2.91	0.9	3.32	1.7	21.2
0.0 hr		*0.005*				*0.019*		*0.011*	
Sulphidisation started 4.5 hr before sample GS4 was taken.									
GS4	1.69	3.5	2.14	0.2	2.89	0.7	3.31	1.5	20.0
4.5 hr		*0.005*				*0.019*		*0.008*	
GS8	-	-	2.27	3.0	-	-	-	-	24.3
434.5 hr				*0.009*					
GS9	-	-	2.27	2.6	-	-	-	-	34.8
816.5 hr				*0.011*					
Orpiment			2.29	2.9	3.20	1.0 **As**	3.56	2.4 **As**	21.2
As_2S_3				*0.005*	**As-As**	*0.016*	**As-As**	*0.020*	
EXAFS reference standard									
Sample	% SL† (wt % As)	R_{As-O}	CN_O $2\sigma^2 o$	R_{As-Fe1}	CN_{Fe1} $2\sigma^2 Fe1$	R_{As-Fe2}	CN_{Fe2} $2\sigma^2 Fe2$	*R* factor	
As(V) on	36.6	1.69	4.0	2.85	0.8	3.31	1.5	22.0	
goethite	(0.24)		*0.004*		*0.019*		*0.011*		

Notes:

† % SL = percentage surface loading, which describes the proportion of available surface sites occupied by adsorbed arsenic. This value was calculated using a maximum surface site density for As(V) of 1.58 sites nm^{-2} on goethite derived from Sun and Doner (1996).

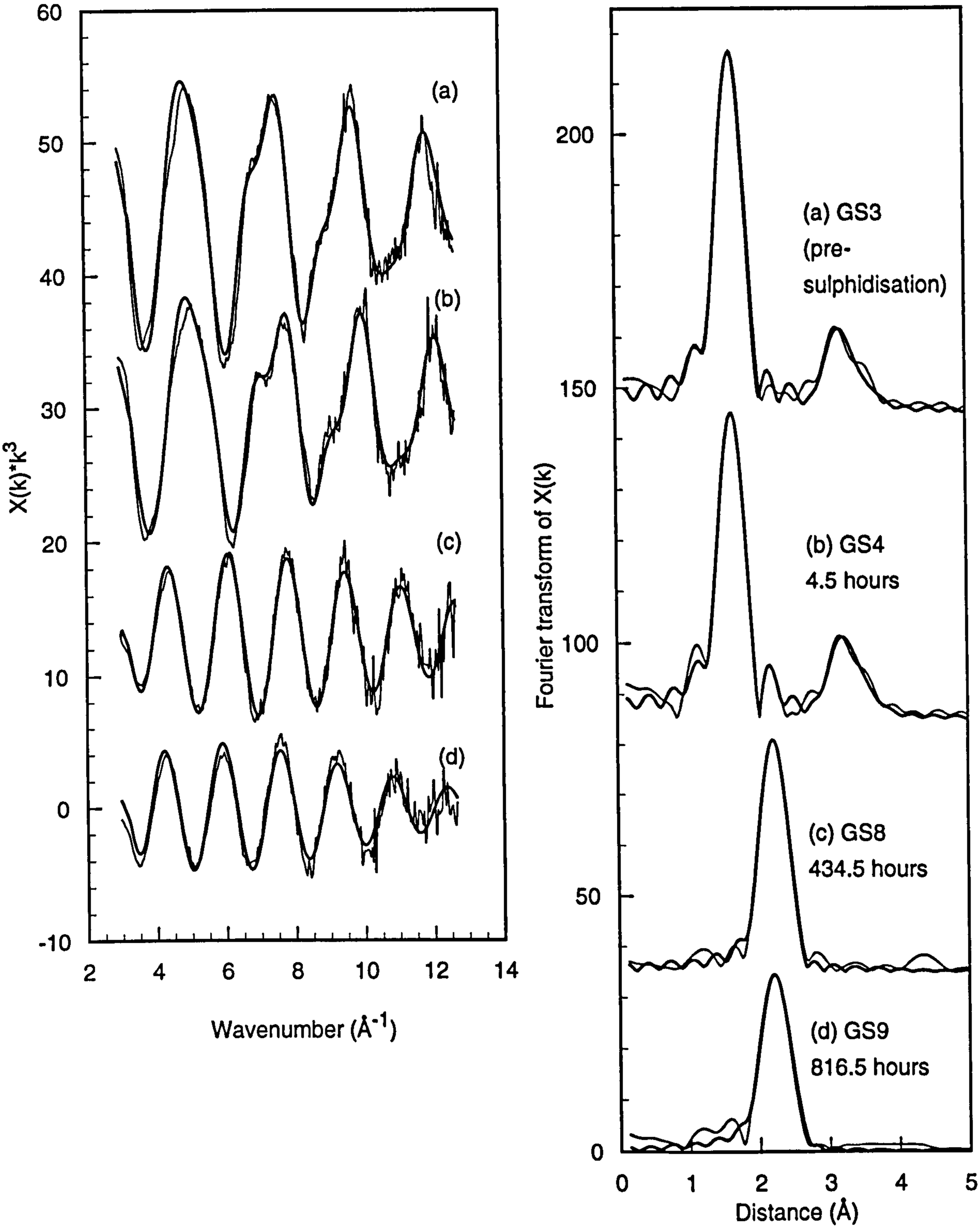

Fig. 5.14. EXAFS (left) and FT (right) plots of As(V)-contaminated goethite (a) that was progressively sulphidised (b, c, d) at pH 5.2±0.1. Samples (a) and (b) are dominated by contributions from As(V) adsorbed via bidentate bridging between adjacent singly coordinated hydroxyls at the goethite surface (~1.6 iron atoms at As-Fe = 3.31 Å). The inclusion of a weak sulphur shell contribution at 2.14 Å slightly improves the quality of the fit in (b), consistent with the onset of sulphidisation. The sulphur shell (3.0 sulphur atoms at 2.27 Å) is fully developed in (c) and (d), and is consistent with the formation of As_2S_3(am). Compare with orpiment data (Fig. 5.4 e).

Sample GS3 was collected prior to the onset of sulphidisation, and the EXAFS results from this sample are essentially the same as those from the As(V) on goethite EXAFS reference standard (Table 5.4). Aside from the inner shell of tetrahedrally coordinated oxygen atoms, there are iron shell contributions at 2.91 Å and 3.32 Å, which suggest that As(V) adsorption occurs by single edge- and double corner sharing adsorption. The results from GS4, which was collected after 4.5 hours of sulphidisation, are slightly different. Whilst both iron shells remain unchanged, there is a weak sulphur shell contribution at an As-S distance of 2.14 Å. Additionally, the oxygen shell coordination number drops from 4.1 in GS3 to 3.5 in GS4. Whilst these changes on their own are relatively minor, when taken together, they suggest the onset of sulphidisation. Remember that increases in the levels of dissolved iron and arsenic at the time GS4 was collected suggested a similar scenario (section 5.3.4.1).

The EXAFS results from GS8 and GS9 show that the arsenic coordination environment in these samples is very different to that in GS3 and GS4. The iron shells have gone, and the shell of tetrahedrally coordinated oxygen atoms has been replaced by one containing 2.6-3.0 sulphur atoms at an As-S distance of 2.27 Å. This is very similar to the first shell coordination environment around arsenic in crystalline and amorphous orpiment (As_2S_3) (Fig. 5.4 e, Table 5.4), but is distinctly different to that in realgar (AsS) (Helz et al., 1995).

It is clear from the low levels of arsenic in solution when GS8 and GS9 were collected (Fig. 5.12) that the majority of arsenic was sorbed in some way at this stage in the reaction. However, the lack of second neighbour contributions in the EXAFS spectra from these two samples (Fig. 5.14) makes it hard to determine the mechanism by which sorption occurred. Helz et al. (1995) have collected EXAFS data from arsenic sulphide solutions that were undersaturated with respect to orpiment. They too were only able to resolve a single sulphur shell around arsenic, but the As-S distance in this case was 2.21-2.23 Å. This was assigned to the $AsS(SH)_2^-$ monomer. Under conditions of oversaturation with respect to orpiment, the trimer $As_3S_4(SH)_2^-$ is additionally present, but no EXAFS data is available for this species. However, Helz et al. (1995) did determine the geometries of the trimers $As_3S_3(SH)_3$ and $As_3S_6^{3-}$ using polarised split valence Hartree-Fock calculations. The calculated As-S distances for these molecules were 2.248 Å and 2.301 Å, respectively. The As-S distance observed in GS8 and GS9 (2.27 Å) is distinctly different to this, suggesting that the arsenic coordination environment observed in GS8 and GS9 is not consistent with adsorbed As(III) sulphide species.

Thus, it seems likely that arsenic was sorbed in the form of orpiment or As_2S_3(am). The lack of an As-As contribution in the EXAFS data is problematic, but may be explained in part by the structure of orpiment. This consists of AsS_3

pyramids polymerised in two dimensions to form sheets (Mullen and Nowacki, 1972). Twisting of the pyramids with respect to one another can produce disorder in the higher coordination shells by changing interatomic distances, whilst leaving the first shell geometry essentially unaffected (Helz et al., 1995). A high degree of incoherency in a given atomic shell would cause the corresponding FT peak to become broader and less intense, and may even cause EXAFS oscillations from that shell to cancel each other out to some extent.

If arsenic is indeed precipitated as As_2S_3(am), the solubility data of Eary (1992) suggests that the dominant aqueous species should be $H_3AsO_3^0$ under acid, sulphide-deficient conditions and $H_2As_3S_6^-$ under acidic, excess sulphide conditions.

5.4 CONCLUSIONS

Ferrihydrite, otherwise known as hydrous ferric oxide (HFO), is one of the most important sorbents of As(V) under oxic conditions. As(V) adsorption on ferrihydrite is strong, and because ferrihydrite is so ubiquitous this mineral plays a very important role in the 'natural attenuation' of As(V). Natural attenuation is a phenomenon whereby naturally occurring sorbents act as a barrier to the migration of contaminant species in the environment. However, since As(V)-contaminated ferrihydrite constitutes a potentially massive reservoir of arsenic, it is essential that we understand changes that this material is likely to undergo over time, and the implications that this has for sorbed arsenic. One of the most likely changes is the ageing of ferrihydrite to more crystalline phases such as goethite (α-FeOOH) or hematite (α-Fe_2O_3). Since this phase transformation is accompanied by a decrease in bulk surface area (and hence the number of sorption sites), there is clearly the potential for the release of adsorbed As(V). However, results presented here show that this does not occur. When ferrihydrite that was contaminated with a relatively small amount of As(V) (bulk As/(As+Fe) = 0.0033) was aged to goethite, all As(V) remained adsorbed because the sorption capacity of the crystalline product was not exceeded. Importantly, there was also no arsenic release from samples whose sorption capacity would have been exceeded if all ferrihydrite had transformed to goethite or hematite. This is due to the fact that sorbed As(V) retarded the ageing process to such an extent that significant amounts of untransformed ferrihydrite remained, and the sorption capacity of the samples was consequently not exceeded. Another important finding is that throughout the ageing process, As(V) persisted as surface complexes whether it was added prior to or after the nucleation of ferrihydrite. It was not incorporated into the iron oxyhydroxide bulk structure, and there was no evidence for the formation of a ferric arsenate phase such as scorodite

($FeAsO_4 \cdot 2H_2O$). This result is in agreement with field observations (e.g. Voigt et al., 1996).

Green rust ($Fe_y^{(II)}Fe_x^{(III)}(OH)_{3x+2y-2z}(SO_4)_z$) is a mixed Fe(II)-Fe(III) oxyhydroxide mineral that is thought to occur under the reducing and mildly acidic to mildly alkaline conditions found in reductomorphic soils and certain sedimentary horizons. Consequently, it is likely to be one of the most important Fe(II)-bearing minerals in immature sediments and soils. Green rust has previously been shown to be capable of reducing Cr(VI) to Cr(III) (see Chapter 6), Se(VI) to Se(0), and nitrate to ammonium. In contrast to these findings, results presented here show that green rust does not reduce As(V) to As(III), irrespective of whether arsenic is added prior to or after green rust formation. This is of great importance because As(III) is far more toxic and mobile than As(V). Following adsorption on green rust, As(V) persists as surface complexes, even after the oxidation of green rust to lepidocrocite (γ-FeOOH). It is not incorporated into the green rust bulk structure and it does not exchange for sulphate anions in the interlayer sites that are present in green rust.

In contrast to the findings with green rust, As(V) is reduced to As(III) during the sulphidisation of an As(V)-contaminated goethite. X-ray diffraction analyses showed that all goethite was consumed during the reaction and that it was replaced by poorly crystalline mackinawite ($Fe_{1+x}S$). Dissolved arsenic concentrations remained low after the formation of this mineral. However, extended X-ray absorption fine structure (EXAFS) spectroscopy results are not consistent with the sorption of arsenic sulphide complexes or the formation of an arsenic-iron sulphide coprecipitate. It is apparent that arsenic partitioned into a discrete amorphous orpiment (As_2S_3(am)) precipitate, and it is likely that this exerted the major control on arsenic solubility. This finding is consistent with field studies which suggest that arsenic concentrations can be controlled by equilibrium with authigenic arsenic sulphides under reducing, sulphidic conditions. A note of caution is that whilst arsenic concentrations remained low following the formation of the solubility-limiting sulphide phase, any arsenic that remained in solution will have been in the toxic and highly mobile As(III) form.

Taken together, the results presented here demonstrate that under the oxic to mildly reducing conditions which favour ferrihydrite and green rust, respectively, dissolved arsenic concentrations will be controlled by equilibrium with adsorbed arsenate species. This will be the case even when immature ferric (oxyhydr)oxide minerals age and become more crystalline, because ferric arsenate minerals do not appear to form easily under low temperature, near surface conditions.

However, under strongly reducing conditions such as those found in sulphidic sediments, dissolution of iron (oxyhydr)oxide sorbents can lead to the release of large quantities of arsenic, presumably in the mobile and toxic As(III)

form. Rather than forming arsenopyrite (FeAsS) or a solid solution with existing iron sulphides such as mackinawite, the liberated arsenic appears to form a discrete precipitate which resembles poorly crystalline orpiment. This will exert the major control on arsenic solubility under reducing, sulphidic conditions. It is important to appreciate that oxidation of the As_2S_3(am) phase would lead to the release of significant amounts of arsenic to solution. Consequently, it is clear that cyclical (e.g. seasonal) changes in soil and sediment redox profiles as well as events such as dredging and large storms have the potential to mobilise large amounts of arsenic.

5.5 REFERENCES

Aggett J. and O'Brien G. A. (1985) Detailed model for the mobility of arsenic in lacustrine sediments based on measurements in Lake Ohakuri. Envrion. Sci. Technol. 19, 231-238.

Aggett J. and Roberts L. S. (1986) Insight into the mechanism of accumulation of arsenate and phosphate in hydro lake sediments by measuring the rate of dissolution with ethylenediamine-tetraacetic acid. Envrion. Sci. Technol. 20, 183-186.

Allman R. (1968) The crystal structure of pyroaurite. Acta Cryst. B24, 972-977.

Belzile N. and Tessier A. (1990) Interactions between arsenic and iron oxyhydroxides in lacustrine sediments. Geochim. Cosmochim. Acta 54, 103-109.

Bernal J. D., Dasgupta D. R. and MacKay A. L. (1959) The oxides and hydroxide of iron and their structural interrelationships. Clay Mineral Bulletin 4, 15-30.

Berner R. A. (1967) Thermodynamic stability of sedimentary iron sulphides. Am. J. Sci. 265, 773-785.

Bhumbla D. K. and Keefer R. F. (1994) Arsenic mobilization and bioavailability in soils. In *Arsenic in the environment, Part. 1: Cycling and characterization* (Ed. Nriagu, J. O.). John Wiley and Sons, New York. pp. 51-82.

Biber M .V., Afonso M. D. and Stumm W. (1994) The coordination chemistry of weathering. 4. inhibition of the dissolution of oxide minerals. Geochim. Cosmochim. Acta 58, 1999-2010.

Binsted N., Campbell J. W., Gurman S. J., and Stephenson P. C. (1991) SERC Daresbury Laboratory EXCURV92 program. Daresbury Laboratory, Warrington, U.K.

Binsted N., Strange R. W., and Hasnain S. S. (1992) Restrained refinement. Biochemistry 31, 12117-12125.

Bowell R. J. (1994) Sorption of arsenic by iron oxides and oxyhydroxides in soils. Applied Geochemistry 9, 279-286.

Branson J. M. and Patrick W. J. (1987) Fixation, transformation, and mobilization of arsenic in sediments. Environ. Sci. Technol. 20, 450-459.

Brennan E. W. and Lindsay W. L. (1996) The role of pyrite in controlling metal ion activities in highly reduced soils. Geochim. Cosmochim. Acta 60, 3609-3618.

Brindley G. W. and Bish D. L. (1976) Green rust: a pyroaurite type structure. Nature 262, 353.

Brown G. E. Jr., Calas G., Waychunas G. A. and Petiau J. (1988) X-ray absorption spectroscopy and its applications in mineralogy and geochemistry. In

Spectroscopic Methods in Mineralogy and Geology (ed. F. Hawthorne). Reviews in Mineralogy Vol. 18. Min. Soc. Am. pp. 431-512.

Brown G. E. Jr., Parks G. A. and O'Day P. A. (1995) Sorption at the mineral-water interface: macroscopic and microscopic perspectives. In *Mineral Surfaces* (eds. D. J. Vaughan and R. A. D. Pattrick). Chapman and Hall. pp. 129-183.

Buurman P. (1980) Paleosols in the Reading Beds (Paleocene) of Alum Bay, Isle of Wight, U.K. *Sedimentology* 27, 593-606.

Canfield D. E. (1989) Reactive iron in marine sediments. Geochim. Cosmochim. Acta 53, 619-632.

Charlet L and Manceau A. (1993) Structure, formation, and reactivity of hydrous oxide particles: Insights from X-ray absorption spectroscopy. In *Environmental Particles*, Vol. 2 (eds. J. Buffle and H. P. van Leeuwen). IUPAC Environmental Analytical and Physical Chemistry Series. pp. 118-164.

Cline J. D. (1969) Spectrophotometric determination of hydrogen sulphide in natural waters. Limnology and Oceanography 14, 454-458.

Combes J. M., Manceau A., Calas G. and Bottero J. Y. (1989) Formation of ferric oxides from aqueous solutions: A polyhedral approach by X-ray absorption spectroscopy: I. Hydrolysis and formation of ferric gels. Geochim. Cosmochim. Acta 53, 583-594.

Cornell R. M. and Scwertmann U. (1979) Influence of organic anions on the crystallization of ferrihydrite. Clays Clay Mineral. 27, 402-410.

Dent A. J. and Mosselmans J. F. W. (1992) *A guide to EXBACK, EXCALIB, and EXCURV92.* Daresbury Laboratory, Warrington, U.K.

Deuel L. E. and Swoboda A. R. (1972) Arsenic toxicity to cotton and soy beans. J. Env. Qual. 1, 317-320.

Eary. L. E. (1992) The solubility of amorphous As_2S_3 from 25 to 90 °C. Geochim. Cosmochim. Acta 56, 2267-2280.

Farmer J. G. and Lovell M. A. (1986) Natural enrichment of arsenic in Loch Lochmond sediments. Geochim. Cosmochim. Acta 50, 2059-2067.

Feitknecht W. and Keller G. (1950) Über die dunkel-grünen Hydroxylverbindungen des Eisens. Z. anorg. allg. Chem. 262, 61-68.

Fendorf S., Eick M. J., Grossl P. and Sparks D. L. (1997) Arsenate and chromate retention mechanisms on goethite. 1. Surface structure. Envrion. Sci. Technol. 31, 315-320.

Ferguson J. F. and Gavis J. (1972) A review of the arsenic cycle in natural waters. Water Res. 6, 1259-1274.

Fischer W. R. and Schwertmann U. (1975) The formation of hemtatite from amorphous iron (III) hydroxide. Clays Clay Mineral. 23, 33-37.

Foster A. L., Brown G. E. Jr., Tingle T. N. and Parks G. A. (1998) Quantitative arsenic speciation in mine tailings using X-ray absorption spectroscopy. Amer. Mineral. 83, 553-568.

Fredrickson J. K., Zachara, J. M., Kennedy D. W., Dong H. L., Onstott T. C., Hinman N. W. and Li S. M. (1998) Biogenic iron mineralization accompanying the dissimilatory reduction of hydrous ferric oxide by a groundwater bacterium. Geochim. Cosmochim. Acta 62, 3239-3257.

Fuller C. C. and Davis J. A. (1989) Influence of coupling of sorption and photosynthetic processes on trace element cycles in natural waters. Nature 340, 52-54.

Fuller C. C., Davis J. A. and Waychunas G. A. (1993) Surface chemistry of ferrihydrite. 2. kinetics of arsenate adsorption and coprecipitation. Geochim. Cosmochim. Acta 57, 2271-2282.

Goldhaber M. B. and Kaplan I. R. (1974) The sulfur cycle. In *The Sea* (ed. E. D. Goldberg). Vol. 5. Wiley. pp. 569-655.

Goldhaber M. B. and Kaplan I. R. (1980) Mechanism of sulfur incorporation and isotope fractionation during early diagenesis in sediments of the Gulf of California. Mar. Chem. 9, 95-143.

Grossl P. R. and Sparks D. L. (1995) Evaluation for contaminant ion adsorption-desorption on goethite using pressure-jump relaxation kinetics. Geoderma 67, 87-101.

Grossl P. R., Eick M., Sparks D. L., Goldberg S. and Ainsworth C. C. (1997) Arsenate and chromate retention mechanisms on goethite. 2. Kinetic evaluation using a pressure-jump relaxation technique. Envrion. Sci. Technol. 31, 321-326.

Guo T. Z., DeLaune R. D. and Patrick W. H. (1997) The influence of sediment redox chemistry on chemically active forms of arsenic, cadmium, chromium, and zinc in estuarine sediment. Environment International 23, 305-316.

Gurman S. J. (1988) The small atom approximation theory. J. Phys. C: Solid State Phys. 21, 3699-3717.

Gurman S. J., Binsted N., and Ross I. (1984) Single scattering rapid curved wave theory. J. Phys. C: Solid State Phys. 17, 143-151.

Gurman S. J., Binsted N., and Ross I. (1986) Multiple scattering rapid curved wave theory. J. Phys. C: Solid State Phys. 19, 1845-1861.

Hansen H. C. B., Borggaard O. K. and Sorensen J. (1994) Evaluation of the free energy of formation of Fe(II)-Fe(III) hydroxide-sulfate (green rust) and its reduction of nitrite. Geochim. Cosmochim. Acta 58, 2599- 2608.

Hansen H. C. B., Koch C. B., Nanckekrogh H., Borggaard O. K. and Sorensen J. (1996) Abiotic nitrate reduction to ammonium - key role of green rus. Environ. Sci. Technol. 30, 2053-2056.

Hedin L. and Lundqvist S. (1969) Effects of electron-electron and electron-phonon interactions on the one-electron states of solids. Solid State Phys. 23, 1-181.

Helz G. R., Tossell J. A., Charnock J. M., Pattrick R. A. D., Vaughan D. J. and Garner C. D. (1995) Oligomerization in As(III) sulfide solutions - theoretical constraints and spectroscopic evidence. Geochim. Cosmochim. Acta 59, 4591-4604.

Herbert R. B., Benner S. G., Pratt A. R. and Blowes D. W. (1998) Surface chemistry and morphology of poorly crystalline iron sulfides precipitated in media containing sulfate-reducing bacteria. Chem. Geol. 144, 87-97.

Hesterberg D., Hansen P. D., Zhou W. and Sayers D. E. (1998) EXAFS study of metal sulphide stability in a contaminated soil. Min. Mag. 62A, pp. 612-613.

Howarth R. W. and Jørgensen B. B. (1984) Formation of ^{35}S-labelled elemental sulfur and pyrite in coastal marine sediments (Limforden and Kysing Fjord, Denmark) during short-term $^{35}SO_4^{2-}$ reduction measurements. Geochim. Cosmochim. Acta 48, 1807-1818.

Hsia T. H., Lo S. L., Lin C. F. and Lee D. Y. (1994) Characterization of arsenate adsorption on hydrous iron oxide using chemical and physical methods. Colloids Surfaces A - Physicochem. Eng. Aspects 85, 1-7.

Huerta-Diaz M. A. and Morse J. W. (1990) Pyritization of trace metals in anoxic marine sediments. Geochim. Cosmochim. Acta 56, 2681-2702.

Huerta-Diaz M. A. and Morse J. W. (1992) A quantitative method for determination of trace metal concentrations in sedimentary pyrite. Mar. Chem. 29, 119-144.

Iimura K. (1981) In *Heavy metal pollution in soil of Japan* (eds. K. Kitagishi and I. Yamane), Jpm. Sci. Soc. Press, Tokyo, pp. 19-26.

Joyner R. W., Martin K. J., and Meehan. P. (1987) Some applications of statistical tests in analysis of EXAFS and SEXAFS data. J. Phys. C: Solid State Phys. 20, 4005-4012.

Kitahama K., Kiriyama R. and Baba Y. (1975) Refinement of the crystal structure of scorodite. Acta Crysta B31, 322-324.

Korte N. (1991) Naturally occurring arsenic in groundwaters of the midwestern United States. Environ. Geol. Water Sci. 18, 137-141.

Krauskopf K. B. and Bird D. K. (1995) *Introduction to geochemistry*. McGraw Hill. pp. 218-220.

Livesey N. T. and Huang P. M. (1981) Adsorption of arsenate by soils and its relation to selected chemical-properties and anions. Soil Sci. 131, 88-94.

Luther G. W. III and Morse J. W. (1998) Chemical influences on trace metal-sulphide interactions in anoxic sediments. Min. Mag. 62A, pp. 925-926.

Manceau A. (1995) The mechanism of anion adsorption on iron oxides: Evidence for the bonding of arsenate tetrahedra on free Fe(O,OH)6 edges. Geochim. Cosmochim. Acta 59, 3647-3653.

Manceau A. and Combes J. M. (1988) Structure of Mn and Fe oxides and oxyhydroxides: A topological approach by EXAFS. Phys. Chem. Min. 15, 283-295.

Mandal B. K., Chowdry T. R., Samanta G., Basu G. K., Chowdry P. P., Chanda C. R., Lodh, D., Karan N. K., Dhar R. K., Tamili D. K., Das D., Saha K. C. and Chakraborti D. (1996) Arsenic in groundwater in seven districts of West Bengal, India - The biggest arsenic calamity in the world. Current Sci. 70, 976-986.

Manning B. A. and Goldberg S. (1996) Modeling competitive adsorption of arsenate with phosphate and molybdate on oxide minerals. Soil Sci. Soc. Of Am. J. 60, 121-131.

Manning B. A., Fendorf S. E. and Goldberg S. (1998) Surface structures and stability of arsenic(III) on goethite: Spectroscopic evidence for inner-sphere complexes. Environ. Sci. Technol. 32, 2383-2388.

Masscheleyn P. H., Delaune R. D. and Patrick W. H. (1991) Effect of redox potential and pH on arsenic speciation and solubility in a contaminated soil. Env. Sci. Technol. 25, 1414-1419.

Melamed R., Jurinak J. J. and Dudley L. M. (1995) Effect of adsorbed phosphate on transport of arsenate through an oxisol. Soil Sci. Soc. Of Am. J. 59, 1289-1294.

Mok W. M., Riley J. A. and Wai C. M. (1988) Arsenic speciation and quality of groundwater in a lead-zinc mine, Idaho. Water Res. 22, 769-774.

Moore J. N., Ficklin W. H. and Johns C. (1988) Partitioning of arsenic and metals in reducing sulfidic sediments. Environ. Sci. Technol. 22, 432-437.

Moore J. N., Luoma S. N. and Peters D. (1991) Downstream effects of mine effluent on an intermontane riparian system. Can. J. Fish. Aquat. Sci. 48, 222-232.

Morse J. W. and Cornwell J. C. (1987) Analysis and distribution of iron sulfide minerals in recent anoxic marine sediments. Mar. Chem. 22, 55-69.

Mullen D. J. E. and Nowacki W. (1972) Refinement of the crystal structures of realgar, AsS, and orpiment, As_2S_3. Zeit. Kristall. 136, 48-65.

Myneni S. C. B., Tokunaga T. K. and Brown G. E. Jr. (1997) Abiotic selenium redox transformations in the presence of Fe(II,III) oxides. Science 278, 1106-1109.

Newman A. C. D. (ed.) (1987) Chemistry of clays and clay minerals. In *Mineralogical Society Monograph 6.* John Wiley and Sons, New York. p 480.

Nriagu J. O. (ed.) (1994) *Arsenic in the environment, Part. 1: Cycling and characterization.* John Wiley and Sons, New York.

Palmer D. C. (1996) CrystalMaker 2.1.0: Interactive crystallography for MacOS.

Petersen W., Wallmann K., Li, P., Schroeder F. and Knauth H. -D. (1995) Exchange of trace elements at the sediment-water interface during early diagenesis processes. Mar. Freshwater Res. 46, 19-26.

Pierce M. L. and Moore C. B. (1982) Adsorption of arsenite and arsenate on amorphous iron hydroxide. Water Res. 16, 1247-1253.

Rickard D. T. (1995) Kinetics of FeS precipitation, Part 1. Competing reaction mechanisms. Geochim. Cosmochim. Acta 59, 4367-4379.

Rickard D. T. (1997) Kinetics of pyrite formation by the H_2S oxidation of iron (II) monosulphide in aqueous solutions between 25 and 125°C: the rate equation. Geochim. Cosmochim. Acta 61, 115-134.

Rickard D. T. and Luther G. W. III (1997) Kinetics of pyrite formation by the H_2S oxidation of iron (II) monosulphide in aqueous solutions between 25 and 125°C: the mechanism. Geochim. Cosmochim. Acta 61, 135-147.

Robins R. G. (1985) The aqueous chemistry of arsenic in relation to hydrometallurgical processes. In *Proc. CIM 15th Annl. Hydrometallurgical Mtg., Vancouver, Canada, Aug. 19-21, 1985.* pp. 1-1-1-26.

Schoonen M. A. A. and Barnes H. L. (1991) Reactions forming pyrite and marcasite from solution, II. Via FeS precursor below 100°C. Geochim. Cosmochim. Acta 55, 1504-1514.

Schwertmann U. and Murad E. (1983) Effect of pH on the formation of goethite and hematite from ferrihydrite. Clays Clay Mineral. 31, 277-284.

Schwertmann U. and Cornell R. M. (1991) *Iron oxides in the laboratory: Preparation and characterization.* VCH Publishers.

Schwertmann U. and Fechter H. (1994) The formation of green rust and its transformation to lepidocrocite. Clay minerals 29, 87-92.

Schwertmann U., Gasser U. and Sticher H. (1989) Chromium-for-iron substitution in synthetic goethites. Geochim. Cosmochim. Acta 53, 1293-1297.

Shinoda K., Matsubara E., Muramatsu A. and Waseda Y. (1994) Local structure of ferric hydroxide $Fe(OH)_3$ in aqueous solution by the anomalous X-ray scattering and EXAFS methods. Materials Trans., JIM 35, 394-398.

Shokes T. E. and Moller G. (1999) Removal of dissolved heavy metals from acid rock drainage using iron metal. Environ. Sci. Technol. 33, 282-287.

Stampfl P. P. (1969) Ein basisches eisen-(II)-(III) karbonat in rost. Corr. Sci. 9, 185-187.

Stanton M. R. and Goldhaber M. B. (1991) An experimental study of goethite sulphidisation - relationships to the diagenesis of iron and sulfur. In *Geochemical, biochemical, and sedimentological studies of the Green River formation, Wyoming, Utah, and Colorado* (ed. Tuttle M. L.). U.S. Geol. Surv. Bull. 1973, chapter E, pp. E1-E20.

Stumm W., Sulzberger B. and Sinniger J. (1990) The coordination chemistry of the oxide-electrolye interface; The dependence of surface reactivity (dissolution, redox reactions) on surface structure. Croatica Chemica Acta 63, 277-312.

Sullivan K. A. and Aller R. C. (1996) Diagenetic cycling of arsenic in Amazon shelf sediments. Geochim. Cosmochim. Acta 60, 1465-1477.

Sun X. H. and Doner H. E. (1996) An investigation of arsenate and arsenite bonding structures on goethite by FTIR. Soil Science 161, 865-872.

Taylor R. M. (1973) Cyrstal structures of some double hydroxide minerals. Mineral. Mag. 39, 377-389.

Trolard F., Genin J. M. R., Abdelmoula M., Bourrie G., Humbert B. and Herbillon A. (1997) Identification of a green rust mineral in a reductomorphic soil by mossbauer and raman spectroscopies. Geochim. Cosmochim. Acta 61, 1107-1111.

Tuhela L., Carlson L. and Tuovinen O. H. (1997) Biogeochemical transformations of Fe and Mn in oxic groundwater and well water environments. J. Environ. Sci. Health Part A - Environ. Sci. Eng. and Toxic and Hazardous Substance Control 32, 407-426.

Vins J., Subrt J., Zapletal V. and Hanousek F. (1987) Preparation and properties of green rust type substances. Collection Czechoslovak Chem. Commun. 52, 93-102.

Voigt D. E., Brantley S. L. and Hennet R. J. -C. (1996) Chemical fixation of arsenic in contaminated soils. Applied Geochem. 11, 633-643.

Waychunas G. A., Rea B. A., Fuller C. C. and Davis J. A. (1993) Surface chemistry of ferrihydrite. 1. EXAFS studies of the geometry of coprecipitated and adsorbed arsenate. Geochim. Cosmochim. Acta 57, 2251-2269.

Waychunas G. A., Davis J. A. and Fuller C. C. (1995) Geometry of sorbed arsenate on ferrihydrite and crystalline FeOOH: Re-evaluation of EXAFS results and topological factors in predicting sorbate geometry, and evidence for monodentate complexes. Geochim. Cosmochim. Acta 59, 3655-3661.

Waychunas G. A., Fuller C. C., Rea B. A. and Davis J. A. (1996) Wide angle X-ray scattering (WAXS) of "two-line" ferrihydrite structure: Effect of arsenate sorption and counterion variation and comparison with EXAFS results. Geochim. Cosmochim. Acta 60, 1765-1781.

Wehrli B. (1990) Redox reactions of metal ions at mineral surfaces. In *Aquatic chemical kinetics* (ed. W. Stumm). J. Wiley and Sons, N.Y. pp. 311-336.

White A. F. and Peterson M. L. (1996) Reduction of aqueous transition metal species on the surfaces of Fe(II)-containing oxides. Geochim. Cosmochim. Acta 60, 3799-3814.

Wilkie J. A. and Hering J. G. (1996) Adsorption of arsenic onto hydrous ferric oxide - effects of adsorbate/adsorbent ratios and co-occurring solute. Colloids and Surfaces A - Physicochem. Eng. Aspects 107, 97-110.

Wilkin R. T. and Barnes H. L. (1996) Pyrite formation by reactions of iron monosulphides with dissolved inorganic and organic sulfur species. Geochim. Cosmochim. Acta 60, 4167-4179.

Wilkin R. T. and Barnes H. L. (1997) Formation processes of framboidal pyrite. Geochim. Cosmochim. Acta 61, 323-339.

Wilson F. H. and Hawkins D. B. (1978) Arsenic in streams, stream sediments, and ground water, Fairbanks area, Alaska. Environ. Geol. 2, 195-202.

World Health Organisation (1993) Guidelines for drinking water quality. Vol. 1. Recommendations, 2nd edn. WHO, Geneva.

Zhuang Y. Y., Allen H. E. and Fu G. M. (1994) Effect of aeration of sediment on cadmium binding. Environ. Toxicol. Chem. 13, 717-724.

Zobrist J., Dowdle P. R., Davis J. A. and Oremland R. S. (1998) Microbial arsenate reduction Vs. arsenate sorption: Experiments with ferrihydrite suspensions. Min. Mag. 62A, pp. 1707-1708.

Chapter 6

The fate of chromium during early diagenetic processes

6.1 INTRODUCTION

Chromium is widely recognised as a toxic contaminant. Although necessary in trace amounts for animal and plant metabolism, it can result in nausea, skin ulcerations, lung cancer and gastro-intestinal and liver diseases when accumulated in excess (Ajmal et al. 1984; Nieboer and Jusys, 1988).

Only the trivalent (Cr(III)) and hexavalent (Cr(VI)) forms of chromium are stable in the natural environment (Calder, 1988). Under low Eh (reducing) conditions, the main aqueous Cr(III) species are Cr^{3+}, $Cr(OH)_2^{+}$, $Cr(OH)^{2+}$, $Cr(OH)_3^{0}$, and $Cr(OH)_4^{-}$ (Fig. 1.9; Rai et al., 1986, 1987). The Cr^{3+} species is prevalent only below pH 3.6, and polymeric Cr(III) species such as $Cr_2(OH)_2^{4+}$, $Cr_3(OH)_4^{5+}$, and $Cr_4(OH)_6^{6+}$ are never significant in natural systems (Rai et al., 1986, 1987). Under oxidising conditions, the dominant chromium species are the Cr(VI) oxyanions $HCrO_4^{-}$ and CrO_4^{2-} (Fig. 1.9; Calder, 1988).

Almost all reported incidents of chromium groundwater contamination have an industrial origin. Major sources of chromium to the environment are the metal plating industries, wood treatment and tannery facilities, chromium mining and milling operations (Calder, 1988) and chemical manufacturing (Richard and Bourg, 1991). Many of these activities produce Cr(VI), which is highly toxic and mobile. Most naturally occurring chromium is, however, in the less toxic and highly immobile Cr(III) form. This explains why natural occurrences of chromium at potentially harmful concentrations are rare (Robertson, 1975).

Wherever Cr(III) is found in nature, it is often in close association with Al(III) and Fe(III) because substitution of one for another can occur in a variety of mineral and organic structures (Bartlett and James, 1988). For instance, Cr(III) can substitute for small amounts of octahedral aluminium in clay minerals (Bartlett and James, 1988), and amorphous [Fe(III), Cr(III)] hydroxide is thought to be the main chromium solubility-controlling phase in natural environments (Rai et al., 1986; Sass and Rai, 1987; Richard and Bourg, 1991). Since it is clear that amorphous Fe(III) hydroxide (ferrihydrite) can exert a strong control on the mobility of Cr(III), it is important to know the fate of sorbed chromium as contaminated ferrihydrite ages. Consequently, one aim of this study was to investigate changes in the coordination environment and aqueous concentration of chromium in a series of Cr(III)-

contaminated ferrihydrite samples. These differed from each other in the amount of Cr(III) that was sorbed before ageing started.

Because chromium exists in two oxidation states that exhibit markedly different toxicities, solubilities and mobilities (Richard and Bourg, 1991), it is also important to understand reactions that can lead to changes in oxidation state. A number of field and laboratory-based studies have shown that fine grained ferrous iron-bearing minerals such as magnetite are very effective reductants of aqueous Cr(VI) (Anderson et al., 1994; Peterson et al., 1996, 1997; White and Peterson, 1996). Green rust is a mixed Fe(II)-Fe(III) oxyhydroxide mineral that is thought to be an intermediate phase in both the formation and the reductive dissolution of ferric oxyhydroxides such as goethite, lepidocrocite and magnetite (Hansen et al., 1994; Schwertmann and Fechter, 1994). It occurs under a range of reducing and weakly alkaline to weakly acidic conditions such as those found in reductomorphic soils (Trolard et al., 1997) and the uppermost layers of lacustrine and marine sediments (Buurman, 1980; Newman, 1987). Whilst relatively little work has been done to investigate the reaction of green rust with trace groundwater components, it is known to be capable of reducing Se(VI) to Se(0) (Myneni et al., 1997) and nitrate to ammonium (Hansen et al., 1994, 1996). In light of this, the second aim of this study was to determine the effect of green rust on aqueous chromium oxidation state.

6.2 EXPERIMENTAL METHODS

6.2.1 General

All reagents used in this study were analytical grade and labware was acid-washed. A glass Willhelm-type reference electrode (Sentek Ltd.) was used in combination with a glass pH electrode and an Orion model 720A meter to make pH measurements. Calibration ± 0.05 pH units was achieved at room temperature with constantly stirred Whatman NBS grade buffers. The Cr(III) and Cr(VI) stock solutions were prepared from $Cr(NO_3)_3 \cdot 9H_2O$ and K_2CrO_4, respectively. All Cr(III) stock solutions were used within 24 hours to minimise polymerisation. The risk of this occurring was further reduced in the stock solution used to prepare the Cr(III) on lepidocrocite EXAFS reference standards by acidifying it with 1% v/v HNO_3. All stock solutions were stored at 4 °C in closed amber-coloured HDPE bottles.

6.2.2 Preparation of Cr(III)-ferrihydrite coprecipitate ageing samples

Three samples of ferrihydrite were nucleated in the presence of different levels of aqueous Cr(III) and aged to goethite according to a method adapted from that of Schwertmann et al. (1989). Initially, 60 ml of a 0.5M Cr(III) stock solution was mixed with 36 ml of 5M KOH. Immediately after thorough mixing, 11, 24 and 30 ml aliquots of this solution were placed in 2 L HDPE screw-top containers, to which 90 ml of a 1M ferric nitrate solution was then added with stirring. Finally, the volume of each sample was made to 1800 ml by the addition of MilliQ water. This method resulted in three suspensions with Cr/(Cr+Fe) ratios of 0.052, 0.111 and 0.140 that are hereafter referred to as 'Low Cr-HFO', 'Med. Cr-HFO' and 'High Cr-HFO', respectively. Following collection of a 100 ml sample from each suspension, they were all placed in a 65±3°C oven for 2686 hours.

Ferrihydrite is known to age into goethite (α-FeOOH) and/or hematite (α-Fe_2O_3) under laboratory conditions, and the relative proportion of each in the final product is strongly dependent on pH: Hematite is dominant between pH 5.5 and pH 9, whereas goethite is dominant under higher and lower pH conditions (Schwertmann and Murad, 1983). In this experiment, I chose to age ferrihydrite at high pH (12.9) to favour goethite as the sole product for two reasons. Firstly, goethite is the most commonly occurring iron oxyhydroxide under temperate conditions (Schwertmann and Cornell, 1991) and secondly, EXAFS data are easiest to interpret when the number of components in a system is minimised.

The samples were aged at 65±3°C to accelerate a process that would normally take weeks to months. Despite this, the results are applicable to low temperature systems because previous studies have shown that the mechanisms of ferrihydrite ageing to goethite and hematite are not temperature dependent between 25°C and 70°C (Fischer and Schwertmann, 1975; Cornell and Schwertmann, 1979; Schwertmann and Murad, 1983).

As time passed, progressive changes in the colour of the suspensions from deep brown to an increasingly yellow ochre colour indicated that mineralogical transformations were occurring. The rate of reaction was clearly highest in the Low Cr-HFO sample and lowest in the High Cr-HFO sample, although the pH of all samples was identical - it deviated little from 12.9 during the course of the reaction. Samples were periodically collected from the suspensions following thorough mixing. Centrifugation (3000 rpm for 10 - 20 mins) was used to separate the samples into viscous pastes (the 'adsorption samples', which were frozen prior to analysis) and supernates. The latter were filtered through 0.2 μm cellulose nitrate filter membranes and then acidified by dilution with 1% v/v HNO_3. All supernates were stored at 4°C and analysed by ICP-AES within one week of collection. Iron was also periodically

analysed for (by ICP-AES) to check for any iron oxyhydroxide dissolution during the ageing process. The bulk chemistry of each Cr-HFO ageing sample was determined by ICP-AES following dissolution of small aliquots of each suspension in warm 50% HCl. This information was used to confirm the expected Cr/(Cr+Fe) ratios. It should be noted that the highly alkaline nature of the supernates necessitated thorough rinsing of the ICP-AES with MilliQ water between samples in order to eradicate memory effects of previous samples.

6.2.3 Preparation of green rust with adsorbed Cr(VI)

The method of Schwertmann and Fechter (1994) was followed to prepare sulphate green rust ($GR2(SO_4^{2-})$) with the expected approximate bulk formula $Fe^{(II)}_2Fe^{(III)}(OH)_5(SO_4)$. Light was excluded from all samples during preparation and analysis to prevent unwanted photoredox reactions. Sample preparation took place in a 500 ml straight-sided polythene beaker. This contained a magnetic follower and was capped by an airtight PVC lid with holes for pH electrodes, gas inlet/outlet ports and sample ports (Fig. 6.1).

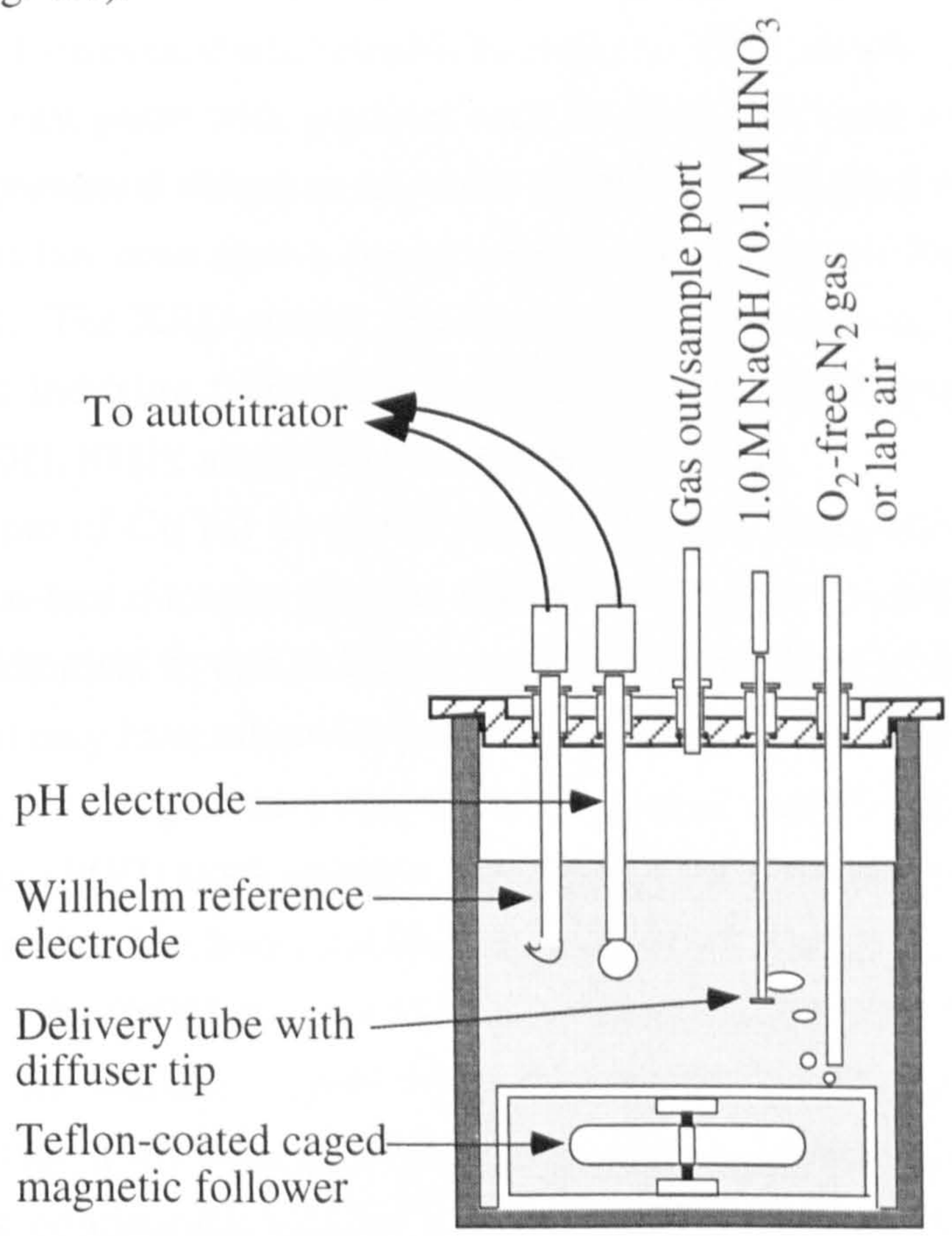

Fig. 6.1. Reaction vessel used to prepare Cr(VI) on green rust sample and associated Cr(III)/Cr(VI) on lepidocrocite EXAFS reference standards. The total volume of the reaction vessel was 500 ml, and it was wrapped in aluminium foil at all times to exclude light which may have otherwise caused unwanted photoredox reactions. The 1.0 M NaOH and 0.1 M HNO_3 were supplied by a Metrohm 718 pH-stating titrator.

Initially, 370 ml of MilliQ water was added to the beaker and purged with oxygen-free N_2(g) for 24 hours to remove dissolved oxygen prior to the addition of 20.57 g of $FeSO_4 \cdot 7H_2O$. The resulting light green solution was continually purged with N_2(g) whilst the pH was raised from an initial value of ~3.4 to pH 7.0 over a 15 minute period by the addition of CO_2/N_2-free 1.0 M NaOH from a Metrohm 718 pH-stat titrator. Once pH 7.0 was reached, the N_2(g) flow was replaced with laboratory air supplied by a small pump *via* an open ended 4 mm ID glass tube. The light green solution started to darken in colour and become more turgid as soon as air flow began. Because the oxidation/hydrolysis reaction liberates protons, the 718 titrator was required to constantly add 1.0 M NaOH throughout the reaction to maintain pH at 7.0 ± 0.1. The rate of base addition was high for the first ~100 minutes of reaction (~0.6 ml/min), but subsequently decreased to a much lower and constant value of ~0.03 ml/min. The solid product was collected by centrifugation after 2 hours of reaction and the resulting viscous paste was stored at 1-4 °C in air-free screw-top centrifuge tubes for a maximum of 2 days prior to use. It was not possible to dry the green rust and store it as a powder because this mineral undergoes rapid oxidation when in contact with air. However, it was possible to make an XRD sample by rapidly mixing a viscous green rust paste with glycerol and smearing this onto a glass disc. The glycerol matrix prevented the green rust from oxidising during analysis (Hansen et al., 1994) and its use has been shown not to introduce any artefacts into the XRD data (section 5.3.3.2). The XRD results showed the sample to consist of pure sulphate green rust (peak indexing from Vins et al., 1987) with clear development of the characteristic (001), (002), and (003) planes (see Fig. 6.8 a).

The sample of Cr(VI) on green rust (92-S) was prepared in the following manner: Oxygen-free nitrogen gas was used to purge 400 ml of MilliQ water in a reaction vessel identical to that in Fig. 6.1. This was wrapped in aluminium foil to exclude light that may have otherwise induced unwanted photoredox reactions. After 12 hours of purging, 2.6 g of the viscous green rust paste was added, followed by 1.2 ml of a 5617 ppm Cr(VI) stock solution. The stirred dark-green suspension began to turn a darker green-black colour soon after the addition of chromium. Prior to this and immediately after the Cr(VI) stock solution had been added, a 100 ml subsample was collected from the reaction vessel and subsequently oxidised by purging with laboratory air over a 12 hour period (97-S). The remaining Cr(VI)-green rust suspension was continually purged with N_2(g) over the course of the 12 hour equilibration period, and the Metrohm 718 pH stat titrator was used to maintain pH 5.9 ± 0.05. This pH was chosen to favour the adsorption of both Cr(III) (Charlet and Manceau, 1992) and Cr(VI) (Van Geen et al., 1994).

The reacted suspensions were collected in brim-full centrifuge tubes, and centrifugation (3000 rpm for 20 min) was used to separate the adsorption samples from their supernates. These were filtered through 0.2 μm cellulose nitrate filter membranes and then acidified by dilution with 1% v/v HNO_3. The acidified supernates were stored at 4°C and analysed by ICP-AES within one week of collection. The adsorption samples were frozen immediately after collection and stored under a nitrogen atmosphere to prevent oxidation prior to EXAFS analysis.

6.2.4 Preparation of EXAFS reference standards

Lepidocrocite was prepared by the oxidation/hydrolysis of a ferrous chloride solution at pH 6.7 - 6.9 (Schwertmann and Cornell, 1991). The bright orange precipitate was collected by centrifugation, cleaned by dialysis against MilliQ water and stored as a refrigerated 20 g L^{-1} stock suspension prior to use. X-ray powder diffraction of a randomly oriented powder sample was used to confirm the identity and purity of the crystalline product. Additionally, its surface area (88 ± 3 m^2g^{-1}) was determined by BET surface area analysis following 12 hours of outgassing with $N_2(g)$.

Cr(III) and Cr(VI) were adsorbed to the laboratory-precipitated lepidocrocite as outlined below. The resulting samples were used as EXAFS reference standards during analysis of data from the 'unknown' samples.

6.2.4.1 Cr(III) on lepidocrocite

Two samples of Cr(III) sorbed on lepidocrocite were prepared with different chromium contents. In both cases, 30 ml of the lepidocrocite stock suspension was added to 370 ml of MilliQ with a 0.1 M $NaClO_4$ background electrolyte in a reaction vessel identical to that shown in Fig. 6.1. A 1135 ppm Cr(III) stock solution was then added in 418 μL aliquots at 45 min intervals until a total of 1208 μL was added to one sample (81-S) and 2926 μL to the other (80-S). A Metrohm 718 pH stat titrator with 0.1 M NaOH was used to maintain pH 6.00 ± 0.05 throughout addition of the stock solution and for a three hour equilibration period after the last aliquot of stock solution was added. Previous work has shown three hours to be sufficient for the establishment of equilibrium during Cr(III) adsorption on ferrihydrite (Amirhaeri et al., 1984).

The stepwise addition of chromium was employed to maintain aqueous chromium concentrations below 25 μM, assuming that the majority of chromium in each aliquot was adsorbed within 45 min. The 25 μM concentration limit was chosen because a solution at pH 6 containing this amount of chromium is only slightly

saturated with respect to chromium hydroxide (Fendorf et al., 1994). Consequently, polymerisation will have been minimal (Fendorf et al., 1994), and chromium would have been present in solution mainly as free ions whilst adsorption was occurring.

Centrifugation (3000 rpm for 20 min) was used to separate the adsorption samples from their supernates. These were filtered through 0.2 µm cellulose nitrate filter membranes and then acidified by dilution with 1% v/v HNO_3. The acidified supernates were stored at 4°C and analysed by ICP-AES within one week of collection. The adsorption samples were refrigerated prior to EXAFS analysis. Percentage surface loading values, which describe the proportion of available surface sites occupied by sorbed Cr(III), were calculated using a maximum surface site density for Cr(III) on goethite of 1.3 sites nm^{-2} (Charlet and Manceau, 1992).

6.2.4.2 Cr(VI) on lepidocrocite

Two samples of Cr(VI) sorbed on lepidocrocite were prepared with different chromium contents. In both cases, exactly 25 ml of the lepidocrocite stock suspension was added to 425 ml of MilliQ with a 0.1 M $NaClO_4$ background electrolyte in a reaction vessel identical to that shown in Fig. 6.1. Precisely 392 µL of a 5617 ppm Cr(VI) stock solution was then added to one sample (83-S) and 1880 µL to the other (84-S). Both samples were equilibrated at pH 5.9 ± 0.05 under ambient temperature and atmospheric conditions for 12 hours with the use of a Metrohm 718 pH stat titrator containing 0.1 M HNO_3. A previous study suggests that equilibration is complete within 10 hours (Mesuere and Fish, 1992).

Centrifugation and sample treatment and analysis were conducted in the same manner as for the Cr(III) on lepidocrocite samples. Percentage surface loading values, which describe the proportion of available surface sites occupied by sorbed Cr(VI), were calculated using a maximum surface site density for Cr(VI) on goethite of 1.44 sites nm^{-2} (derived from Mesuere and Fish, 1992).

It should be noted that a maximum of 1.5 ml of HNO_3 was added to the Cr(VI) on lepidocrocite samples to achieve the desired pH, and that this addition resulted in minimal changes in total sample volume. It was, however, necessary to add a maximum of 30 ml of NaOH to the Cr(III) on lepidocrocite samples to maintain the target pH. This was mainly because the Cr(III) stock solution used to prepare these samples was mildly acidic.

6.2.5 EXAFS theory, data collection and analysis

6.2.5.1 General description of EXAFS spectroscopy

An EXAFS spectral scan is obtained by measuring X-ray absorption over a range of photon energies which includes the 'absorption edge' of the element of interest (e.g. Brown et al., 1988, 1995; Charlet and Manceau, 1993). Curve fitting allows the determination of the *average* number (N_j) (± 20 %) of atoms in the jth atomic shell, their distance (R_j) (± 0.02 Å) from the central excited cadmium atom, their identity, and the associated Debye-Waller factor ($2\sigma_j^2$) (e.g. Brown et al., 1988). The latter parameter represents the mean square of variation in distances from the element of interest to the shell under consideration. It accounts for damping of the EXAFS oscillations due to thermal vibration (σ_T) and static disorder (σ_S) within atomic shells (e.g. Brown et al., 1995). The quality of the fit between the experimental and simulated EXAFS functions is represented by the *R* factor:

$$R_{EXAFS} = \sum_i \frac{1}{\sigma}(|\chi_i(k)^{exp} - \chi_i(k)^{theory}|) \times 100\%$$

where σ is the standard deviation of the difference between experimental ($\chi^{experiment}$) and theoretical (χ^{theory}) EXAFS functions over a specified k range. For poorly ordered mineral-aqueous systems such as those described here, an *R* value between 20% and 40% indicates an acceptable match between theory and experiment (Dent and Mosselmans, 1992).

6.2.5.2 Data collection

EXAFS data were collected at the CLRC Synchrotron Radiation Source at Daresbury Laboratory, U.K. EXAFS spectra were collected at the chromium K-edge (5.9892 keV) [Fe K-edge = 7.1120 keV] under room temperature conditions on station 8.1. This station uses a water cooled, harmonic rejecting double crystal Si(111) monochromator and a 13 element Ge diode detector. During all data collection, the monochromator was detuned to reject higher harmonics from the EXAFS spectra.

The storage ring energy was 2.0 GeV and the beam current varied between 130 and 240 mA during the collection of all data. Each adsorption sample was presented to the X-ray beam as a viscous paste held by Sellotape in a 2 mm thick Teflon slide with a 4 x 15 mm sample slot. EXAFS data were collected from all adsorption samples during three to six fluorescence mode scans. It would have been preferable to analyse the air sensitive Cr(VI) on green rust sample at 77 K. Although this was not possible, the similarity of successive spectra collected from this sample suggest that

analysing it at room temperature did not induce artificial changes in chromium oxidation state or sorbent surface chemistry.

6.2.5.3 Data analysis

EXAFS data reduction was performed using Daresbury Laboratory software (EXCALIB and EXBACK) (Binsted et al., 1991). EXCALIB was used to calibrate from monochromator position (millidegrees) to energy (eV) and to average multiple spectra from individual samples. EXBACK was used to define the start of the EXAFS oscillations and perform background subtraction.

The exact curved wave theory EXAFS analysis program EXCURV98 (Gurman et al., 1984, 1986; Joyner et al., 1987; Gurman, 1988; Binsted et al., 1991, 1992) was then used to analyse the EXAFS data. This process involved the comparison of experimental data with theoretical EXAFS oscillations that were derived by EXCURV98 from model clusters. The geometry of these clusters was based on the predicted geometry of the adsorption complexes. For each sample, the cluster that provided the closest initial fit underwent least squares refinement of: Debye-Waller factor, number of atoms per shell, Cr-X distance and Fermi energy to improve the fit between its theoretical oscillations and the experimental data. This caused the composition and geometry of the model cluster to approach the true structure and chemistry of the adsorption complex. Whilst the values of some parameters were held constant in the early stages of fitting, it was normal for all parameters to be unconstrained during the final stages of data analysis.

The model clusters initially consisted of only one atomic shell. Successive shells were added to the theoretical model until each significant peak in the Fourier transform of the EXAFS data was accounted for. Statistical tests (Joyner et al., 1987) were performed to ascertain the significance of each new atomic shell, and only those which improved the fit between theory and experiment at the 99% level of confidence were retained. Refining theoretical models to find agreement with experimental data in this way provided shell parameters that describe the average local coordination environment around sorbed chromium. However, it should be noted that EXAFS cannot discriminate between chromium and iron as backscatterers because of their similar mass and electronic structure.

The phase-shift functions used in the curve fitting were derived by *ab initio* methods in EXCURV98 using Hedin-Lundqvist potentials (Hedin and Lundqvist, 1969) and von Bart ground states. The fact that the EXAFS parameters reported here compare very well with published data from similar systems (e.g. Charlet and Manceau, 1992) confirms the accuracy of the theoretical phase-shift values that were used in this study.

6.3 RESULTS AND DISCUSSION

6.3.1 Ageing of Cr(III)-contaminated ferrihydrite

6.3.1.1 X-ray diffraction results from aged Cr(III)-ferrihydrite samples

The XRD results show that the sole ageing product of Cr(III)-contaminated ferrihydrite with Cr/(Cr+Fe) between 0.052 and 0.140 is goethite, irrespective of initial chromium loading (Fig. 6.2 b-d). There is no evidence to suggest the formation of chromium hydroxide phases, although this is perhaps not surprising since $Cr(OH)_3$(s) and γ-CrOOH are both X-ray amorphous (Christensen, 1976; Rai et al., 1987). Even a crystalline phase such as bracewellite (α-CrOOH; JCPDS card 25-1497) would be very hard to resolve by XRD because it would constitute such a small fraction of each sample.

Schwertmann et al. (1989) suggest that there is an upper limit of 12% for chromium substitution in goethite. Whilst High Cr-HFO (Fig. 6.2 d) exceeds this limit (14% substitution; Cr/(Cr+Fe) = 0.140), it should be noted that this sample has not transformed completely to goethite. The broad humps between 30-40 and 55-65 degrees 2θ that are evident at the start of the ageing process in Fig. 6.2 (d) are characteristic of two-line ferrihydrite (Schwertmann and Cornell, 1991), which was the starting material. Although goethite peaks do initially develop quite quickly in High Cr-HFO, they never grow to be as intense as those in Low Cr-HFO and Med. Cr-HFO. Additionally, the broad humps from the ferrihydrite precursor are still evident, and the background noise remains high (a sign of low crystallinity) relative to that in the other Cr-HFO samples, even after 2686 hours of ageing. Both of these lines of evidence suggest that a fraction of the ferrihydrite remained untransformed. This may be because sorbed chromium stabilised it against dissolution, which is an integral step in the transformation to goethite (Schwertmann and Murad, 1983). This is a likely explanation because sorbed chromium is known to stabilise goethite against dissolution (Schwertmann et al., 1989). Furthermore, the relative peak intensities in Fig. 6.2 (d) are noticeably different to those in Fig. 6.2 (a) and Figs. 6.2 (b) and (c). This suggests that high levels of sorbed Cr(III) influence the extent to which the various crystal planes in the goethite structure grow as it ages from ferrihydrite.

Low Cr-HFO and Med. Cr-HFO appear to have transformed completely into goethite. The low background noise and sharp diffraction peaks are an indication of the high level of crystallinity of the ageing product in both samples. It is evident that the majority of transformation was complete after 24 hours in Low Cr-HFO (Fig. 6.2 b) but not until after 144.5 hours in Med. Cr-HFO (Fig. 6.2 c). This finding supports the hypothesis that increasing levels of Cr(III) result in increased stabilisation of the

ferrihydrite precursor against dissolution. Despite the fact that ageing in Low Cr-HFO (Cr/Cr+Fe) = 0.052) and Med. Cr-HFO (Cr/(Cr+Fe) = 0.111) took place at slightly different rates, diffraction patterns from the final ageing products are identical.

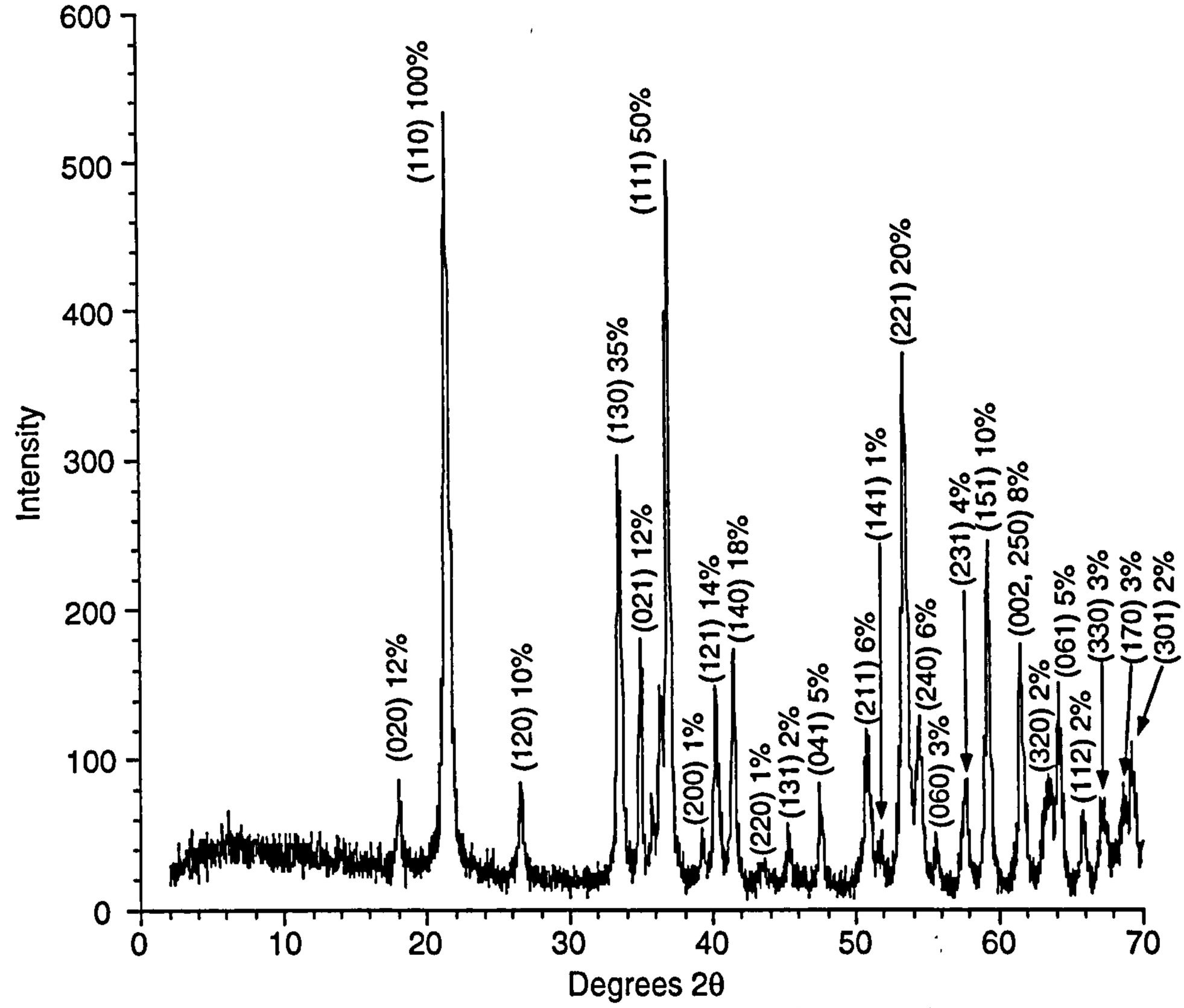

Fig. 6.2 a. Goethite XRD reference standard. Numbers in parentheses are published relative peak intensity values.

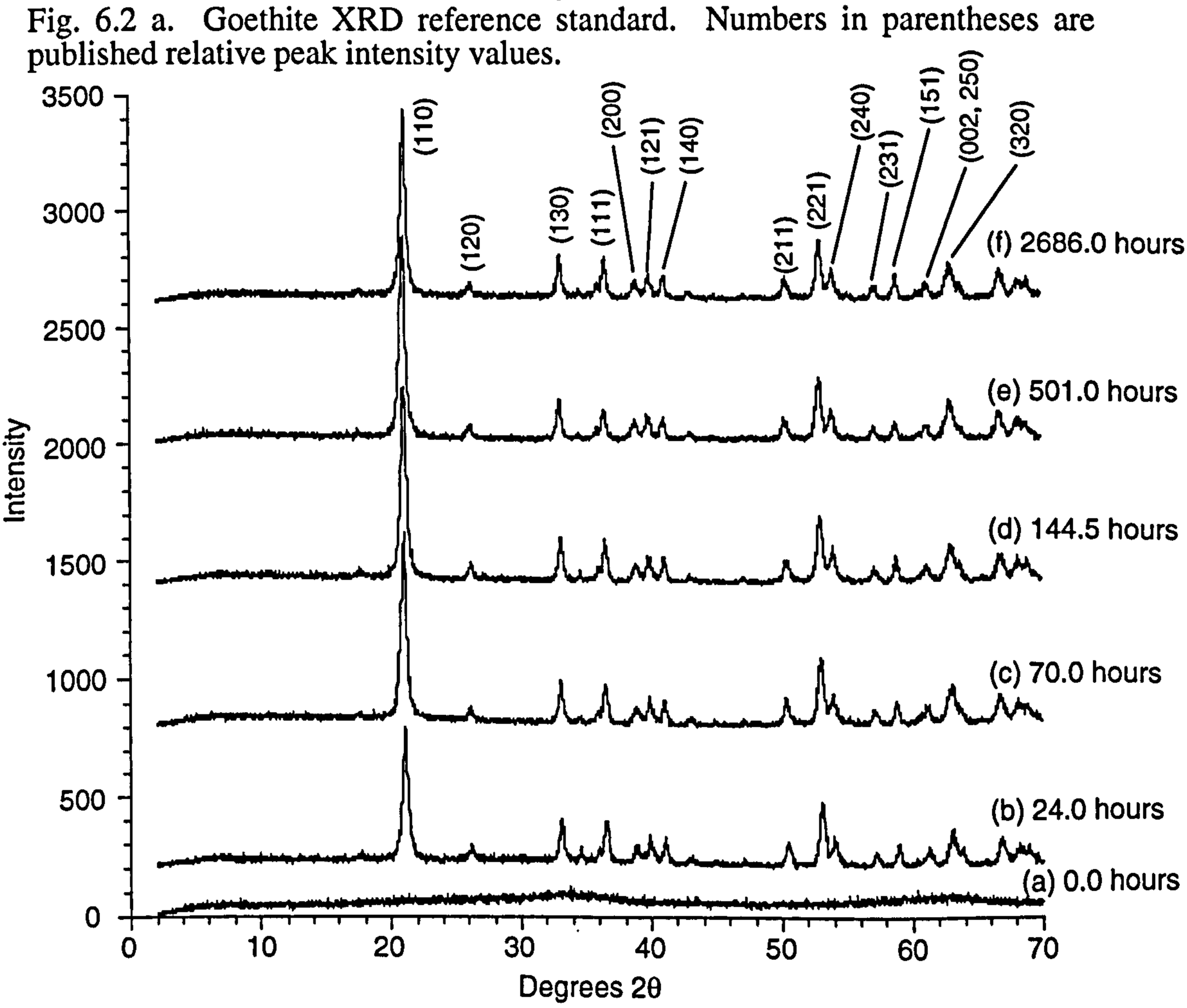

Fig. 6.2 b. XRD powder patterns from samples of Low Cr-HFO (Cr/(Cr+Fe) = 0.052) at various stages in the ageing process.

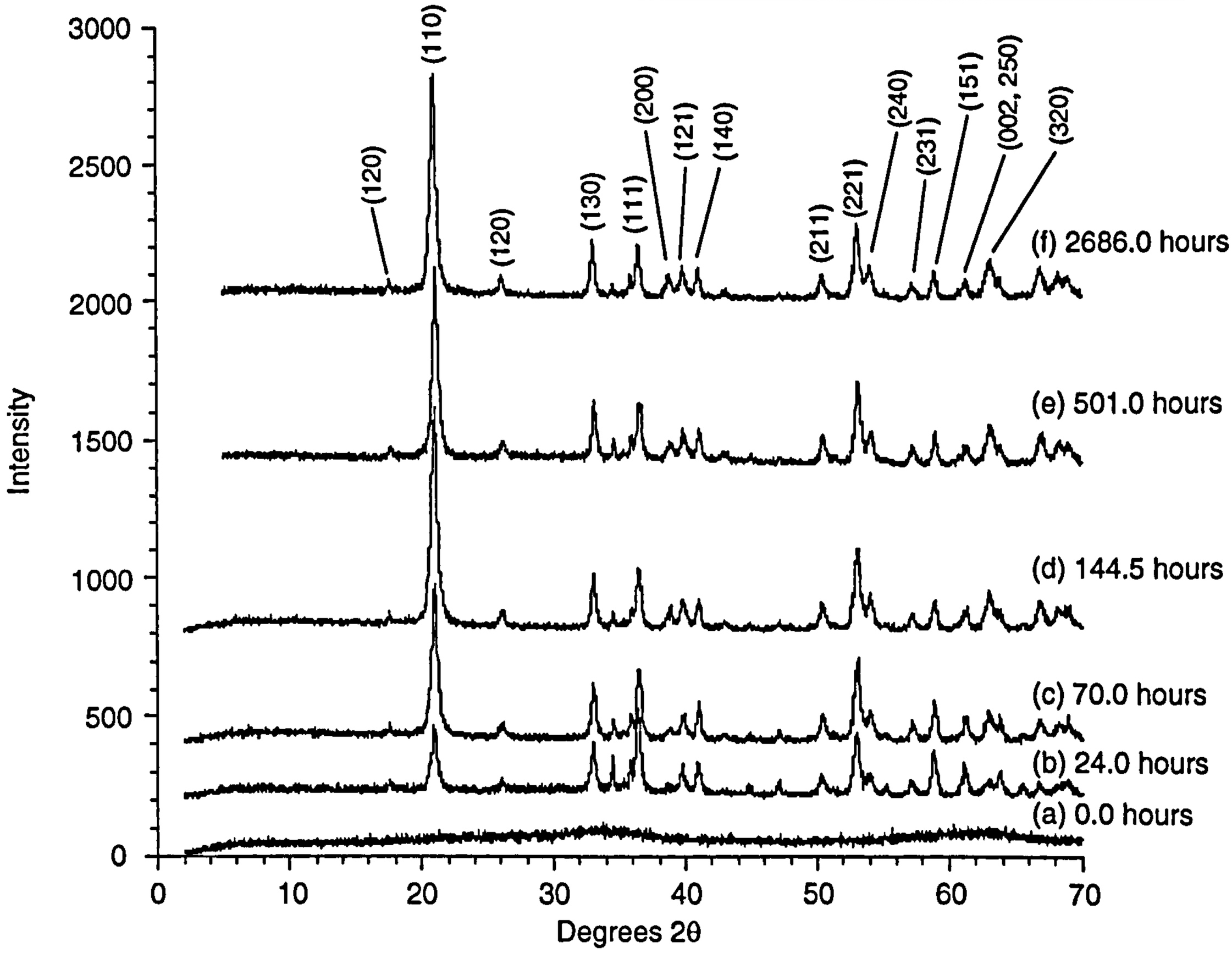

Fig. 6.2 c. XRD powder patterns from samples of Med. Cr-HFO (Cr/(Cr+Fe) = 0.111) at various stages in the ageing process.

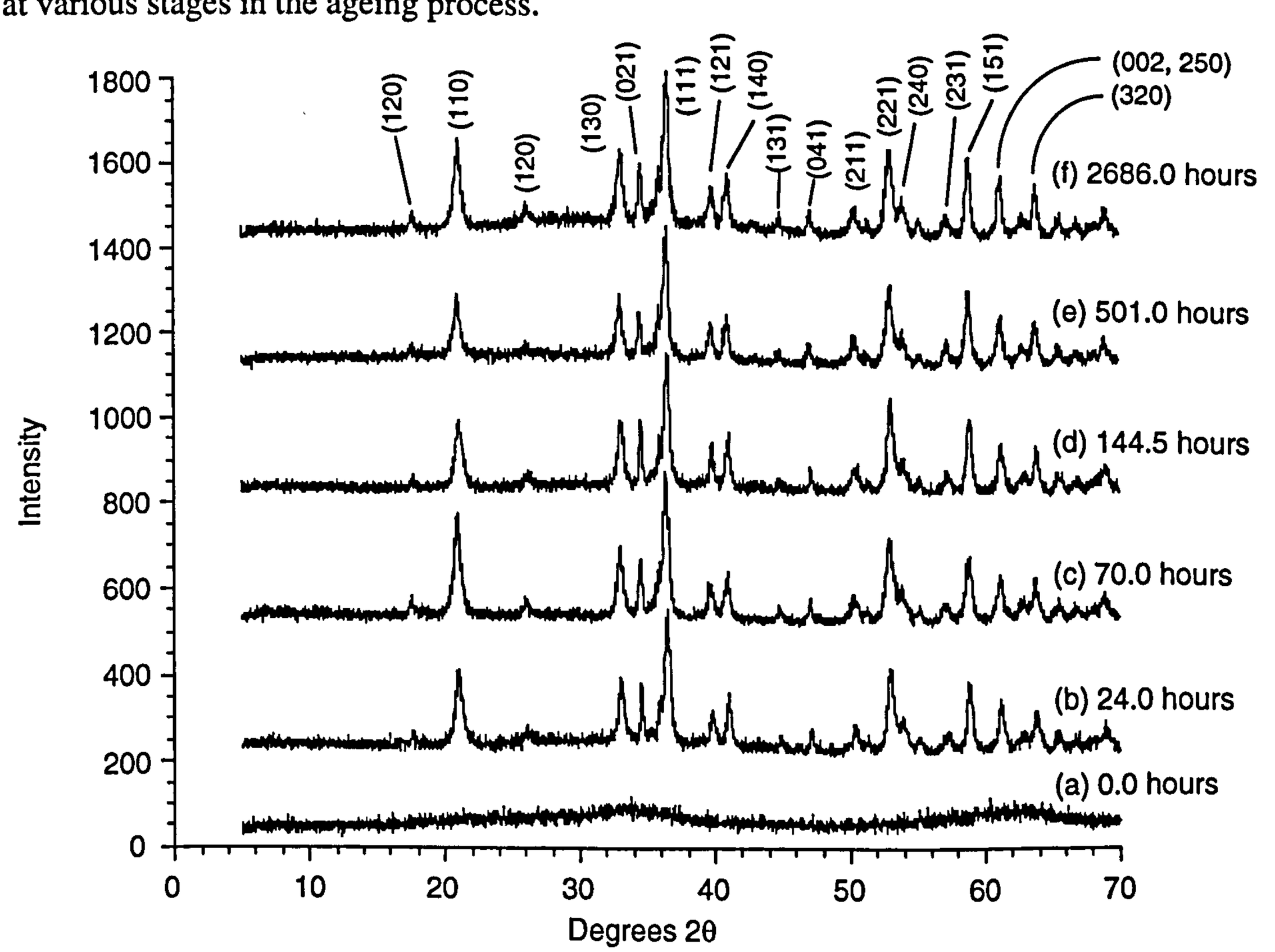

Fig. 6.2 d. XRD powder patterns from samples of High Cr-HFO (Cr/(Cr+Fe) = 0.140) at various stages in the ageing process.

Finally, it should be noted that the XRD data presented here is not of sufficiently high resolution to establish whether or not increasing chromium content resulted in a change in goethite unit cell dimensions.

6.3.1.2 Chemical observations from aged Cr(III)-ferrihydrite samples

Changes in the concentration of dissolved chromium as a function of ageing time for Low, Med. and High Cr-HFO are shown in Fig. 6.3. It is clear that chromium is released to solution from all Cr-HFO samples as ageing proceeds, and that the rate of release is greatest near the start of reaction. Whilst the release rate gradually decreases with time in all cases, only in Low Cr-HFO does it appear that equilibrium between dissolved and solid phase chromium is close to being reached. In both other samples, chromium was still being released to solution at a significant rate when the reaction was stopped, and the amount of chromium released to solution always followed the same order: Low Cr-HFO < Med. Cr-HFO < High Cr-HFO. However, it is clear from Fig. 6.4 that the expelled chromium constitutes just 0.4 - 0.6% of the initial chromium loading. It is also clear from this plot that the differences in dissolved chromium concentration correlate very closely with differences in initial chromium loading throughout most of the ageing reaction.

The sorption capacity of ferrihydrite is very high because it has a high surface area (commonly 200-300 $m^2\ g^{-1}$; Schwertmann and Cornell, 1991) and low crystallinity. Consequently, it is not surprising that fresh ferrihydrite was capable of sorbing all available Cr(III) from solution (Fig. 6.3). However, surface area (and hence the number of reactive surface sites) decreases whilst crystallinity increases during ageing (Fuller et al., 1993), and goethite consequently has a much lower sorption capacity than ferrihydrite. The release of some chromium to solution during ageing should therefore be expected, and is best explained simply as a consequence of changes in surface area and crystallinity. Indeed, Schwertmann et al. (1989) observe that goethite formed by the ageing of Cr(III)-ferrihydrite never sorbs all available Cr(III) from solution.

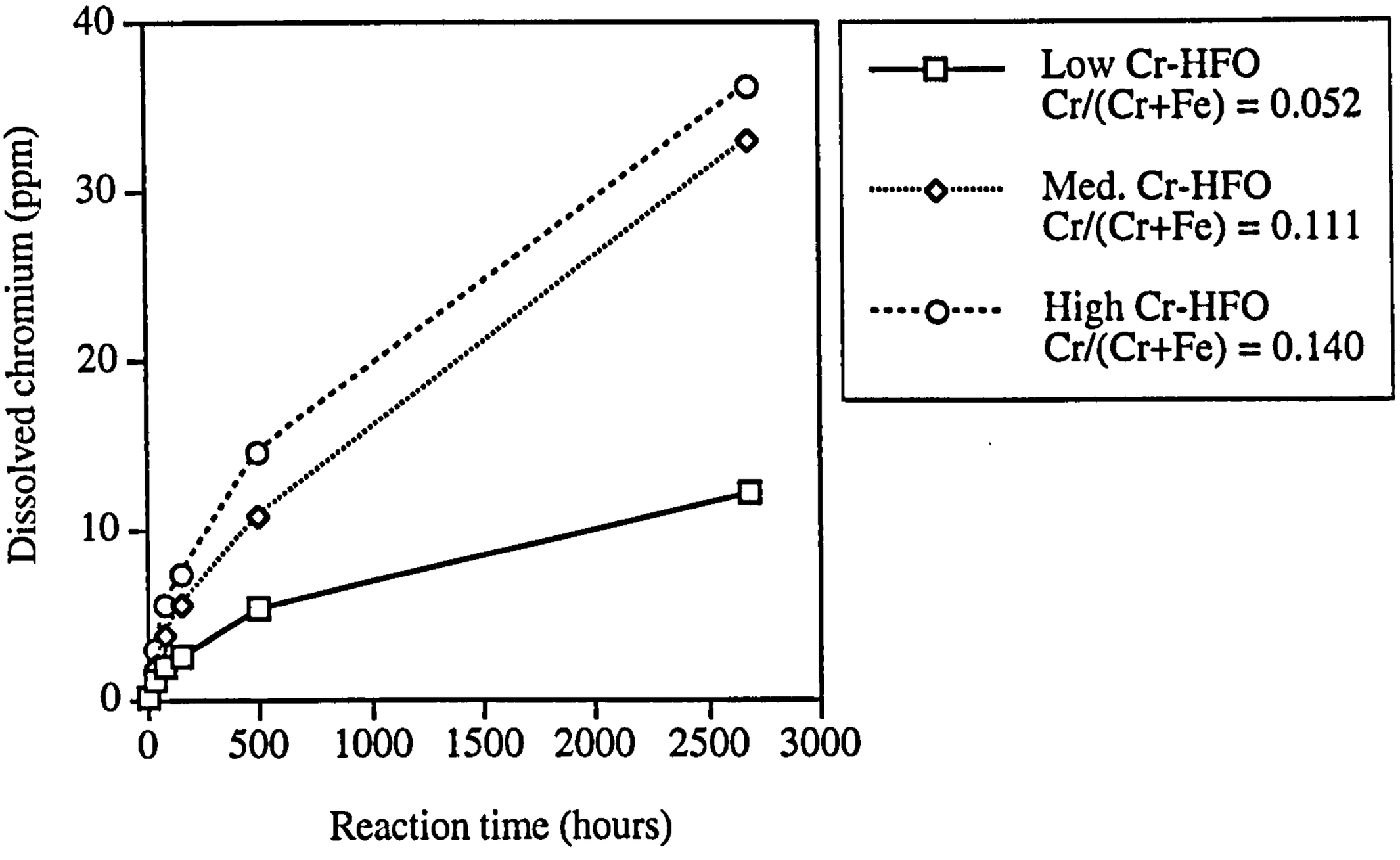

Fig. 6.3. The release of chromium to solution during the ageing of ferrihydrite samples with differing loadings of contaminant Cr(III).

It is interesting to note that chromium was still being released from Low Cr-HFO and Med. Cr-HFO, albeit at a decreasing rate, after the ageing process was complete according to the XRD data. Indeed, the rate of chromium release from Med. Cr-HFO relative to that from the other two samples appeared to increase after 2686.0 hours of ageing (last data points in Figs. 6.3 and 6.4). The first of these observations may be explained by the continued transformation of residual Cr(III)-contaminated ferrihydrite that is not detected by XRD because (a) it constitutes a small fraction of the bulk sample and (b) the high intensity of the goethite diffraction peaks swamps out the low intensity of the broad diffraction humps that are characteristic of ferrihydrite. The second observation is harder to explain. However, it may in fact be due to decreases in the rate of chromium release from Low Cr-HFO and High Cr-HFO rather than an increase in the rate of release from Med. Cr-HFO. This is possible because the approach to equilibrium of Low Cr-HFO and the retardation of the ageing reaction in High Cr-HFO (section 6.3.1.1) could have caused the rate of chromium release to decline in both cases. Since neither of these conditions applied to Med. Cr-HFO, the rate of chromium release from this sample would have declined more slowly, thereby *appearing* to increase relative to the two other samples.

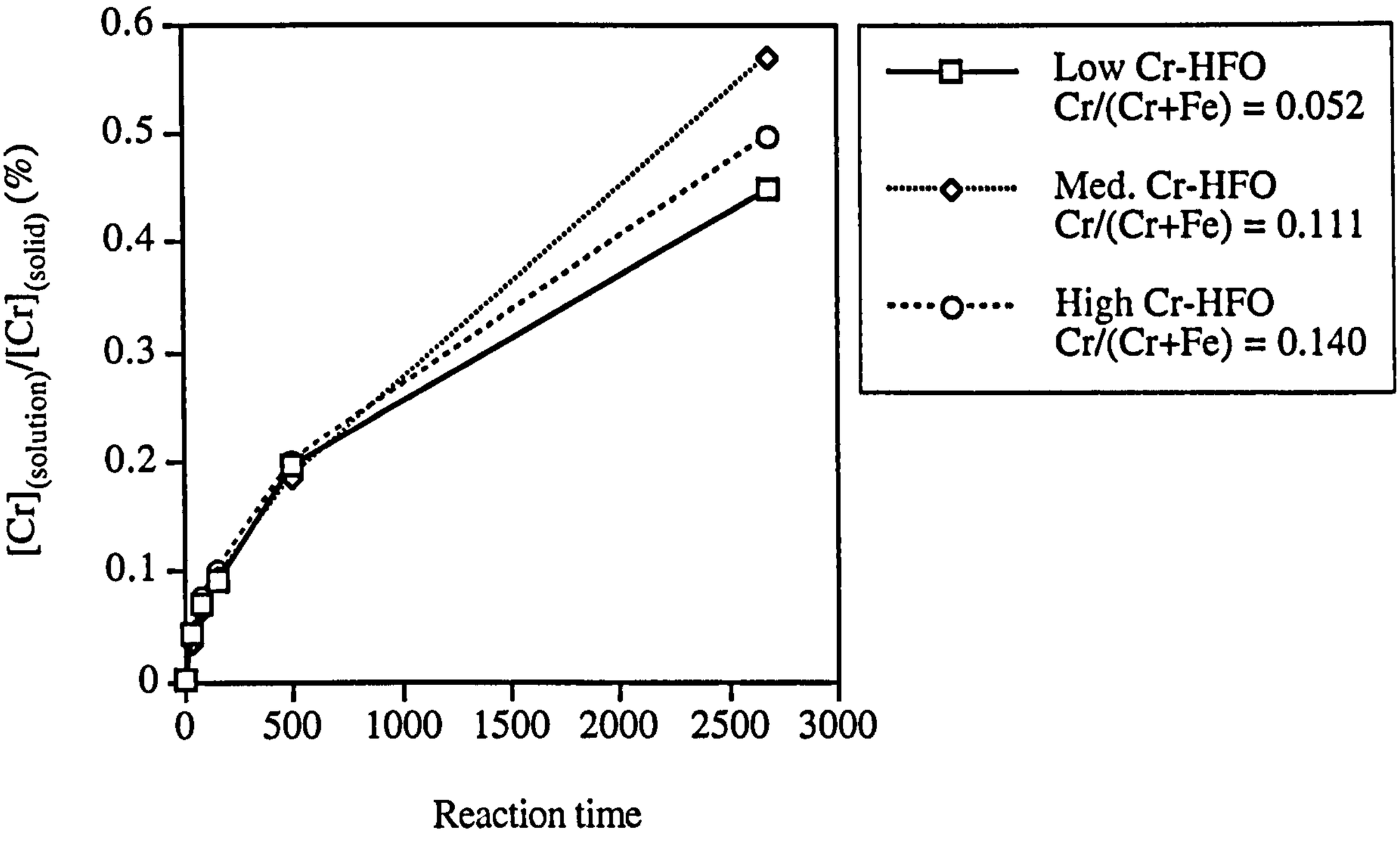

Fig. 6.4. Chromium release to solution during the ageing of Cr(III)-contaminated ferrihydrite as a function of initial Cr(III) loading.

One final important observation is that there was no release of iron to solution during ageing. This is proof that chromium was not released to solution simply by dissolution of the host FeOOH phase.

6.3.1.3 EXAFS results from aged Cr(III)-ferrihydrite samples

The EXAFS results from Cr-HFO samples at various stages in the ageing process are shown in Fig. 6.5 (a)-(c) and summarised in Table 6.1.

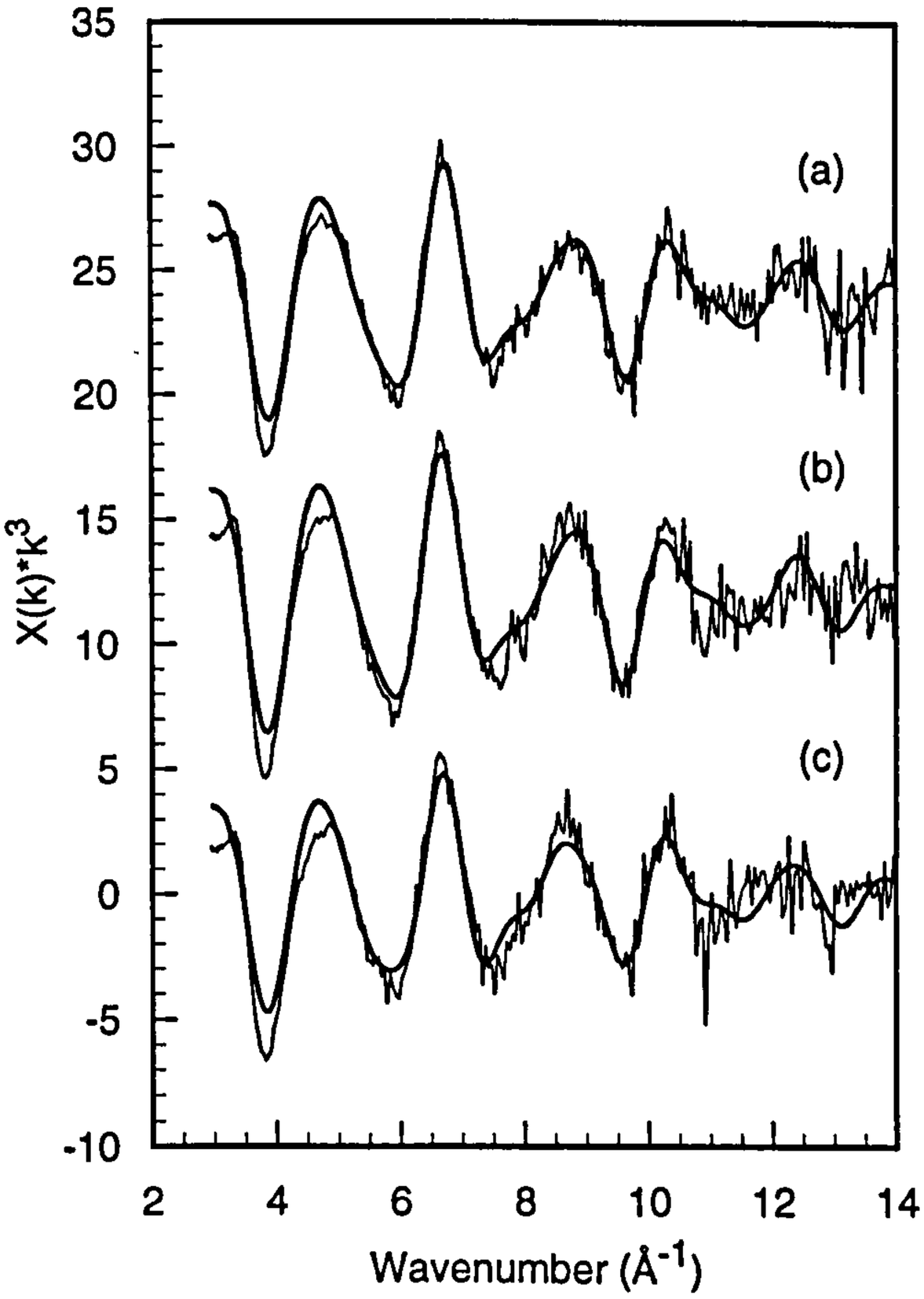

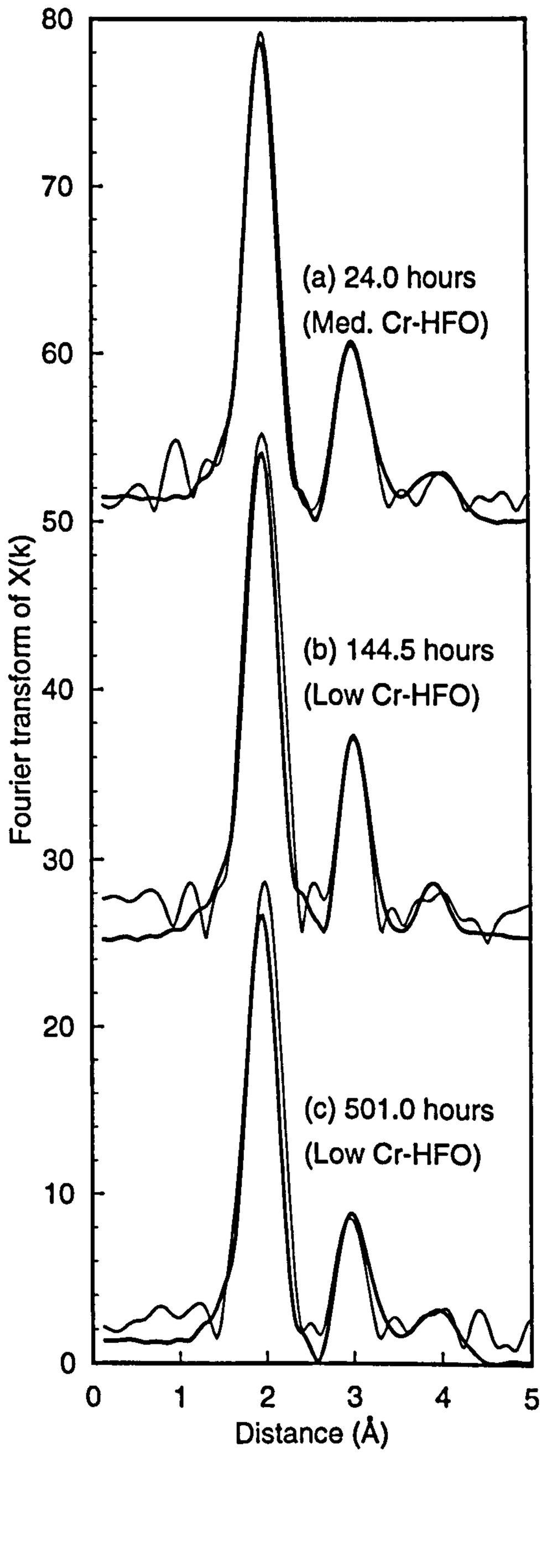

Fig. 6.5. EXAFS (left) and FT (right) plots from samples of chromium-contaminated ferrihydrite (Cr-HFO) that were aged at 65±3°C. All samples are dominated by a shell of oxygen atoms in octahedral coordination at a Cr-O distance of 1.98-1.99 Å. (Cr,Fe) shell contributions at 3.00 Å and 3.95 Å suggest that chromium sorbed predominantly as a Cr(III) hydroxide precipitate with a gamma-CrOOH-type structure. There also appear to be 3.45 Å (Cr,Fe) contributions (suggesting that some chromium existed in a goethite-like environment), but a Cr,Fe shell at this distance could not be resolved in the EXAFS data.

Table 6.1. EXAFS results from Low Cr-HFO and Medium Cr-HFO coprecipitate samples. CN_X is the number of atoms in a shell at distance R_X (Å) from the central cadmium atom. $2\sigma^2_X$ is the associated Debye-Waller factor (Å^2). The *R* factor gives a measure of the agreement between experimental and theoretical EXAFS curves. $R < 20\%$ indicates a very good fit whereas $R \leq 40\%$ is acceptable. Note that EXAFS cannot distinguish between chromium and iron as backscattering atoms; Me denotes both types of atom in this table.

Sample	Reaction time (hr)	$R_{Cr\text{-}O}$	CN_O $2\sigma^2_O$	$R_{Cr\text{-}Me1}$	CN_{Me1} $2\sigma^2_{Me1}$	$R_{Cr\text{-}Me2}$	CN_{Me2} $2\sigma^2_{Me2}$	*R* factor
Med. Cr-HFO	24.0	1.98	4.5	3.00	2.0	3.94	1.4	34.0
21/03/98			*0.009*		*0.012*		*0.015*	
Low Cr-HFO	144.5	1.98	5.1	3.01	2.0	3.95	2.0	39.2
26/03/98			*0.009*		*0.012*		*0.015*	
Low Cr-HFO	501.0	1.99	4.3	3.00	1.6	3.91	1.5	42.6
10/04/98			*0.009*		*0.012*		*0.015*	

The spectra of all samples are dominated by a shell of 4.3-5.1 oxygen atoms at a Cr-O distance of 1.98-1.99 Å. This Cr-O distance is characteristic of Cr(III) in octahedral coordination (Charlet and Manceau, 1992; Fendorf et al., 1994), and is distinctly different to the oxygen coordination environment around Cr(VI) (4.0 oxygen atoms at Cr-O = 1.69 Å; section 6.3.2.2). Because EXAFS-derived coordination numbers are only ever equal to or less than the true values ($CN_{EXAFS} \leq CN_{real}$; Charlet and Manceau, 1992), the observed oxygen coordination numbers taken together with the Cr-O distance suggest that the samples contained only Cr(III) and no Cr(VI). Further evidence for this assertion is that the raw EXAFS data (not shown) contain no trace of the sharp pre-edge feature that is characteristic of Cr(VI) (e.g. Fendorf et al., 1997).

Aside from the oxygen shell, the Fourier transform (FT) plots are dominated by shells containing 1.6-2.0 Cr,Fe atoms at Cr-(Cr,Fe) = 3.00-3.01 Å and 1.4-2.0 Cr,Fe atoms at Cr-(Cr,Fe) = 3.91-3.95 Å (remember that EXAFS cannot discriminate between chromium and iron as backscatterers). These Cr-(Cr,Fe) distances and coordination numbers are in good agreement with EXAFS results obtained from both a hydrous Cr(III) gel ($Cr(OH)_3 \cdot nH_2O$) (Manceau and Charlet, 1992) and Cr(III) sorbed at high surface coverage on ferrihydrite (Charlet and Manceau, 1992). The 3.00-3.01 Å and 3.91-3.95 Å Cr-(Cr,Fe) contributions are respectively assigned to single edge- and single corner sharing mechanisms of polyhedral attachment, suggesting that $Cr(OH)_3 \cdot nH_2O$ possesses a γ-CrOOH-like structure (Manceau and

Charlet, 1992; Fig. 6.6). Thus, it is apparent that the majority of Cr(III) sorbed to the Cr-HFO samples as $Cr(OH)_3 \cdot nH_2O$ with a γ-CrOOH-like local structure.

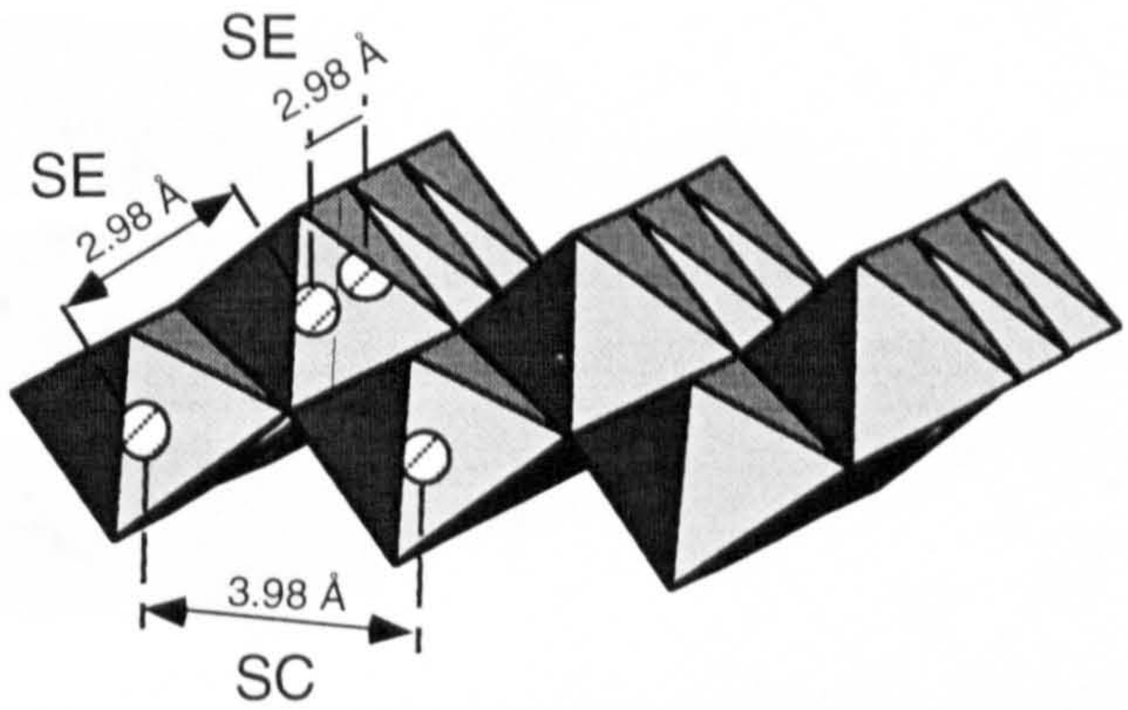

Fig. 6.6. The structure of γ-CrOOH. Each octahedron represents a $Cr(O,OH)_6$ unit, and the hatched white spheres represent chromium atoms. SE and SC denote single edge- and single corner sharing mechanisms of polyhedral attachment, respectively. Diagram constructed in CrystalMaker 2.1.0 (Palmer, 1996) using crystallographic data for γ-FeOOH, lepidocrocite.

Goethite (α-FeOOH) has characteristic Fe-Fe interactions at 3.01 Å (single edge-), 3.28 Å (double edge-) and 3.46 Å (double corner sharing), and the local structure of ferrihydrite is very similar to this (Manceau and Combes, 1988; Combes et al., 1989; Shinoda et al., 1994). Note that the structures of goethite and ferrihydrite are distinctly different to that of γ-CrOOH, which has Cr-Cr interactions at 2.98 Å and 3.98 Å (Manceau and Charlet, 1992).

A 3.45 Å Cr-(Cr,Fe) contribution is visible in the FT plots (Fig. 6.5), raising the possibility that some Cr(III) sorbed to ferrihydrite or goethite by isomorphic substitution for Fe(III). However, the 3.45 Å contribution is too weak to be resolved in the EXAFS fits. This makes it clear that after as little as 24 hours of ageing, the majority of Cr(III) sorbed was to ferrihydrite and the α-FeOOH ageing product as a discrete $Cr(OH)_3 \cdot nH_2O$ precipitate with a γ-CrOOH structure. It is not possible to state whether this is located exclusively at the mineral-water interface or whether some of it is also occluded in the α-FeOOH structure.

My finding that the majority of Cr(III) sorbed in the form of a discrete $Cr(OH)_3 \cdot nH_2O$ precipitate appears to be at odds with the results of Schwertmann et al. (1989). Based on changes in unit cell dimensions, these workers suggested that Cr(III) was incorporated into goethite by structural substitution of Cr(III) for Fe(III). In resolving this apparently contradictory evidence, it is important to realise that α-CrOOH belongs to space group $R\bar{3}m$ (Douglass, 1957; Hamilton and Ibers, 1963; Christensen, 1976) and is *not* isostructural with goethite (space group *P*nma). It actually has a structure much more like that of gibbsite, in which each $Cr(O,OH)_6$

octahedron shares six edges with neighbouring octahedra. This results in a single Cr-Cr distance of 2.98 Å (Fig. 6.7).

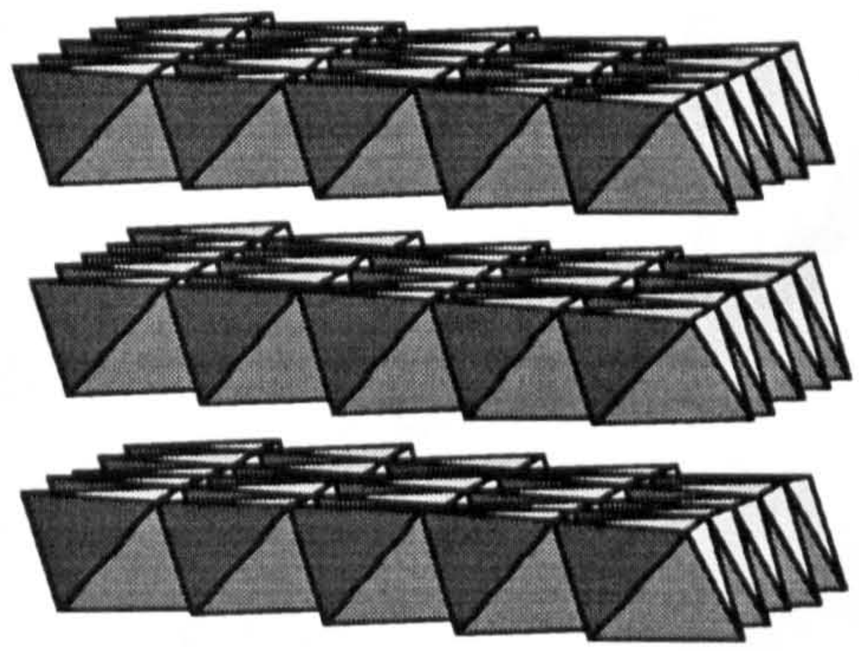

Fig. 6.7. The structure of α-CrOOH is similar to that of gibbsite ($Al(OH)_3$). It consists of $Cr(O,OH)_6$ octahedra that share edges with each other to form sheets which are linked by hydrogen bonding. There is only one Cr-Cr interaction, at a distance of 2.98 Å. Diagram constructed in CrystalMaker 2.1.0 (Palmer, 1996).

Consequently, Cr(III) should not be expected to form a solid solution with Fe(III) in crystalline α-FeOOH. Whilst Sass and Rai (1987) do provide compelling evidence for extensive solid solution between Cr(III) and Fe(III) in amorphous iron oxyhydroxide (ferrihydrite), this may only be made possible by the poor long range crystallinity of ferrihydrite relative to goethite. Indeed, further evidence for the lack of a Cr(III)-Fe(III) solid solution in goethite is provided by comparing the results of Sass and Rai (1987) with those of Schwertmann et al. (1989). Whilst the former find up to 89 mol% Cr(III) for Fe(III) substitution in ferrihydrite, the latter find that Cr/(Cr+Fe) reaches a maximum of 12% in goethite.

The results presented here can be reconciled with those of Schwertmann et al. (1989) if it is assumed that a small amount of sorbed Cr(III) does in fact substitute for Fe(III) in the goethite structure, with the remainder forming a discrete γ-CrOOH-like $Cr(OH)_3 \cdot nH_2O$ precipitate. This would explain why changes in the α-FeOOH unit cell dimensions might occur despite very weak EXAFS evidence for Cr(III) with a goethite-like local structure. It should be noted that any γ-CrOOH or α-CrOOH that did form in the samples examined by Schwertmann et al. (1989) would not have been detected because it would have constituted ≤ 12 mol% of the sample. Furthermore, γ-CrOOH is X-ray amorphous (e.g. Christensen, 1976).

6.3.2 Interaction of Cr(VI) with green rust

6.3.2.1. General observations for Cr(VI) interaction with green rust

The XRD powder pattern from pure green rust is shown in Fig. 6.8 (a). The sole product of the interaction of this material with aqueous Cr(VI) is magnetite (sample 92-S, Fig. 6.8 b).

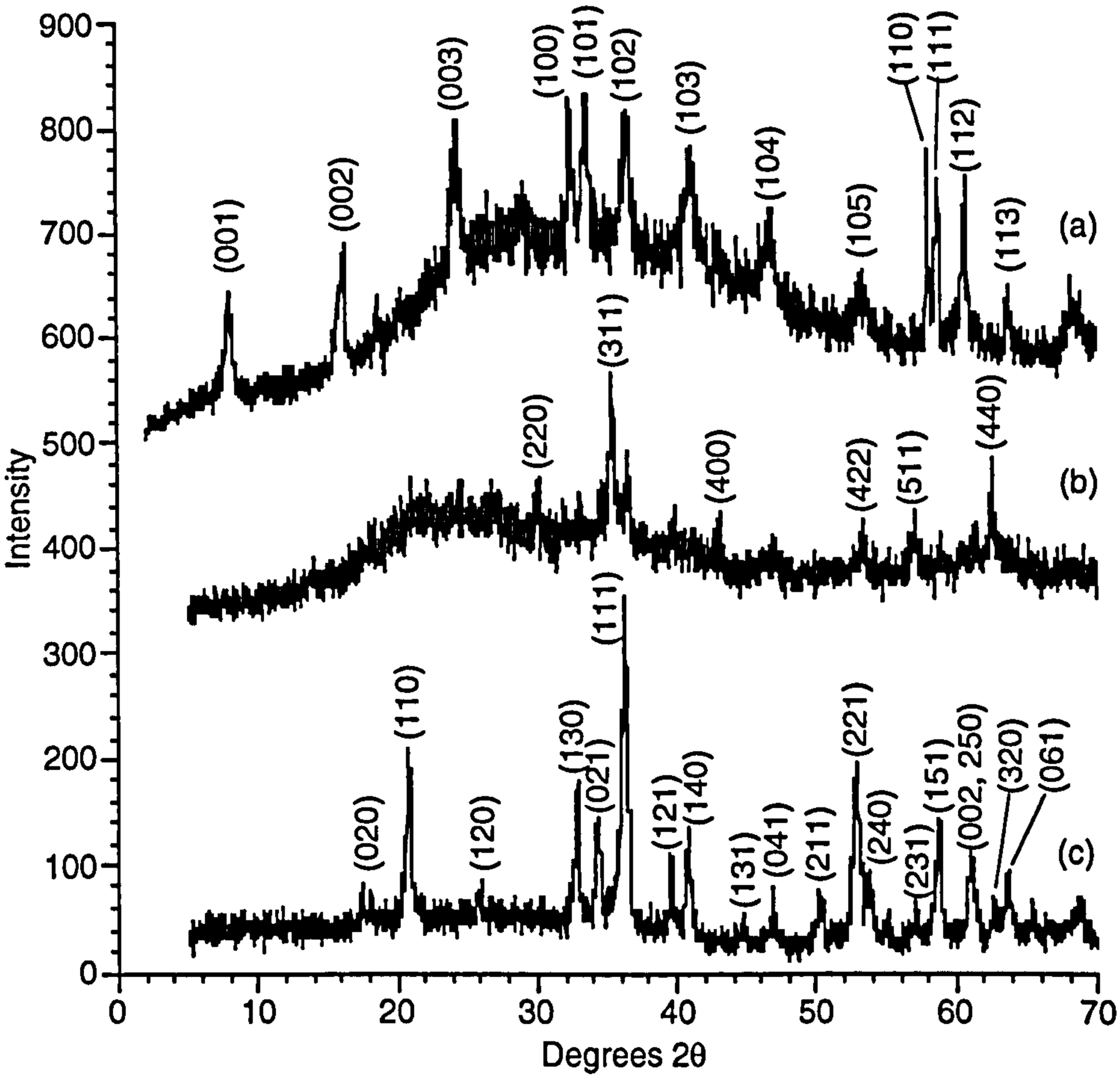

Fig. 6.8. (a) XRD powder pattern from green rust prior to Cr(VI) addition. Addition of aqueous Cr(VI) resulted in the rapid transformation of green rust to magnetite under anoxic conditions (sample 92-S; b). Air oxidation of a portion of the green rust suspension immediately after Cr(VI) addition resulted in the formation of goethite (sample 97-S; c).

As previously noted in section 6.2.3, the dark-green green rust suspension began to turn a darker green-black colour consistent with the formation of magnetite very soon after the addition of Cr(VI). This observation suggests that the oxidation of green rust to magnetite occurs very rapidly. It has previously been shown that Se(VI) can oxidise green rust to magnetite and/or lepidocrocite (Myneni et al., 1997) whilst nitrite oxidises it to goethite (Hansen et al., 1994). Indeed, it is thought that the oxidation of green rust can lead to the formation of goethite, lepidocrocite, maghemite or magnetite depending on oxidation rate and the extent of green rust dehydration (Hansen et al., 1994).

When the Cr(VI)-green rust suspension was reacted under oxic conditions, the sole mineralogical product was goethite (sample 97-S, Fig. 6.8 c). It is interesting to note that the (110) line is poorly developed in 97-S relative to that in pure goethite (Fig. 6.2 a) and that the powder pattern in Fig. 6.8 (c) is very similar to that from High Cr-HFO (Fig. 6.2 d). This may be due to Cr(III) interfering with crystal growth in both 97-S and High Cr-HFO.

6.3.2.2 EXAFS results for Cr(VI) interaction with green rust

The EXAFS results from samples of Cr(VI) sorbed on green rust under anoxic and oxic conditions and the associated EXAFS reference standards (Cr(III) and Cr(VI) on lepidocrocite) are shown in Fig. 6.9 and summarised in Table 6.2.

Table 6.2. EXAFS results from samples of Cr(VI) on green rust (GR) that were reacted under anoxic (92-S) and oxic (97-S) conditions, in addition to samples of Cr(III) and Cr(VI) sorbed on lepidocrocite (γ-FeOOH). CN_X is number of atoms in a shell at distance R_X (Å) from the central cadmium atom. $2\sigma^2_X$ (Å^2) is the associated Debye-Waller factor. The *R* factor gives a measure of the agreement between experimental and theoretical EXAFS curves. $R < 20\%$ indicates a very good fit whereas $R \leq 40\%$ is acceptable. Note that EXAFS cannot distinguish between chromium and iron as backscattering atoms; Me denotes both types of atom in this table.

Sample	% SL *wt% Cr*	$R_{Cr\text{-}O}$	CN_O $2\sigma^2_O$	$R_{Cr\text{-}Me1}$	CN_{Me1} $2\sigma^2_{Me1}$	$R_{Cr\text{-}Me2}$	$CN_{Cr\text{-}Me2}$ $2\sigma^2_{Me2}$	*R* factor
Cr(VI) on GR(SO_4^{2-}) (92S)	0.5†	1.98	5.6 *0.009*	3.01	1.3 *0.011*	3.91	1.7 *0.011*	35.3
Oxidised portion of 92-S (97S)	N/A	1.97	5.4 *0.008*	3.06	1.3 *0.012*	3.87	1.2 *0.013*	34.1
EXAFS reference standards								
Cr(III) on γ-FeOOH (83S)	30§ *0.28*	1.99	6.1 *0.012*	3.07	2.3 *0.015*	3.99	1.6 *0.015*	31.2
Cr(III) on γ-FeOOH (84S)	70§ *0.72*	1.98	6.1 *0.012*	3.04	1.7 *0.019*	3.97	2.4 *0.015*	37.0
Cr(VI) on γ-FeOOH (81S)	50¥ *0.50*	1.65	4.2 *0.003*	-	-	-	-	44.3

Notes:

SL stands for surface loading.

† Value ± ca. 20% due to uncertainty of exact mass of green rust in sample.

¥ Values derived from maximum adsorption site density of 1.3 sites nm^{-2} for Cr(III) on goethite (Charlet and Manceau, 1992).

§ Values calculated using maximum adsorption site density of 1.44 sites nm^{-2} for Cr(VI) on goethite (derived from Mesuere and Fish, 1992).

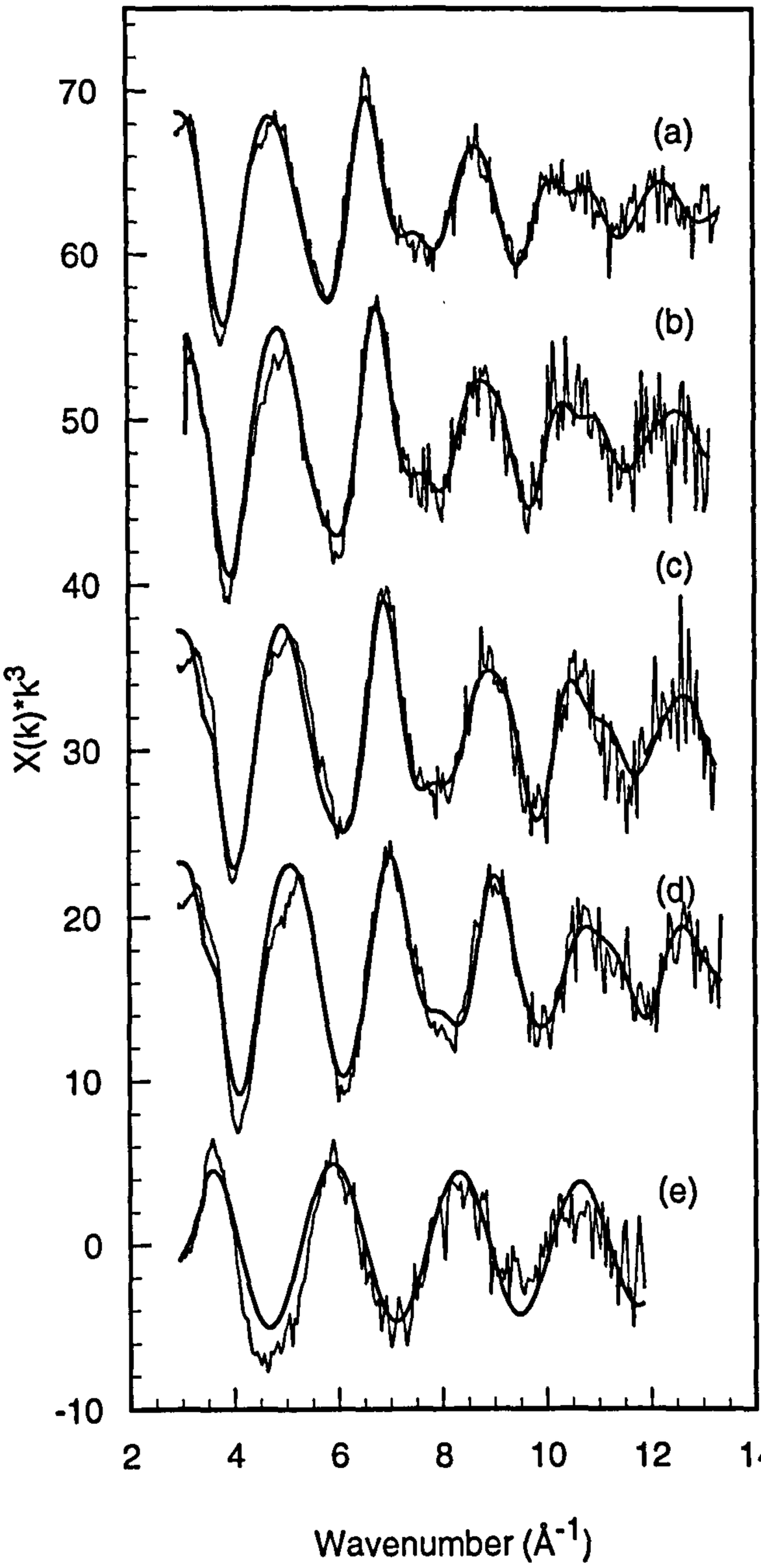

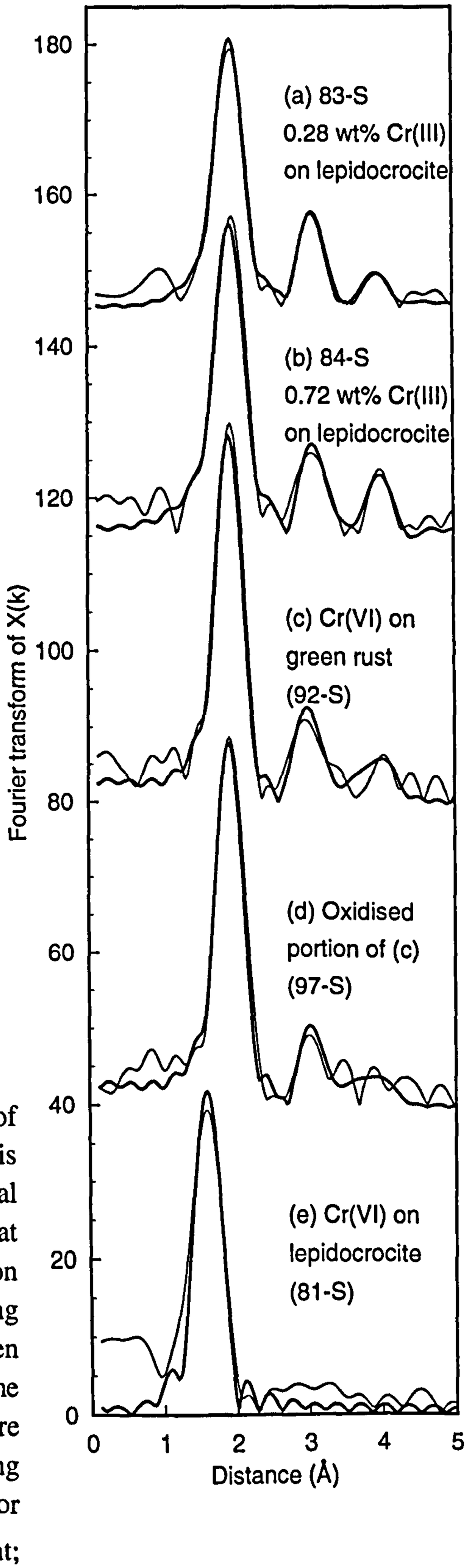

Fig. 6.9. The coordination environment of Cr(III) on lepidocrocite (gamma-FeOOH), is identical to that in gamma-CrOOH (octahedral shell of O atoms at 1.99 Å and Cr,Fe shells at 3.04 Å and 3.99 Å). The chromium coordination environment is very similar to this following sorption on green rust, making it clear that green rust reduces sorbed Cr(VI) (compare with the Cr(VI) coordination environment in (e)). There is a weak 3.45 Å contribution in (c), suggesting that some chromium is adsorbed or coprecipitated in an α-FeOOH-type environment; this feauture becomes stronger following reaction of 92-S under oxic conditions (97-S, d).

Spectra from all samples except Cr(VI) on lepidocrocite are dominated by a shell of 5.4-6.1 oxygen atoms at a Cr-O distance of 1.97-1.99 Å that immediately shows the sorbed chromium to be in the Cr(III) form. Conversely, Cr(VI) is surrounded by a shell of four oxygen atoms at a Cr-O distance of 1.65 Å, in good agreement with the findings of previous studies of Cr(VI) sorption on iron oxyhydroxides (e.g. Fendorf et al., 1997).

Aside from the oxygen shell, spectra from the Cr(III) on lepidocrocite EXAFS reference standards (Figs. 6.9 a and b) are dominated by Cr,Fe contributions at Cr-(Cr,Fe) distances of 3.04-3.07 Å and 3.97-3.99 Å. These distances, along with the associated coordination numbers (Table 6.2), are entirely consistent with Cr(III) sorption in the form of a $Cr(OH)_3 \cdot nH_2O$ precipitate with γ-CrOOH structure (Manceau and Charlet, 1992), despite the fact that an effort was made to minimise Cr(III) polymerisation prior to sorption (section 6.2.4.1). The theory that $Cr(OH)_3 \cdot nH_2O$ is isostructural with lepidocrocite (Manceau and Charlet, 1992) is supported by the fact that it develops so well on this mineral (Figs. 6.9 a and b). Note that there is no trace of the speculative 3.45 Å contribution noted for Cr(III) sorption on ferrihydrite and α-FeOOH (goethite) (section 6.3.1.3). Although the Cr-(Cr,Fe) distances do not change as Cr(III) surface loading increases from 30% to 70% (Fig. 6.9, Table 6.2), the 3.97-3.99 Å shell Cr,Fe coordination numbers increase whilst those for the 3.04-3.07 Å shell decrease. A similar phenomenon has previously been observed following increases in Cr(III) surface loading on ferrihydrite (Charlet and Manceau, 1992). These workers assigned the change to a decrease in the ratio of edge- to corner sharing linkages during development of the γ-CrOOH precipitate.

The spectra in Fig. 6.9 (c) unambiguously demonstrate that green rust reduced all available Cr(VI) to Cr(III). Furthermore, the strong similarity between the EXAFS results from this sample and those from the Cr(III) on lepidocrocite reference standards suggests that chromium was sorbed as a $Cr(OH)_3 \cdot nH_2O$ precipitate with γ-CrOOH-like structure following reduction. Note that the sorbent is magnetite (Fe_3O_4) rather than green rust since the latter was oxidised during Cr(VI) reduction (Fig. 6.8 b). A likely reaction scheme for the reduction of Cr(VI) by green rust is as follows:

$$HCrO_4^- + 3Fe^{(II)}_2Fe^{(III)}(OH)_5(SO_4) =$$
$$Cr(OH)_3 \cdot nH_2O + 3Fe_3O_4 + 3SO_4^{2-} + 5H^+ + 4\text{-}nH_2O$$

Previous work has shown that magnetite is also capable of reducing aqueous Cr(VI) (Peterson et al., 1996, 1997; White and Peterson, 1996). Whilst anoxic conditions are required for this reaction to proceed at an appreciable rate (White and Peterson, 1996), it is apparent that this constraint does not apply to Cr(VI) reduction by green rust (Fig. 6.9 d). Although this is an interesting result, the importance of

this reaction in nature will be minimal because green rust itself cannot persist for long outside reducing environments.

It is noteworthy that the Cr(VI) on green rust sample reacted under anoxic conditions has a weak ~3.45 Å contribution (see FT plot in Fig. 6.9 c), and that this becomes stronger following reaction under oxic conditions (Fig. 6.9 d). Although these contributions cannot be resolved in the EXAFS data, they do suggest that a small fraction of the Cr(III) may have sorbed by isomorphic substitution for Fe(III).

Finally, it is clear that re-oxidation of Cr(III) to Cr(VI) did not occur during reaction with green rust under oxic conditions (Fig. 6.9 d). Although oxygen has been shown to oxidise Cr(III) to Cr(VI) under laboratory conditions (Schroeder and Lee, 1975; Nakayama et al., 1981), the rate of oxidation at room temperature is very low. Consequently, Cr(III) is more likely to be involved in faster concurrent reactions such as sorption or precipitation, explaining why the oxidation of Cr(III) by dissolved oxygen has not been observed in field studies (e.g. Kent et al., 1994).

6.4 CONCLUSIONS

It has previously been suggested that aqueous Cr(III) concentrations will be controlled by equilibrium with amorphous [Fe(III),Cr(III)] hydroxide (Cr(III)-contaminated ferrihydrite) wherever this occurs in nature (Richard and Bourg, 1991). However, it is clear that after Cr(III)-contaminated ferrihydrite has been aged for as little as 24 hours at 65±3°C, the Cr(III) that was present during its nucleation is sorbed as a discrete $Cr(OH)_3 \cdot nH_2O$ precipitate with the γ-CrOOH structure. It remains in this form during further ageing to crystalline goethite (α-FeOOH). Evidence for Cr(III) with a goethite-like local structure is weak, perhaps because α-CrOOH is *not* isostructural with α-FeOOH. This suggests that the extensive Cr(III)-Fe(III) solid solution observed by previous workers in amorphous [Fe(III),Cr(III)] hydroxide (Sass and Rai, 1987) does not occur in goethite. This assertion is supported by the fact that Cr(III) for Fe(III) substitution can reach 89 mol% in [Fe(III),Cr(III)] hydroxide (Sass and Rai, 1987) but just 12 mol% in goethite (Schwertmann et al., 1989). Hence, my results suggest that $Cr(OH)_3 \cdot nH_2O$ will exert the dominant control on Cr(III) solubility following the ageing of Cr(III)-contaminated ferrihydrite. This is important because pure $Cr(OH)_3$ is much more soluble than any [Fe(III),Cr(III)] hydroxide solid solution (Sass and Rai, 1987). The phase transformation from ferrihydrite to goethite is retarded by increasing Cr(III) content, and is accompanied by the expulsion of a small fraction of sorbed Cr(III), even when initial loadings are relatively low (e.g. Cr/Cr+Fe) = 0.052).

Data presented here shows that green rust can rapidly reduce Cr(VI) to Cr(III) with the concomitant production of magnetite. A likely scheme for this reaction is as follows:

$$HCrO_4^- + 3Fe^{(II)}_2Fe^{(III)}(OH)_5(SO_4) =$$
$$Cr(OH)_3{\cdot}nH_2O + 3Fe_3O_4 + 3SO_4^{2-} + 5H^+ + 4\text{-}nH_2O$$

This observation is important because it shows that green rust, which is thought to occur quite widely under reducing and weakly acidic-alkaline conditions, can rapidly reduce chromium from its toxic and highly mobile Cr(VI) form and precipitate it as $Cr(OH)_3{\cdot}nH_2O$. This phase will then exert the major control on Cr(III) solubility.

The hypothesis that γ-CrOOH is isostructural with lepidocrocite (γ-FeOOH) (Manceau and Charlet, 1992) is supported by the fact that γ-CrOOH develops so well on γ-FeOOH.

The results presented here have two broad implications for the mobility of chromium in the environment. Firstly, whilst equilibrium with [Fe(III),Cr(III)] hydroxide can be expected to maintain low Cr(III) solubility in immature sediments and soils, Cr(III) will partition into a discrete chromium hydroxide phases as this material ages. Since $Cr(OH)_3$ is more soluble than any [Fe(III),Cr(III)] hydroxide, dissolved Cr(III) concentrations should be expected to increase over time.

Secondly, green rust is capable of reducing the mobile and toxic Cr(VI) species and precipitating it as $Cr(OH)_3{\cdot}nH_2O$. This reaction may be very important in limiting the mobility of Cr(VI) because (a) it occurs rapidly and (b) current opinion is that green rust is relatively ubiquitous.

6.5 REFERENCES

Ajmal M., Nomani A. A. and Ahmad A. (1984) Acute toxicity of chrome electroplating wastes to microorganisms: adsorption of chromate and chromium(VI) on a mixture of clay and sand. Water, Air, Soil Poll. 23, 119-127.

Amirhaeri S., Koons R., Martin M. and Patterson H. (1984) A chemi-luminescence technique for studying dynamic behavior of trace-element species in environmental systems. Water Res. 18, 87-90.

Anderson L. D., Kent D. B. and Davis J. A. (1994) Batch experiments characterizing the reduction of Cr(VI) using suboxic material from a mildly reducing sand and gravel aquifer. Environ. Sci. Technol. 28, 178-185.

Bartlett R. J. and James B. R. (1988) Mobility and bioavailability of chromium in soils. In *Chromium in the natural and human environments* (eds. J. O. Nriagu and E. Nieboer). John Wiley and Sons, N. Y.

Binsted N., Campbell J. W., Gurman S. J., and Stephenson P. C. (1991) SERC Daresbury Laboratory EXCURV92 program. Daresbury Laboratory, Warrington, U.K.

Binsted N., Strange R. W., and Hasnain S. S. (1992) Restrained refinement. Biochemistry 31, 12117-12125.

Brown G. E. Jr., Calas G., Waychunas G. A. and Petiau J. (1988) X-ray absorption spectroscopy and its applications in mineralogy and geochemistry. In *Spectroscopic Methods in Mineralogy and Geology* (ed. F. Hawthorne). Reviews in Mineralogy Vol. 18. Min. Soc. Am. pp. 431-512.

Brown G. E. Jr., Parks G. A. and O'Day P. A. (1995) Sorption at the mineral-water interface: macroscopic and microscopic perspectives. In *Mineral Surfaces* (eds. D. J. Vaughan and R. A. D. Pattrick). Chapman and Hall. pp. 129-183.

Buurman P. (1980) Paleosols in the Reading Beds (Paleocene) of Alum Bay, Isle of Wight, U.K. Sedimentology 27, 593-606.

Calder L. M. (1988) Chromium contamination of groundwater. In *Chromium in the natural and human environments* (eds. J. O. Nriagu and E. Nieboer). John Wiley and Sons, N. Y.

Charlet L. and Manceau A. A. (1992) X-ray absorption spectroscopic study of the sorption of Cr(III) at the oxide-water interface, II. Adsorption, coprecipitation and surface precipitation on hydrous ferric oxide. J. Coll. Interface Sci. 148, 443-458.

Charlet L and Manceau A. (1993) Structure, formation, and reactivity of hydrous oxide particles: Insights from X-ray absorption spectroscopy. In *Environmental Particles*, Vol. 2 (eds. J. Buffle and H. P. van Leeuwen). IUPAC Environmental Analytical and Physical Chemistry Series. pp. 118-164.

Christensen A. N. (1976) Hydrothermal preparation and magnetic properties of α-CrOOH, β-CrOOH, and γ-CrOOH. Acta Chem. Scand. A30, 133-136.

Combes J. M., Manceau A., Calas G. and Bottero J. Y. (1989) Formation of ferric oxides from aqueous solutions: A polyhedral approach by X-ray absorption spectroscopy: I. Hydrolysis and formation of ferric gels. Geochim. Cosmochim. Acta 53, 583-594.

Cornell R. M. and Scwertmann U. (1979) Influence of organic anions on the crystallization of ferrihydrite. Clays Clay Mineral. 27, 402-410.

Dent A. J. and Mosselmans J. F. W. (1992) *A guide to EXBACK, EXCALIB, and EXCURV92.* Daresbury Laboratory, Warrington, U.K.

Douglass R. M. (1957) The crystal structure of $HCrO_2$. Acta Cryst. 10, 423-427.

Eary L. E. and Rai D. (1988) Chromate removal from aqueous wastes by reduction with ferrous ion. Environ. Science Technol. 22, 972-977.

Fendorf S. E., Lamble G. M., Stapleton M. G., Kelley M. J. and Sparks D. L. (1994) Mechanism of chromium(III) sorption on silica. 1. Cr(III) surface structure derived by extended X-ray absorption fine structure spectroscopy. Environ. Sci. Technol. 28, 284-289.

Fendorf S., Eick M. J., Grossl P. and Sparks D. L. (1997) Arsenate and chromate retention mechanisms on goethite. 1. Surface structure. Environ. Sci. Technol. 31, 315-319.

Fischer W. R. and Schwertmann U. (1975) The formation of hemtatite from amorphous iron (III) hydroxide. Clays Clay Mineral. 23, 33-37.

Fuller C. C., Davis J. A. and Waychunas G. A. (1993) Surface chemistry of ferrihydrite. 2. kinetics of arsenate adsorption and coprecipitation. Geochim. Cosmochim. Acta 57, 2271-2282.

Gurman S. J. (1988) The small atom approximation theory. J. Phys. C: Solid State Phys. 21, 3699-3717.

Gurman S. J., Binsted N., and Ross I. (1984) Single scattering rapid curved wave theory. J. Phys. C: Solid State Phys. 17, 143-151.

Gurman S. J., Binsted N., and Ross I. (1986) Multiple scattering rapid curved wave theory. J. Phys. C: Solid State Phys. 19, 1845-1861.

Hamilton W. C. and Ibers J. A. (1963) Structures of $HCrO_2$ and $DCrO_2$. Acta Cryst. 16, 1209-1212.

Hansen H. C. B., Borggaard O. K. and Sorensen J. (1994) Evaluation of the free energy of formation of Fe(II)-Fe(III) hydroxide-sulfate (green rust) and its reduction of nitrite. Geochim. Cosmochim. Acta 58, 2599- 2608.

Hansen H. C. B., Koch C. B., Nanckekrogh H., Borggaard O. K. and Sorensen J. (1996) Abiotic nitrate reduction to ammonium - key role of green rust. Environ. Sci. Technol. 30, 2053-2056.

Hedin L. and Lundqvist S. (1969) Effects of electron-electron and electron-phonon interactions on the one-electron states of solids. Solid State Phys. 23, 1-181.

Joyner R. W., Martin K. J., and Meehan. P. (1987) Some applications of statistical tests in analysis of EXAFS and SEXAFS data. J. Phys. C: Solid State Phys. 20, 4005-4012.

Kent D. B., Davis J. A., Anderson L. C. D., Rea B. A. and Waite T. D. (1994) Transport of chromium and selenium in the suboxic zone of a shallow aquifer: Influence of redox and adsorption reactions. Water Resources Res. 30, 1109-1114.

Manceau A. and Combes J. M. (1988) Structure of Mn and Fe oxides and oxyhydroxides: A topological approach by EXAFS. Phys. Chem. Min. 15, 283-295.

Manceau A. and Charlet L. (1992) X-ray absorption spectroscopic study of the sorption of Cr(III) at the oxide-water interface, I. Molecular mechanism of Cr(III) oxidation on Mn oxides. J. Coll. Interface Sci. 148, 425-443.

Mesuere K. and Fish W. (1992) Chromate and oxolate adsorption on goethite. 1. Calibration of surface complexation models. Environ. Sci. Technol. 26, 2357-2364.

Myneni S. C. B., Tokunaga T. K. and Brown G. E. Jr. (1997) Abiotic selenium redox transformations in the presence of Fe(II,III) oxides. Science 278, 1106-1109.

Nakayama E., Kuwamoto T., Tsurubo S., Tokoro H. and Fujinaga T. (1981) Chemical speciation of chromium in seawater. 1. Effect of naturally occuring organics materials on the complex formation of Cr(III). Analyt. Chim. Acta 130, 289-294.

Nieboer E and Jusys A. A. (1988) Biologic chemistry of chromium. In *Chromium in the natural and human environments* (eds. J. O. Nriagu and E. Nieboer). John Wiley and Sons, N. Y.

Newman A. C. D. (ed.) (1987) Chemistry of clays and clay minerals. In *Mineralogical Society Monograph 6*. John Wiley and Sons, New York. p 480.

Palmer D. C. (1996) CrystalMaker 2.1.0: Interactive crystallography for MacOS.

Peterson M. L., Brown G. E. Jr. and Parks G. A. (1996) Direct XAFS evidence for heterogeneous redox reaction at the aqueous chromium/magnetite interface. Colloids and Surfaces A - Physicochem. Eng. Aspects 107, 77-88.

Peterson M. L., Brown G. E. Jr., Parks G. A. and Stein C. L. (1997) Differential redox and sorption of Cr(III/VI) on natural silicate and oxide minerals: EXAFS and XANES results. Geochim. Cosmochim. Acta 61, 3399-3412.

Rai, D., Zachara J. M., Eary L. E., Girvin D. C., Moore D. A., Resch C. T., Sass B. M. and Schmidt R. L. (1986) Geochemical behaviour of chromium species. Final Report EPRI EA-4544. Electric Power Research Institute, Palo Alto, CA.

Rai, D., Sass B. M. and Moore D. A. (1987) Chromium(III) hydrolysis constants and solubility of Cr(III) hydroxide. Inorganic Chem. 26, 345-349.

Richard F. C. and Bourg A. C. M. (1991) Aqueous geochemistry of chromium - a review. Water Research 25, 807-816.

Robertson F. N. (1975) Hexavalent chromium in the groundwater in Paradise Valley, Arizona. Ground Water 13, 516-527.

Sass B. M. and Rai D. (1987) Solubility of amorphous chromium(III)-iron(III) hydroxide solid solutions. Inorg. Chem. 26, 2228-2232.

Schroeder D. C. and Lee G. F. (1975) Potential tranformations of chromium in natural waters. Water, Air, Soil Pollut. 4, 355-365.

Schwertmann U. and Murad E. (1983) Effect of pH on the formation of goethite and hematite from ferrihydrite. Clays Clay Mineral. 31, 277-284.

Schwertmann U. and Cornell R. M. (1991) *Iron oxides in the laboratory: Preparation and characterization*. VCH Publishers.

Schwertmann U. and Fechter H. (1994) The formation of green rust and its transformation to lepidocrocite. Clay minerals 29, 87-92.

Schwertmann U., Gasser U. and Sticher H. (1989) Chromium-for-iron substitution in synthetic goethites. Geochim. Cosmochim. Acta 53, 1293-1297.

Shinoda K., Matsubara E., Muramatsu A. and Waseda Y. (1994) Local structure of ferric hydroxide $Fe(OH)_3$ in aqueous solution by the anomalous X-ray scattering and EXAFS methods. Materials Trans., JIM 35, 394-398.

Trolard F., Genin J. M. R., Abdelmoula M., Bourrie G., Humbert B. and Herbillon A. (1997) Identification of a green rust mineral in a reductomorphic soil by mossbauer and raman spectroscopies. Geochim. Cosmochim. Acta 61, 1107-1111.

Van Geen A., Robertson A. P., and Leckie J. O. (1994) Complexation of carbonate species at the goethite surface: Implications for adsorption of metal ions in natural waters. Geochim. Cosmochim. Acta 58, 2073-2086.

Vins J., Subrt J., Zapletal V. and Hanousek F. (1987) Preparation and properties of green rust type substances. Collection Czechoslovak Chem. Commun. 52, 93-102.

White A. F. and Peterson M. L. (1996) Reduction of aqueous transition metal species on the surfaces of Fe(II)-containing oxides. Geochim. Cosmochim. Acta 60, 3799-3814.

Chapter 7

Overview and future directions

7.1 INTRODUCTION

The work presented in this report was motivated by a desire to better understand some of the processes that lead to 'natural attenuation', which is a phenomenon whereby naturally occurring materials act as a barrier to the migration of contaminants. A related aim was to identify situations where natural attenuation could not be relied upon to limit contaminant mobility.

Arsenic, cadmium and chromium are highly toxic to humans when accumulated in excess (e.g. Nieboer and Jusys, 1988; Mandal et al., 1996; Jin et al., 1998; Lehoczky et al., 1998). However, all three have become significant contaminants in many soil and sediment systems around the world, largely as a consequence of anthropogenic activities. Fortunately, As(V), Cd(II) and Cr(III) are strongly adsorbed by the poorly crystalline secondary iron- and/or manganese (oxyhydr)oxide minerals that occur widely in soils and sediments. This limits the mobility of these contaminants, and forms the basis of natural attenuation.

Although the oxyhydroxide minerals are very effective in reducing contaminant mobility by sorption, they constitute a huge reservoir of pollutants as a result. Consequently, it is essential that we understand the long-term changes in composition and mineralogy that the oxyhydroxide minerals will undergo, and the implications that these changes have for the mobility of sorbed species. It is also vital that reactions that can bring about a change in arsenic or chromium oxidation state are understood because, as will be shown, these can also have important implications for the mobility of these contaminants.

7.2 CADMIUM

The aqueous chemistry of cadmium is relatively simple because it only exists in the +2 oxidation state (Fig. 1.4). Except where there are high concentrations of other ligands, cadmium is present in solution as the aquo ion, $[Cd(H_2O)_6]^{2+}$. Under favourable pH conditions (generally ≥ pH 6), this adsorbs to iron (oxyhydr)oxide minerals *via* the formation of strong inner sphere bonds with ≡Fe-O(H) functional groups at the mineral surface (e.g. Spadini et al., 1994).

A number of 'surface complexation models' (SCM's) have been developed to derive thermodynamic data that describes the sorption process (e.g. Davis and Leckie,

1978; Davis and Kent, 1990; Hayes et al., 1991; Hiemstra and Van Riemsdijk, 1996; Venema et al., 1996a, b). This data is used in reactive transport models that predict the migration of contaminants such as cadmium in groundwater, and the effectiveness of these predictions is clearly dependent on the quality of the input thermodynamic data. SCM's require chemically and physically realistic representations of both the surface complexes and the oxyhydroxide mineral surface in order to generate reliable data. Unfortunately, the use of SCM's is currently limited by an incomplete understanding of the chemistry that takes place during adsorption. Consequently, a major aim of this work was to elucidate how the structure and composition of cadmium surface complexes varies as a function of pH and surface loading on the following oxyhydroxide minerals: goethite (α-FeOOH), lepidocrocite (γ-FeOOH), akaganeite (β-FeOOH), schwertmannite ($Fe_8O_8(OH)_6SO_4$) (Chapter 3) and cryptomelane (KMn_8O_{16}) (Chapter 4). Extended X-ray absorption fine structure (EXAFS) spectroscopy was used to probe the short range (≤4 Å) structure around sorbed cadmium *in situ* (i.e. the samples were analysed as viscous pastes, with no need for drying or the use of ultra-high vacuum during analysis). Importantly, the high X-ray flux used during EXAFS analysis allowed data to be collected from samples with as little as 0.1 wt% cadmium. *Ab initio* quantum mechanical modelling using density functional theory (DFT) calculations was used to complement and assist EXAFS data interpretation for samples of cadmium adsorbed on goethite.

7.2.1 Cadmium adsorption on iron oxyhydroxides

The EXAFS data show that cadmium adsorbs to goethite predominantly *via* a corner sharing mechanism at 'low affinity' sites on the dominant (110) surface (Fig. 3.5). DFT calculations and consideration of the likely relative surface hydroxyl group reactivities strongly suggest that this adsorption is achieved by corner sharing with two **A**-type hydroxyls rather than one **C**-type hydroxyl (Fig. 3.3). The EXAFS data provide no evidence for the edge sharing adsorption which previous studies (e.g. Spadini et al., 1994) and our quantum mechanical modelling indicate to be energetically favourable over corner sharing adsorption. I suggest that the goethite morphology precludes significant cadmium adsorption at edge sharing sites because these are only present on the crystal ends which are estimated to comprise only ~2% of the total surface area (Fig. 3.2). Note that synthetic and natural goethites share a very similar morphology (Smith and Eggleton, 1983; Schwertmann, 1984; Mann et al., 1985; Amouric et al., 1986; Schwertmann and Cornell, 1991; Hiemstra and Van Riemsdijk, 1996). Consequently, it seems likely that cadmium adsorption on goethite could be adequately modelled by assuming that bonding occurs only by bidentate

corner sharing adsorption. This will be especially true under conditions of moderate to high cadmium surface loading and/or when other competing ions are present in solution. I suggest that the single site surface complexation constants reported by Gunneriusson (1994) and partially revised by Palmqvist et al. (1997) are currently the most reliable for describing cadmium adsorption on goethite:

$$\equiv FeOH + Cd^{2+} \leftrightarrow \equiv FeOHCd^{2+}; \quad \log \beta^{s}_{0,1,1,0}(int) = 5.4$$

$$\equiv FeOH + Cd^{2+} \leftrightarrow \equiv FeOCd^{+} + H^{+}; \quad \log \beta^{s}_{-1,1,1,0}(int) = -2.22 \pm 0.05$$

By contrast, edge sharing mechanism(s) are responsible for the majority of cadmium adsorption on lepidocrocite (Fig. 3.7). This mineral has a far greater proportion of edge sharing sites than goethite, and this result confirms the notion that cadmium is preferentially adsorbed at 'high affinity' edge sharing- rather than 'low affinity' corner sharing sites at the surface of iron oxyhydroxide minerals. The overall mechanism of cadmium adsorption on goethite and lepidocrocite appears to be insensitive to changes in pH and surface loading.

The results presented here also demonstrate that akaganeite and schwertmannite are capable of adsorbing significant amounts of cadmium from solution. Whilst this adsorption clearly occurs *via* inner sphere bonding, it has not been possible to unambiguously assign definite adsorption mechanism(s).

7.2.2 Cadmium sorption on manganese oxide

Cryptomelane is a manganese oxide with the hollandite structure (Fig. 4.1), in which there are ~4.6 Å tunnels (Vicat et al., 1986). In natural cryptomelane the tunnel sites are occupied primarily by K^{+} cations, although variable amounts of other cations (commonly Sr^{2+}, Ba^{2+}, Na^{+}, Pb^{2+}) and water are also present (Post et al., 1982). Cryptomelane is the major manganese oxide in some lateritic weathering profiles (Parc et al., 1989; Ostwald, 1992; Vasconcelos et al., 1994; Ruffet et al., 1996), where it commonly forms by authigenic precipitation (Vasconcelos et al., 1994). The presence of cryptomelane is documented in weathered ultramafic rocks (Llorca and Monchoux, 1991). It has also been identified as an important vein and/or fracture-lining manganese mineral in volcanic tuffs (such as that at the proposed Yucca Mountain high-level nuclear waste repository) (Carlos et al., 1993), in rocks surrounding granites (Nakashima and Imaoka, 1991), and in fault zones and related karsts in marbles (Nimfopoulos and Pattrick, 1991).

The work presented here has shown cryptomelane to be capable of sorbing large amounts of cadmium from solution under low pH conditions (≥ pH 2). EXAFS

results indicate that cadmium sorption at pH 2.0 occurs predominantly at tunnel sites in the cryptomelane structure by ion exchange for H^+ ions, which are likely to be in the tunnels in addition to potassium. This conclusion is supported by the lowering of pH during cadmium sorption. This is an important result for K-Ar dating techniques which use natural cryptomelane (Vasconcelos et al., 1992, 1994; Lippolt and Hautmann, 1995; Dammer et al., 1996; Ruffet et al., 1996; Henocque et al., 1997), because the possibility of potassium replacement by competing cations would increase dating uncertainties. Sorbed cadmium is displaced from the ideal tunnel cation position (special position 2a (0, 0, 0)) in order to achieve a separation of 2.24 Å from the tunnel wall O^{2-} ions with which it is coordinated. EXAFS results show that cadmium has a complete octahedral solvation shell, but this cannot be due to tunnel wall O^{2-} ions alone. I suggest that tunnel cadmium is also partly coordinated with free water in the tunnels in order to complete its solvation shell. Although this study demonstrates that cadmium is able to sorb at tunnel sites in cryptomelane, it has not been possible to identify the exact location of sorbed cadmium because of structural disorder and the likely existence of a number of different sorption sites.

7.2.3 The influence of organic matter on trace metal adsorption

It should be noted whilst dissolved organic material and organic coatings (biofilms) can exert a significant control on the behaviour of trace metals in the environment (e.g. Lion et al., 1988; Lamy et al., 1991; Tipping and Hurley, 1992; Sanchez-Martin and Sanchez-Camanzano, 1993), all experiments reported in this study were performed under organic-free conditions. This was done so that the fundamental inorganic reactions could be explored in detail, and thus form the basis for future experiments involving organics. It is important to realise that the influence of organics on trace metal speciation and mobility is limited under conditions of near neutral to alkaline pH in lakes (Tessier et al., 1985, 1996) and soils (Anderson and Christensen, 1988). Indeed, Tessier et al. (1985, 1996) have shown that trace metal adsorption under these conditions takes place by direct bonding to inorganic mineral surfaces, even in the presence of organics. An EXAFS spectroscopy study has proven this conclusively for cadmium adsorption on iron oxyhydroxides (Collins et al., 1999).

7.2.4 Cadmium adsorption - summary

Cadmium adsorbs from solution to goethite, lepidocrocite, akaganeite and schwertmannite by the formation of inner sphere bonds with the mineral surface. The strongest adsorption takes place at 'edge sharing' sites. The majority of adsorption will occur at these sites except where crystal morphology dictates that they constitute a minor fraction of the total available surface sites. Adsorption on goethite is a good example of such a situation. In this case, edge sharing sites occur on just ~2% of the total crystal surface area. As a consequence, adsorption occurs predominantly at the less energetically favourable bidentate 'corner sharing' sites. Note that this situation can also arise when other ions such as Pb^{2+} and Zn^{2+} and Ca^{2+} compete for adsorption sites, thereby forcing cadmium onto the corner sharing sites even when edge sharing sites are theoretically available. Thus, in goethite-rich environments, cadmium mobility is most likely to be controlled by equilibrium with species adsorbed *via* a bidentate corner sharing mechanism. Conversely, stronger edge sharing adsorption is more likely to be important in environments where lepidocrocite dominates. Reactive transport modelling approaches should take account of this.

By contrast to its adsorption on iron oxyhydroxides, cadmium predominantly sorbs to cryptomelane *via* ion exchange for protons that exist in the structural tunnels in this mineral. Since this can occur at pH $\geq$ 2 (remember that cadmium adsorption on iron oxyhydroxides only becomes important above ~pH 6), this mineral may constitute an important sorbent for cadmium when adsorption on iron (oxyhydr)oxides is minimal.

It is expected that the results presented here will allow existing thermodynamic sorption data to be critically assessed on the basis of whether a physically realistic chemical model was used during its derivation. By the same token, the results should act as a guide for future attempts to generate thermodynamic data. They also provide direction for workers attempting to apply *Ab initio* methods to reactions at the mineral-water interface.

7.3 ARSENIC AND CHROMIUM

Naturally occurring, poorly crystalline iron oxyhydroxides such as ferrihydrite are known to be very effective sorbents of As(V) and Cr(III) (e.g. Aggett and Roberts, 1986; Belzile and Tessier, 1990; Richard and Bourg, 1991; Petersen et al., 1995). Ferrihydrite is metastable and over time it ages into more crystalline phases such as goethite (α-FeOOH) and/or hematite (α-Fe_2O_3). The fate of adsorbed and coprecipitated contaminants upon ageing of ferrihydrite is unclear; they could simply

remain adsorbed as surface complexes or they may be incorporated into the bulk crystal structure. In this case, they could only be released upon dissolution of the host mineral. Conversely, they could be expelled from the crystal structure and desorbed during ageing, in which case their mobility and bioavailability would be vastly increased. This is a possibility because amorphous iron (oxyhydr)oxides such as ferrihydrite have a much higher sorption capacity per unit mass than crystalline ageing products such as goethite (e.g. Bowell, 1994).

Understanding the risks posed by arsenic and chromium contamination is complicated by the fact that both elements exist in two different oxidation states (Figs. 1.1 and 1.9). Whereas the As(V) and Cr(III) species are strongly adsorbed and therefore relatively immobile, the opposite is true of the more toxic As(III) and Cr(VI) forms. Because of this, it is vital that the geochemical processes that can bring about changes in the oxidation state of arsenic and chromium are also understood. A molecular scale understanding of redox processes is also useful from a mechanistic point of view. This is because the elucidation of adsorption equilibria and the structure of precursor complexes such as ($\equiv Fe^{III}$-O-Fe^{II}) at the mineral surface is a prerequisite for the study of heterogeneous redox kinetics (Wehrli, 1990).

Amongst the most important processes that can lead to changes in oxidation state are (a) interaction of an oxidised species with a reductant, and (b) changes in the Eh and composition of porewater with the onset of with early diagenesis. These processes have the potential to liberate arsenic and chromium and turn many contaminated areas into persistent sources of pollution. This risk can only be mitigated by an understanding of the processes that will control the long-term mobility of arsenic and chromium.

7.3.1 Ageing of contaminated ferrihydrite

When ferrihydrite that was contaminated with a relatively small amount of As(V) (bulk As/(As+Fe) = 0.0033) was aged to goethite, all As(V) remained adsorbed because the sorption capacity of the crystalline product was not exceeded. Importantly, there was also no arsenic release from samples with a sorption capacity that would have been exceeded if all ferrihydrite had transformed to goethite or hematite. This is explained by the fact that sorbed As(V) retarded the ageing process to such an extent that significant amounts of untransformed ferrihydrite remained, and the bulk sorption capacity of the samples was consequently not exceeded. Another important finding is that throughout the ageing process, As(V) persisted as surface complexes whether it was added prior to or after the nucleation of ferrihydrite. It was not incorporated into the iron oxyhydroxide bulk structure, and there was no evidence

for the formation of a ferric arsenate phase such as scorodite ($FeAsO_4 \cdot 2H_2O$). This result is in agreement with field observations (e.g. Voigt et al., 1996), and suggests that dissolved arsenic concentrations will be controlled by equilibrium with adsorbed species irrespective of ongoing ageing processes.

It was apparent that increasing arsenic levels favoured the formation of hematite over goethite; this is thought to be because sorbed As(V) facilitates the aggregation of ferrihydrite particles and stabilises iron oxyhydroxides against dissolution. It is interesting to note that although the bulk ageing products were always goethite and/or hematite, the local coordination environment around As(V) on the ageing products was different to that of As(V) adsorbed on pure goethite or hematite. This difference is assigned to As(V)-induced poisoning of crystal growth that was limited to the mineral-water interface where the arsenic was adsorbed.

In contrast to the As(V)-ferrihydrite ageing experiments, ageing of Cr(III)-contaminated ferrihydrite resulted in a persistent release to solution of Cr(III), although there was no release of iron. Increasing levels of Cr(III) did slow the ageing process, but goethite (α-FeOOH) was always the sole ageing product. EXAFS analysis showed that Cr(III) sorbed *via* the formation of a hydrous Cr(III) oxide with a γ-CrOOH-type structure. This persisted throughout the ageing process, and there was only weak evidence for Cr(III) for Fe(III) substitution, perhaps because α-CrOOH is *not* isostructural with α-FeOOH. This suggests that the extensive Cr(III)-Fe(III) solid solution observed by previous workers in amorphous [Fe(III),Cr(III)] hydroxide (Sass and Rai, 1987) does not occur in goethite. This assertion is supported by the fact that Cr(III) for Fe(III) substitution can reach 89 mol% in [Fe(III),Cr(III)] hydroxide (Sass and Rai, 1987) but just 12 mol% in goethite (Schwertmann et al., 1989).

It has previously been suggested that aqueous Cr(III) concentrations will be controlled by equilibrium with amorphous [Fe(III),Cr(III)] hydroxide (Cr(III)-contaminated ferrihydrite) wherever this occurs in nature (Richard and Bourg, 1991). However, the results presented here suggest that $Cr(OH)_3 \cdot nH_2O$ will exert the dominant control on Cr(III) solubility following the ageing of Cr(III)-contaminated ferrihydrite. This is important because pure $Cr(OH)_3$ is more soluble than any [Fe(III),Cr(III)] hydroxide solid solution (Sass and Rai, 1987).

7.3.2 Interaction with green rust

Green rust ($Fe_y^{(II)}Fe_x^{(III)}(OH)_{3x+2y-2z}(SO_4)_z$) is a mixed Fe(II)-Fe(III) oxyhydroxide mineral that is thought to occur under the reducing and mildly acidic to mildly alkaline conditions found in reductomorphic soils and certain sedimentary

horizons (e.g. Hansen et al., 1994; Schwertmann and Fechter, 1994; Trolard et al., 1997). Consequently, it is likely to be one of the most important Fe(II)-bearing minerals in immature sediments and soils, and its mixed valence makes it of potentially great importance to trace metal mobility. Green rust has previously been shown to be capable of reducing Se(VI) to Se(0) (Myneni et al., 1997) and nitrate to ammonium (Hansen et al., 1994). In contrast to these findings, results presented here show that green rust does not reduce As(V) to As(III), irrespective of whether arsenic is added prior to or after green rust formation. This is of great importance because As(III) is far more toxic and mobile than As(V). Following adsorption on green rust, As(V) persists as surface complexes, even during the oxidation of green rust to lepidocrocite (γ-FeOOH). It is not incorporated into the green rust bulk structure and it does not exchange for sulphate anions in the interlayer sites that are present in green rust. Therefore, aqueous arsenic concentrations will be controlled exclusively by equilibrium with sorbed As(V) species.

In contrast, Cr(VI) undergoes instantaneous reduction to Cr(III) following interaction with green rust with the concomitant production of magnetite. A likely scheme for this reaction is as follows:

$$HCrO_4^- + 3Fe^{(II)}_2Fe^{(III)}(OH)_5(SO_4) =$$
$$Cr(OH)_3{\cdot}nH_2O + 3Fe_3O_4 + 3SO_4^{2-} + 5H^+ + 4\text{-}nH_2O$$

This observation is important because it shows that green rust can rapidly reduce chromium from its toxic and highly mobile Cr(VI) form and precipitate it as $Cr(OH)_3{\cdot}nH_2O$. This phase will then exert the major control on Cr(III) solubility.

7.3.3. Sulphidisation of As(V)-contaminated goethite

Whereas iron (oxyhydr)oxides generally limit the mobility of As(V) under oxic conditions, arsenic mobility is limited by equilibrium with authigenic iron and/or arsenic sulphides under reducing, sulphur-rich environments (e.g. Moore et al., 1988; Huerta-Diaz and Morse, 1990, 1992). Aqueous trace metal concentrations can increase dramatically during the reductive dissolution of (oxyhydr)oxides (Korte, 1991; Petersen et al., 1995), a reaction that is known to take place during the early diagenesis of sediments. Under such conditions, there is the potential for significant amounts of arsenic to be transported away from the site of contamination, and pose a risk to human health. It is clearly of importance that these reactions are understood so that the potential release of contaminants can be predicted. This is especially true when it is realised that external factors such as seasonal changes in groundwater level

or reservoir water depth can cause the reduction/oxidation reactions to occur on a repeating, cyclical basis (Moore et al., 1988).

The results presented here demonstrate that sulphidisation of As(V)-contaminated goethite leads to the reductive dissolution of the iron oxyhydroxide with a resultant release to solution of both iron and arsenic. The iron is subsequently removed from solution by the formation of poorly crystalline mackinawite ($Fe_{1+x}S$). Arsenic concentrations similarly decrease, but EXAFS analysis shows that the first coordination shell around As(III) is identical to that in poorly crystalline orpiment (As_2S_3(am)). This suggests that arsenic does not sorb by coprecipitation with iron. Although dissolved arsenic concentrations remain low following the establishment of stable sulphide-rich conditions, presumably by equilibrium with As_2S_3(am), it should be noted that any arsenic that does remain in solution will be in the mobile and toxic As(III) form.

7.3.4. Arsenic and chromium - summary

Arsenic and chromium are both strongly sorbed by ferrihydrite, but they behave in very different ways as this mineral ages following contamination. As(V) persists as surface complexes throughout the ageing process, and no As(V) is released to solution. Consequently, dissolved As(V) concentrations would be expected to be maintained below drinking water limits by adsorption on ferrihydrite and its ageing products. Very high As(V) loadings prevent the ageing process from occurring, explaining why the bulk As(V) sorption capacity of grossly contaminated samples is not exceeded. Conversely, Cr(III) partitions out of a supposed solid solution in [Cr(III),Fe(III)] hydroxide during ageing, and forms a discrete hydrous Cr(III) oxide phase with γ-CrOOH structure. This reaction is accompanied by the persistent release of a *minor* fraction of the initial Cr(III) load.

Thus, aqueous concentrations of As(V) and Cr(III) in immature sediments will be controlled by equilibrium with adsorbed species and [Cr(III),Fe(III)] hydroxide, respectively. As the sediments age and the constituent iron (oxyhydr)oxides become more crystalline, As(V) will still be controlled by equilibrium with adsorbed species, but aqueous concentrations of Cr(III) will be controlled by equilibrium with hydrous Cr(III) oxide (e.g. $Cr(OH)_3{\cdot}nH_2O$). Although $Cr(OH)_3{\cdot}nH_2O$ is more soluble than [Cr(III),Fe(III)] hydroxide, it is sufficiently insoluble that dissolved Cr(III) drinking water limits should not be exceeded.

Green rust cannot reduce As(V) to As(III), and instead adsorbs it in surface complexes that are very similar to those observed on ferric oxyhydroxide minerals. This is very important because As(V) is essentially rendered immobile by adsorption,

even during the oxidation of green rust to lepidocrocite. Reduction to As(III) would have potentially disastrous consequences because this species is far more toxic and mobile than the As(V) form. Whilst green rust cannot reduce As(V), it can reduce Cr(VI) to Cr(III), which is then sorbed as a γ-CrOOH-like precipitate very similar to that observed on aged Cr(III)-ferrihydrite.

These results all suggest that ferrihydrite- and green rust-rich sediments and soils will constitute an effective barrier to the migration of As(V), Cr(III) and Cr(VI) (the latter is only attenuated in the presence of green rust), and that these contaminants will not be released in significant quantities as the sorbents age.

The same is not necessarily true during the sulphidisation of As(V)-contaminated goethite. In this case, there is a period of time when both iron and arsenic concentrations are high. This is because solubility limiting phases are at a minimum during the reductive dissolution of the iron oxyhydroxide and prior to the formation of new iron and arsenic sulphide phases. During this time, the majority of dissolved arsenic is most likely to exist in the mobile and highly toxic As(III) form, and the risk of groundwater flow carrying this species away from the site of contamination will be high. Under steady state reducing, sulphide-rich conditions, it appears that As_2S_3(am) suppresses dissolved arsenic concentrations. However, it is important to realise that this material would be easily oxidised if events such as dredging or large storms exposed it to oxygenated conditions.

7.4 FUTURE DIRECTIONS

In order to isolate and fully understand some of the fundamental inorganic reactions that can affect the mobility of arsenic, cadmium and chromium, the experiments described in this dissertation have been performed in the absence of both organics and microbes. Relatively recent work has suggested that both of these factors can play an important role in determining the fate of a number of contaminants. Consequently, I feel that the next logical step for this work would be to repeat some of the experiments but to include in them a highly characterised organic or microbial component. Comparison of results generated in this way with those reported here will provide some direct information regarding the relative importance of inorganic, organic and microbially mediated reactions.

EXAFS spectroscopy is clearly the technique of choice for determining the mechanism of trace metal sorption in poorly crystalline systems that approximate those found in the environment. However, samples have often had to contain the 'element of interest' at concentrations of ≥ 0.1 wt% in order that data of an acceptable quality can be collected. This in itself can preclude the incorporation of a biotic component in

sample preparation because the high contaminant concentrations would kill the microbes. However, recent developments in synchrotron radiation technology make it possible to analyse samples with ≥0.02 wt% of the element of interest. This, in turn, makes biotic sample preparation feasible.

The results presented in Chapter 3 demonstrate the applicability of *ab initio* quantum mechanical techniques to modelling the structure of sorption complexes. Whilst the information derived in this way provides a useful independent guide for the analysis of EXAFS data, the calculations are physically unrealistic in the sense that the molecular clusters are very small, and they cannot take account of solvation effects. Increasing computing power and the development of new software make it likely that future modelling attempts will use a molecular dynamic approach. This allows much larger molecular units and solvation effects to be considered. I feel that the use of *Ab initio* predictions as a guide to which samples to prepare and analyse by EXAFS should increase in the future. This is especially true when it is remembered that EXAFS beamtime comes at a high premium.

7. 5 REFERENCES

Aggett J. and Roberts L. S. (1986) Insight into the mechanism of accumulation of arsenate and phosphate in hydro lake sediments by measuring the rate of dissolution with ethylenediamine-tetraacetic acid. Envrion. Sci. Technol. 20, 183-186.

Amouric M., Baronett A., Nahon D., and Didier P. (1986) Electron microscopic investigations of iron oxyhydroxides and accompanying phases in lateritic iron crust pisolites. Clays Clay Mineral. 34, 45-52.

Anderson P. R. and Christensen T. H. (1988) Distribution coefficients of cadmium, cobalt, nickel and zinc in soils. J. Soil Sci. 39, 15-22.

Belzile N. and Tessier A. (1990) Interactions between arsenic and iron oxyhydroxides in lacustrine sediments. Geochim. Cosmochim. Acta 54, 103-109.

Bowell R. J. (1994) Sorption of arsenic by iron oxides and oxyhydroxides in soils. Applied Geochemistry 9, 279-286.

Carlos B. A., Chipera S. J., Bish D. L. and Craven S. J. (1993) Fracture-lining manganese oxide minerals in silicic tuff, Yucca Mountain, Nevada, USA. Chem. Geol. 107, 47-69.

Collins C.R., Ragnarsdottir K.V., and Sherman D.M. (1999) Effect of inorganic and organic ligands on the adsorption of Cd^{2+} to goethite. Geochim. Cosmochim. Acta. (submitted).

Dammer D., Chivas A. R. and McDougall I. (1996) Isotopic dating of supergene manganese oxides from the Groote Eylandt deposit, Northern Territory, Australia. Econ. Geol. Bull. Soc. Econ. Geol. 91, 386-401.

Davis J. A. and Leckie J. O. (1978) Surface ionization and complexation at the oxide/water interface. 2. Surface properties of amorphous iron oxyhydroxide and adsorption of metal ions. J. Colloid Interface Sci. 67, 90-105.

Davis J. A. and Kent D. B. (1990) Surface complexation modelling in aqueous geochemistry. In *Mineral-Water Interface Geochemistry* (eds. M. F. Hochella and A. F. White). Reviews in Mineralogy Vol. 23, pp. 177-260. Min. Soc. Am.

Gunneriusson L. (1994) Composition and stability of Cd(II)-chloro and Cd(II)-hydroxo complexes at the goethite (α-FeOOH)/water interface. J. Colloid Interface Sci. 163, 484-492.

Hansen H. C. B., Borggaard O. K. and Sorensen J. (1994) Evaluation of the free energy of formation of Fe(II)-Fe(III) hydroxide-sulfate (green rust) and its reduction of nitrite. Geochim. Cosmochim. Acta 58, 2599- 2608.

Hayes K. F., Redden G., Ela W., and Leckie J. O. (1991) Surface complexation models: An evaluation of model parameter estimations using FITEQL and oxide mineral titration data. J. Colloid Interface Sci. 142, 448-469.

Henocque O., Ruffet G., Colin F. and Feraud G. (1997) The $^{40}Ar/^{39}Ar$ dating of supergene minerals as a new investigation tool of lateritic dynamics. Abs. Supplement 1, Abs. of European Union of Geosciences 9, Terra Nova, 9. Cambridge, Cambridge, U.K, pp. 583.

Hiemstra T. and Van Riemsdijk W. H. (1996) A surface structural approach to ion adsorption: The charge distribution (CD) model. J. Colloid Interface Sci. 179, 488-508.

Huerta-Diaz M. A. and Morse J. W. (1990) Pyritization of trace metals in anoxic marine sediments. Geochim. Cosmochim. Acta 56, 2681-2702.

Huerta-Diaz M. A. and Morse J. W. (1992) A quantitative method for determination of trace metal concentrations in sedimentary pyrite. Mar. Chem. 29, 119-144.

Jin T. Y., Lu J. and Nordberg M. (1998) Toxicokinetics and biochemistry of cadmium with special emphasis on the role of metallothionein. Neurotoxicology 19, 529-535.

Korte N. (1991) Naturally occurring arsenic in groundwaters of the midwestern United States. Environ. Geol. Water Sci. 18, 137-141.

Lamy I., Djafer M. and Terce M. (1991) Influence of oxalic acid on the adsorption of cadmium at the geothite surface. Water, Air, Soil Poll. 57-58, 457-465.

Lehoczky E., Szabo L., Horvath S., Marth P. and Szabados I. (1998) Cadmium uptake by lettuce in different soils. Comm. In Soil Sci. and Plant Anal. 29, 1903-1912.

Lion L. W., Shuler M. L., Hsieh K. M. and Ghiorse W. C. (1988) Trace metal interactions with microbial biofilms. CRC Crit. Rev. Environ. Con. 17, 273-306.

Lippolt H. J. and Hautmann S. (1995) $^{40}Ar/^{39}Ar$ ages of Precambrian manganese ore minerals from Sweden, India and Morocco. Mineralium Deposita 30, 246-256.

Llorca S. and Monchoux P. (1991) Supergene cobalt minerals from New Caledonia. Canadian Mineral. 29, 149-161.

Mandal B. K., Chowdry T. R., Samanta G., Basu G. K., Chowdry P. P., Chanda C. R., Lodh, D., Karan N. K., Dhar R. K., Tamili D. K., Das D., Saha K. C. and Chakraborti D. (1996) Arsenic in groundwater in seven districts of West Bengal, India - The biggest arsenic calamity in the world. Current Sci. 70, 976-986.

Mann S., Cornell R. M., and Schwertmann U. (1985) The influence of aluminium on iron oxides: XII. High-resolution transmission electron microscopic (HRTEM) study of aluminous goethites. Clay Minerals 20, 255-262.

Moore J. N., Ficklin W. H. and Johns C. (1988) Partitioning of arsenic and metals in reducing sulfidic sediments. Environ. Sci. Technol. 22, 432-437.

Myneni S. C. B., Tokunaga T. K. and Brown G. E. Jr. (1997) Abiotic selenium redox transformations in the presence of Fe(II,III) oxides. Science 278, 1106-1109.

Nakashima K. and Imaoka T. (1991) K-rich cryptomelane from Mt. Kumogi area, Shimane Prefecture, Southwest Japan. Neues Jahrb. Mineral.-Monatsh. 113-128.

Nieboer E. and Jusys A. A. (1988) Biologic chemistry of chromium. In *Chromium in the natural and human environments* (eds. J. O. Nriagu and E. Nieboer). John Wiley and Sons, N. Y.

Nimfopoulos M. K. and Pattrick R. A. D. (1991) Mineralogical and textural evolution of the economic manganese mineralization in Western Rhodope Massif, N. Greece. Mineral. Mag. 55, 423-434.

Ostwald J. (1992) Genesis and paragenesis of the tetravalent manganese oxides of the Australian continent. Econ. Geol. Bull. Soc. Econ. Geol. 87, 1237-1252.

Palmqvist U., Ahlberg E., Lövgren L., and Sjöberg S. (1997) In situ voltammetric determinations of metal ions in goethite suspensions: Single metal ion systems. J. Colloid Interface Sci. 196, 254-266.

Parc S., Nahon D., Tardy Y. and Vieillard P. (1989) Estimated solubility products and fields of stability for cryptomelane, nsutite, birnessite, and lithiophorite based on natural lateritic weathering sequences. Amer. Mineral. 74, 466-475.

Petersen W., Wallmann K., Li, P., Schroeder F. and Knauth H. -D. (1995) Exchange of trace elements at the sediment-water interface during early diagenesis processes. Mar. Freshwater Res. 46, 19-26.

Post J. E., Von Dreele R. B. and Buseck P. R. (1982) Symmetry and cation displacements in hollandites: Structure refinements of hollandite, cryptomelane, and priderite. Acta Crystallogr. B38, 1056-1065.

Richard F. C. and Bourg A. C. M. (1991) Aqueous geochemistry of chromium - a review. Water Research 25, 807-816.

Ruffet G., Innocent C., Michard A., Feraud G., Beauvais A., Nahon D. and Hamelin B. (1996) A geochronological $^{40}Ar/^{39}Ar$ and $^{87}Rb/^{87}Sr$ study of K-Mn oxides from the weathering sequence of Azul, Brazil. Geochim. Cosmochim. Acta 60, 2219-2232.

Sanchez-Martin M. J. and Sanchez-Camanzano (1993) Adsorption and mobility of cadmium in natural, uncultivated soils. J. Env. Qual. 22, 737-742.

Sass B. M. and Rai D. (1987) Solubility of amorphous chromium(III)-iron(III) hydroxide solid solutions. Inorg. Chem. 26, 2228-2232.

Schwertmann U. (1984) The influence of aluminium on iron oxides: IX. Dissolution of Al-goethites in 6M HCl. Clay Minerals 19, 9-19.

Schwertmann U. and Cornell R. M. (1991) *Iron oxides in the laboratory: Preparation and characterization.* VCH Publishers.

Schwertmann U. and Fechter H. (1994) The formation of green rust and its transformation to lepidocrocite. Clay minerals 29, 87-92.

Schwertmann U., Gasser U. and Sticher H. (1989) Chromium-for-iron substitution in synthetic goethites. Geochim. Cosmochim. Acta 53, 1293-1297.

Smith K. L. and Eggleton R. A. (1983) Botryoidal goethite: A transmission electron microscope study. Clays Clay Mineral. 31, 392-396.

Spadini L., Manceau A., Schindler P. W., and Charlet L. (1994) Structure and stability of Cd^{2+} surface complexes on ferric oxides. 1. Results from EXAFS spectroscopy. J. Colloid Interface Sci. 168, 73-86.

Tessier A., Rapin F. and Carignan R. (1985) Trace metals in oxic lake sediments; possible adsorption onto iron oxyhydroxides. Geochim. Cosmochim. Acta 49, 183-194.

Tessier A., Fortin D., Belzile N., DeVitre R. R. and Leppard G. G. (1996) Metal sorption to diagenetic iron and manganese oxyhydroxides and associated organic-matter - narrowing the gap between field and laboratory measurements. Geochim. Cosmochim. Acta 60, 387-404.

Tipping E. and Hurley M. A. (1992) A unifying model of cation binding by humic substances. Geochim. Cosmochim. Acta 56, 3627-3641.

Trolard F., Genin J. M. R., Abdelmoula M., Bourrie G., Humbert B. and Herbillon A. (1997) Identification of a green rust mineral in a reductomorphic soil by mossbauer and raman spectroscopies. Geochim. Cosmochim. Acta 61, 1107-1111.

Vasconcelos P. M., Becker T. A., Renne P. R. and Brimhall G. H. (1992) Age and duration of weathering by $^{40}K/^{40}Ar$ and $^{40}Ar/^{39}Ar$ analysis of potassium-manganese oxides. Science 258, 451-455.

Vasconcelos P. M., Renne P. R., Brimhall G. H. and Becker T. A. (1994) Direct dating of weathering phenomena by $^{40}Ar/^{39}Ar$ and K-Ar analysis of supergene K-Mn Oxides. Geochim. Cosmochim. Acta 58, 1635-1665.

Venema P., Hiemstra T., and Van Riemsdijk W. H. (1996a) Comparison of different site binding models for cation sorption: description of pH dependency, salt dependency, and cation-proton exchange. J. Colloid Interface Sci. 181, 45-59.

Venema P., Hiemstra T., and Van Riemsdijk W. H. (1996b) Multisite adsorption of cadmium on goethite. J. Colloid Interface Sci. 183, 515-527.

Vicat J., Fanchon E., Strobel P. and Tran Qui D. (1986) The structure of $K_{1.33}Mn_8O_{16}$ and cation ordering in hollandite-type structures. Acta Crystallogr. B42, 162-167.

Voigt D. E., Brantley S. L. and Hennet R. J. -C. (1996) Chemical fixation of arsenic in contaminated soils. Applied Geochem. 11, 633-643.

Wehrli B. (1990) Redox reactions of metal ions at mineral surfaces. In *Aquatic chemical kinetics* (ed. W. Stumm). J. Wiley and Sons, N.Y. pp. 311-336.

Published in Chemical Geology Vol. 151, pp. 95-106.

An EXAFS Investigation of Cadmium Sorption on Cryptomelane (KMn_8O_{16})

Simon R. Randall*, David M. Sherman, and K. Vala Ragnarsdottir

Department of Geology, University of Bristol, Bristol, BS8 1RJ, U.K.

Abstract- The mobility of cadmium in the environment is strongly inhibited by sorption onto Fe and Mn (hydr)oxide minerals such as cryptomelane (KMn_8O_{16}). Adsorption experiments showed that cryptomelane was able to sorb two thirds of available cadmium from solution at pH as low as 2.0. EXAFS was used to determine whether cadmium had sorbed to the external surfaces of the mineral, or migrated into the ~4.6 Å diameter tunnels which exist in the cryptomelane structure. The Mn coordination environment around sorbed cadmium (4.9 ± 1.0 Mn at 3.65 ± 0.02 Å) at pH 2.0 strongly indicates that the majority of sorbed cadmium is located inside the tunnels, and that it is displaced from the ideal tunnel cation position (special position 2a (0, 0, 0)). The oxygen coordination environment around cadmium (6.5 ± 1.3 O at 2.24 ± 0.02 Å) is consistent with this conclusion, but also suggests that sorbed cadmium is partially hydrated. The dominant tunnel cation (K^+) was not significantly released to solution during cadmium sorption. Thus, it seems likely that cadmium exchanged with H^+ in the tunnels rather than K^+. This is supported by the lowering of pH during cadmium adsorption and corresponding charge balance calculations. Cadmium sorption at the tunnel sites is likely to be energetically favourable because it allows occupation of those tunnel sites which K^+ cannot fill, thus resulting in a more effective balancing of the negative structural charge in cryptomelane. This is the first EXAFS study of cation sorption on a mineral with the hollandite structure.

Keywords: Cadmium, Cryptomelane, Hollandite, Manganese oxides, EXAFS, Ion Exchange

* Corresponding author. E-mail: Simon.Randall@bris.ac.uk Fax: 44 (0) 117 9253385

Published as an extended abstract in Mineralogical Magazine Vol. 62A, pp. 1231-1232.

An EXAFS Investigation of the Mechanisms of Cadmium Attenuation on Fe and Mn (Oxyhydr)oxide Minerals

S. R. Randall
D. M. Sherman
K. V. Ragnarsdottir

Department of Earth Sciences
University of Bristol
Bristol, BS8 1RJ, U.K.

Introduction

The structure of aqueous cadmium sorption complexes on the iron oxyhydroxide minerals goethite (α-FeOOH), lepidocrocite (γ-FeOOH), akaganeite (β-FeOOH), schwertmannite ($Fe_8O_8(OH)_6SO_4$), and cryptomelane (KMn_8O_{16}) have been determined *in situ* (in the presence of water) using Extended X-Ray Adsorption Fine Structure (EXAFS) spectroscopy. Sorption on these minerals may limit the mobility of Cd in soils and groundwater.

Experimental

All minerals were prepared in our laboratory according to methods reported in the literature. Samples for EXAFS analysis were prepared by adding a known concentration of Cd stock solution to suspensions of the chosen mineral and equilibrating for approximately 24 hr. CO_2-free conditions were maintained throughout the adsorption step of sample preparation to prevent the formation of $CdCO_3$(s).

EXAFS data were collected at the CLRC Synchrotron Radiation Source (SRS) at Daresbury Laboratory, U.K. Spectra were collected in multiple fluorescence mode scans at the Cd K-edge under room temperature conditions on station 9.2. Sample were presented to the X-ray beam as a wet paste held by Sellotape in a 2 mm thick plastic slide with a 4 x 15 mm sample slot. EXAFS data were also collected from β-$Cd(OH)_2$(s), for use as a reference standard in later curve fitting.

EXAFS data reduction and analysis was performed using native Daresbury Laboratory software packages (EXCALIB, EXBACK, and EXCURV92) (Binsted et al., 1991). All reported atomic shells are significant at the 1% level. The phase shift functions used in the curve fitting were derived by *ab initio* methods in EXCURV92.

Results

The EXAFS results show that in all adsorption samples and the β-$Cd(OH)_2$(s) standard, Cd is surrounded by an inner atomic shell containing approximately 6 O,OH,OH_2 groups (EXAFS cannot distinguish between these three possibilities) at a distance of 2.24 - 2.28 Å. At least one additional atomic shell containing Fe or Mn atoms is observed outside the O shell but within 4 Å of the central Cd atom, showing that Cd must adsorb *via* an inner sphere mechanism. There is no evidence for a Cd shell in theoretical fits to experimental data from the adsorption samples, and this indicates that Cd did not adsorb *via* the precipitation of a solid phase such as $Cd(OH)_2$(s) or $CdCO_3$(s). These results are in general agreement with an earlier EXAFS-based study of Cd sorption on goethite and hydrous ferric oxide by Spadini et al. (1994).

The EXAFS results for various 'wet paste' goethite adsorption samples are effectively the same regardless of pH (pH 5.4 to 9.3 range) or surface loading (24 % to 53 % range). In all cases, a shell containing between 1.1 and 1.8 Fe atoms is present between 3.75 and 3.80 Å from the central Cd atom in addition to the O shell (Fig. 1). This Cd-Fe separation suggests that Cd adsorbs *via* a corner-sharing mechanism, and there is no support for an Fe shell at 3.3 Å, which would indicate edge-sharing adsorption.

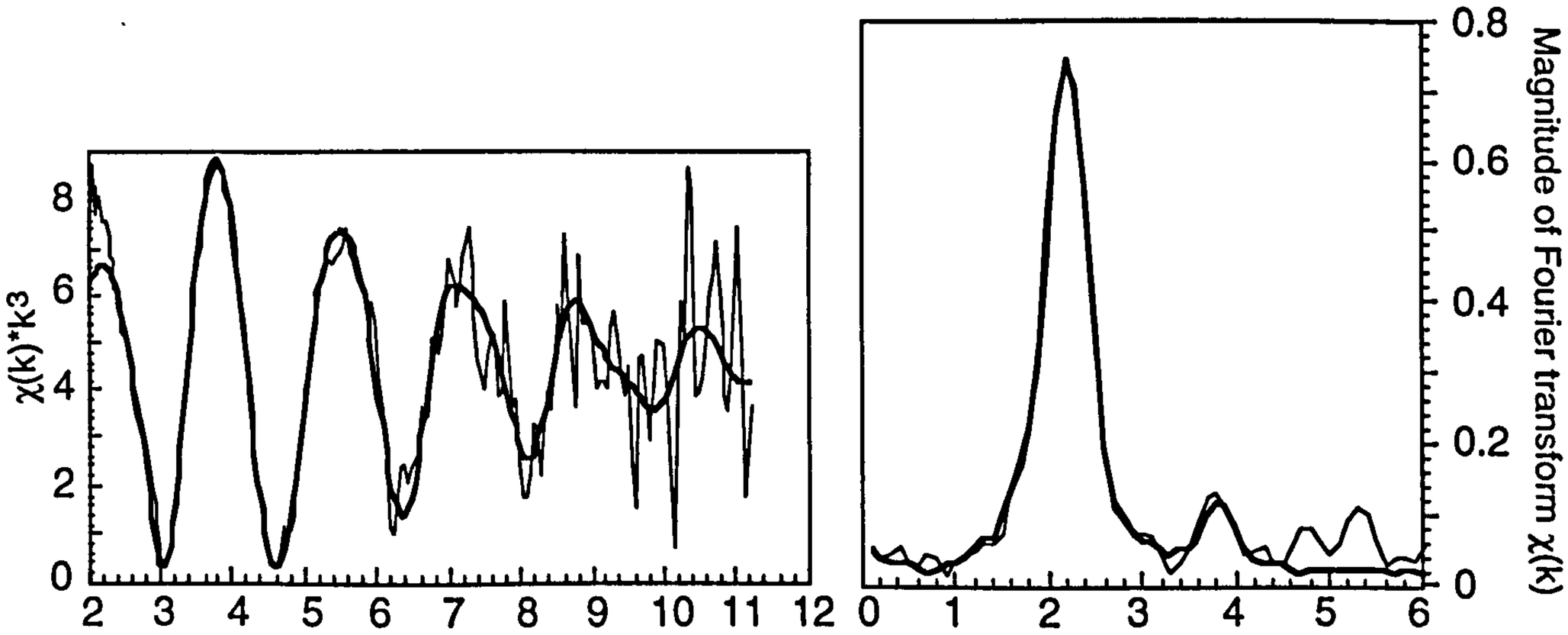

Fig. 1. Representative EXAFS plot (left) and radial distribution function (right) for Cd adsorbed on goethite.

Corner-sharing adsorption can occur if adsorbed Cd forms a bidentate bridge between two adjacent **A**-type hydroxyls or undergoes monodentate adsorption with one **C**-type

hydroxyl (Fig. 2). These two mechanisms are regarded as double corner (DC) and single corner (SC) adsorption, respectively, and can occur on both the dominant (110) faces and the much smaller (110) faces of goethite. Because these DC and SC adsorption complexes result in identical Cd-Fe separations and Fe coordination numbers, they are indistinguishable by EXAFS. However, the supposed inertness of the **C**-type hydroxyls suggests that adsorption is most likely to occur by DC bridging of two **A**-type hydroxyls.

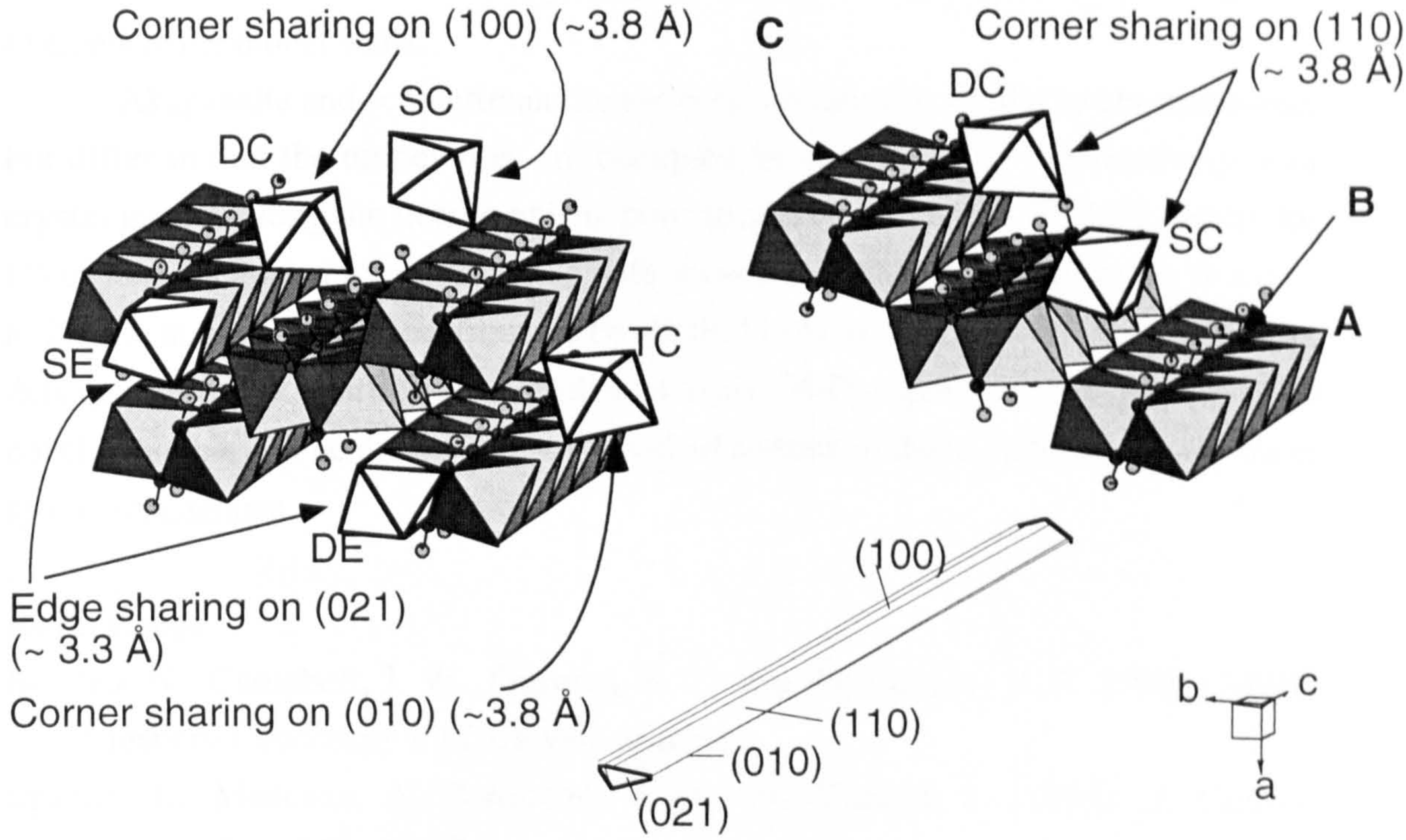

Fig 2. Interpretation of EXAFS results for Cd adsorbed on goethite.

Edge-sharing adsorption is thought to be energetically favoured over corner-sharing adsorption, and the fact that edge sharing is not observed (even at a surface loading as low as 24 %) is consistent with the morphology of goethite crystals: edge sharing can only occur on the (021) faces which constitute just ~5 % of the total surface area.

In contrast to the results from goethite, the Fe shell in the lepidocrocite samples contains 1.1 - 1.5 Fe atoms at 3.26-3.30 Å (indicative of edge-sharing adsorption) rather than the 3.75-3.80 Å. This difference can be explained in terms of crystal morphology: Lepidocrocite crystals are typically more platey and broad than the narrow acicular goethite needles. As a consequence, far more edge-sharing sites are available on lepidocrocite, and it is these which Cd preferentially bonds to. Relatively small changes in pH (6.0 - 7.0) and surface loading (27 % - 45 %) have no significant effect on the EXAFS results from lepidocrocite.

Cryptomelane consists of a framework structure containing 2 x 2 tunnels ~4.6 Å in diameter which are partly occupied by K^+ and H^+. This mineral was able to sorb up to two thirds of the available Cd^{2+} from solution at pH as low as 2.0, with a concomitant release of H^+ to maintain charge balance (although no K was released during Cd sorption). The EXAFS results show that Cd is surrounded by one shell containing 6.5 O atoms at 2.24 Å, and another containing 4.9 Mn at 3.65 Å. These results indicate that Cd sorbed at sites within cryptomelane's tunnel structure, but that it shifted off the ideal tunnel cation position (on the tunnel axis) to allow bonding with O atoms in the tunnel walls.

Akaganeite and schwertmannite are both structurally similar to cryptomelane, but differ in that the tunnel sites are occupied by Cl^- and SO_4^{2-}, respectively, and crystal growth along the needle axis is poor in schwertmannite. EXAFS results for Cd on akaganeite and schwertmannite both show the omnipresent shell of six O atoms at 2.28 Å and a contribution from an Fe shell(s) between 3 and 4 Å. Unfortunately, data quality was not sufficient to resolve an exact Cd-Fe separation, and the only firm conclusion that can be drawn is that Cd sorbed to both of these minerals *via* an inner sphere mechanism.

References

Binsted, N., Campbell, J. W., Gurman, S. J., and Stephenson, P. C. (1991) SERC Daresbury Laboratory EXCURV92 program.

Spadini, L., Manceau, A., Schindler, P. W., and Charlet, L. (1994) *J. Colloid Interface Sci.*, **168**, 73-86.

Geochimica et Cosmochimica Acta (in press)

The Mechanism of Cadmium Surface Complexation on Iron Oxyhydroxide Minerals

S. R. Randall, D. M. Sherman, K. V. Ragnarsdottir
and Clare R. Collins
Department of Earth Sciences, University of Bristol, Bristol, BS8 1RJ, U.K.

Abstract- Many sediment and soil systems have become significantly contaminated with cadmium, and earth scientists are now required to make increasingly accurate predictions of the risks that this contamination poses. This necessitates an improved understanding of the processes that control the mobility and bioavailability of cadmium in the environment. With this in mind, we have studied the composition and structure of aqueous cadmium sorption complexes on the iron oxyhydroxide minerals goethite (α-FeOOH), lepidocrocite (γ-FeOOH), akaganeite (β-FeOOH), and schwertmannite ($Fe_8O_8(OH)_6SO_4$) using Extended X-Ray Adsorption Fine Structure (EXAFS) spectroscopy. The results show that adsorption to all of the studied minerals occurs *via* inner sphere adsorption over a wide range of pH and cadmium concentrations. The bonding mechanism varies between minerals and appears to be governed by the availability of different types of adsorption site at the mineral surface. The geometry and relative stability of cadmium adsorption complexes on the goethite surface was predicted with *ab initio* quantum mechanical modelling. The modelling results, used in combination with the EXAFS data, allow an unambiguous determination of the mechanism by which cadmium bonds to goethite.

Cadmium adsorbs to goethite by the formation of bidentate surface complexes at corner sharing sites on the predominant (110) crystallographic surface. There is no evidence for significant cadmium adsorption to goethite at the supposedly more reactive edge sharing sites. This is probably because the edge sharing sites are only available on the (021) crystallographic surface, which comprises just ~2 % of the total mineral surface area. Conversely, cadmium adsorption on lepidocrocite occurs predominately by the formation of surface complexes at bi- and/or tridentate edge sharing sites. We explain the difference in EXAFS results for cadmium adsorption on goethite and lepidocrocite by the greater availability of reactive edge sharing sites on lepidocrocite than on goethite. The structures of cadmium adsorption complexes on goethite and lepidocrocite appear to be unaffected by changes in pH and surface

loading. There is no support for cadmium sorption to any of the studied minerals *via* the formation of an ordered precipitate, even at high pH and high cadmium concentration. Cadmium adsorption on akaganeite and schwertmannite also occurs *via* inner sphere bonding, but the mechanism(s) by which this occurs remains ambiguous.

Appendix of tables

Table I. Details of analytical methods that were applied to samples of ferrihydrite to which As(V) was added after formation (As-HFO series) and prior to nucleation (pH 4 As-HFO coprecipitate series). All samples were aged at ~ pH 4 in a 60°C oven.

Date	No As-HFO	Low As-HFO	Medium As-HFO	High As-HFO	pH 4 As-HFO
	As/(As+Fe) = 0.0	As/(As+Fe) = 0.0033	As/(As+Fe) = 0.016	As/(As+Fe) = 0.032	As/(As+Fe) = 0.0054
27/6	XRD, S(As)	XRD, S(As), **EXAFS** (3717-3722)	XRD, S(As)	XRD, S(As)	-
	0.0 hr	**0.0 hr**	**0.0 hr**	**0.0 hr**	
28/6	XRD, S(As)	XRD, S(As)	XRD, S(As)	XRD, S(As)	
5/7	-	-	-	-	XRD, S(As), **EXAFS** (3723-3728) **0 hr**
6/7	XRD, S(As)	XRD, S(As), **EXAFS** (3707-3710)	XRD, S(As), **EXAFS** (3706)	XRD, S(As)	XRD, S(As)
	210.5 hr	**210.5 hr**	**210.5 hr**	**210.5 hr**	**20.25 hr**
10/7	XRD, S(As)	XRD, S(As)	XRD, S(As)	XRD, S(As)	XRD, S(As), **EXAFS** (3729-3731; 3735-3737))
	303.5 hr	**303.5 hr**	**303.5 hr**	**303.5 hr**	**113.25 hr**
16/7	XRD, S(As)	XRD, S(As)	XRD, S(As)	XRD, S(As)	XRD, S(As)
	452.5 hr	**452.5 hr**	**452.5 hr**	**452.5 hr**	**262.25 hr**
26/7	XRD, S(As)	XRD, S(As), **EXAFS** (3711-3716)	XRD, S(As)	XRD, S(As)	XRD, S(As), **EXAFS** (3738-3743)
	692.5 hr	**692.5 hr**	**692.5 hr**	**692.5 hr**	**502.25 hr**
11/8	XRD, S(As)	S(As), **EXAFS** (4027-4034)	XRD, S(As)	XRD, S(As)	XRD, S(As), **EXAFS** (4035-4040)
	1076.5 hr	**1076.5 hr**	**1076.5 hr**	**1076.5 hr**	**886.25 hr**

Key:

XRD	X-ray diffraction
S(As)	Supernate [As] (ICP-AES)
EXAFS	Sample analysed by EXAFS. Data on XRSSERV1 in '***' file. Numbers in parentheses are Daresbury laboratory run numbers, the full format of which is r****.dat

Table II. Details of analytical methods applied to samples of green rust to which As(V) was added after formation (As-GR sample series) and prior to nucleation (As-GRCO sample series). Both sets of samples were gradually oxidised to lepidocrocite (γ-FeOOH).

Arsenic adsorbed on pre-existing green rust (As-GR sample series)			**Arsenic coprecipitated with green rust (As-GRCO sample series)**		
Sample	Reaction time (hr)	Details	Sample	Reaction time (hr)	Details
As-GR1	0.83	XRD, S(As), S(Fe)	As-GRCO1	0.92	XRD, S(As), S(Fe), **EXAFS** (4067-4070)
As-GR2	1.17	XRD, S(As), S(Fe), **EXAFS** (4052-4055)	As-GRCO2	2.17	XRD, S(As), S(Fe)
As-GR3	2.08	XRD, S(As), S(Fe)	As-GRCO3	4.00	XRD, S(As), S(Fe), **EXAFS** (4086-4089)
As-GR4	3.17	XRD, S(As), S(Fe), **EXAFS** (4091-4094)	As-GRCO4	6.00	XRD, S(As), S(Fe)
As-GR5	4.50	XRD, S(As), S(Fe)	As-GRCO5	18.50	XRD, S(As), S(Fe), **EXAFS** (4078-4081)
As-GR6	6.00	XRD, S(As), S(Fe)			
As-GR7	20.00	XRD, S(As), S(Fe), **EXAFS** (4058 & 4064-4066)			

Key:

XRD	X-ray diffraction
S(As)	Supernate arsenic concentration (ICP-AES)
S(Fe)	Supernate iron concentration (ICP-AES)
EXAFS	Sample analysed by at 77K on Station 16.5. Numbers in parentheses are Daresbury laboratory run numbers.

Table III. Details of analytical methods applied to a 5.05 gL^{-1} goethite suspension that was contaminated with 29.6 ppm As(V) and then gradually sulphidised. As/(As+Fe) ratio in the system was 6.89×10^{-3}, and 90% of the goethite surface sites were initially occupied.

Sample	Sulphidisation time (hr)	Details
GS2	-	S(As), S(Fe)
GS3	-	S(As), BC, **EXAFS** (4047-4050)
GS4 (08/07/98)	4.5	XRD, S(As), S(Fe), S(ΣS), **EXAFS** (3745-3746, 3747?, 3748-3749)
GS5 (09/07/98)	29.0	XRD, S(As), S(Fe)
GS6 (15/07/98)	174.0	S(ΣS)
GS7 (20/07/98)	287.5	XRD, S(As), S(Fe), S(ΣS)
GS8 (26/07/98)	434.5	XRD, S(As), S(Fe), S(ΣS), **EXAFS** (3750-3753)
GS9 (11/08/98)	816.5	XRD, S(As), S(Fe), S(ΣS), **EXAFS** (4042, 4044-4046)

Key:

XRD	X-ray diffraction
S(ΣS)	Total dissolved sulphides (spectrophotometry)
S(As)	Supernate arsenic concentration (ICP-AES)
S(Fe)	Supernate iron concentration (ICP-AES)
BC	Bulk chemistry (arsenic and iron by ICP-AES)
EXAFS	Sample analysed by at 77K on Station 16.5. Numbers in parentheses are Daresbury laboratory run numbers.

Table IV. Analytical methods applied to EXAFS reference standards in chapter 5

EXAFS standards	**EXAFS** filename	Conditions
As(V) on goethite pH 3.9, 0.24 wt% As, 37 % SL	4023-4026; 3759???	Paste at room temp., fluorescence data on 16.5. S(As)
As(V) on hematite pH 3.9, 0.29 wt%	4019-4022; 4082-4085	Paste at room temp., fluorescence data on 16.5. S(As)
As(V) on lepidocrocite 24/7/98. pH 7.0, 0.3 wt% As, 17% SL	4072, 4074-4076	Paste @ 77K, fluoro. S(As)
Scorodite $FeAsO_4 \cdot 4H_2O$	3758; 4095-4096	3 layers of powder on Sellotape at room temp., transmission data on 16.5. XRD
Orpiment As_2S_3	3755 & 3757(?)	3 layers of powder on Sellotape at room temp., transmission data on 16.5. XRD

Key:

S(As)	Supernate arsenic concentration (ICP-AES)
SL	Surface loading. Values calculated using As(V) adsorption site density of 1.58 sites nm^{-2} derived from Sun and Doner (1996).

Table V. Details of analytical methods applied to Low-, Med.- and High Cr-HFO samples which were progressively aged at 65±3°C.

Sample date	20/3	21/3	23/3	26/3	10/4	10/7
Reaction time (hr)	**0.0**	**24.0**	**70.0**	**144.5**	**501.0**	**2686.0**
Low Cr-HFO *Cr/(Cr+Fe) = 0.052*	XRD, S(Cr),	XRD, S(Cr), BC	XRD, S(Cr)	XRD, S(Cr) **EXAFS (102-S)**	XRD, S(Cr), **EXAFS (100-S)**	XRD, S(Cr), S(Fe)
Medium Cr-HFO *Cr/(Cr+Fe) = 0.111*	XRD, S(Cr)	XRD, S(Cr) **EXAFS (101-S)**	XRD, S(Cr),	XRD, S(Cr)	XRD, S(Cr)	XRD, S(Cr), S(Fe)
High Cr-HFO *Cr/(Cr+Fe) = 0.140*	XRD, S(Cr)	XRD, S(Cr)	XRD, S(Cr)	XRD, S(Cr)	XRD, S(Cr)	XRD, S(Cr), S(Fe)

Key:

XRD	X-ray diffraction
S(Cr)	Supernate [Cr] (ICP-AES)
S(Fe)	Supernate [Fe] (ICP-AES)
BC	Bulk chemical analysis (Fe by ICP-AES, Cr by ICP-MS)
EXAFS	Sample analysed by EXAFS. Data on XRSSERV1 in 'crferrihydrite' file.

Table VI. Details of analytical methods applied to samples of Cr(VI) on green rust that were reacted under anoxic (92-S) and oxic conditions (97-S), and the associated Cr(III)/Cr(VI) on lepidocrocite EXAFS reference standards.

Sample	Reaction time (hr)	Details
92-S	12	Cr(VI) on sulphate green rust (pH 6). Paste @ RT, fluoro., **EXAFS** (44973 & 44975; 45001-45003)
97-S	12	Oxidised portion of Cr(VI)-sulphate green rust coppt. Paste @ RT, fluoro., **EXAFS** (44995-44997)

EXAFS standards	**EXAFS** filename	Conditions
80-S ~100% SL (~1 wt%) Cr(VI) on lepidocroc.	44970-44971	Paste @ RT, fluoro. (same result as 81-S?)
81-S ~50% SL (0.5 wt%) Cr(VI) on lepidocroc.	44953-44955; 44957-44959	Paste @ RT, fluoro.
83-S ~30% SL (0.28 wt%) Cr(III) on lepidocroc.	44961-44962; 44964-44966	Paste @ RT, fluoro.
84-S ~70% SL (0.72 wt%) Cr(III) on lepidocroc.	44967-44968	Paste @ RT, fluoro.

Key:

S(Cr)	Supernate chromium concentration (ICP-AES or ICP-MS)
EXAFS	As data collected at room temperature on station 8.1. Numbers in parentheses are Daresbury laboratory run numbers.
SL	Surface loading - the proportion of available surface sites occupied by sorbed chromium. Values calculated using a surface site density of 1.44 sites nm^{-2} for Cr(VI) on goethite (derived from Mesuere and Fish, 1992), and 1.3 sites nm^{-2} for Cr(III) on goethite (Charlet and Manceau, 1992).